Investigation on the Influence of Different Thermal Processing Conditions in Laser Surface Hardening of Bearing Steel and Bearing Elements

Submitted in partial fulfilment of the requirements for the award of the degree of

DOCTOR OF PHILOSOPHY

By

E. Anusha

(Roll No. 701620)

Under the supervision of

Prof. Adepu Kumar
HOD, Mechanical Engineering Department,
National Institute of Technology
Warangal.

Dr. S M Shariff
Scientist – F, International Advanced Research
Centre for Powder Metallurgy and New
Materials (ARCI), Hyderabad.

DEPARTMENT OF MECHANICAL ENGINEERING

NATIONAL INSTITUTE OF TECHNOLOGY

WARANGAL (Telangana) INDIA 506 004

DECEMBER 2020

**NATIONAL INSTITUTE OF TECHNOLOGY
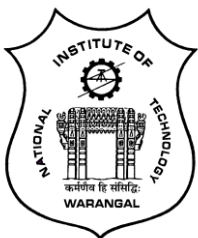WARANGAL (T.S) INDIA 506 004**

CERTIFICATE

This is to certify that the thesis entitled **"Investigation on the Influence of Different Thermal Processing Conditions in Laser Surface Hardening of Bearing Steel and Bearing Elements"**, being submitted by **Ms. E. Anusha** in partial fulfilment for the award of Doctor of Philosophy in the Department of Mechanical Engineering, National Institute of Technology, Warangal, is the record of bonafide research work carried out by her under our guidance and supervision. The results of embodied in this thesis have not been submitted to any other Universities or Institutes for the award of any degree or diploma.

Prof. Adepu Kumar

HOD, Mechanical Engineering Department,

National Institute of Technology

Warangal.

Dr. S M Shariff

Scientist – F, International Advanced Research

Centre for Powder Metallurgy and New

Materials (ARCI), Hyderabad.

NATIONAL INSTITUTE OF TECHNOLOGY
WARANGAL (T.S) INDIA 506 004

Thesis Approval for Ph.D

This thesis entitled **"Investigation on the Influence of Different Thermal Processing Conditions in Laser Surface Hardening of Bearing Steel and Bearing Elements"** which is submitted by **Ms. E. Anusha (Roll No.701620)** is approved for the degree of **Doctor of Philosophy** in Mechanical Engineering.

Examiners

Dr. Satyajit Chatterjee
(Indian Examiner)
Associate Professor, Mechanical Engineering
Department, IIT Indore

Prof. G. V. S. Nageswara Rao
(NITW Director Nominee)
Professor, Metallurgical and Materials Engineering
Department, NIT Warangal

Supervisors

Prof. Adepu Kumar
(Supervisor)
Head, Department of Mechanical Engineering,
National Institute of Technology Warangal

Dr. S M Shariff
(Co-Supervisor)
Scientist – F, International Advanced Research- Centre
for Powder Metallurgy and New Materials (ARCI),
Hyderabad.

Chairman

Prof. Adepu Kumar
Head, Department of Mechanical Engineering
National Institute of Technology Warangal

Date: 14-06-2021
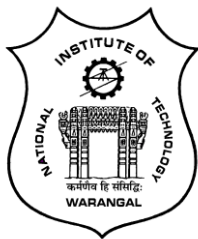
NATIONAL INSTITUTE OF TECHNOLOGY
WARANGAL (T.S) INDIA 506 004

DECLARATION

This is to certify that the work presented in the thesis entitled **"Investigation on the Influence of Different Thermal Processing Conditions in Laser Surface Hardening of Bearing Steel and Bearing Elements"**, is a bonafide work done by me under the supervision of Prof. Adepu Kumar and Dr. S M Shariff and was not submitted elsewhere for the award of any degree.

I declare that this written submission represents my idea in my own words and where other's ideas or words have not been included. I have adequately cited and referenced the original sources. I also declare that I have adhered to all principles of academic honesty and integrity and have not misinterpreted or fabricated or falsified any idea/data/fact/source in my submission. I understand that any violation of the above will be a cause for disciplinary action by the Institute and can also evoke penal action from the sources which have thus not been properly cited or from whom proper permission has not taken when needed.

Date: 14-06-2021   **(Ms. E. Anusha)**

Place: Warangal   Part-time Research Scholar,

                                                  Roll No.701620

Dedicated

to

my

Father Venkat Reddy Epparla

Mother Ramadevi Epparla

Brother Uday Reddy Epparla

Husband Aravind Reddy Yella

Abstract

The present thesis work comprehensively investigates various aspects of controlling heat input in laser surface hardening of bearing steels by varying laser processing parameters, laser processing mode (continuous and pulsed mode), processing under different conditions/setups yielding varied heat-transfer coefficients (involving external fluid contact) and high speed rotating quasi-stationery laser beam processing of thin-sectioned cylindrical parts. The study aims to elaborate the underlying mechanism and improvement in surface properties of the surface transformation hardened layers. Preliminary study conducted on influence of prior-treatment conditions on laser surface hardening of bearing steel using a fiber coupled high power diode laser illustrated influence of prior-microstructure on hardening of bearing steel. Among different prior-treatment conditions, laser surface hardened layer with prior-hardening treatment under spheroidized steel condition (SPH+CHT+LT) yielded highest hardness improvement with dissolution of globular carbides in hard refined martensite matrix coupled with precipitation of nano-carbides. Laser surface hardening processed by different modes showed precise control in peak temperatures with improved cooling rates by adopting Pulsed Wave (PW) mode of processing overcoming deleterious effects of large Heat Affected Zone (HAZ) and retention of core properties. PW mode of processing at optimum conditions resulted in 1000-1020 $HV_{0.5}$ hardness as compared to Continuous Wave (CW) mode processed counterpart whose maximum hardness achieved was 890-910 $HV_{0.5}$, whereas, hardness of untreated prior-hardened (CHT) one was in the range of 760 – 800 $HV_{0.5}$. Tribological performance assessment of laser treated layers, un-lubricated and lubricated sliding wear at appropriate Hertzian contact pressures that simulate close-to-real bearing contact conditions, indicated vast improvement in sliding wear resistance. Results showed five-fold and three-fold improvements in un-lubricated and lubricated conditions of laser processed layer as compared to that of untreated one.

Detailed studies conducted on laser surface hardening of bearing steel by employing different thermal processing conditions - PW mode with fluid contact (PW-UF) induced largest compressive residual stress of -530 ± 10 MPa and exhibited best wear resistance performance. Hardness in the treated layer with microstructural refinement increased with increase in cooling rate in the order of CHT<CW<CW-UF (CW mode with fluid contact) <PW<PW-UF. A two-to-

three fold improvement could be visualized in wear resistance of the laser treated surface processed under PW-UF steel sample when compared to CHT counterpart owing to the vast improvement in hardness and compressive residual stress level.

To overcome the tempering effects in overlapped regions, when processing cylindrical bearing elements such as rollers, a quasi-stationary laser beam processing technique proposed and experimented with integration of a high-speed rotary axis to 6+2 axis robot integrated high power diode laser system to obtain a uniform hardened layer along the entire surface. Optimization of high-speed laser hardening process be effectively achieved by adopting response surface methodology (RSM-statistical model) with desirability approach of optimization of responses such as case depth and mean hardness through-depth and differential hardness along the treated layer length. Maximum hardened depth of 350 µm in 12 mm diameter bearing steel rod with maximum hardness of 860-880 $HV_{0.5}$ and minimal differential hardness of 55 – 60 $HV_{0.5}$ could be achieved with optimal parameters of laser power - 3.5 KW, linear speed - 8 mm/s and rotary axis speed - 2000 RPM. Combining Finite Element Modelling (FEM) and RSM methodologies help facilitated in optimizing high-speed laser hardening process with < 5% error when compared with validated result.

An attempt made to develop and implement the laser surface hardening process on actual bearing elements of taper roller bearing with design and development of various fixturing and processing setups and studied their effects on distortion control and surface properties improvement with core retention. Roundness variations in bearing element such as outer racer was lowest when processed with PW-UF mode (60-70 µm) when compared to other processing modes. Finite element modeling and simulation of the process also could provide close approximation for estimating peak surface temperatures during laser treatment and case depth estimation.

Thesis work is believed to add significant contribution to the existing literature from the point of both industrial importance and academic interest.

TABLE OF CONTENTS

LIST OF FIGURES

LIST OF TABLES

ABBREVIATIONS

Abbreviations	Description
CHT	Conventionally Hardened and Tempered
LSH	Laser Surface Hardening
SPH	Spheroidized
CW	Continuous Wave mode of processing
CW-UF	Continuous Wave mode of processing with fluid beneath the sample
PW	Pulsed Wave mode of processing
PW-UF	Pulsed Wave mode of processing with fluid beneath the sample
HZ	Hardened Zone
SSZ	Super-Soft Zone
TCZ	Tempered Core Zone
UCZ	Unaffected Core Zone
TRB	Tapered roller bearing
HPDL	High Power Diode Laser
HV	Vickers Hardness
FWHM	Full-width Half-maximum
EDS	Energy Dispersive Spectrometer
XRD	X-Ray Diffraction
SEM	Scanning Electron Microscope
BSE	Back Scattered Emission
RPM	Revolutions per minute
RH	Relative Humidity
RSM	Response Surface Methodology
ANOVA	Analysis of Variance
DOE	Design of Experiments
E-MAqS	Emission Matrix Acquiring System
FEM	Finite Element Modelling
TCD	Total hardened case-depth
MHC	Mean hardness cross-sectional

DHL   Differential hardness longitudinal

CHAPTER 1

Introduction

1.1   About bearing and bearing elements

Bearing is a kind of machine part that supports shaft and transmit load from shaft to other connected parts. There exist movement and interaction within bearing elements during operation, such as rolling and/or sliding between rollers and raceways and frictional contact with external load [1-3]. Bearings are broadly classified into category of rolling and plain type. Rolling bearings provide advantages of low friction resistance, subtle starting performance, high efficiency, easy lubrication, and good interchangeability so that they can be widely used for diverse application [4]. Rolling bearings entail low friction by rolling with balls or rollers and minimize relative motion between them. A bearing assembly generally constitutes inner racer, outer racer, rolling elements such as rollers or balls and a cage. Bearing racer functions for supporting and locating rotating elements and/or fixed parts, wherein, its inner face having grooves constrain the passage of rollers/balls. The load bearing carrying of a bearing is determined by the sum of all contact points between rolling elements and racers, maximum contact stress at all these points summed up together [5]. In some cases, inner and outer racers are replaced by a corresponding mainframe. Depending on application requirements, some bearings are assembled with dust cover, sealing ring and adapter sleeve for adequate mounting and adjustment. Since rolling bearings are not only used in everyday objects such as blenders or bicycles, but also in complex machines such as jet engines, generators, motors etc. myriad applications possible.

Bearings are of different types based on applied load, speed, dimensions, lubrication, and temperature requirements. Deep groove ball bearing (Figure 1.1a) is one such versatile, robust, and widely used type applied for high speed and axial loads due to deep fitting of balls inside the

grooves of raceway [6]. Another type of ball bearing is with angular contact (Figure 1.1b) designed to support load radially and axially shouldering opposite sides of inner and outer raceways [7]. Ball bearing self-aligned (Figure 1.1c) have concave outer raceway with two inner raceways and two rows of balls to accommodate shaft misalignment, whilst maintaining low friction [6]. In contrast, cylindrical ball bearings (Figure 1.1d) accommodate high radial load at moderate speeds coupled with adequate misalignment resistance due to high contact between rolling elements and racers. Additionally, slight cambered profile across raceways help facilitate elimination of stress concentrations. Tapered roller bearings (Figure 1.1e) are another type similar to cylindrical ones with tapered raceways and rolling elements that facilitate accommodating heavy combined loads [8]. Roller bearings of spherical type (Figure 1.1f) are another type similar to self-aligning ball bearings but with barrel-shaped rolling elements, which accommodate higher radial load carrying capacity with self-aligning capability. Needle bearing (Figure 1.1g) is another type of bearing akin to cylindrical roller bearing but with thin and long rollers that offer low load bearing capacity with high-speed movement, oscillatory motion and lower radial dimensions [9]. Apart from such types, thrust bearings (Figure 1.1h) are another well-known type having contact angle of ninety, operable at high speed and axial load [9].
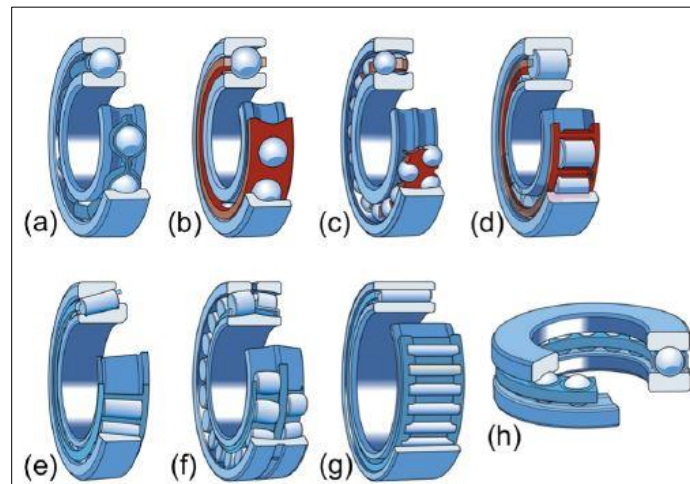
Fig. 1.1 Configurations of different bearings used in industrial applications [14]: a) deep groove (ball) , b) angular contact (ball), c) self-aligning (ball), d) cylindrical (roller), e) tapered (roller), f) spherical (roller), g) needle (roller) , h) thrust (ball)

The current study targets development of laser surface transformation hardening process for thin-sectioned high-precision tapered roller bearings. These type of bearings are generally

designed to withstand high radial and thrust loads operated at moderate to high speeds. Another unique advantage of this type of bearing is its capability to withstand high repeated shock loads. The inner and outer racers possess raceways segmented with cones and rollers tapered to their conical contact surfaces of the raceways and the roller axes projected, all converging at a common point on principal axis of the bearing. This type of conical geometry is preferred to provide high contact patch, which permit greater load carrying capacity than that of spherical (ball) bearing. Wear will degenerate its tolerance normally held in the bearing and can lead to other bottlenecks. Pure rolling in a tapered roller bearing can effectively reduce rapid wear. As the flange of the inner ring guides roller, it prevents roller from sliding out at high speed. The axial load bearing capacity of a bearing is largely determined by its contact angle α .Larger the half angle of these cones, larger the axial force the bearing can withstand. Tapered roller bearings are separable elements such as outer racer, inner racer, rollers and cage assembly. Appropriate internal clearance is generally provided during mounting by axial position of the cone relative to the cup. Figure 1.2 illustrates a typical steel tapered roller bearing assembly comprising outer racer (cup), inner racer (cone) and tapered rollers used in the current study. The principal advantages of using tapered roller bearings includes dimensional stability, long life even in contaminated lubricant and durable steel cage.
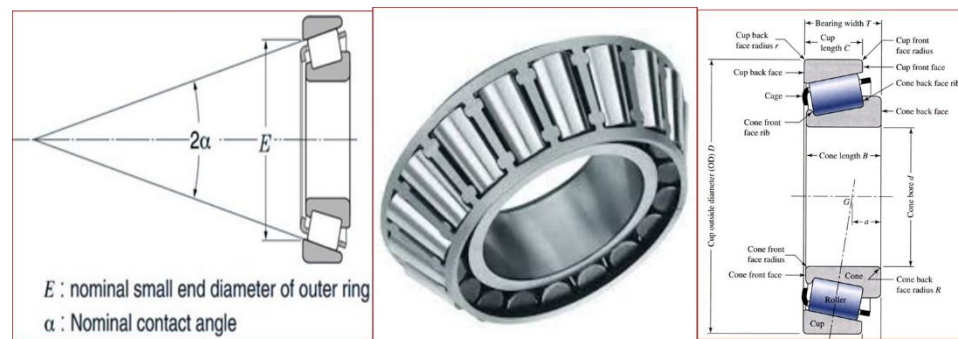
Fig. 1.2 Elements in Tapered roller bearing assembly [10]

1.2   Steels for roller bearing application

For mechanical bearings, basic properties of material depend on the functionality and design of the bearings. In general, bearing steel should have high contact fatigue strength; better wear resistance, high yield strength, hardness, toughness and good dimensional stability [11, 12].

In order to ensure these, the chemical compositional cleanliness, microstructure with carbide inhomogeneity, surface decarburization layer needs to be controlled strictly for its metallurgical quality. Additionally, superior machinability, high dimensional accuracy of the steel part needs to be maintained precisely. As Zaretsky mentions, Stribeck and Hess's work demonstrated on tool steel entailed its suitability for bearing as early as 1900. This further enabled application of high carbon and high chromium steel (1C-1.5Cr) for rolling bearing applications [13]. Since, initiation of manufacture in 1905 by Fichtel and Sachs, variation of 1C-1.5Cr steel, nowadays, referred to as 52100 type steel, is most widely applied as bearing steel [14, 15]. Bhadeshia listed numerous alloy variations possible in the bearing steel [14]. Nonetheless, many applications still rely on a handful of alloys chosen based on operating temperature, ambient condition and toughness (Table 1.1). If the working temperature fall below 422K, the choice of alloy goes for through-hardened AISI 52100, else, case-hardenable steel AISI 8620 or AISI 9310. In few stringent and adverse environment, corrosion-resistant martensitic stainless steel such as AISI 440C and through-hardened tool steel such as M50 and case-carbonitrided M50NiL and corrosion-resistant AMS-5749 are also used for bearings [13]. In the present study, AISI 52100 / EN-31 bearing steel has been chosen for all test-coupons such as flat plates, cylindrical rods and tapered roller bearing elements.

Table 1.1 Chemical composition of some common bearing steels [13, 14]

Alloy	C	Mn	Si	Cr	Ni	Mo	V	S	P
AISI 52100	1.00	0.35	0.39	1.50	-	-	-	<0.025	<0.025
AISI 8620	0.21	0.80	0.25	0.50	0.55	0.20	-	<0.040	<0.035
AISI 9310	0.10	0.54	0.28	1.18	3.15	0.11	-	<0.025	<0.025
AISI 440C	1.03	<1.0	0.41	17.30	-	0.75	0.14	<0.014	<0.018
M50	0.80	0.30	0.25	4.00	-	4.25	1.00	<0.030	<0.030
M50 NiL	0.13	0.30	0.25	4.00	3.50	4.25	1.20	<0.030	<0.030
AMS 5749	1.15	0.50	0.30	14.50	-	4.00	1.20	<0.010	<0.015

1.3   Manufacturing process for bearings

Figure 1.3 illustrates a typical industrial manufacturing process for a tapered roller bearing. The process involves various stages from selection of appropriate raw material to the final finishing operation required for its manufacture. Melting of steel is generally carried out at about $1700 - 1730^0$C to purify steel with maximum cleanliness before casting into blooms/billets with control of requisite chemistry designated for bearing steel. From the preliminary block, it is formed to necessary required shape and size for production depending on the types of bearing required, such as wire, plate, tube, bar and so on. In case of producing bearing elements such as racers, blocks are forged into rings by blanking, whereas, wires are extruded from raw material to requisite diameters for rollers. The basic alloying chemistry of steel for bearing, especially, En31 or AISI 52100 grade, is maintained in the range of $1.0 - 1.1$ % for C, $1.35 - 1.65$% Cr, $0.25 - 0.45$% Mn and $0.15 - 0.35$% Si. Depending on the bearing size, the forming process will be in multiple stages with multiple passes and stations. Generally, induction heating with working temperature ranging from $850 - 1150^0$C is preferred. The rolled bar is cut into size of required diameter and fed to the press to form the work piece. The preformed work piece (in case of racers) is subjected to press piercing in various stations. Figure 1.4 illustrate various production stages for manufacturing of bearing rings [16]. The principal reason of bearing racer forging was to obtain the semi-finished ring as per the intended design to reduce material wastage and mechanical machining work as much as possible. Additionally, the process intended to eliminate inner defects present if any, in the material, and ensure good compactness and thereby enhance the life of bearings. After forging, turning is the next step involved for semi-finished bearing ring and roller. The racer rings taken from the tube are hot-rolled and then subjected to spheroidization and then machined in two steps. The first step of turning involves machining of inner diameter of the ring by longitudinal turning [17]. In a second step, their outer diameter machined by longitudinal turning as well.

After turning, heat treatment is the next critical step involving heating and cooling under controlled atmospheric condition to impart requisite desired characteristics and properties. Critical property of the steel material such as hardness, strength, fracture toughness, machinability is maintained by controlling microstructure and stress state. Initially, the soft-machined material is fed into furnace, washed and then sent to a heating chamber to austenetized in the temperature of range of $840\ ^0$C - 850^0C temperature. Subsequent to soaking of the part for designated duration, in the next chamber, it will be quenched in an oil tank at 25^0C. After

quenching, the semi-finished bearing element will be tempered for about 90 minutes at 170 ^{0}C before drying and cooling in air. Thus, the bearing material is hardened to obtain the desired properties. Figure 1.5 illustrates the systematic flowchart of the entire heat treatment process involved for bearing elements in an industrial setup. As laser surface treatment of the present study is a surface hardening process, different types of through-hardening, case hardening and surface hardening process practiced in bearing industry are discussed in detail in later sections of the thesis.
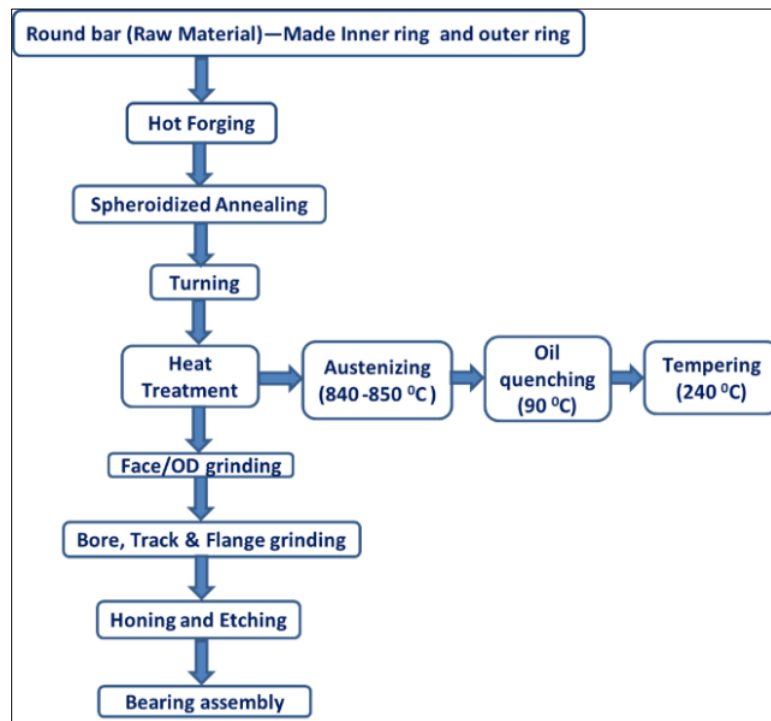
Fig. 1.3. A typical manufacturing process for bearing
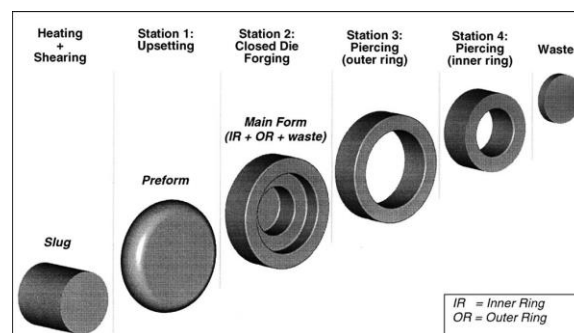
Fig. 1.4. Production stages of bearing rings [16]

6

Subsequent to heat-treatment, grinding is carried out as final process for bearing ring and roller in most of the cases, also called as finished product processing. The grinding process generally involves in two phases; one prior to heat treatment and other finish grinding. For the grinding of the outer ring (cup), outer diameter, face and track grinding are performed sequentially. During the entire grinding process, coolant is always supplied to flow between the wheels and work piece to prevent burning of metal on the surface. After OD Grinding operation, the job is subjected to Face and Track Grinding operations. Subsequent to track grinding, outer ring, is subjected to honing, a known superfinishing process. The same process in sequential way applies to the inner ring (cone). Similar to bearing racers, rollers are also subjected to end grinding where the end-face of roller is grinded after end-face grinding and finally to honing as super finishing process.

Super finishing is the most important process involving removal of very small amount of material (for ex. 5µm to 0.01mm) to finish the work piece surface. Some super finishing operation are honing, lapping, buffing etc. In Taper Roller Bearing, honing is generally carried out on ID Track (cup), OD Track (cone), and Flange surfaces. Honing is mainly used to correct some out of roundness, taper, and tool marks left by previous operation or axial distortion. Honing is generally done by bonded abrasive grit stick stones (of aluminium oxide or silicon carbide) applied on surface to be honed under controlled pressure and with a combination of rotary and reciprocating motion of stones. Due to relative motion between work piece and abrasive stones and its hardness, a very small amount of material get removed from the work piece
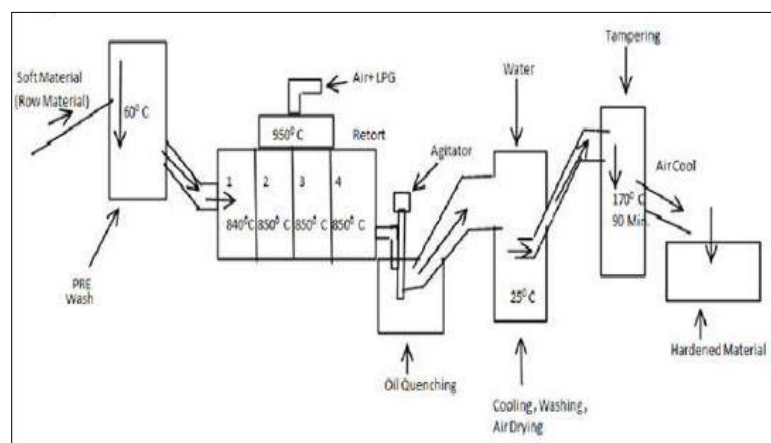
Fig. 1.5. Heat treatment process for bearing rings

Subsequent to manufacture of all bearing elements, assembling of bearing is the last stage of manufacture is very important for its performance. The purpose is to assemble the finished components constituting bearing elements with precision and clearance fits. Appropriate steps involved in assembling of bearing include, dimensional checking, washing, marking, rough assembling, weight measurement, demagnetization, noise/vibration testing and oiling. Nowadays, assembling of bearings are carried out by employing specially designed robots with high precision and speed. The final assembling operation involves riveting of racers already placed with rollers with retainer and sealed. The assembled units are cleaned and greased by squeezing evenly into the raceway, before, sealing, if necessary. Appropriate tests for bearings carried out for their durability, performance and noise level evaluation prior to shipping.

1.4 Methods of heat treatment for bearings

As previously mentioned, heat treatment plays a pivotal role in obtaining desired properties after metallurgical characteristics, necessary to meet application requirements. Anticipated metallurgical properties in bearings include chemical cleanliness, hardness/strength, and microstructural control. Thus, the method of hardening treatment depends on chemical composition of the steel and its hardenability associated with material characteristics. Commonly used heat treatment processes [as shown in Figure 1.6] used for bearing include:

Through Hardening	
Martensitic heat treating	
Bainitic heat treating (Austempering)	
Diffusion Methods	**Coating and Surface modification**
Carburising and hardening	Hard chromium plating
Nitriding	Electroless nickel plating
Nitrocarburising	Thermal Spraying
Carbonitriding	Weld hardfacing
Applied energy methods	Physical vapor deposition
Flame Hardening	Chemical vapor deposition
Induction Hardening	Ion Implantation
Electron-beam Hardening	

Fig. 1.6. Heat Treatments and Surface modifications methodologies used for Bearings

1.4.1 Through hardening of bearing

Two most common methods applied for bearing are martensitic heat-treating and bainitic heat-treating. As most commonly used steel in current bearing is high-carbon high-chromium steel [13-14, 18], standard practice of martensitic hardening impart to it. The process cycle include austenitization at 815-855^{0}C for 15 – 40 minutes (additional ½ hour for every inch of thickness) followed by quenching to 150 ^{0}C in agitated oil or water and then tempering at 150– 230 ^{0}C for 2–4 h, depending on the steel chemistry and part design. Tempering temperatures vary depending on the desired hardness intended for the bearing based on application (Figure 1.7 illustrates hardness that can be obtained in tempered bearing steel based on tempering temperature). Another alternative to martensitic hardening of through-hardening processes in bearing steels is bainitic heat-treating, also called an austempering. As against martensite formation in martemepering, bainite is produced in isothermal austempering treatment. The mechanism of bainite formation in this heat treatment method constitute shear as well as diffusion [19]. Although, bainite transformation imparts better toughness compared to martensite, prolonged treatment duration add additional cost to the manufacture [14].
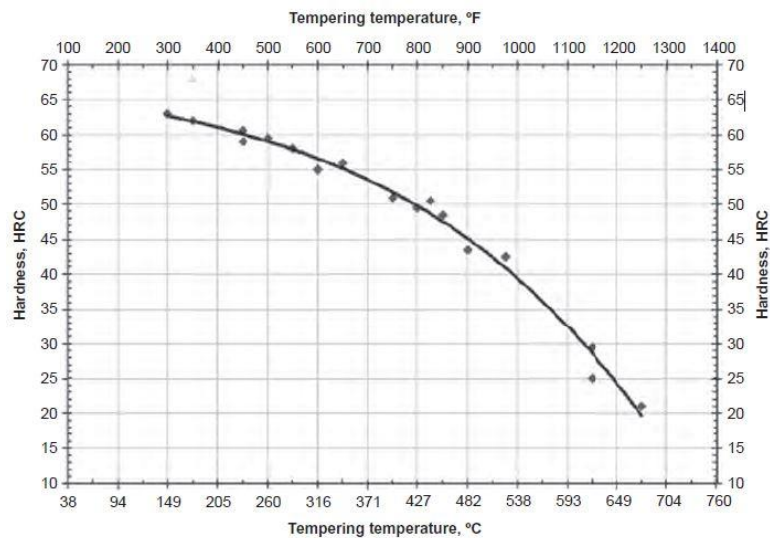
Fig. 1.7. Tempering response of hardened SAE 52100 steel [19]

1.4.2 Diffusion based surface modification processes for bearings

Apart from through-hardening methods, different variety of surface modification techniques such as diffusion coatings with addition of carbon or nitrogen are also used for

bearings, especially low-carbon low alloy steel bearings. Generally, termed as carburising or carbonitriding or nitro-carburizing followed by hardening and/or nitriding [20]. In carburizing, carbon is diffused into the surface, whereas, in nitriding, nitrogen is diffused. The hardness obtained in the case due to carburising is governed by the amount of carbon and its depth as a function of carburizing time. As nitriding involves low temperature ($500 - 550^0$C), distortion will be lower as compared to that of carburising. However, in case of carbonitriding, wherein both nitrogen and carbon diffuses, higher hardness can be achieved in the treated case, as compared to that of even high alloy carburised and hardened steel. Although, such diffusion methods are effective in enhancing hardness in low carbon low alloy steels, certain disadvantages in terms of requirement of masking for parts, loss in toughness due to prolonged process duration and difficulty in disposal of toxic residual elements persist.

1.4.3 Other case hardening methods

Instead of diffusion-control batch hardening of carburizing and/or carbonitriding followed by hardening and/or nitriding, selective localized hardening by employing tools such as flame, induction, arc, plasma and electron beam are applied for bearings, depending on the application. In flame hardening, an oxy-acetylene flame will be utilized for surface heating to above upper critical temperature followed by quenching [Figure 1.8]. In case of induction hardening, heat generated by eddy currents produced from electromagnetic induction of the coil produces hardened case [Figure 1.9] without melting and relatively high coverage rates possible. The process is easily adoptable for symmetric components, whereas, desired results cannot be achieved in parts of complex geometries. Instead of flame, a welding arc or plasma can also be used for imparting localized surface hardening in some components based on the application requirements with affordable cost and quality. The process is more controllable than flame hardening and thereby distortion control. Another similar localized surface hardening process in line these case hardening methods is electron beam hardening, wherein, a defocused electron beam is used as heat source to harden the surface of a part with precision and cleanliness.
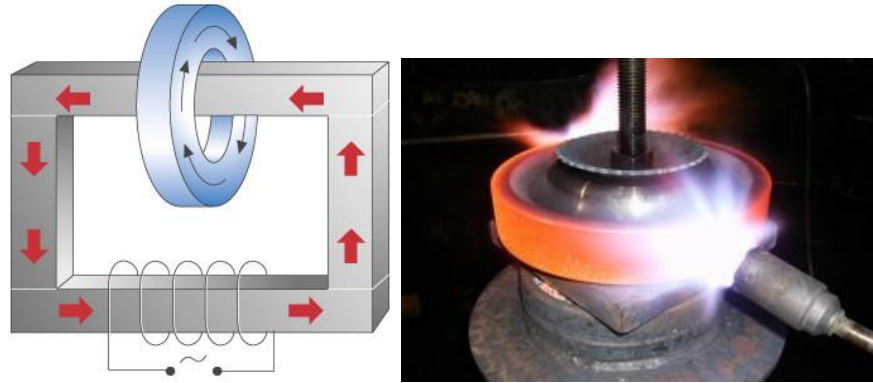
Fig. 1.8. Flame hardening on bearing; Fig. 1.9. Induction hardening on bearing

1.5   Mechanical and tribological properties required for bearings

Bearings need to possess properties (as shown in Figure 1.10) to ensure adequate bearing life. Apart from the main requirement of rolling contact fatigue resistance coupled with wear resistance, various other mechanical and tribological properties such as dimensional stability, rolling contact fatigue, wear, compressive strength, impact resistance, corrosion resistance, seizure resistance, conformability are required to be imparted for improving bearing life, depending on the application of the bearing. Load bearing capacity of a bearing is often considered as fatigue strength in terms of a maximum value of cycling stress the bearing steel can withstand after infinite cycles. Hence, if bearing loading exceeds fatigue strength, fatigue cracks nucleate and propagate leading to flaking of material and thereby catastrophic failure. In order to avoid fatigue failure, the bearing steel should have adequate endurance limit and requisite compressive strength to withstand shape change and dimensional stability. If bearing elements are properly loaded and operated under suitable elasto-hydro-dynamic lubrication, then material fatigue limits its working life [22]. Dimensional stability is another most important factor to be maintained in all bearing elements of the assembly. Since, bearing elements are often hardened, retained austenite that remain in transformed structure of the part entail dimensional change in the geometry of the bearing element after completion of transformation. If this dimensional change is sufficiently large, cracking occur that makes the rejection of the bearing. Thus, control of retained austenite in hardened bearing parts to needs to be ensured for improved fatigue life. Apparently, imparting compressive residual stress in the hardened bearing element is

11

another way of reducing crack propagation rate and thereby improve contact fatigue resistance and bearing life.

Rolling contact fatigue (RCF) often referred as a type of fatigue caused due to rolling between rollers and raceways produces alternating stresses over a small volume. In bearings, failure often happens due to RCF that manifests in different modes with most widely observed on surface or subsurface originated spalling as shown in Figure 1.11 [23]. In current industrial practices, high-quality bearings have superior surface finish with clean lubricating environment to extend further working life. Often, subsurface spalling mechanism is dominant factor to assess life of such bearings [25]. In contrast, with classical fatigue that occur due to bending or torsion or shear, by uniaxial normal or shear stress, RCF is a multi-axial fatigue problem. Figure 1.12 illustrates one such illustrating RCF case depicting stress history. Lundberg and Palmgren postulated that RCF is a shear driven phenomena observed with alternating shear stress [26].
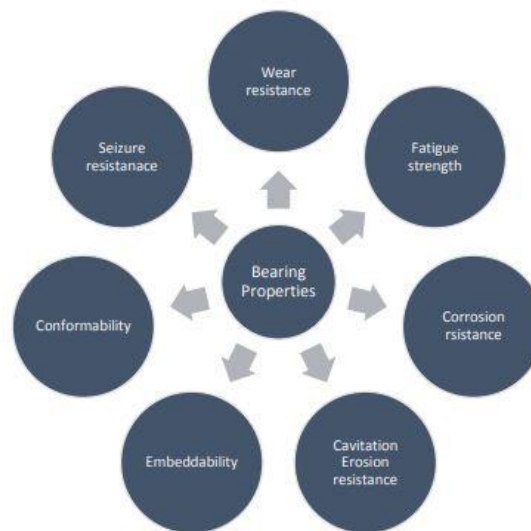
Fig. 1.10. Desired properties applicable to bearing [21]
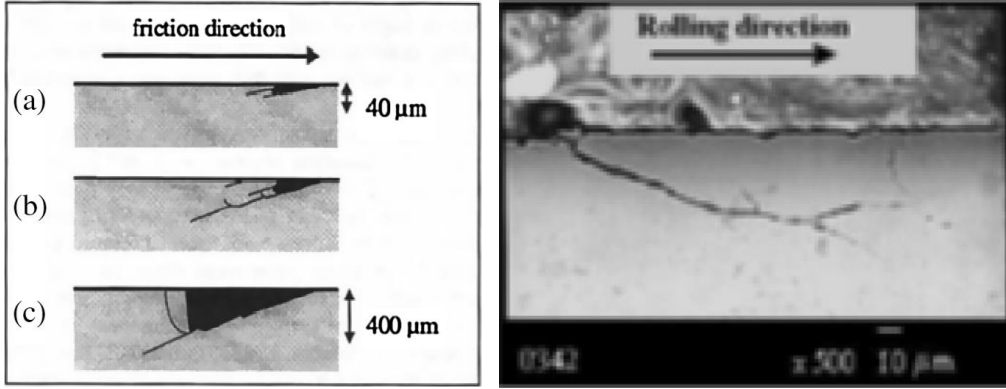
Fig. 1.11. Typical failure defects observed in bearing over its usage: (a) surface pitting and (b) subsurface spalling [24]
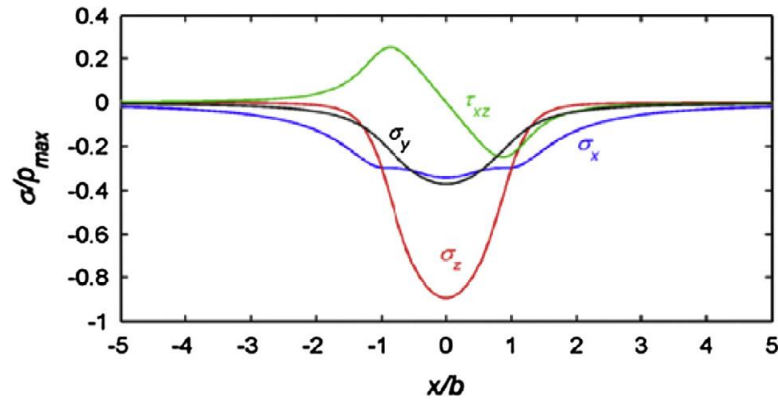
Fig. 1.12. Typical history of RCF stresses under plane strain condition [24]

Impact strength is another important property required for bearing to withstand sometimes fracture because of sharp blows a bearing undertakes. High impact strength provides additional protection against cracking and thereby prevents spalling in racers of a bearing. This entails balancing of mechanical properties with control in retained austenite content in a bearing application (Figure 1.13). Apart from tribological properties requirements in a bearing such as low friction and good wear resistance, other properties such as seizure resistance, conformability and embeddability are also required for a bearing assembly [27]. Often wear in bearing happens due to the prevailing adverse non-ideal operation conditions associated with contamination or poor lubrication or general misuse as depicted in Figure 1.14. The removal of surface material in bearing is often mild in asperity length scale by adhesion and abrasion or spalling or pitting damage [28]. Nonetheless, failure of bearing was found to often associate with wear and fatigue.

13

Therefore, bearing steel is expected to possess as much higher surface hardness to impart higher wear resistance and fatigue life. Apart from the high dimensional stability, wear and RCF resistance, a bearing is expected to possess seizure resistance to survive momentary contact with counter surface when oil film break down occur [29]. The mechanism of seizure-failure was often found to depend on lubrication, steel property, contact configuration and working environment [30]. Apart from the seizure resistance, appropriate conformability, embeddability and corrosion (oxidation) resistance were also needs to be maintained in the bearing elements to entail desired bearing life with intended performance.
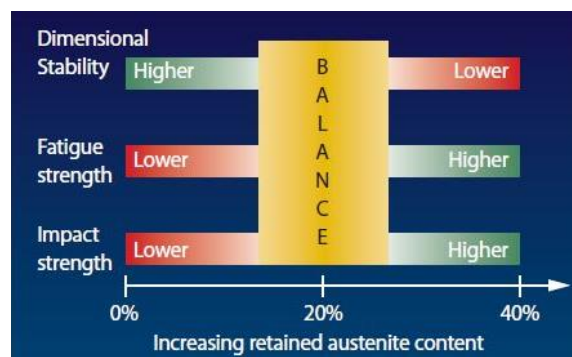
Fig. 1.13. Balancing of properties for a bearing with retained austenite content [19]

Fig. 1.14. Lubrication failure of bearing [28]

1.6 Challenges to enhance performance of bearing steel and bearing elements

Although bearings processed with conventional methods involving through hardening, high-frequency induction hardening, flame hardening, and case hardening technologies had shown considerable promise in improving their strength and thereby fatigue life, they were found to fail over a period of their usage. Although enhancement in surface hardness with conventional process improve wear resistance, high post-process grinding requirement and improper clearance control fit, owing to lack of distortion control in the treatment processes due to uncontrollable heat input. The common problems encountered in bearing heat treatment process are deformation due to heat treatment, overheating, surface decarburization and cracking during to quenching.

When a steel bearing element is through or case hardened, internal stresses developed within the material alters differently based on part design and processing conditions.. Since it can vary with processing temperature, rate of heating, rate of cooling, ambient condition, part shape and size, part deformation or distortion is obvious. Impact collisions with movement of parts during heat treatment can also cause significant distortion or surface damage of the part. However, this distortion be reduced and avoided with improved heat treatment operation. Overheating is another problem often encountered during heat treatment of steel bearing components. Increase in the retained austenite content in the superheated structure leads to poor dimensional tolerance. Due to the overheating of the quenched structure, the coarse crystal of the steel causes reduces toughness, the impact strength reduces and as a result, life of the bearing shortens.

Many a times, hardness distribution in the heat treated bearing element remains non-uniform and non-compliant with the surface contour due to several factors like inadequate heating, irregular quenching, uncontrollable cooling rate and heavy distortion effects. In case or through hardening, surface decarburization may seriously reduce hardness and thereby impair wear resistance and fatigue life. During the heat treatment of steel bearing elements, sometimes surface oxidizes to reduce carbon diffusion on part surface, resulting in surface decarburization. If the depth of decarburization exceeds beyond post-process machining allowance, then part entails rejection. Sometimes, crack forms in the bearing part due to the internal stress develops during quenching. The reason for such cracking are often attributed to excess quenching temperature, irregular cooling rate within the portions of the part and non-uniform liquid contact

within the part. The stress developed when metal mass volume change happens is greater than the fracture strength of the steel, internal defects induce in the steel during quenching and as a result quenching cracks appear on surface or part of the component hardened.

Therefore, there is a need of a system for treating the surface of bearing element and a process thereof alleviating the mentioned drawbacks of the conventional surface treatment systems. This envisages exploring of newer surface modification technique that can impart high surface hardness with enhanced compressive residual stresses and thereby improve load bearing capacity and life.

1.7   Promise of high power lasers for surface modification

Any conventional heat source such as a flame, plasma, induction etc. harden surface of a hardenable steel (without addition of any extraneous material), it possess certain inherent disadvantages like poor controllability, complex design requirements, possibility of part distortion environmental pollution etc. These make their utility difficult for surface modification of complex contours, specific locations like contact surfaces of racers and rollers, which are curvilinear with small sectional thickness of tapered roller bearing component is a challenging project.

Laser surface hardening (by transformation hardening or re-melting or glazing or shock hardening) has become widespread and popular in diverse industrial sectors. Laser transformation hardening of steel surfaces has many advantages over other conventional techniques (like casehardening with carburizing, induction hardening, nitriding etc.). These include high productivity, high speed processing, high precision, no quenching medium requirement, minimal distortion, ease of integration with CNC/Robotic machines, multiple-component processing capability, multiple-process adaptability with a single laser source and many more. As a result, the technology of laser surface hardening has become a powerful surface modification tool increasingly applied in various applications of generic as well as complex engineering solutions in diverse industrial fields.

1.7.1 Lasers for surface modification applications

Lasers are powerful devices capable of producing concentrated coherent light beams by stimulated electronic and molecular transitions that can be gainfully utilized for various purposes. From an engineering standpoint, laser is a non-contact energy input tool that transfers energy to electromagnetic radiation to specific optical beam to irradiate any material of interest for the application intended. The lasing can be from a primary source into a beam of electromagnetic radiation at some specific frequency. The lasing can be in any active medium, which may be a gas or a solid or a liquid, when excites by pumping energy for short duration, result in spontaneous emission of radiation and governed by the characteristics of the optical cavity. The significance of these energy emitting sources for surface modification techniques arises due to their inherent ability to impart rapid heating and cooling rates in the near surface region while the deposition energy is inadequate the temperature of the surrounding bulk material [31]. This entails precise control altering the near-surface region to be modified under extant conditions with negligible detrimental effect on bulk properties of the material/part.

The types of lasers widely acknowledged to be suitable for manufacturing or modification processing are CO_2, Nd:YAG, Diode, Fiber, Disc etc. Lasers are in use for materials processing for various manufacturing operations like marking, cutting, welding, drilling, hardening, cladding, alloying, glazing, rapid prototyping etc. [31]. Integration of lasers with CNC or Robotic workstations has enabled increasingly precise processing of complex shaped components. The utility of laser for any specific process is governed by factors constituting principally laser power density and laser interaction time involved as illustrated in Figure 1.15 [32]. The optical cavity and the medium of lasing determine output laser beam characteristics that govern its suitability for variety of processing applications.

Variety of surface modification techniques are possible by employing laser as a powerful heating tool. With deposition of suitable coatings (supplied in powder or wire or otherwise forms) it is possible to modify the surface of by alloying / cladding. Laser surface modification by alloying / cladding is also widely used to tailor the surface of components to impart suitable properties like wear resistance, corrosion resistance etc. and thereby enhance life by manifold [33]. Reclamation of the worn out or defective components by laser surface cladding is also an emerging technology. High cooling rates associated with laser cladding/alloying process facilitate in producing refined microstructures that gainfully utilize for imparting improved

properties in the coatings. The excellent metallurgical bonding possible with minimal dilution facilitate in reducing distortion and post-process machining requirements. With even mixing the coating materials in definite proportions, it is possible to produce functionally graded and composite coatings to suite multifunctional requirements of the coating [34].

With recent developments, it has become realistically possible to integrate compact laser to even conventional processing tools of welding, induction hardening, machining etc. to make hybrid-processing machines. The distinct advantage of producing minimal heat affected zones and extremely refined microstructures makes the laser surface modification process a powerful tool to impart novel coating properties. The laser surface irradiation with or without extraneous material addition induces very exotic phenomena in coupling thermal and structural fields [34-35]. Due to the precise control of conditions being possible with laser with wide variation in parameters (spatial and temporal distribution), well-defined textured surfaces can also be conceived depending on the material involved. High cooling rates associated with laser processing, can also facilitate to produce exotic and non-equilibrium structures that stimulate great research interest for seeking novel properties and functions. Depending on the power density, interaction duration and extraneous material added, diverse surface engineering and/or coating technologies be realized as depicted in Table 1.2 [36]. Elaborating these different processes is beyond the scope of the present research as laser surface transformation hardening process is the current scope to this thesis work.
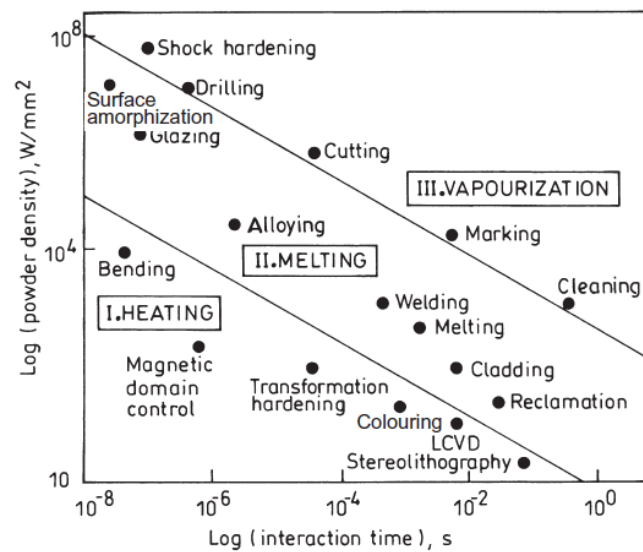
Fig. 1.15 Spectrum of power-density and interaction time range applicable for various processes using laser [29]

Table 1.2. Various laser based surface engineering techniques similar to laser surface hardening [28]

Technique	Laser Source	Description
Shock hardening	CO_2, Fiber, Nd:YAG, Disc, Excimer	Induces shock waves at surface using laser pulses to create hardened layer
Laser glazing	CO_2, Fiber, Disc, Nd:YAG, Diode, Excimer	Produces ultrafine microstructure in glasses
Surface alloying	CO_2, Fiber, Disc, Nd:YAG, Diode	Selective addition of alloy to change surface properties
Surface impregnation	CO_2, Fiber, Disc, Nd:YAG, Diode	Fusion with addition of a solid fraction, e.g. Tungsten carbides
Surface texturing	CO_2, Fiber, Disc, Nd:YAG, Excimer	Develop patterns on surface
Photochemical modification	Excimer	Produces local changes for marking, bonding or change of surface hydrophobicity
Surface ablation	Excimer, Fiber, CO_2, Nd:YAG	Controlled removal of surface layer without damaging the substrate
Surface refining	Excimer	Rapid, shallow melting to vaporize inclusions and impurities

1.7.2 Lasers surface hardening

Laser surface heat treatment / hardening is a selective surfacing process (without addition of any material) wherein the laser beam of specific size and intensity distribution, with required power density, scans the desired surface of material (steel) resulting in a hardened case under extremely high cooling rates upon self quenching. The process can yield a case hardened to a

desired depth with required metallurgical and mechanical properties, depending upon the material characteristics and processing parameters adopted. The principal mode of transfer of heat in laser surface transformation hardening process is conduction into the substrate and is mainly governed by its thermal cycle leading to solid-state phase transformation. Laser surface heat treatment is broadly classified into four different categories, namely transformation hardening, re-melting, glazing and shock hardening, with power density - interaction time window being distinct for each case. Shock hardening and glazing generally required lasers with high peak powers and low interaction times, whereas, laser transformation hardening and re-melting process are conventionally implemented with continuous wave lasers. Figure 1.16 schematically illustrates a typical laser surface hardening process.

Among the above four different categories of laser assisted heat treatment processes, surface transformation hardening without any trace of melting is most widely used in industrial applications. In transformation hardening, the part is heated to the extent where austenitization occurs in the desired region of a steel surface and, upon rapid self-quenching leads to hard martensite transformation to a depth governed by the processing conditions and characteristics of the steel. The depth of hardening depends on several parameters like laser energy coupling, thermal conductivity; phase transformation temperatures, thermal diffusivity etc. The chart depicted in Figure 1.17 elucidates various parameters related to laser beam, material and process that eventually determine the treated layer characteristics. The several advantages and few shortcomings of laser hardening compared to other competing technologies are summarized in Table 1.3.
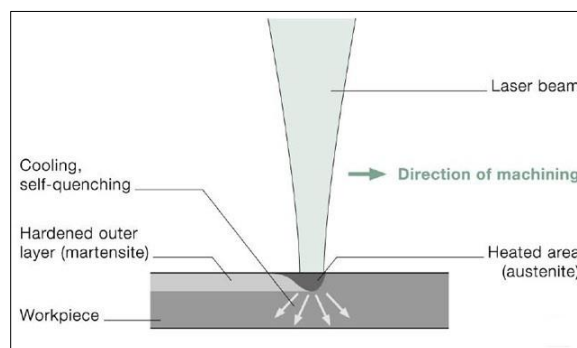
Fig. 1.16. Schematic illustration of laser surface transformation hardening process on steel
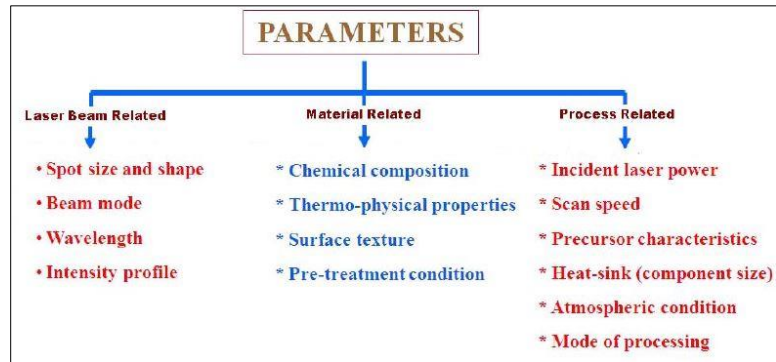
Fig. 1.17. Chart illustrating various parameters that influence laser surface hardening process

1.8   Applications of laser based surface hardening processes

Laser surface hardening process is a surface heating technique principally requiring uniformly distributed wide laser beam with moderate quality as compared to other manufacturing process. Although, its basic concept was established long back in the history of industrial era, manufacturing industry has been slow in adopting for applications other than machining of low volume of parts. This could plausibly due to high cost a laser processing system requires and lack of expertise in operation and maintenance of the and lack of understanding of process complexity. However, with recent introduction of high wall plug efficiency lasers such as diode lasers, this overlooked technology is gaining momentum for use in processing of generic as well as complex parts [37]. Some of the latest applications in the field of laser surface transformation hardening used in engineering industries are depicted in Figure 1.18.

1.8.1 Challenges of laser hardening applicable to bearing materials and elements

Unfortunately, these approaches require a sufficient amount of bulk material to produce the self-quenching effect, and therefore tend to be unsuitable for use with components that are fabricated using low-hardenability materials, thin-sectioned and intricate metallic components that lead to ineffective heat dissipation effects. Although various works with variants in processing setups and methodologies has been tried to lessen these deleterious effects, there are still certain bottlenecks that needs to be resolved to adopt such technologies. The following are some issues:

1. Effective control of peak temperature and thereby eliminate deleterious effects like distortion, cracking, retention of core properties, warpage etc.
2. Control of cooling rate with requirement of sufficient heat sink (section thickness) to produce the effective self-quenching effect.
3. Unsuitability for materials with low-hardenability, prior-treatment conditions, intricate components with different profiles and low heat dissipation effects.
4. Difficult to process large area as multi-track overlapping is required which will lead to softening at the overlapped regions.
5. Requirement of precursors/pre-treatments in some cases due to low laser absorptivity, surface texture and prior-treatment structure/texture.
6. Processing circular components (overlapping effects).
7. Control of microstructure of hardened case (like carbides, retained austenite etc.).

Process	Advantages	Disadvantages
Laser	☑ Minimal part distortion ☑ Selective hardening ☑ No quenchant required ☑ Thin case capability ☑ Case depth controllable ☑ Post processing not required ☑ Amenable to automation ☑ High productivity ☑ Improves fatigue life	☒ High equipment cost ☒ Coverage area restricted ☒ Absorbent coatings sometimes required ☒ Multiple passes result local tempering
Induction	☑ Fast Processing rates ☑ Deep case obtainable ☑ Lower capital cost than laser ☑ High coverage area	☒ Downtime for coil change ☒ Quenchant required ☒ Part distortion ☒ Coil placement critical ☒ Large thermal penetration ☒ Electro-magnetic forces may spoil surface ☒ Fabrication of complex coils for specific purposes
Flame	☑ Cheap ☑ Flexible ☑ Mobile process	☒ Poor reproducibility ☒ Lacks rapid quench ☒ Component distortion likely ☒ Environmental problems
Arc (TIG)	☑ Relatively cheap ☑ Flexible process	☒ Section thickness limited ☒ Large thermal penetration ☒ Stirring takes place ☒ Poor control to avoid melting
Electron Beam	☑ Minimal distortion ☑ Selective hardening	☒ High equipment cost ☒ Requires vacuum

Table 1.3 Comparison of laser surface hardening process vis-à-vis other competing processing technologies

Fig. 1.18. Typical industrial applications employing laser surface hardening process

1.9   Statistical Modelling and optimization

Notwithstanding that any process development involves cumbersome experimentation with repeated analysis of experimentation and optimization of numerous processing parameter, a suitable design of experiments approach is always required to co-relate effect of various processing parameters on relevant output responses. In the past decades, statistical modelling with design of experiments (DOE) approach had been extensively used successfully on variety of manufacturing processes and products, thereby, facilitating vast reduction in experiments. DOE methodology provides a strategic approach for co-relating process variables with output responses of a system or a process [38]. Although, experiments can be designed with variation of one factor at a time, requirement of several runs for obtaining precision in estimation becomes mandatory and thereby loss of generality. Apparently, factorial design of experimentation allows one to vary many levels of factors simultaneously, rather than cumbersome time-consuming approach of one at a time, and thereby facilitating effective optimization A full factorial design demand inclusion of all possible combinations of levels-of- factor in a model and will be effective for linear fitting with interaction effects. To assess model with quadratic terms, two well-known second-order response surface methodology (RSM) designs are in use – namely, a

central composite design (CCD) and Box-behnken design (BBD). RSM with BBD is one such suitable and effective method that allow researchers to effectively understand the influence of process variables, particularly in situations where several process inputs potentially influence process response such as a quasi-stationary beam assisted laser surface hardening of a cylindrical rod. Since influence of one parameter depend on level of other interdependent parameters, simultaneous effect of it needs to be investigated and as such in most RSM problems, relationship between responses and process parameters are unknown and needs to be effectively established.

The objective of statistical RSM is to govern a suitable approximation for establishing an effective functional relationship between process parameters and their responses. Since, many-a-times, response variables of a process are dependent in non-linear fashion with the input parameters, the second order polynomial preferred in few parametric regimes, where curvature is involved in the process. Historical analyses indicate that the quadratic model is usually noteworthy for the optimum design. Although CCD method employing two-level factorial design with addition of centre points and axial points is useful for chronological experimentation, it requires five levels that burden experimenters. On the other hand, BBD entails to use only three levels for each parameter and thereby reduce the burden on conducting many experiments. However, use of BBD confines to situations wherein predicting extreme values of response is not of utmost importance. Thus, BBD that can effectively provide high quality predictions when studying linear and quadratic interactions of the process.

1.10 Numerical Modelling and Simulation

Even though, statistical mathematical modelling help us to understand quickly influence of processing parameters on required responses of a process such as laser surface hardening, development of a suitable numerical model help us to understand physics of the process and thereby help in reducing experimental trails. Numerical modelling of a particular physics help us not only to understand the actual mechanism of the physics proceeding but also aid us with optimization methodology to save huge capital income if the same is tried experimentally. The basic categories of the modelling are broadly for semi-quantitative, parametric and detailed understanding to analyse various mechanism for effective prediction with analytical and numerical models [39]. Some of the inferences, a model can provide for laser material

processing point of interest are non-equilibrium change in the microstructure of processed layer or weld or coated layer, graphical representation of solidification front to understand Marangoni effects in the weld pool and cladding processes, to understand the weld /clad bead formation. (c) With the help of the stress history and residual stresses, the reason for cracking and distortion can be assessed in laser welded or coated materials. (d) With the help of the melted depth isotherms within thermally sensitive materials, one can predict temperature at interaction zone need to be maintained.

The researchers in the computational field of engineering with the help of reputed mathematicians and software developers provided many FEM and FVM software packages. These software packages help researchers to solve their problem using discretization technique which provides them the authority to optimize the problem according to their requirements. The most commonly used FEM packages are COMSOL Multiphysics, ANSYS and ABAQUS. For the fluid dynamics physics, Finite Volume Method is most commonly used. The common FVM tools are Fluent and COMSOL Multiphysics. In the present work, COMSOL Multiphysics employed for numerical simulation of laser surface hardening of bearing steel and bearing elements.

COMSOL Multiphysics® is a generic software, established on advanced numerical methods, for modelling and simulating physics and mechanics-based problems [40]. With the help of COMSOL Multiphysics, coupled or Multiphysics phenomena can be modelled at ease. It has many modules starting from Acoustics to Wave optics. The available modules include Heat transfer physics and exploited for this work. As for as the material processing is concerned, COMSOL Multiphysics is the most suggested FE package by most of the researchers. It works based on the governing equations. It has the provision to modify the governing equations with user defined functions can be implemented in the simulation at ease. The geometry modelling module of the COMSOL Multiphysics has various options like primitive solid objects, interpolation curves, parametric curves, 3D modelling options like extrude, revolve, sweep and it has very powerful CAD import and export facilities. The meshing strategy and the finite element method uses selected physics that automatically provides provision to modify if required. Specialized elements like Hermite and Argyris also provided for the better simulation results. The software platform is capable of solving simple as well as complex second-order systems of

nonlinear partial differential equations (PDEs), Algebraic equations, Ordinary differential equations (ODEs) and Differential algebraic equations (DAEs) as well.

The inbuilt materials module has also got large number of material databases, non-linear material properties as a function of physical quantity and user-defined composite structures. The visualization of the results of the simulation can also be done with wide range of plots available in the software. The various plots provided gives us clear idea about how the actual process happens with more concentration on the variables and parameters. It has a separate optimization module in terms of a facility called the sensitivity analysis in COMSOL. These are the features of the COMSOL Multiphysics, which makes it stay distinguished from other software packages in the market. There are still discussions about the best software in general, but each software has its own advantage. For instance, ANSYS for structural analysis, ABAQUS for non-linear analysis and on that way, COMSOL Multiphysics stays ahead of the other two in the Multiphysics simulation.

CHAPTER 2

Literature Review, Motivation and Research Objectives

As discussed in the previous chapter, bearings are subjected to withstand wide ranging axial and radial loads depending on speed and environmental conditions. With the continuous increase in demand of load bearing capacity and harshness in the environmental conditions, new technologies to impart surface modification at the contact surfaces is increasing in demand. Surface treatment processes imparted to thin-sectioned bearings and high-precision parts in conventional route often imparts deleterious effects due to uncontrollable heat-input such as large heat affected zone, surface deformation, and inhomogeneous hardness distribution. Further, the conventional techniques/systems often fail to obtain the desired mechanical and/or tribological properties of the bearings due to abrupt/improper heating, thereby reducing the life of the bearings. In an effort to identify gap that exist in our existing knowledge of surface modification approaches on bearing steels and components, a comprehensive review of the literature on various aspects has been undertaken. Various trends in control of heat input with latest surface modification technologies on bearing materials and on components as well as performance evaluation methodologies addressed and this effort summarized in the present chapter. Literature review on various aspects of numerical modelling and statistical optimization methodologies adopted in laser surface hardening also summarized in this chapter.

2.1 Recent developments on surface hardening of bearing steel

In 1984, F. M. Kustas and co-workers reported a comprehensive study on implantation of titanium ions on 52100 steel for improving the wear resistance. Results showed that the static sliding COF reduced about 24% for titanium implanted 52100 steel cylinder and rings. Compared with that on baseline specimen, a uniform smooth wear zone observed with reduced

surface relief. Apparently, metal tearing was not observed in the above steel due to the formation of wear-resistant titanium carbide and induced compressive residual stresses [41]. Chen et al. carried out plasma immersion ion implantation technique (PIII) on 52100 steel and reported maximum improvement in hardness about 21% [42]. But PIII was carried out at high implantation energy resulted in uncontrolled ion dose rate and substrate temperature. The solution proposed was to perform ion implantation at low energy which is more economical and independent control of the substrate temperature during implantation may offer an added benefit of attaining a greater case depth in a shorter time, due to the superimposed effect of thermally activated diffusion. In another reported study, PIII of nitrogen ions in bearing steel was carried out at low energy (1 keV) and at 300–500 ^{0}C [43]. The results showed that the hardness improved by a factor of three of four with a 40 µm case depth. These improvement is attributed to solid solution and precipitation dispersion hardening due to the finely distributed Fe_xN (x= 2,3,4) nitrides. Yafeng Lian et al. in another detailed study on the tribological behavior of un-implanted and cerium-ion implanted bearing steel, reported that with increasing dose of cerium during implantation showed increase in wear resistance by 0.1-4.2 times and reduced COF was observed due to the increased cohesive strength of the oxide film. Furthermore, ion implantation of cerium into bearing steel increased the anti-adhesive transfer and anti-abrasive abilities of GCr15 bearing steel [44].

A. Erdemir et al., evaluated the potential of TiN coatings with varying thicknesses deposited on bearing steel substrates by two PVD techniques for improving tribological characteristics [45-46]. Results showed that improvement in RCF lives with coatings <1-µm thicknesses. Thick coatings got delaminated and chipped when tested under high loads and thereby shortened fatigue life of bearing steels [shown in Figure 2.1(a)]. However, thick coatings were effective in increasing the fatigue lives under low load conditions. In addition, these and other researchers reported that TiN as a thin coating possessed relatively better adhesion, high wear resistance and low coefficient of friction [shown in Figure 2.1(b)] under both lubricated and unlubricated tribological test conditions [47-50]. F.A.P. Fernandes et al., conducted a comprehensive study on wear and corrosion behavior of niobium carbide coated on AISI 52100 bearing steel [51]. The carbide coating yielded average hardness and elastic modulus of 26 GPa and 361 GPa, respectively. Dry wear tests resulted in worn volumes by an order (see Figure 2.2) smaller for the NbC-coated steel, comparatively to the untreated substrate, at three different

applied loads. Polarization experiments showed that niobium carbide layer improved corrosion performance, although for applied potentials inferior than 250mV. At higher potentials, both substrate and NbC layer underwent significant corrosion damage. Xiaoming He et al. demonstrated improvement in tribological behavior and properties of amorphous hard carbon films deposited on 52100 bearing steel. Carbon films synthesized by Ion-beam-enhanced deposition with Ne + bombardment at 200 eV composed of carbon atoms in an amorphous structure. The minimum friction coefficient of hard carbon film reported was 0.1 measured under a wear load of 2N. The stable process of friction with much lower wear coefficient of 1.53×10^{-6} maintained at wear load of 2N [52].
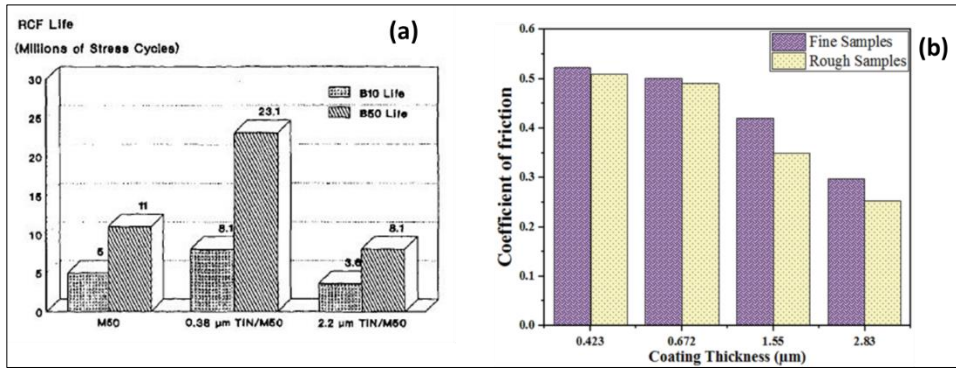
Fig. 2.1.(a) Rolling contact fatigue performance of TiN-coated and uncoated MS0 at 5.42 GPa Hertzian stress [6], (b) Mean COF of fine and rough samples against TiN coatings thickness [49].
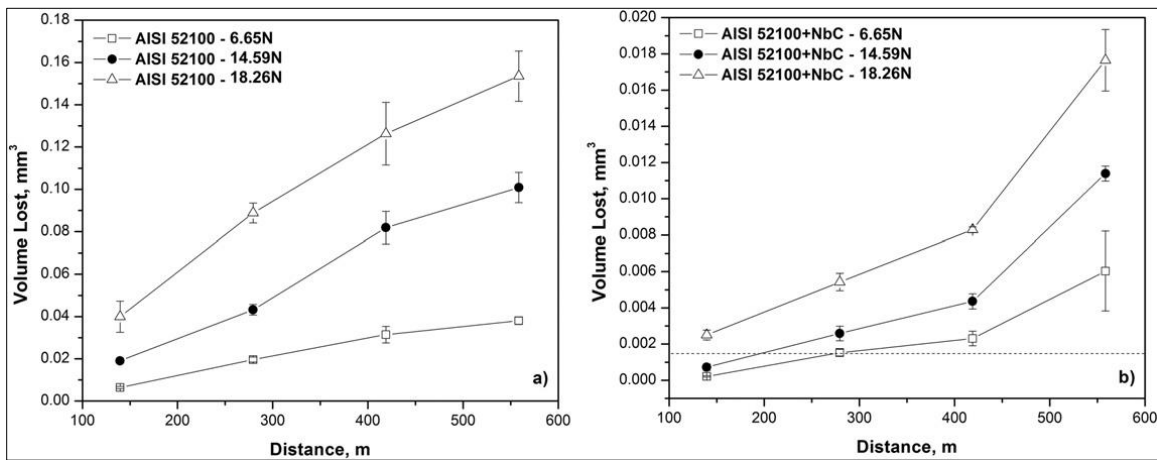
Fig. 2.2 Volume loss curves of the: (a) AISI 52100 substrate and (b) NbC coated AISI 52100, with 6.65, 14.59 and 18.26 N of applied load [50].

A. Rahbar-kelishami et al. reported that spraying high-Cr steel on AISI 52100 steel increased the wear resistance of worn parts; however, this technique was susceptible to high porosity and weak bonding of the sprayed material. Applying friction stir processing (FSP) on the as-sprayed coating significantly improved the microstructure and mechanical properties. They reported that FSP improved the wear resistance and hardness of sprayed AISI 52100 steel about seven and half times more than those of as-sprayed coating, respectively as shown in Figure 2.3. The FSP could simultaneously increase both hardness and toughness, ideal for wear resistance improvement. It also reduced the sprayed material porosities and improved the contact between the sprayed layer and base metal [53]. Indeed, conventional coating and thermochemical treatments for surface modification possessed inherent deficiencies such as poor adhesion and excessive base metal tempering. Coating thicknesses obtained were also very low which may peel off at high stress loading conditions.
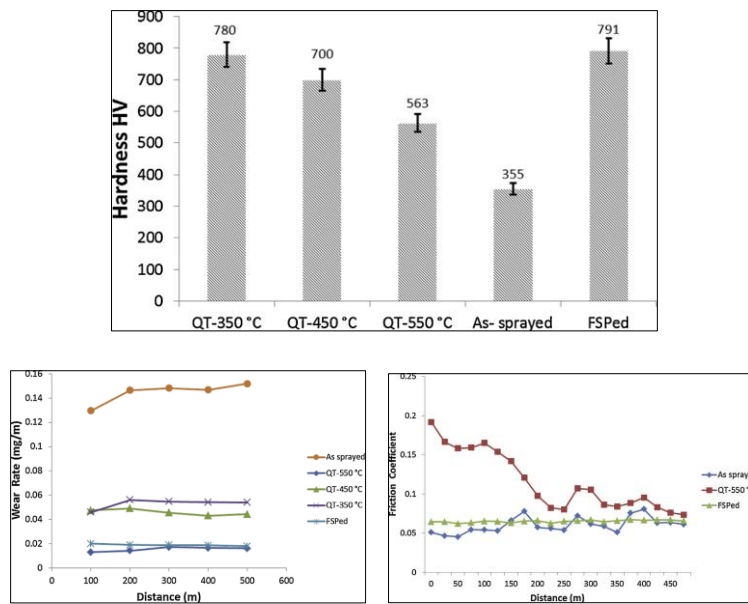
Fig. 2.3. Hardness, wear rate of different samples (mg/m) and friction coefficient of heat treated (quenched and tempered from 350 to 550 0C), as-sprayed and FSPed sprayed samples [54].

T.Y. Hsu et al. in their study on isothermal treatment on 52100 ball bearing steel observed two types of isothermal martensite forms after quenching from 1150^0C and isothermal holding at temperature between Ms and room temperature, one continued growth of athermal martensite with fresh nucleation and growth, other from retained austenite. The morphology of

30

the isothermal martensite was lathe type with inner twins. Five percent of isothermal martensite formed in as-quenched specimen as against less than 1% in quenched and subzero-treated specimen after isothermal holding for 10 hours. The kinetics and mechanism of formation of isothermal martensite with isothermal treatment was clearly explained [54]. In another study, bearing steel treated by austenitization at 880 ^{0}C followed by isothermal holding at 200 ^{0}C for 6 h, excellent combination of mechanical properties were obtained with refined uniform microstructure. Under optimum heat treatment condition, the impact strength and hardness also increased by 28.8% and 5.2% respectively, while the tensile strength reduced by 3.7%, compared to that of the conventionally processed ones [55].

Few studies reported improvement in tribological and rolling contact fatigue life of bearings by employing diffusion methods. Ravindra Kumar et al., proposed plasma nitriding of ball bearing steel (AISI 52100) for high surface hardness. Plasma nitriding was carried out on a quenched and tempered material at temperature around 460–580^{0}C with process temperature being lower by ∼50^{0}C to the tempering temperature. AISI 52100 ball bearing steel is not very much suitable for standard plasma nitriding process because this steel has got tempering temperature ∼170–200^{0}C, which is much lower than the standard processing temperature needed for plasma nitriding treatment. This could be the reason for restricted plasma nitriding of this specific ball bearing steel by conventional plasma nitriding mechanism. In their reported work, Plasma nitriding of annealed sample was carried out at higher temperature (>560^{0}C), whereas for quenched and tempered samples at lower temperature to control reduction in core hardness. The argon and nitrogen gas mixture gave higher surface hardness on the annealed samples [56]. In another study, nitrided 52100 steel surface with usage of poly-α olefin (PAO) synthetic base oil, with organotungsten additive decreased friction coefficient to 24.8%, and wear scar diameter by 7.2%, compared with that of substrate surface [57]. R. Ramesh and co-workers reported that the fretting behavior of liquid nitrided bearing steel material was superior compared to that of as-received material at different normal loads. The mono-phase epsilon iron-nitride structure of compound layer formed in liquid nitriding process offered improved fretting wear resistance [58]. Karthikeyan Rajan et al. showed that endurance tests with 90% reliability on carbo-nitrided bearings exhibit nearly ten times more life (as shown in Figure 2.4) than the non carbo-nitrided bearings. They attributed it to synergic combination of retained austenitic, fine martensitic microstructure and ultrafine carbide precipitates obtained by carbonitriding treatment [59].

31

Sukru Taktak showed improved tribological behavior of 52100 bearing steel when borided by pack boronizing method at 950 °C for 2 h. The thickness and hardness of borided layers on the 52100 bearing steel was 56 ± 6 μm and 1970 HK, respectively. Dry sliding wear tests conducted on these borided steels against Si_3N_4 bearing ball at elevated temperatures illustrated different phenomena. Results indicated that the wear rates of un-borided and borided steels increased with temperature and borided 52100 steels exhibited considerably lower wear rate at all temperatures, compared with un-borided counterparts. At temperature of 600^0C, borided 52100 steels had wear resistance of about 3 times higher than that of un-borided steels. Examination of the worn surface of borided steels showed that, worn surfaces were covered with a discontinuous compact layer especially above temperature of 300^0C [60].
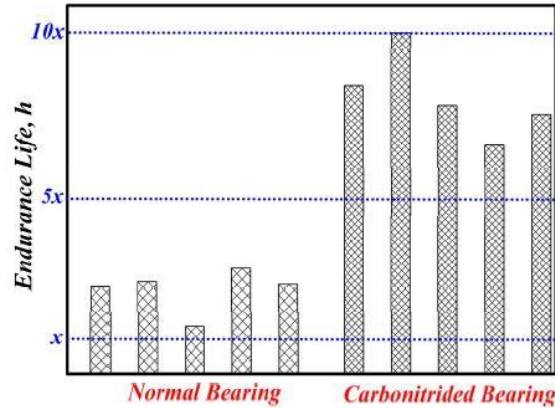
Fig. 2.4. Comparison of endurance test of normal ball bearing (non-carbonitrided) and carbonitrided ball bearing. "x"-denoted the target L10 life [58].

Sukru Taktak et al. investigated tribological behavior of thermo-reactive diffusion chromized and duplex treated bearing steels. The surface hardness and scratch resistance of coating increased with duplex treatment of chromizing followed by plasma nitriding, resulting in high wear resistance [61]. Zhaoxi Cao and co-workers reported that the vacuum carburization of 52100 bearing steel resulted in 30-vol% cementite and ~20-vol% retained austenite in surface layer, significantly higher than those processed by the conventional heat treatment and RCF life significantly increased by 10 times by carburization, as depicted in Figure 2.5. This improvement was attributed to the presence of plate/rod cementite and retained austenite [62]. Although, such diffusion methods are effective in enhancing hardness in low carbon low alloy steels, certain

32

disadvantages in terms of requirement of masking for parts, loss in toughness due to prolonged process duration and difficulty in disposal of toxic residual elements persist.
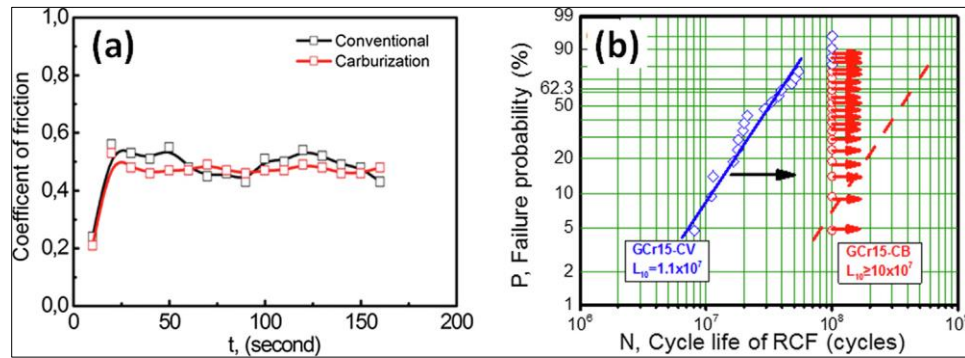
Fig. 2.5. Coefficient of friction for wear testing and failure probability versus cycle life of rolling contact fatigue of the high carbon bearing steel processed by conventional (CH) heat treatments and carburized surface hardening (SH) heat treatments. [61].

J. Chakraborty et al. determined optimum processing parameters for developing bainitic + martensitic microstructure in SAE 52100 bearing steel through appropriate austempering and quenching schedule. They showed that optimum austempering (270^0C, 30 min) followed by water quenching developed bainite + martensite duplex microstructure and improved levels of hardness (62HRc), tensile strength (2250 MPa) and impact strength (53 J). They observed that such excellent combination of hardness, strength and toughness is difficult to realize in SAE 52100 through conventional hardening and tempering route [63]. In another study, imparting prior cold deformation was found to be an effective way to refine the thickness and size of bainitic sheaves and thereby enhance impact strength with high levels of hardness and tensile strength (as shown in Figure 2.6). Judicious combination of austempering and hardening could produce a bainite + martensite duplex microstructure [64-66]. In a similar study reported by Yuming Pan et al., they showed that lower bainite could be realized when austempering temperatures were ranging from 232-343 ^{0}C with coarsen ferrite plates, whereas, upper bainite formed when austempering temperature was ranging from 372-427 ^{0}C. They also reported that hardness decreased with increase in isothermal temperature or holding time [67].
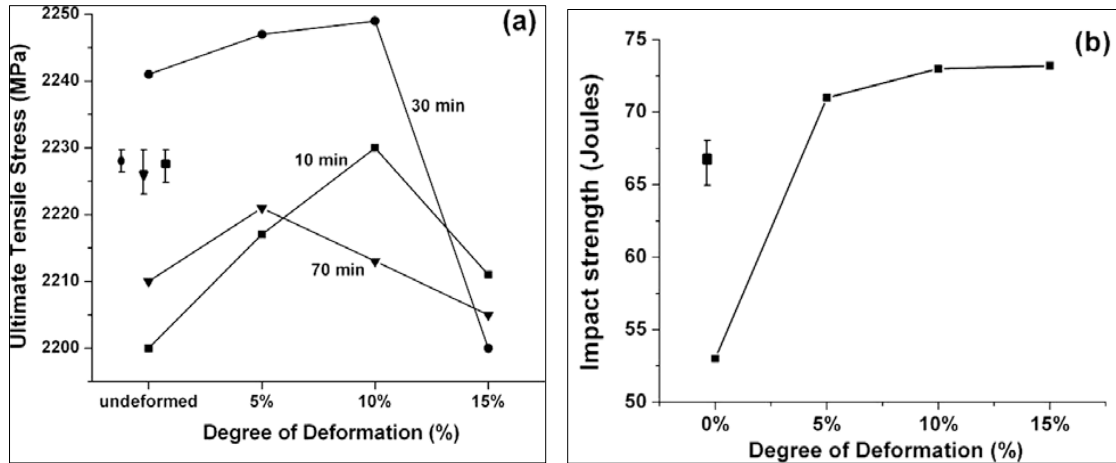
Fig. 2.6. Variation of (a) ultimate tensile stress and (b) impact strength with degree of prior cold deformation of material austempered at 270 ^{0}C for 30 min [63].

E. C. Santos et al. reported enhancement in fatigue strength by three fold of 52100 bearing steel by induction heating and repeated quenching due to decrease in prior austenite grain size along with refined martensitic structure and increase in retained austenite content [68]. In another detailed study investigated on the effect of the induction hardened microstructure and residual stress on the tribological behavior of GCr15 steel, the residual stress profile generated by induction hardening with rapid heating and quenching revealed a surface in a high and deep compressive residual stress state. Higher compressive residual stress remained in the hardened layer contributed to decrease of coefficient of friction and increase in wear resistance. Worn surface topographies showed the compressive residual stresses could effectively delay growth of cracks generated during the wear test [69]. However, induction process could not produce desired result for hardening of complex geometries and localized areas. On the other hand, some distortion realized during induction hardening due to relatively large heat input. Moreover, it could not produce shallow hardening depth. A. Amanov and co-workers investigated the migration of Fe_3C particles towards the surface by employing ultrasonic nano-crystalline surface modification (UNSM) technique in AISI 52100 bearing steel. The UNSM treatment generated nano-grains with high number of grain boundaries by severe plastic deformation and as a result migrated Fe_3C particles towards the surface by diffusion pumping induced by elastic deformation with increasing number of dislocations that dissolve the Fe_3C particles. They reported that gradient nano-grains exhibited nearly 3 times higher hardness compared to that of the coarse grain one [70]. Yan-Li Song et al., reported improvement in tribological properties of GCr15

34

bearing steel by an alternating magnetic treatment, due to a higher hardness caused by homogeneous distribution of carbide particles [as shown in Figure 2.7] and dislocations after magnetic treatment [71].
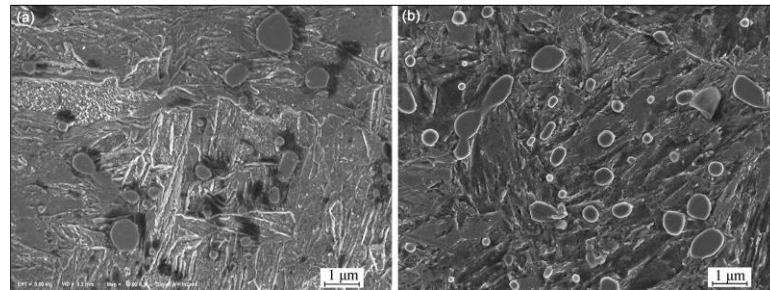
Fig. 2.7. Carbide distribution of GCr15 before and after the magnetic treatment: a before treatment; b after treatment [70].

Matteo Villa et al. investigated the effect of longer duration of isothermal holding at cryogenic temperature on precipitation of transition carbides during tempering. They reported that sub-zero treatments are effective in reducing retained austenite and enhanced precipitation was obtained during tempering in high carbon steels [72]. In another study, deep cryogenic treatment improved hardness and toughness when compared to that of conventionally heat-treated one without cryogenic treatment. Thus increasing hardness due to elimination of retained austenite and as result improvement in mechanical properties [73-74].

2.2 Recent Developments in application of laser based surface hardening processes on bearing steels and elements

Many studies are also available on laser surface hardening of different bearing steels employing high power lasers with variation in processing modes and setups for improvement in wear and fatigue properties. M.S. Devgun et al. investigated the effect of laser heat treatment on microstructure, hardness and sliding wear properties of 52100 bearing steel utilizing continuous wave CO_2 laser and compared with conventionally treated counterpart. Even though substantial improvement in wear resistance was observed in laser treated specimens, over tempered zone persists in the multi-pass specimen and as resulted decrease in hardness [75]. Iryna Yakimets et al. studied the effect of laser peening (LP) on hardness, residual stress and tribological behavior

of 100Cr6 rolling steel. They observed that LP treatment generated compressive residual stresses (approximately, -400MPa) accompanied by hardening (+10% on hardness) on sample surface. Tribological tests carried out in linear rolling-sliding contact highlighted the improvement in the resistance of treated metal to wear, particularly when below a critical pressure of 100MPa: the reduction in friction coefficients and wear rates under the combined effect of the hardening and residual stress conditions. However, when tested at higher load, greater 100MPa, LP treatment did not show improvement in the resistance to wear because of wavy surface generated by the treatment [76]. Basu et al. studied the improvement in wear resistance of 52100 steel treated with laser surface hardening (LSH) and attributed improvement wear resistance due to enhanced hardness [77]. S. Lei et al. investigated the effect of laser heat treatment on microstructure, hardness and sliding wear properties of GCr15 bearing steel utilizing CO_2 laser and compared with conventionally treated counterpart. They reported hardness enhancement in laser-hardened layer due to grain refinement and formation of supersaturated martensite during wide band laser quenching. The tribological tests carried out on block-on-wheel friction and wear test machine highlighted the improvement in resistance of treated metal to wear and reduction in coefficient of friction at low load of 150N. Under higher load (higher than 150N), laser treated layers did not show improvement in the resistance to wear [78]. Hong Zhou and co-workers demonstrated the improvement in wear resistance of ball bearing steel (GCr15) processed with biomimetic units on the surface with laser surface melting. They studied the effect of varying medium (air and water) and thickness of water film on wear behavior of bio-inspired wearable surface under dry sliding condition. An ultra-fine homogeneous microstructure (martensite + carbides) with residual austenite in melted zone of the biomimetic units processed under water film and resulted in hardness improvement to the tune of 1100 HV. They attributed improvement in wear resistance of biomimetic units achieved when laser surface melted under water film of 3 mm thickness to high-hardness ultra-fine microstructure comprising strengthening phases [79].

In another variance of approach to improve surface hardness in bearing steel to that of conventionally treated counterpart, R. Akhter and co-workers applied subzero cooling treatment after LSH on GCr15 bearing steel ring (see Figure 2.8 (a & b) and obtained significant improvement in hardness. However, they did not analyze any mechanical and tribological properties of the treated surface [80]. Donato Sorgente et al. also observed similar improvement in microstructure and hardness on 52100 bearing steel when subjected to high power fiber laser

hardening treatment [81]. Peng Yu Lin and co-workers demonstrated 44% improvement in wear resistance of bearing steel with laser surface re-melting underwater as compared to untreated substrate [82]. Niroj Maharajan et al. applied under water laser surface hardening process on 52100 bearing steel using Ytterbium-doped fiber laser and investigated its effects on hardening based on microstructure and hardness of hardened layers and compared with conventionally treated specimens. Even though higher hardness achieved, depth and width of treated layer was very smaller when processed under water. They have also shown that at lower scanning speeds (as shown in Figures 2.9 and 2.10), the technique proposed was unfeasible due to convection motion of water on the surface [83]. Although hardness improvement achieved in treated layer processed under water with low heat affected zone and distortion, the hardened case was found to be irregular, on account of refraction of the laser beam in water. Additionally, these approaches require suitable control of fluid flow to overcome difficulty in processing industrial components of complicated and intricate design. WU Gan et al., reported that improvement in hardness up to 13.9% and wear rate by 15.4% in laser nitrided samples as compared to that of conventional nitrided counterpart. Even though substantial improvement in wear resistance observed in laser nitrided specimens, micro-cracks and micro-pores were observed due to laser rapid melting and subsequent quenching that affect surface topography of work piece [84]. L. Tricarico et al. demonstrated single-pulse laser surface treatment on 52100 steel samples using a high power fiber laser by varying process parameters such as laser power, pulse energy and defocusing distance. Numerical FE model developed to predict thermal history of the surface during LST process assisted to predict the time required between two consecutive pulses to restore the ambient temperature and thereby distance between adjacent laser spots to avoid back-tempering effects [85].
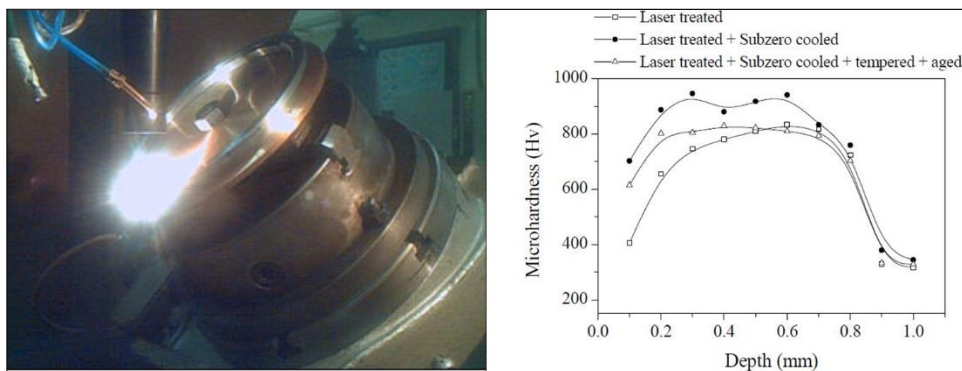
Fig. 2.8. (a) Laser transformation hardening on GCr15 ring (b) Comparison of the microhardness of the GCr15 steel after laser and various treatments [79].
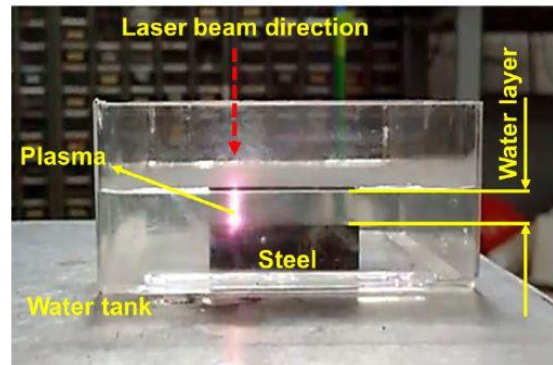
Fig. 2.9 Image showing plasma formation during under water laser hardening process [82].
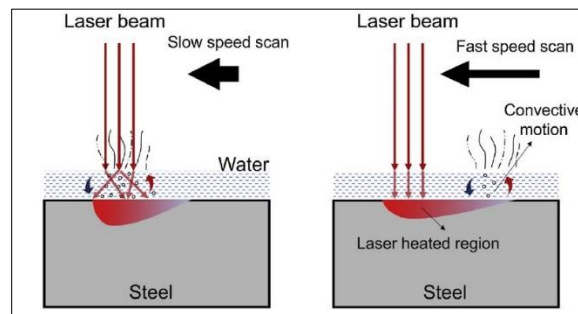
Fig. 2.10 Schematic showing (a) convection motion of water and vapor formation above the irradiated area during the slow scanning speed and (b) absence of disturbance in water above the irradiated area during fast scanning speed [82].

F. Gutierrez Guzman and co-workers confirmed the applicability of an energetic approach i.e., using a laser surface treatment to predict the appearance of White Etching Layer (WEL) in oil-lubricated rolling/sliding contacts when tested at select operating conditions and showed the influence of selected parameters on WEL formation. With increase in laser energy input, depth of treated layer increased accompanying WEL formation. They observed WEL on inner rings of cylindrical roller bearings when tested using two-disc test rig. However, influence of operating conditions on the morphology of WEL was not reported [86]. Although the reported works on laser surface hardening of prior-treated bearing steel showed significant improvement in hardness with retention of bulk properties, they nicely ignored reporting deleterious soft zone

formation below the hardened layer, which is inevitable, due to the induced soft-tempering temperature effect associated with the laser processing thermal cycle. As such, no reports are available on improvement of the tribological and mechanical properties (other than hardness) of the laser hardened bearing steel with prior hardening treatment. Additionally, quenching media is required to avoid those softened zone depths as far as thin-sectioned prior-hardened steels are concerned. Otherwise, the process involving methods reported by previous studies will lead to drastic loss in retention of core properties.

2.3 Recent developments on controlling heat input in laser surface hardening processes

2.3.1 Pulsed laser transformation hardening

Although many reports are available highlighting applicability of conventional Continuous wave (CW) mode of laser hardening processing of steels, the effective control of microstructure by controlling process cooling rate (peak temperature), softening effects of prior hardened (either laser-based or otherwise) surfaces when processed at multiple locations with control of distortion are negligible. In CW mode, continuous increase in temperature happens along the treated track although constant power maintained and as a result, comparatively high heat accumulation with higher peak temperature achieved with scanning duration. In recent years, pulsed mode of selective laser surface hardening attracted researchers due to better process control than CW mode of laser processing. In Pulsed Wave (PW) mode of processing, the laser pulses modulate, alternatively with ON/OFF sequence, depending on the pulse duration and frequency and thereby better control in heating cycle and surface temperature uniformity on the work piece. In PW mode, the short pulse duration can increase peak power and minimize thermal diffusion to the surrounding bulk, leading to localized heating. PW mode allows better control of surface temperature with enhanced uniformity and thermal diffusion in the treated zone. Thus, these two modes of laser processing will result in different cooling rate, which will directly affect the microstructural changes, hardness distribution and stress condition in treated case.

Danileiko et al. reported that the pulse mode of laser processing is better suitable compared to that of CW mode due to additional controlling process parameters available such as pulse frequency, pulse duration and peak laser power. Controlling these parameters will help facilitate in enhancement in microstructural and mechanical properties due to better homogenization of austenitic phase, microhardness distribution and hardening depth profile [87]. Habedank et al. also reported that pulsed mode of laser hardening with lower pulse frequencies resulted in higher case depths and hardness in the treated layers when compared to that of CW mode of laser processing and resulted in higher compressive residual stresses leading to higher endurance limits [88]. Wu et al. proposed a 3D model for the pulsed laser transformation hardening and considered spatial and temporal laser intensity distribution. They have reported that temporal pulse shape had great effects on surface hardening [89]. Miokovic et al. reported increase in surface hardness and case depth with increase in number of laser pulses in the AISI 4140 work piece [90]. However, the hardened depth saturated as the number of pulses increased beyond three (Figure 2.11). Kostov et al. [91] also exhibited similar effect on nature of extension of the hardened zone in lateral direction accompanied with slight material softening due to repeated austenite-martensite transformations induced by laser surface hardening. They also reported the generation of compressive residual stresses on surface and tensile stresses inside subsurface induced by the laser hardening process. The compressive stress zone increased along depth with the number of repetitive laser pulses (Figure 2.12).
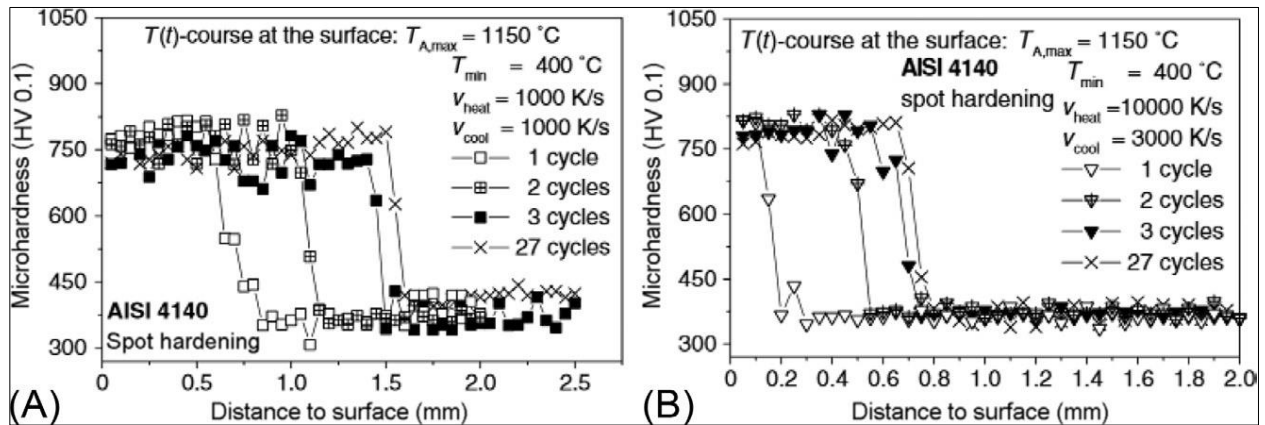
Fig. 2.11 Microhardness vs. distance to the surface after laser surface hardening with heating and cooling rates of 1000 K/s (A) and a heating rate of 10,000 K/s and a cooling rate of 3000 K/s (B)

after 1 cycle and after cyclic time-temperature change in the austenite region with 2, 3, and 27 cycles [89].
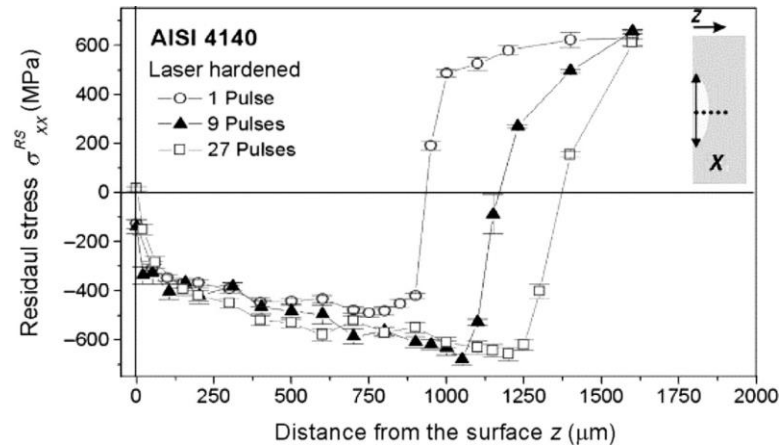
Fig. 2.12 Residual stress distribution in the depth z after laser surface hardening by means of 1, 9, and 27 laser pulses [90].

The temperature history for a laser heating and cooling cycle was also studied numerically and analytically by several researchers it will help quickly to optimize process with minimization of experimentation [92–94]. Smurove et al. proposed numerical modelling and analysed solidification by changing velocity and position of phase boundaries [92]. Yilbas and co-workers proposed a close-form solution for predicting temperature during pulsed laser heating and cooling cycle [93]. Similar authors assessed influence of varying laser pulse parameters on melting zone by numerical simulation [94]. More recently, Mahmoudi et al. [95] studied the effects of varying laser process parameters such as pulse duration, frequency, scanning speed on case depth and hardness distribution of AISI 420 martensitic stainless steel using a pulsed Nd: YAG laser. They have also reported improved corrosion resistance in laser treated specimens compared to that of a conventionally heat-treated specimen. However, overlapping of subsequent tracks caused tempering of phase with deposition of carbide that entailed decrease in corrosion resistance. Jiang et al. [96] presented a slightly different approach. They have proposed spot laser surface hardening and few discrete spots were distributed over a selected region of AISI O1 tool steel workpiece using a pulsed Nd:YAG laser. The effect of varying laser processing parameters on characteristics of laser-treated spots studied and reported that laser pulse durations greater

41

than 8 ms does not alter hardness and that the laser pulse energy was the influencing parameter affecting the depth and diameter of the spot hardening.

Nath et al. [97] presented analytical solutions for temperature profiles during heating and cooling cycles of repetitive laser pulse irradiation along with effects of various process parameters such as laser power, beam diameter, scan speed, pulse duration, repetition frequency, and duty cycle on surface hardening. They observed lowering of average heating rate with repetitive laser pulses. Additionally, soaking time above phase transformation temperature on which the homogeneity of microstructure and the depth of hardening depends is longer in PW than that of CW. This validated with their experimental results on laser hardening of AISI 1055 steel using modulated-power of fiber laser by demonstrating increase in depth of hardness with increase in number of laser pulses at low-frequency range. Similar effects was also observed with reduction in inter-pulse duration illustrate an example obtained by Kostav et al. [91]).

2.3.2 Effect of external heat sink to reduce heat input in laser transformation hardening of thin sections

Some studies reported alternative methods of controlling deformation in LSH of steel by employing variety of heat sinks. Combining heat sink with thin steel sheet can increase the hardenability of the thin steel sheet. Ki et al. [98] studied the effect of heat sinks on laser transformation hardening of DP 590 and boron steel. Thermal conductivity of heat sink and thermal contact resistance between steel sheet and heat sink were two important parameters for controlling the process. The study showed that in presence of heat sinks, both cooling and carbon diffusion are similar to that of the thick plate case whereas the heat-treatable region remains same to that of no heat sink case. In a similar study, Kim et al. [99] proposed two different thermal deformation mechanisms in laser transformation hardening of steel by using heat different heat sink materials (Figure 2.13).
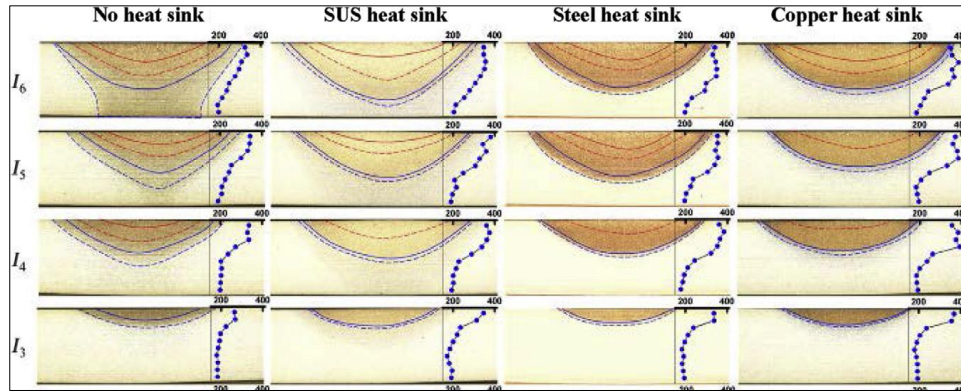
Fig. 2.13 Optical micrographs showing the cross-sections of heat treated DP 590 steel specimens for ti = 1.13 s. From bottom to top, intensity level increases from I1 to I6 [98].

Further Sehyeok and co-workers demonstrated two concepts, namely, Effective carbon diffusion time [ECDT] and Effective cooling time [ECT] and predicted hardness and deflection angle due to thermal deformation respectively using 3D thermal analysis [100]. Hyungson Ki and co-workers reported similar process maps of ECDT and ECT for determining the optimal process parameters [101]. However, control in treated case uniformity and distortion posed challenge, since, maintaining uniform contact with heat sink was not that easy during processing. Biao Jin and co-workers disclosed an underwater laser surface hardening process employing a 200W Fiber laser with a Gaussian-mode energy distribution to harden the surface of tool steel [102]. The hardening depth and heat-affected zones were significantly smaller in underwater hardening (material immersed in water) method than that processed under air due to refraction of beam in the water. Although improvement in hardness of the treated layer was observed when processed under water due to enhanced cooling rate, the treated profile was of low depth and uncontrollable in terms of uniformity. Additionally, the approach required suitable method to control fluid flow and a laser beam whose wavelength is transparent to fluid media used. The method adopted imparts difficulty in processing components of complicated and/or intricate design.

2.4 Statistical methodologies applied for laser surface hardening processes

Due to the higher complexity levels involved in such laser surface modification techniques entailing multiple influences of parameters on the process response, traditional methods of designing, manufacturing, and testing failed to control the process effectively and afford satisfactory results. The recent advancements in optimization techniques helped to quickly develop and often use in various industrial sectors to control and optimize the manufacturing processes. Response Surface Methodology (RSM) is one such numerical approach that helps to optimize the process by understanding and calculating the quantitative influence of the control parameters. By introducing systematic variations in the input parameters, the response of the process be assessed and inferences can be drawn effectively based on the quantitative analysis of the results [103]. Few reports are available on RSM regression analysis of laser surface hardening process to determine the effect of various laser-processing parameters on resulting quality of the hardened layer. Issa and his co-workers used RSM approach to optimize laser-microchannel fabrication process using a CO_2 laser (pulsed) to fabricate micro-channels in 2 mm thick glass [104]. The microchannel dimensions constituting surface roughness and morphologies were assessed by optimizing laser processing input parameters using RSM and the results were found to be in good agreement with predicted ones [104].

P. Dinesh Babu et al., carried out a systematic investigation on LSH of high strength low alloy medium carbon EN25 steel using Design of Experiments (DOE) and determined the optimal laser hardening conditions according to the design optimization criteria [105-106]. Similarly, S. Guarino et al., successfully investigated the influence of laser operating parameters on the fatigue endurance of the components using DOE [107]. D.A. Lesyk et al., could optimize the LSH process combined with ultrasonic impact treatment by implementing multi-factor experimental design using ANOVA and determine the optimal technological regimes on responses such as roughness, surface hardness and depth of hardened layer [108]. Mahmoud Moradi et al., and Changrong Chen et al. optimized diode laser surface hardening process on AISI 4340, 410 and 1045 steels respectively using DOE and analyzed the effect of laser input parameters on responses such as case depth and hardness distribution [109-111]. They successfully obtained optimum settings of laser parameters by adopting the desirability approach. D. S. Badkar et al., successfully investigated the influence of laser operating parameters (laser power, scanning speed and focal point position) on the heat input, hardened-bead geometry and angle of entry of hardened bead profile with the surface using Box-Behnken design matrix

method available in response surface methodology [112]. A.R. Hamad and co-workers carried out statistical modeling of the microhardness as a function of process factor in laser nitriding process with re-melting of pure titanium. They reported that to achieve a maximum microhardness of 1920 HV, the optimum process parameters settings were 2.84 kW laser power, 5 mm/s scanning speed and 2076 l/h nitrogen flow rate [113].

Recently, Sagar V. Telrandhe et al. optimized laser surface heat treatment process on rotating Ti6Al4V cylindrical specimens by adopting numerical modelling approach and correlated with experimental results. Optimization of input power with modification in simulated model approach (polynomial power variation) helped in achieving uniform distribution of heat penetration and case depth in treated layer with close agreement in predicting temperature profiles [114]. In another study, Noureddine Barka et al. successfully adopted Taguchi optimization analysis for optimizing laser-hardening process on AISI 4340 cylindrical steel specimens to obtain uniform case depth with hardness distribution [115]. Recently Rachid Fakir et al. analyzed the mechanical behavior in terms of static and dynamic fatigue strength of AISI 4340 laser treated steel specimens of cylindrical geometry employing high rotary speeds. Statistical analysis predicting relationship of mechanical properties with laser processing parameters revealed that increase in fatigue endurance by 40% and average strain rate of about 0.30% be achieved due to laser surface hardening [116]. Notwithstanding these reports on development of models to optimize laser surface treatment process on rotating parts with different methodologies and approaches, lack of knowledge in terms of understanding the physics and dynamics of the high speed laser processing still persists and further studies needs to be undertaken to effectively implement in practical purposes.

2.5 Numerical simulation applied for laser surface hardening processes

Heat transfer is the most critical phenomena for understanding surface hardening process such as laser surface hardening. COMSOL Multiphysics simulation software is one such recently used tool taken in the present work for making analyzing the processes of heat transfer.

COMSOL Multiphysics (formerly FEMLAB) is a finite element analysis, solver and Simulation software / FEA Software package used for various physics and engineering applications, especially coupled phenomena, or multi-physics.

The numerical modelling strategy adopted by researchers in laser surface hardening starts from the thermal modelling of the actual process to determine the thermal gradients and predict the hardened region. The research works continued further to determine the metallurgical characteristics of the hardened samples through numerical modelling. Leung et al. developed a model in heat transfer physics using Klein-Gordon equation for moving the beam source in the laser surface hardening of AISI 1050 steel specimen [117], Shiue and Chen [118] utilized equations from Ashby and Easterling [119] model of temperature prediction, for estimating the carbon diffusion time during laser surface hardening of AISI 4340 steel. So and Ki [100] developed 1D heat conduction model for evaluating the capacity for self-quenching in plates according to their thickness. The results were validated with laser hardening experiments on AISI 1020 steel specimens were in full agreement with predicted ones. Ki et al. [120] evaluated the effect of different heat sinks on improving the properties in laser transformation hardening of 2mm thick carbon steel sheets.

Sun et al. [121] developed 3D FEM model to predict the temperature distribution in LSH of 42CrMo cast steel. Two different beam shapes namely stripy spot with uniform intensity array spots, and a stripy spot with intensity blow-up in the edge have been used in hardening steel to obtain the desired case depth. For effective comparison, a Gaussian laser beam used for the purpose. In another study, Shuja and Yilbas used three-beam laser heating on a moving steel sheet, and validated with experimentation [122]. Temperature distribution and stress fields were predicted and effectively assessed. Li et al. [123] done a comparative study on two different types of lasers for laser surface hardening on AISI-1045 steel - diode laser and CO_2 laser. The effect of different process parameters such as laser power, scanning speed on case depth and hardness were examined. Marco et al. [124] studied the heat transfer model and experimental investigations to observe the microstructure evolution of the alumina with single laser treated track. The influence of laser energy density on the surface temperature and cooling rates were assessed.

Ahmed et al. [125] developed rectangular beam by superimposing multiple Gaussian sources and results compared with a single circular Gaussian source model as well as experimental results from a high power diode laser with a rectangular beam. They observed that melt depth, melt pool profile and its progression predicted by modeling compared well with experimental results in melting of Inconel 625. Semak et.al [126], developed a numerical model for simulation of the temperature field when a laser is impinged on metal surface. Oberferg et.al [127], developed a two dimensional thermal model for laser surface hardening and concluded that the depth of the Hardened zone depends on the austenitization temperature for short irradiation times and heat conductivity when the irradiation time is long. In order to measure the stress history, Fanrong kong et.al [128], developed a thermomechanical-metallurgical FE model for laser heat treatment in general. The thermal load obtained from the thermal analysis when converted as the body force or load and stress history could be determined, providing information about the residual stress and distortion. Yan et.al [129], developed an analytical model for single pass laser surface hardening using greens function to determine the temperature profile at the hardened region. Ahmed et al [130] developed a simplified thermal model for Laser surface hardening using COMSOL Multiphysics to determine the hardened region dimensions. Khajeh et al. [131] developed a finite element model on reducing the edge effect problem by controlling power as a function of maximum surface temperature. High laser scanning speed with large beam size was another alternative proposed for controlling melting. Sehyeok Oh et al. [132] developed a 3D heat conduction model and an extensive experimental study employed to study the laser transformation hardening of AISI H13 tool steel. They presented predictive models for hardness distribution and thermal deformation using the concepts of effective carbon diffusion time (ECDT) and the effective cooling time (ECT). Stefano Guarino and co-workers developed a FEM model for laser surface hardening process on AISI 1040 steel to increase its fatigue life and validated with the experimental results by adopting a HPDL source. Good correlation between both experimental and numerical results observed for both heat affected zone and fatigue life with error less than 8% [133].

V. R. Barath et al., proposed an iterative numerical simulation approach model with conditional looping to achieve a uniform surface temperature during the laser hardening of a complex geometry with a variable heat sink. By controlling laser power, any complex geometries can be easily processed without any melting by maintaining uniform surface temperature. The

model was validated with experimental results [134]. Saeed Talesh Alikhani et al., developed 3D FEM model of laser surface hardening process on AISI 4130 steel to predict the depth and width of hardness based on the critical austenitization temperature (A_{c3}) [135].

2.6   Motivation and Research Objectives

Bearings made of high carbon low alloy steel are widely used in diverse engineering applications to impart load bearing capacity and lubrication during motion between different components. Bearings are designed and manufactured as per international standards of specification suiting different design criteria based on application requirements. These are generally subjected to withstand wide ranging axial and radial loads depending on speed and environmental conditions. With the continuous increase in demand of load bearing capacity and harshness in the environmental conditions, new technologies to impart surface modification at the contact surfaces is increasing in demand. Conventionally, bearings are subjected to surface treatments such as high-frequency induction hardening, flame hardening and case hardening technologies for improving their strength and wear resistance according to the application requirements. Typically, bearings are made of either through-hardened high carbon low-alloyed steels or casehardened low-carbon low-alloyed steels, depending upon the performance required under designated lubricating environment. It requires high hardness with wear and fatigue resistance coupled with sufficient toughness since they are used in a poor/adverse working environment. Many a times, high abrasion and wear induced environment lead to their premature failure and as a result, require improvement in surface properties. However, surface hardening of thin-sectioned and high-precision parts in conventional route often becomes uncontrollable due to overheat or melt. Moreover, uncontrolled heat-input imparts deleterious effects such as large heat affected zone, surface deformation, and inhomogeneous hardness distribution. Conventionally, while performing surface treatment, the bearing components are exposed to a large amount of heat, for prolonged time period to achieve desired uniform phase transformation. Further, various quenching media are used during the quenching process to enhance different desired microstructure to obtain the required properties of the bearing. The conventional surface treatment techniques/systems require a large setup for heating and then quenching the bearing along with a post treatment setup to obtain the desired properties of the bearing, thereby making

48

the entire process expensive and time consuming. For example, in an induction hardening process, quenching process is required followed by subsequent induction -heating to achieve desired property of the bearing. Additionally, the quenching media needs to be maintained at an appropriate temperature to achieve target properties. Further, the conventional techniques/systems also fail to obtain the desired mechanical and tribological properties of the bearings due to abrupt/improper heating, and thereby reducing the life of the bearings. Therefore, there is felt a need of a system for treating a surface of bearing components and a process thereof that alleviates the above mentioned drawbacks of the conventional surface treatment systems.

The advent of high-power lasers led to their use as a vital tool for improving surface hardness by transformation hardening mechanism. The surface hardening technology employing laser has emerged as a promising tool to improve life of machine components such as dies, tools, gears and camshafts. As compared to conventional case hardening techniques, laser surface hardening produces higher hardness with refined microstructure that significantly improve surface properties of parts at affordable costs and thus provide tremendous technological and economic benefits. Additionally, laser surface hardening process can precisely be imparted with greater controllability at required localized contact regions of the bearing assembly parts and thereby vastly controlling distortion, which eventually help in vast reduction in post-process grinding operations and improved clearance fits. However, a lack of understanding of the underlying hardening mechanism coupled with the stringent control of part deformation/distortion still hinders its widespread application in industries.

Although many works reported on laser surface hardening of bearing steel showed significant improvement in surface hardness, controlling of case uniformity and distortion posed a challenge. Reported works on surface hardening of prior-treated bearing steels ignored deleterious soft zone formation below the hardened layer, which is inevitable, due to the laser processing thermal cycle. Additionally, quenching media is required to avoid those deleterious soft-zones as far as thin-sectioned prior-hardened bearing steels are concerned. Otherwise, the processes developed will lead to drastic loss in core properties.

Further to the these problem identifications, present research targeted was to control the laser heat input by varying laser processing parameters, different modes of processing (pulsed mode entails better control of temperature and thereby enhances cooling rates with greater

49

uniformity), processing under different conditions/setups yielding varied heat-transfer coefficients (involving external fluid contact) and cooling rates. To overcome the tempering effects in overlapped regions, when processing cylindrical bearing elements such as rollers, a quasi-stationary laser beam processing technique proposed and experimented with integration of a high-speed rotary axis to obtain a uniform hardened layer along the entire surface. An attempt made to develop and implement the developed laser surface hardening process on actual bearing elements of taper roller bearing with design and development of various fixturing and processing setups and studied their effects on distortion control and surface properties improvement with core retention. Various work elements constitute:

(a) Comprehensive study on the influence of prior-hardened conditions on laser surface-hardening of bearing steel and their tribological performance evaluation.

(b) Study on control of laser heat input (different modes of processing) and different thermal processing conditions with analysis of treated layer characteristics and assessment of their sliding wear performance.

(c) Setting up of high-speed laser processing apparatus for surface hardening of cylindrical thin-sectioned steel parts/components using quasi-stationery laser beam approach.

(d) Finite element analysis with development of a FEM model and statistical modelling with multi objective optimization employing RSM with desirability approach for high-speed laser surface hardening process on cylindrical part.

(e) Application development of laser surface hardening process on actual tapered roller bearing elements with assessment of their engineering advantages in comparison with conventional methods.

This study brings together knowledge about the control of heat input and optimizing the laser treatment process like pulsed mode of processing, external heat sink effects, quasi-stationary laser beam processing technique using high speed mini lathe for processing large thin sectioned cylindrical components and application of the above processes on actual bearing elements. To the best of our knowledge, there are no such reports on laser hardening of bearing steels with emphasis on the above studies. It is believed that the present thesis work will add significant contribution to the existing literature from the point of view of both industrial importance and academic interest.

2.7   Overview of the thesis

The thesis comprises of ten chapters. Chapter 1 presents overview of technical background, with motivation and targeted objectives of the study, whereas, Chapter 2 discusses review of literature on various reported selective hardening methods applied on bearing steel and bearing elements. Chapter 3 discusses experimental setups with details of processing methods along with characterization and tribological performance evaluation of laser-treated layers. Additionally, Statistical approach of design of experiments for process optimization and finite element modelling with experimental validation deliberated. Discussion of results with analysis of various work elements carried out in Chapters 4 – 9. Chapter 4 deals with the study of influence of prior-treatment conditions on laser surface hardening of bearing steel and its tribological performance evaluation. Chapters 5 – 6 discusses comprehensive study on control of laser heat input as well as different thermal processing conditions in laser surface hardening of bearing steel and its assessment of sliding wear performance. Chapter 7 presents a finite element analysis with prediction of temperature distribution in laser surface hardening process. Chapter 8 explains setting up of a high-speed laser processing apparatus for surface hardening of cylindrical steel part using a quasi-stationery laser beam approach and its statistical analysis employing RSM with desirability approach. Chapter 9 deals with development of laser surface hardening process on actual tapered roller bearing elements. Chapter 10 summarizes the work and outlines direction for future investigation.

CHAPTER 3

Experimental Details

3.1 Methodology

This chapter gives a detailed description of materials used for experimentation, laser hardening experimental setup, methodology adopted, characterization techniques used for studying the macro and microstructural features and mechanical testing for evaluating the properties of the laser treated layers. Methods adopted targeting control of laser heat input by varying laser processing parameters and different modes of processing, processing under different conditions/setups yielding varied heat-transfer coefficients. A quasi-stationary laser beam processing technique established for processing cylindrical components such as rods, rollers and processing on actual bearing elements of taper roller bearing with subsequent characterization of the treated layers also presented in this chapter. Comprehensive flow chart explaining all these methods and analyses are illustrated in Figure 3.1.
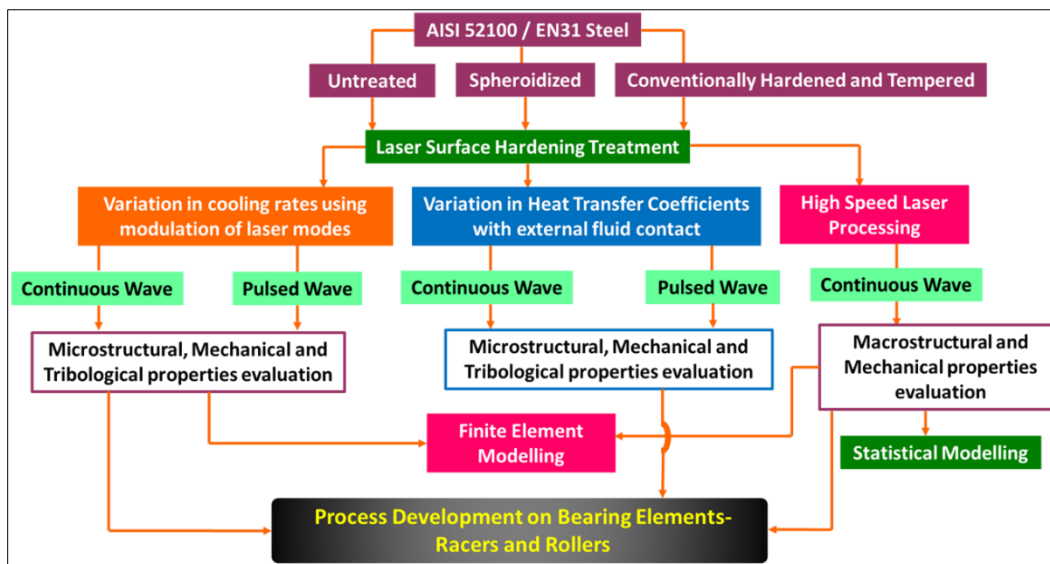
Fig. 3.1 Flow chart of methodology adopted for LSH experiments

3.2 Materials

Base Metal: The chemical composition of AISI 52100 grade bearing steel used in the present study, along with their thermophysical and mechanical properties, referred from literature [136] are provided in Tables 3.1-3.2 and Figure 3.2. The material chosen for investigation was in the form of 4mm thick flat plates which was received in hot forged condition. The chemical composition of the steel analyzed by subjecting to wet-chemical analysis methods. The average of three readings obtained by chemical analysis reported in the table. The pseudo-binary Fe–C equilibrium phase diagram of the steel, shown in Figure 3.3(a) [137]. The Acm ($\gamma \rightarrow \gamma + Fe_3C$) and A_{c1} ($\gamma + Fe_3C \rightarrow \alpha + Fe_3C$) temperatures were determined to be 910 ^{0}C and 735 ^{0}C, respectively. The TTT diagram for the steel used in the present work referred from literature [137]. The TTT diagram of Figure 3.3(b) clearly shows the temperature ranges at which specific microstructures comprising martensite, austenite, ferrite, or carbide realized. Martensite can be obtained by quenching below the Ms Temperature of 210 ^{0}C. Bainite formed during transformation can be in the temperature range of 210–450 ^{0}C. Whereas, Pearlite can be realized during transformation in the temperature range of 450–730 ^{0}C. Fine pearlite, with an inter-lamellar spacing λ less than 50 nm, can be obtained after an isothermal annealing at 550 ^{0}C. Coarse pearlite, with an inter-lamellar spacing λ larger than 200nm, can be obtained after an isothermal annealing at 700 ^{0}C.

Table 3.1 AISI 52100 Bearing steel composition (wt. %)

C	Cr	Mn	Si	P	S	Fe
1.0	1.5	0.36	0.28	0.007	0.001	Bal.

Table 3.2 and Fig. 3.2 Thermo-physical and mechanical properties of bearing Steel

Properties	
Elastic Modulus (GPa)	210
Thermal expansion coefficient ($0\ ^0$C- $600\ ^0$C),x $10^{-6}\ C^{-1}$	11.4

Hardness HV$_{0.5}$	260 ± 20
Poisson's ratio	0.3
Melting point (T$_m$)	1493 ^{0}C
Ac$_1$ Temperature	735 ^{0}C
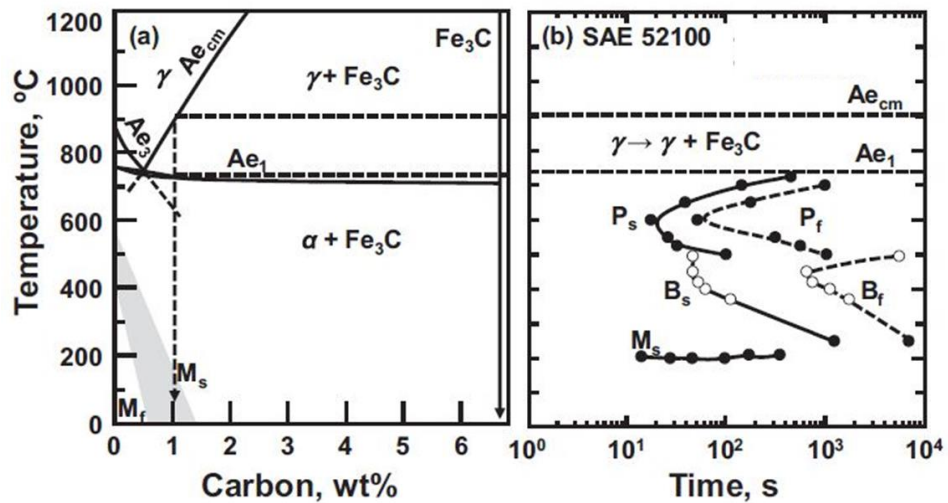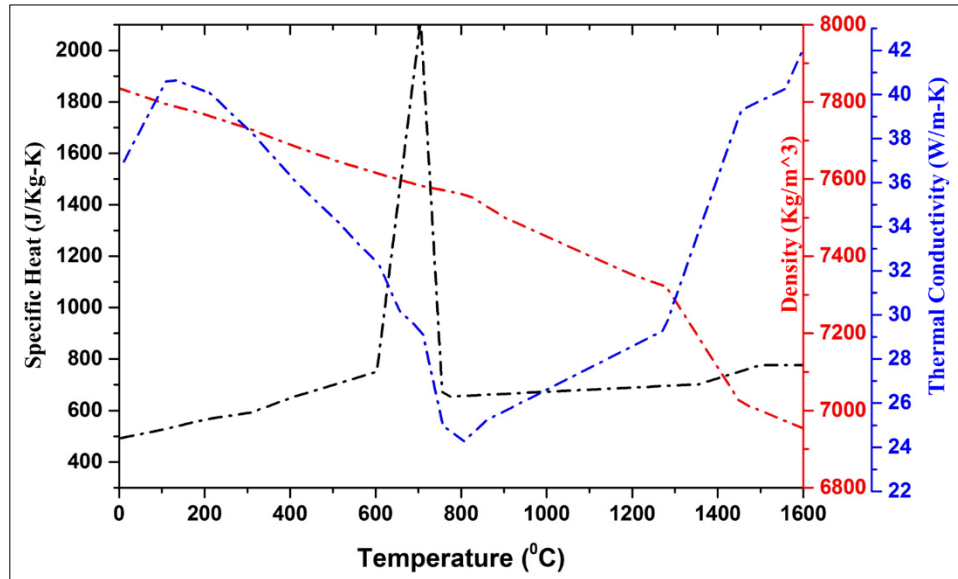
Fig. 3.3 a) Pseudo-binary Fe–C equilibrium phase diagram and b) TTT diagram for bearing steel [137]

3.3 Process flow chart for bearing elements

The process flow chart for bearing component can be visualized in Figure 3.4, in which, laser surface hardening treatment is applied after grinding. Spheroidization and conventionally hardening and tempering process applied for bearing components are mentioned below:
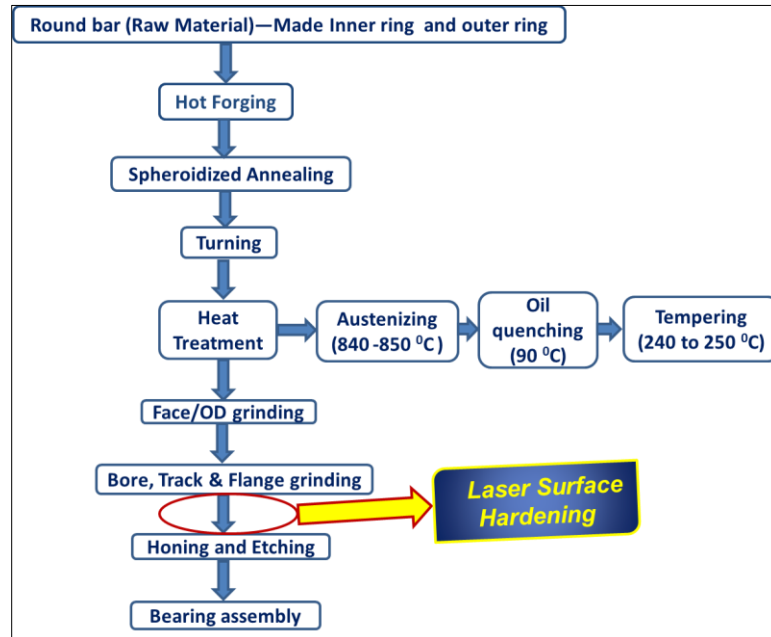
Fig. 3.4 Process chart for bearing component

3.3.1 Spheroidization annealing process

Spheroidization annealing, commonly called soft annealing is a standard operation for all high carbon bearing steels. It ensures carbide spheroidization, resulting in hardness decrease, good formability, and favourable structure for hardening [138-139]. The spheroidization (SPH) treatment is performed on 4-mm thick bearing steel plates. The treatment cycle involved austenitization at 840 ^{0}C for 2 hr. and then two-stepped cooling, one to 750 ^{0}C at a cooling rate of 25 ^{0}C/h followed by cooling to 690 ^{0}C at 10 ^{0}C/h in controlled baths and then finally to room temperature in furnace as per cycle mentioned in Figure 3.5(a). The method employed is similar to that adopted by Luo and co-workers reported in their study for bearing steel [140]. The final microstructure obtained due to spheroidization constitutes ferritic/pearlitic matrix with the distribution of globules of chromium rich spheriodized iron carbides (as shown in the Figure 3.5(b)). SEM analysis shows clearly the formation of alloy carbides of size <10µm. This initial

microstructure will influence the kinetics of subsequent heat treatment process, a fine dispersion of globular cementite creates a homogenous carbon distribution within the austenetized matrix [141].
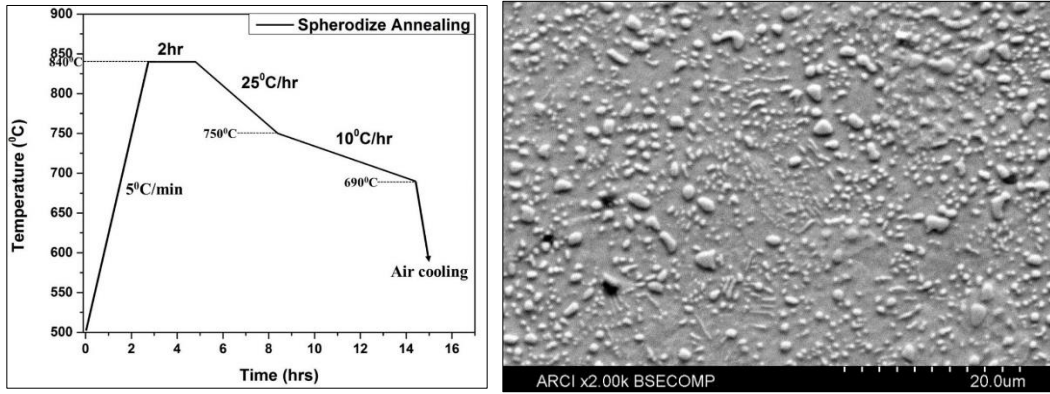
Fig. 3.5 (a) Schematic illustration of Spheroidization (SPH) heat treatment for investigated steel (b) SEM microstructure of SPH bearing steel

3.3.2 Conventional Hardening and Tempering (CHT) process

Once the plates are machined, they are austenetized at 840-850 ^{0}C for 1 hr. and then quenching in oil at 90 ^{0}C as shown in Figure 3.6 to form martensite after which it will have a hardness of 780-800 HV$_{0.5}$. Since the hardness is directly proportional to the life of the bearing, a fully martensitic microstructure with a minimum hardness of 780 HV$_{0.5}$ at the operating temperature is desired. In fact, a 40-50 HV$_{0.5}$ increase can result in a 35% life enhancement [142]. In order to reach a balance of properties after quenching, bearing steel tempered at 240 ^{0}C in controlled bath for 2.5 hours. This process improves toughness and precipitates a variety of transitional hardening carbides like η-Fe$_2$C, χ-Fe$_5$C$_2$, and ε-Fe$_{2-3}$C depending on tempering time, whilst decomposing some of the retained austenite [139, 143-144]. The CHT treatment of SPH steel specimens resulted in obtaining a final microstructure of tempered martensitic matrix with the dispersion of MC alloy carbides (M being Fe and Cr) and pockets of retained austenite as evident from the Figure 3.7(a). The hardness distribution across the thickness was ranging from 760-780 HV$_{0.5}$ [see Figure 3.7(b)]. This structure exhibited compressive residual stress of -30 ± 15 MPa (± indicates measurement uncertainty), indeed tempering followed by surface polishing induced such stress level, as reported in many studies [145].
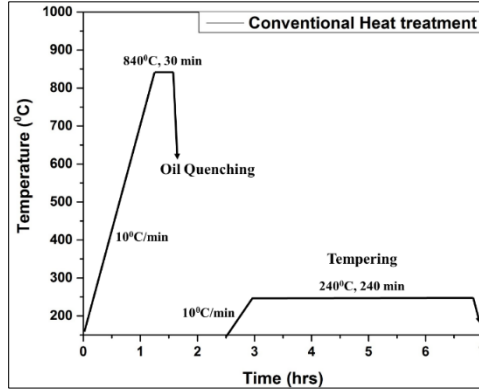
Fig. 3.6 Schematic illustration of Conventional heat treatment (CHT) for investigated steel
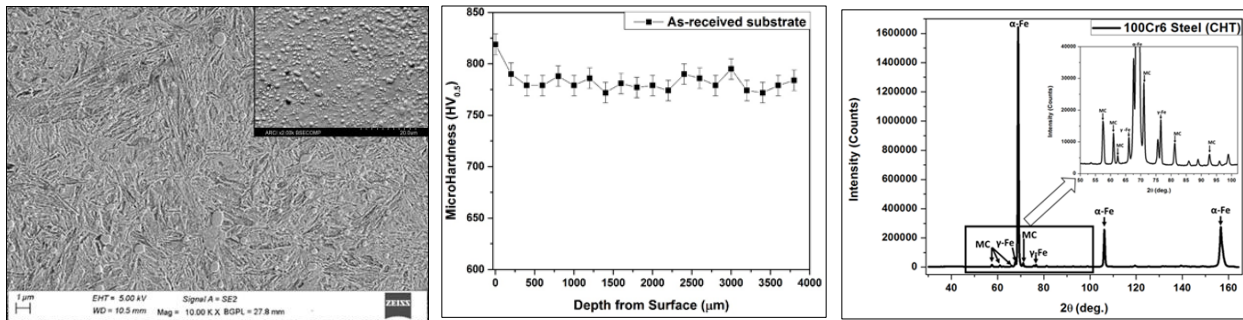
Fig. 3.7 (a) SEM Microstructure, (b) Hardness along the depth and (c) Surface X-ray diffraction profile of SPH and CHT bearing steel

Image analysis of SEM image using *Image J software 1.8.0* integrated to optical microscopy indicated volume fraction of 12 - 15% of MC carbides in the matrix of pearlite after SPH. With CHT treatment, these globular carbides more or less retained (although few are elongated) with variation in sizes ranging from 1 - 2 µm upon CHT treatment. The volume fraction estimated from quantitative assessment of phases as per XRD analysis of retained austenite and globular MC carbides in CHT microstructure was determined to be 14-16% and 6-7% respectively. The inhomogeneous distribution of globular carbides with few elongated and irregularly shapes could be due to incomplete dissolution associated with the treatment cycle [146]. The EDS analysis carried out on globular MC carbides in conjunction with crystallographic XRD phase analysis, shown in Figure 3.7(c), indicated that they are M_3C type (M being Cr and Fe) as reported by various studies employing spheroidization treatment of bearing steels [147].

3.4 Laser surface hardening utilizing high power diode laser (HPDL)

As diode laser is better suited for laser hardening compared to other conventional lasers like CO_2 or Nd: YAG, on account of its numerous advantages, a suitable high power diode laser integrated with robotic workstation is used for the entire work. Although, other lasers like YAG and CO_2 are available at cheaper costs with higher beam-qualities, Diode laser is most preferred due to its robustness; wide area coverage for processing with ease, economic viability and adaptability to manufacturing environment as far as hardening and cladding applications are concerned. Although, direct diode laser is better suited for laser hardening applications with cheaper cost, fiber-coupled selected to provide various advantages like high beam quality / uniformity with fiber-coupling, reduction of back reflection effects during processing, adaptation of time-sharing beam-switch with multiple-outputs, ease of automation with workstation (like robot) and modularity in adding stacks as and when required for improving output power. The diode lasers have the least size of all identified lasers that are available in millimetres size and less than that also.

Principle: The laser comprises of a semiconducting diode, for example, gallium arsenide with equivalent faces at the split ends of the optical cavity. The whole laser device is very lesser in size and fused on a circuit board if necessary. Semiconductor is the material whose electrical conductivity lies between a conductor and an insulator. The gallium-arsenic compounds of semiconducting materials produces radiation in infrared region when pumped with some outward electrical source. It infers, the semiconductors can change electrical energy into light. In any case, those were normal light beams does not produce by laser action. Only when the gallium arsenide semiconductor is present, then only, the laser activity takes place. Numerous semiconductors are available as laser materials and they made to 'lase' to get laser light.

Two kinds of semiconductors are available, i.e., p-type and n-type. It is important to have knowledge about the nature of the energy levels in a semiconducting material to comprehend the working of these devices. Every semiconductor has its own permitted energy states isolated by prohibited energy gap regions. In an un-doped semiconductor, enough electrons are there to fill the highest occupied energy level leaving the following higher level empty. In an n-type semiconductor, some of the impurity has been included deliberately with the goal that the

material is abundant with electrons, which in this way winds up negative. Then again, by including different types of impurities in p-type semiconductor, the material possess high number of holes thus winds up positive. A small slab of gallium arsenide will be there in semiconductor laser. At the point when the n-type and p-type materials make a contact, the boundary turns into a p-n junction. At the point when DC is connected the electrons transfer from n-type to p-type material which has an abundance of holes. Recombination happens in this procedure of transferring the electrons into the holes that promote the radiation emission.

The high power diode laser (HPDL) system delivers 915-980 nm diode laser beam with 110 mm X mrad quality (multi-mode) through two-way beam switch connected by 20-meter long fibers (1000 μm and 1500 μm for 6kW diode laser) and (600 μm and 1000 μm for 10kW diode laser) in Continuous Wave (CW) as well as Pulsed Wave (PW) modes (with minimum pulse width of 2 ms). These optical fibers with coupler at both ends and sensors are integrated to a modular optical head fixed on to the sixth arm of the Robot (REIS Robotics, Germany (Model: RV40-RSV)). The system integrated with an additional rotary and tilt axis. As the diode laser beam is highly divergent, appropriate optical components like collimators, special array optics, focusing lenses and homogenizers were used to tailoring beam into various spots suitable for wide variety of processes. Various critical features like modular stack management, wavelength selection module, operation in different modes (single-pulse, programmable-pulse, manual/programmable controlled modes) and shutter control were incorporated in the system. The system is also integrated with a DCAM software with teach unit for easy programming and simulation of complex components. The present HPDL system has six stacks (for 6kW diode laser) coupled with polarization and three different wavelengths, viz., 915 nm, 940 nm and 980 nm using suitable dielectric mirrors and prisms (Glan-taylor). The schematic of laser system with technical specifications presented in Figure 3.8 and Table 3.3, respectively. Figure 3.9(a-b) shows the integrated HPDL system view inside as well as outside laser safety cabin.
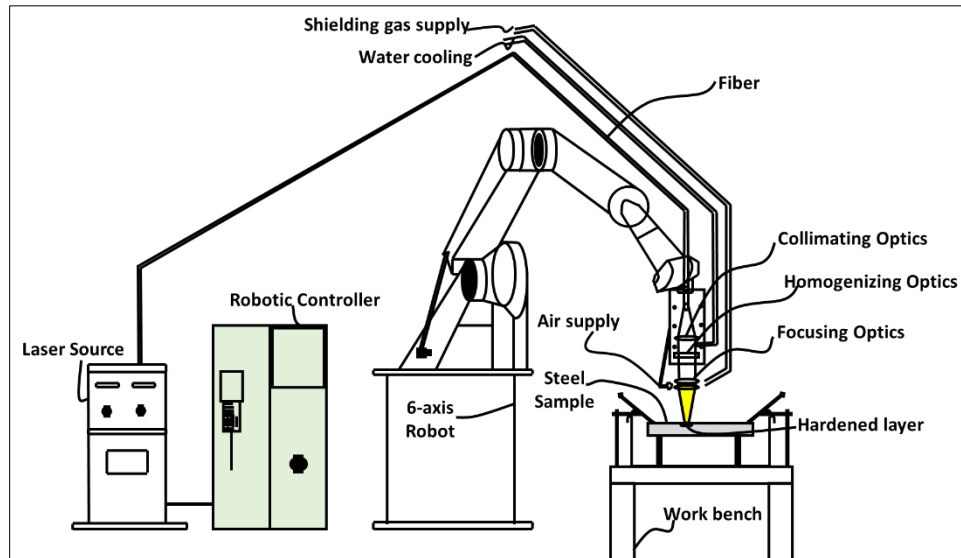
Fig. 3.8 Schematic of a fiber coupled high power diode laser

Table 3.3 Technical Specifications of High Power Diode Laser

Laser type / Model	Fibre-Coupled Diode Laser (LDF-6000 and 10000, Laserline GmBH, Germany)
Wavelength and Output Power	915-980 nm 200-10000 W (CW/Pulsed)
Work station	6-axis Robotic system with Turn and Tilt axis
Other attachments	• Focussed spot sizes : 1.5 mm Circular to 34 x 2 mm^2 Rectangular • Camera and Pyrometer based temperature controller • Co-axial and off-axis cladding nozzles with twin-hopper semiautomatic powder feeder • DCAM, LompocPro
Processes possible	Hardening, Cladding, Alloying, Conduction welding, Direct metal deposition, plastic welding and Brazing
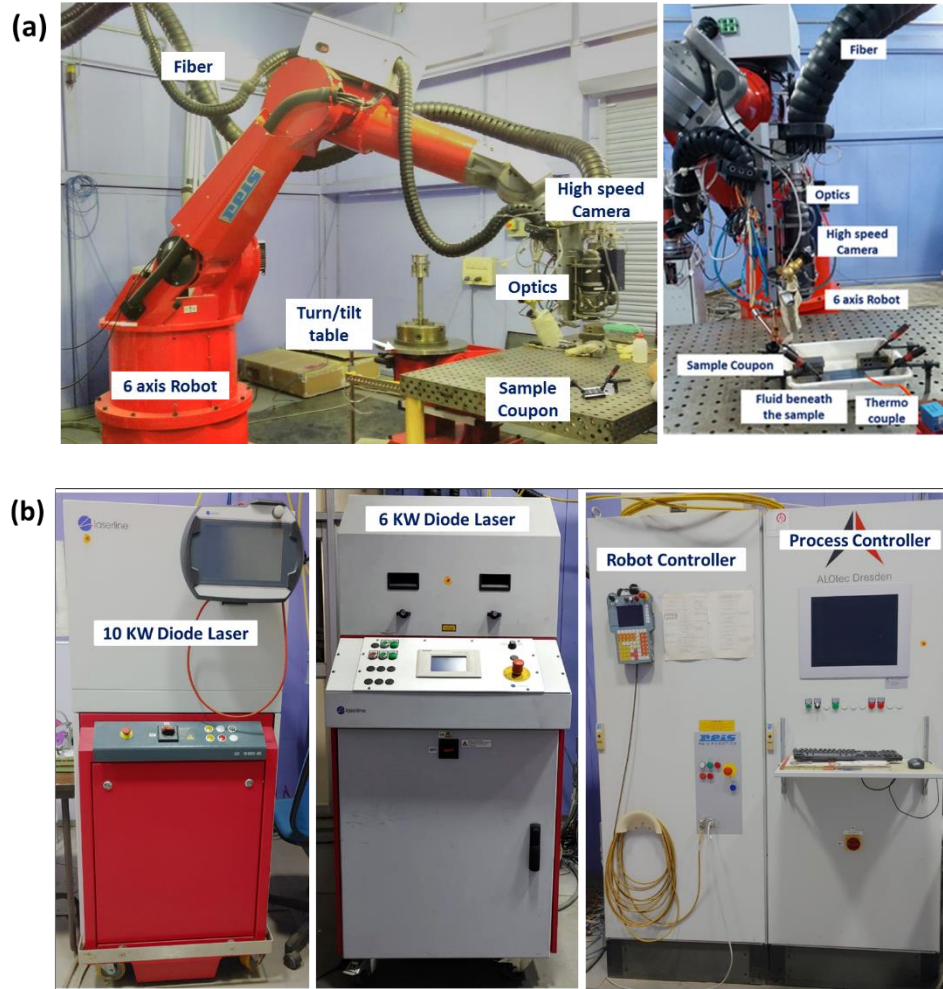
Fig. 3.9 Fiber Coupled Diode Laser System setup (a) inside and (b) outside of the laser safety cabin used for diode laser processing

3.4.1 Different modes of laser processing

In the present study, control of laser heat input by different modes of laser processing is utilized to assess the sliding wear behavior of bearing steel under high Hertzian contact pressure; Experiments were carried out with the HPDL system. Although many reports are available highlighting applicability of conventional Continuous wave (CW) mode of laser hardening processing of steels, the effective control of microstructure by controlling process cooling rate (peak temperature), softening effects of prior hardened (either laser-based or otherwise) surfaces when processed at multiple locations with control of distortion are negligible. In CW mode, continuous increase in temperature happens along the treated track although constant input power maintained and as a result, comparatively high heat accumulation with higher peak

61

temperature obtained with scanning duration. In recent years, pulsed mode of selective laser surface hardening attracted researchers due to better process control than CW mode of laser processing. In Pulsed Wave (PW) mode of processing, the laser pulses be modulated, alternatively with ON/OFF sequence, depending on the pulse duration and frequency and thereby better control in heating cycle and surface temperature of the work piece. In PW mode, the short pulse duration can increase peak power and minimize thermal diffusion to the surrounding bulk material, leading to localized heating. PW mode allows better control of surface temperature and thermal diffusion in the treated zone. Although it depends on the type of modulation, it entails better control of processing temperature and thereby enhancing cooling rate with uniformity. Thus, these two different modes will entail varied cooling-rate, which directly affect the microstructural changes in the treated case, and as a result, significant improvement in various mechanical/tribological properties envisaged with retention of core strength. Figure 3.10 illustrates different modes of laser scanning operations used for LSH treatment. In the current study, the effect of pulsed-wave (PW) mode on surface hardening of bearing steel with prior hardened condition investigated and compared with CW mode. Influence of different processing modes (CW & PW) on microstructure, hardness and the wear behavior of bearing steel discussed in detail in Chapter 5.
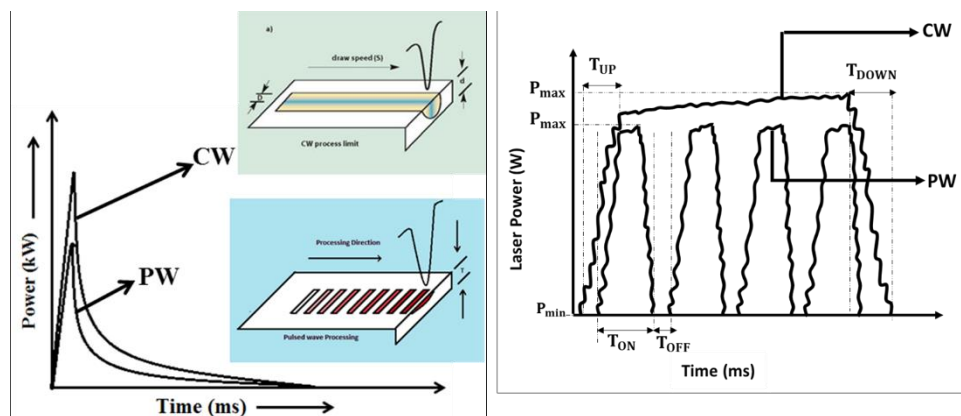
Fig. 3.10 Schematics showing different modes of laser scanning operations used for LSH treatment

The laser surface transformation hardening treatment on grinded prior-hardened (CHT) – conventionally hardened and tempered steel specimens was carried out by employing a 1500 µm fiber-coupled diode laser system integrated to 6+2 axis Robotic workstation. The setup includes

an optical module to tailor the multi-mode laser beam into a rectangular spot of 20 mm X 5 mm, as shown in Figure 3.9(a). Laser treatment was always carried out at a fixed working distance of 300 mm to have uniform laser intensity distribution throughout the experimentation. An additional 25-mm wide nozzle jet to supply argon gas at a pressure of two bar was employed to shield the treated layer against atmospheric contamination. Experiments are always performed thrice with laser surface hardening treatment being carried out each time on fresh CHT plate. In-situ high-speed camera based surface temperature monitoring and controlling system with E-Maqs (Lasertronic-Lompocpro 7.6, Fraunhofer IWS, Germany) and two color pyrometer (utilizing LASCON Software version 2.12.0) integrated to LASCON process controller LPC03 (Dr. Mergenthaler GmbH & Co KG, Germany) were used for measuring surface temperatures during LSH treatment. Table 3.4 elucidates the LSH process parameters utilized for the study. Appropriate optimized parameters with the calibration of Lasertronic-Lompocpro system and two-color pyrometer employed to enable measurement of surface temperatures during laser processing at different conditions.

Table 3.4 Laser processing parameters and conditions used for different processing modes and thermal processing conditions studies

Laser setup	
Laser type	Fiber-Coupled Diode Laser (915-980 nm)
Workstation	8-Axis Robotic System
Fiber	1.5 mm
Diode laser Beam Spot (FWHM)	20 x 5 mm
Working Distance	300 mm
Modes of Processing (CW & PW)	
Laser Power	3200 W
Scanning speed	20 mm/s
Pulse Duration	90 ms
Pulse Frequency	20 Hz
Duty cycle	90 % (PW)

3.4.2 Different thermal processing conditions

To employ different thermal processing conditions that induce specific processing surface temperature and cooling rate, experiments were conducted with a fixed peak laser power and

different laser processing modes and setups (with and without fluid contact beneath the steel plate), whose schematics are represented in Figure 3.11. Laser processing parameters and conditions used for different thermal processing condition studies are similar to that of previous conducted study carried out with different operating modes, mentioned in Table 3.4. Figure 3.11 shows four different schematics illustrating different modes of laser irradiation and setups employed for experimentation with appropriate arrangement to induce fluid (water) contact beneath the bottom surface of the work piece to enhance the heat transfer coefficient. The nomenclature used for different conditions of laser processing include CHT indicating previously conventionally hardened and tempered without any laser treatment; CW and PW indicating laser treated specimen processed under CW and PW modes respectively without any fluid contact; CW-UF and PW-UF indicating laser processed under CW and PW modes with fluid (water) contact beneath the steel specimen. Apparently, during laser processing under both CW/PW modes without fluid contact beneath the steel specimen, temperature measurements were monitored using thermocouple fixed at the bottom of the steel specimen as shown in the schematic of Figure 3.11(a). Indeed, it helped in clearly analyzing the contact temperature, and thereby assess and analyze tempering effects in the laser treated steel.
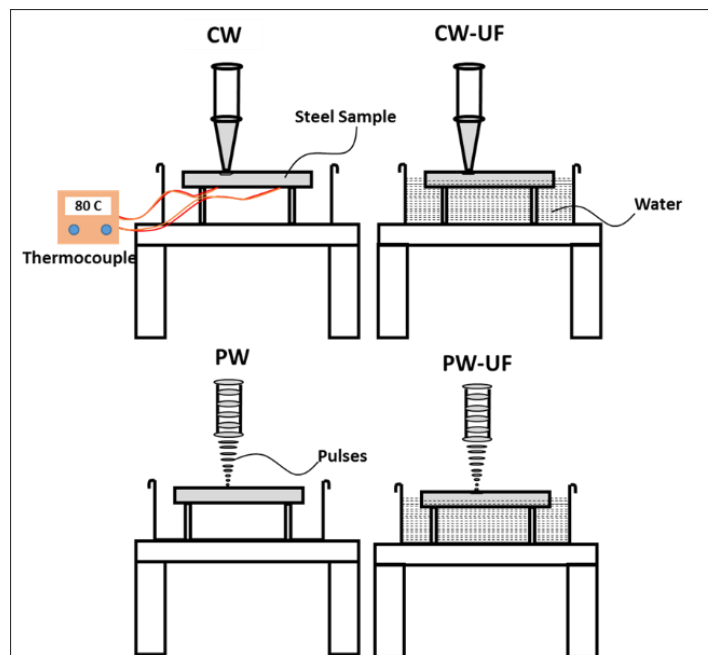
Fig. 3.11 Schematics showing different thermal processing conditions used for LSH treatment

3.4.3 Measurement of temperature utilizing E-MAqS high speed camera and Two-Colour pyrometer integrated to process controller

E-MAqS is an acronym of "Emission Matrix Acquiring System". It is an industrial black and white camera as shown in Figure 3.12 with improved sensitivity in infrared region. It is capable of measuring temperatures from 700 ^{0}C to 1400 ^{0}C at 50 Hz measuring rate. It can also be attached with pyrometer which can measure up to 2500 ^{0}C. It has special filters to eliminate the visible light and the laser from the incoming radiation, which makes it to generate image with the radiation of 740 nm. The camera measures the grey scale light available at 740 nm and all grey scale values assigned to a specific temperature on a scale. The system calibrated with the black body radiator as reference. In the present system used, E-MAqS is integrated to a *LompocPro 7.6* software. LompocPro is a monitoring system for measurement and control of devices developed by Fraunhofer IWS, Germany. Based on the application, various temperature-measuring devices can be integrated with LompocPro. Here, laser power will be the controlled and regulated for different calibrated set value of surface temperature etc. The controller is connected to camera-based system E-MAqS or to any other standard pyrometer. This integration provides provision to control and carry out the experiments with constant power to monitor the change in temperature and vice versa. While doing experiments the images recorded by the E-MAqS are also displayed in the continuous loop through the output monitor with LompocPro software interface for the better understanding of the temperature profile evolution.
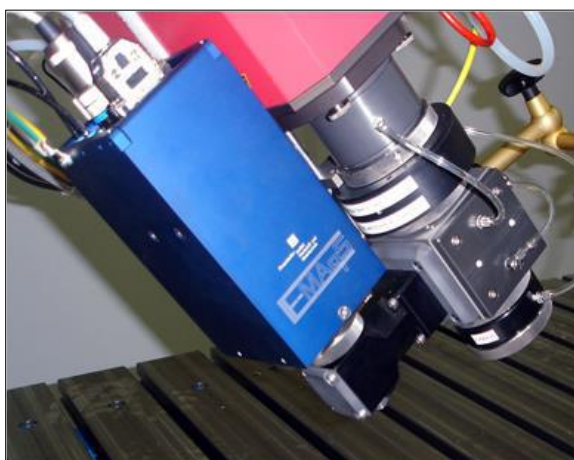
Fig. 3.12 E-MAqS high speed Camera integrated with the Laser optic
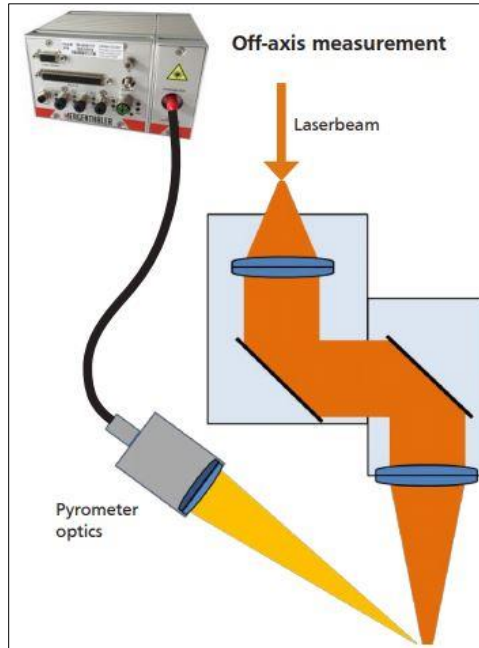
Fig. 3.13 Two Color Pyrometer integrated to LASCON controller

Two color pyrometer (utilizing LASCON Software version 2.12.0) integrated to LASCON process controller LPC03 (Dr. Mergenthaler GmbH & Co. KG, Neu-Ulm, Germany, model LASCON V3.76)) as shown in Figure 3.13 were used for measuring surface temperatures during LSH treatment processed in pulsed mode. A two-color pyrometer detects the thermal radiation of a measuring object at two different wavelengths. The ratio of the two spectral radiances φ varies almost proportionally to the temperature. Connected to the spectral radiances is the respective emissivity ε of the measuring surface for these two wavelengths. It is capable of measuring temperatures from 200 ^{0}C to 2200 ^{0}C with a response time of 100μs. In the present system used, two-color (ratio) pyrometer integrated with the LASCON process manager software for measurement and closed loop control, storage and visualization of measurement, calibration of pyrometer. Appropriate optimized parameters with the calibration of Lasertronic-Lompocpro system and two-color pyrometer were employed to enable measurement of surface temperatures during laser processing at different conditions.

3.4.4 Beam Profilometer

Laserscope UFF-100 and Lasermeter devices used in the present work are manufactured by *Prometec monitoring solutions*. The actual laser beam size, shape and energy distribution for

the selected laser beam spot are measured with the help of Laserscope UFF 100. It has a needle made up of copper material with a pinhole at the end of the needle as shown in Figure 3.14(a). The needle attached to a moving structure, which rotates along its own axis and provides linear movement in the direction normal to the focused beam. The Laser beam that focuses on the pin hole of the needle, reflects twice with the help of reflectors and finally reaches the detector, where the data will be stored. The needle scans the laser beam transversely and when the needle goes out of the focused Laser beam, the moving structure makes a displacement in horizontal direction to scan the rest of the Laser beam. In this way, the focused Laser beam is discretized and the stored data are then combined to give the actual beam shape and energy distribution.

Lasermeter is a device used to measure the actual power of the laser beam coming out of the laser optic module as shown in Figure 3.14(b). The laser beam enters through the beam entry aperture (B) and focused by a water-cooled gold plated rotational paraboloid reflector (M). The laser beam focused on the reflector (M) gets deflected through a small window (W) into a water-cooled absorber tube (A). The deflected Laser beam towards the absorber tube forms an Ulbricht globe along with the small aperture at the beginning. The Ulbricht globe formed prevents the incident radiation from leaving the absorber tube, which ensures full absorption. Inside the absorber and the reflector, the power of the incident radiation dissipates to a cooling water flow in the form of heat. Finally the signals from the high precision metering turbine (FMT) and two precision temperature measurement sensors (T1 and T2) are connected to the analyze by computer to measure the absorbed beam power to an accuracy greater than 1 % of the measured value. In this way, the actual power of focused laser beam be measured using the Lasermeter.
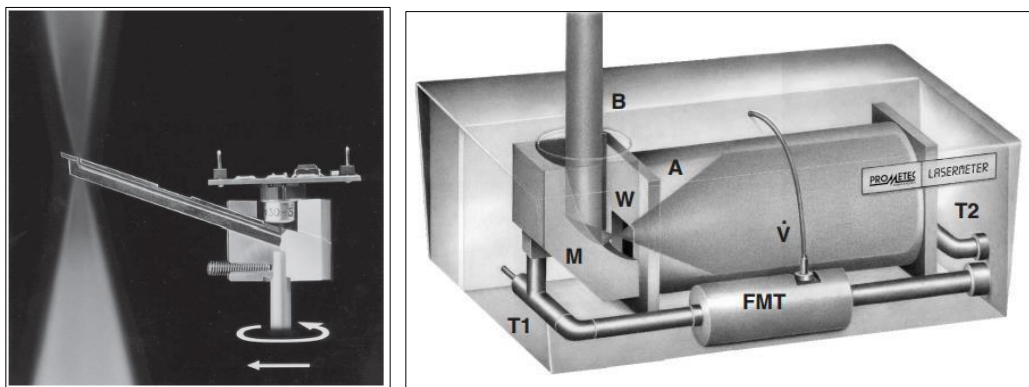
Fig. 3.14 (a) Needle of the Laserscope UFF 100 (b) Lasermeter

The Laser beam used for FEM analysis of LSH on flat plates and cylindrical components has a rectangular and square optics with the profile dimensions of 20 mm x 5 mm and 4 mm x 4 mm respectively which has a top hat energy distribution in slow axis and Gaussian distribution in fast axis movement. For the accurate prediction and evaluation of the heat-affected zone, modelling of the actual beam profile and its energy distribution should be substantial. Figure 3.15 (a-b) shows the, (a) energy distribution, (b) actual beam profile and (c) cross sectional views of fast and slow axis at 86% of power magnitude measured using Laserscope for both 20 mm x 5 mm and 4 mm x 4 mm optics.
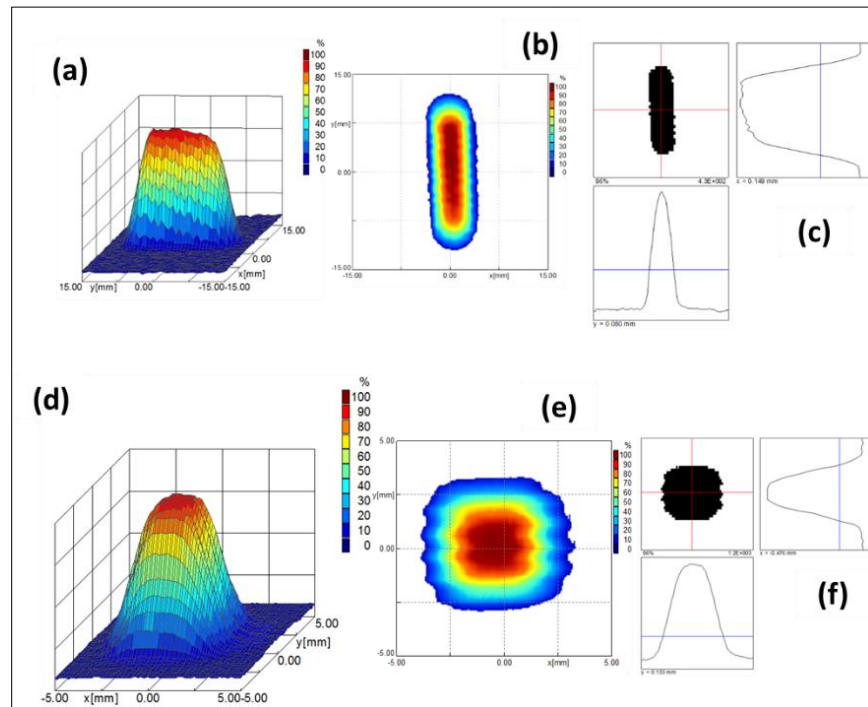
Fig. 3.15 Laser scope data for Laser beam with rectangular and square optics of 20 x 5 mm and 4 x 4 mm respectively (a,d) energy distribution of the beam, (b,c) beam profile of the laser beam at focus, and (c,f) cross-sectional views of the X and Y axes

3.5 Setting up of high speed laser surface processing facility

Further to develop laser surface hardening process on bearing elements such as rollers, work to setup high speed laser processing facility has been taken up. The high-speed rotation required for the process enables to obtain a quasi-stationary beam, a virtual ring-shaped laser spot that traverses complete circumferential periphery of the cylindrical rod or bearing element

to be processed. This setup enables complete elimination of softening inevitable due to the overlap of subsequent tracks when processed with low rotating job adopted in conventional helical laser hardening setup. Figure 3.16 illustrates the schematic difference obtained in the quality of laser-hardened track across the length of the cylindrical rod due to variation in process dynamics. In case of high-speed rotational process, the laser spot rotates multiple times within the circumferential periphery resulting in virtual ring-shaped laser beam termed as quasi-stationery beam spot that envelops the diameter of the cylindrical rod. The fast moving laser spot (high rotational speed) entails sufficient self-quenching of the bulk and thereby promoting self-quenching effect vital for austenitization of the surface to a depth of hundreds of microns determined by the power density and laser beam profile intensity. As the thermal interaction in between rotations is so small, in millisecond level, enveloping entire circumferential periphery of the rod, the question of reduction in temperature below austenitization level ($Ac_1 - 735\ ^0C$) does not arise. Thus, tempering of subsequent tracks eliminated and the resulting hardness profile will not have reduced hardness along the treated track when laser beam traversed, as qualitatively presented in Figure 3.16(b). The dip in hardness that happens when processed in conventional helical way of processing presented in Figure 3.16(a) gets completely eliminated. Similar analogy has been reported by various studies involving high-speed laser hardening of cylindrical parts, although with different types of lasers and beam sizes [148-149].
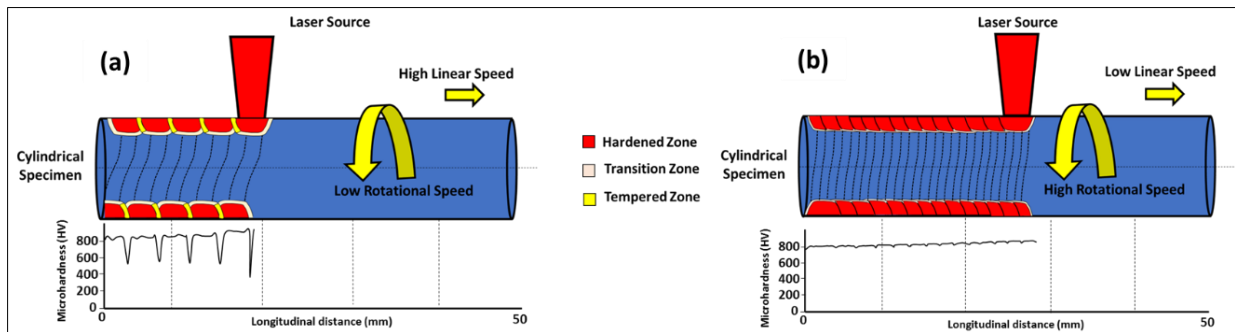
Fig. 3.16 Schematics showing process setup and kinematics (a) Conventional Helical laser hardening (b) High rotary speed laser hardening

Figure 3.17 illustrates the actual laser processing setup utilized for the study. A high-speed rotating mini lathe machine was integrated to a 1000 μm (NA: 0.22) fiber-coupled 10 kW diode laser and a 6-axis robotic workstation. An optical head that tailor the laser beam spot into a uniformly distributed 4 mm X 4 mm area, integrated by employing appropriate collimating,

homogenizing and focusing optics as shown in Figure 3.17. The multi-mode square beam of top-hat intensity distribution in long axis and Gaussian distribution in short axis enables wide area processing that enable effective quenching as compared to other narrow laser beams with Gaussian distribution. A self-centering chuck with tailstock enabled the holding of 12 mm diameter En-31 cylindrical solid steel rod of 50 mm length to rotate in straight horizontal axis of rotation with almost negligible runout. A fixed focusing distance of 150 mm between focusing optic and surface of cylindrical rod maintained throughout the processing period to entail uniform hardened layer formation. Prior to laser processing, the cylindrical rod was machined to straightness and grinded to a surface finish of 0.5 µm Ra.
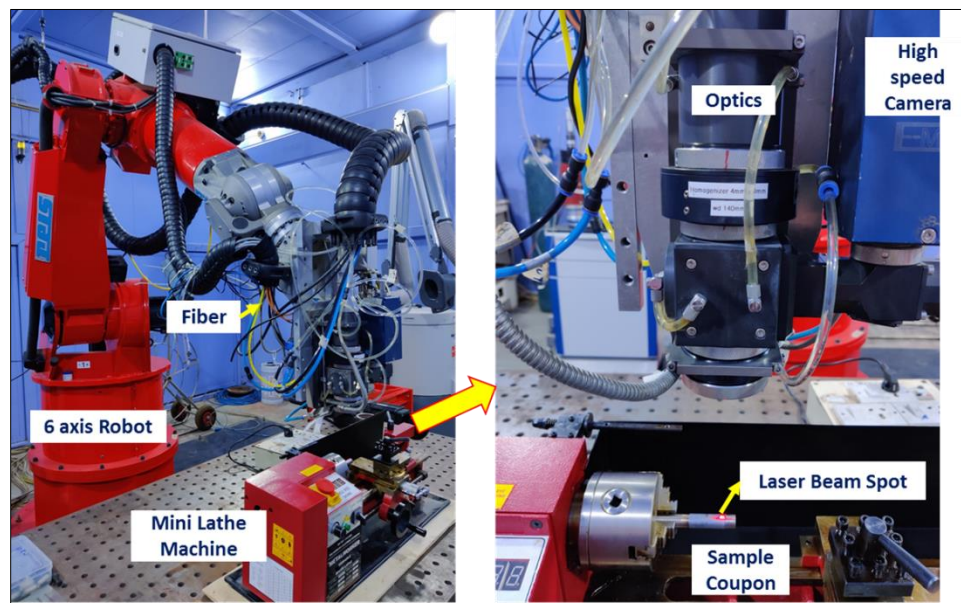
Fig. 3.17 Setting up of mini-lathe machine for high speed LSH process

3.6 Numerical simulation of laser material interaction

3.6.1 Theoretical modelling and governing equations for simulation of laser surface hardening of thin sectioned plates

The 3-dimensional heat-transfer simulation model was inbuilt in COMSOL Multiphysics 5.5. The variation in temperature profile and case depth developed in the treated region for various modes of laser processing and conditions were predicted using this simulation model. The equation (3) determines the heat transfer equations used in this simulation of flat plate

studies of LSH under different processing modes. Whereas equation (1) gives addition of Gaussian shape energy distribution in equation (3).

Where Q is the heat flux (W/m^2), Q_0 is laser power (W), A_c is absorption coefficient, r_b radius of laser beam, x and y are the axis of the coordinates system. As the laser beam used in our case has a rectangular profile of 20mm x 5mm area with top hat energy distribution, a model developed by superimposing an array of Gaussian heat sources with spatial distribution as represented in Figure 3.18(a). The dimensions of simulated rectangular beam constructed in a way that all Gaussian beams appropriately overlap in area leading to the equivalent area of actual laser beam spot used for the experimentation. The strategy adopted for superimposition is similar to that reported in the study modelling the laser surface-treatment process employing rectangular laser beam spots [150]. The modelled energy distribution for rectangular spot laser beam consist of seven superimposed circular Gaussian sources in a two-dimensional array with radius $r_b = 2.5$ mm and has an equivalent power share as shown in Figure 3.18(a). The total power density of the laser heat source was modified with summation of all individual seven beam sources (measured intensity of each source considered) as represented in equation (2). Q_{01} indicates the first laser spot of volumetric heat source term, Q_{02} is the second laser spot of volumetric heat source term, and Q_{03} is the source term due to the third spot and so on until seventh spot, respectively. The loci of the intensities were changed in conjunction with laser scanning direction by changing the x and y coordinates in the Gaussian field equation. Whereas, x_1 and y_1 are the distance between the origin of the coordinates system and first beam center, x_2 and y_2 are the distance between the origin of the coordinate system and the second beam center along the x and y coordinate respectively. In the same fashion, the beam centers are located by varying the distance between beam centers coordinates from the origin. Thus the volumetric source term of the final beam developed, until seventh source, summed up to the linearity of the model to form as per equation (2). Thus, the final modelled laser beam profile obtained with its energy distribution shown in Figure 3.19(a). Indeed incorporation of the actual energy profile distribution measured from Laserscope into the model help facilitated in obtaining close-to-approximation in laser beam source for modelling the process. As depicted in Figure 3.15(a), the rectangular beam intensity profile represents cross-sectional views of actual measured profile in both fast and slow axis with 86% power magnitude. The modelled beam profile obtained using the superimposing of Gaussian heat sources illustrated comparable distribution with close approximation to that of

71

measured laser beam profile. Indeed, the comparison shows that the cross sectional beam profiles modelled are in good correlation with the actual beam profiles. The governing equation to solve the temperature distribution T(x,y,z,t) across the steel substrate during the laser–material interaction is given by the equation (3).

$$Q = Q_0 * \frac{A_c}{(\pi * r_b{}^2)} * e^{-2[((x-x_c)/r_b{}^2)^2 + ((y-y_c)/r_b{}^2)^2]} \dots\dots\dots\dots\dots Eq.1$$

$$Q = Q_{01} + Q_{02} + \cdots \dots + Q_{07} \dots\dots\dots\dots\dots\dots\dots\dots\dots\dots\dots Eq.2$$

Where, $Q_{01} = Q_0 * \frac{A_c}{(\pi * r_b{}^2)} * e^{-2[((x-x_1)/r_b{}^2)^2 + ((y-y_1)/r_b{}^2)^2]}$

$$Q_{02} = Q_0 * \frac{A_c}{(\pi * r_b{}^2)} * e^{-2[((x-x_2)/r_b{}^2)^2 + ((y-y_2)/r_b{}^2)^2]}$$

$$Q_{03} = Q_0 * \frac{A_c}{(\pi * r_b{}^2)} * e^{-2[((x-x_3)/r_b{}^2)^2 + ((y-y_3)/r_b{}^2)^2]} \dots$$

$$\dots Q_{07} = Q_0 * \frac{A_c}{(\pi * r_b{}^2)} * e^{-2[((x-x_7)/r_b{}^2)^2 + ((y-y_7)/r_b{}^2)^2]}$$

$$\rho C_p \frac{\partial T}{\partial t} + \nabla(-k\nabla T) = Q + h\left(T_{amb} - T\right) + \sigma\varepsilon(T_{amb}^4 - T^4) \dots\dots\dots\dots Eq.3$$
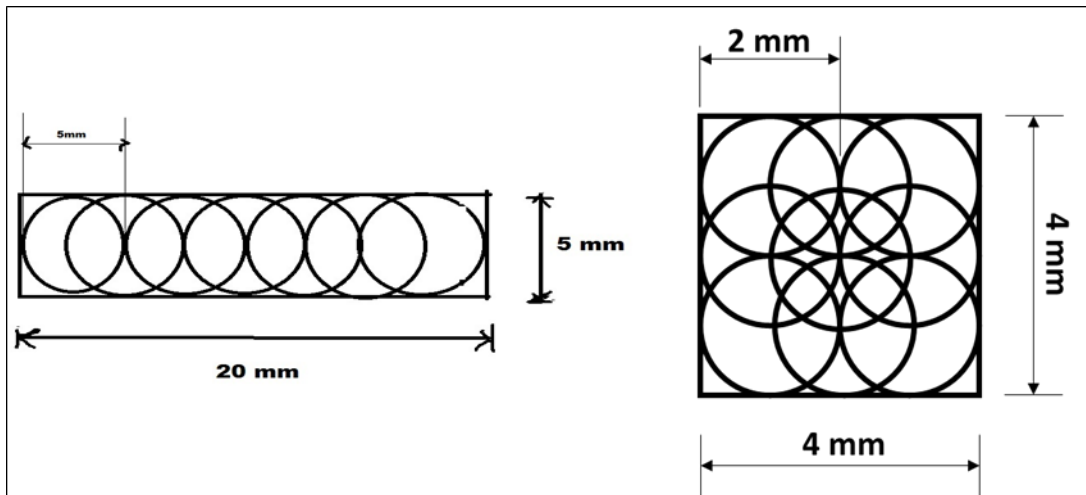
Fig. 3.18 Arrangement of laser beam spot sources in the modeling work
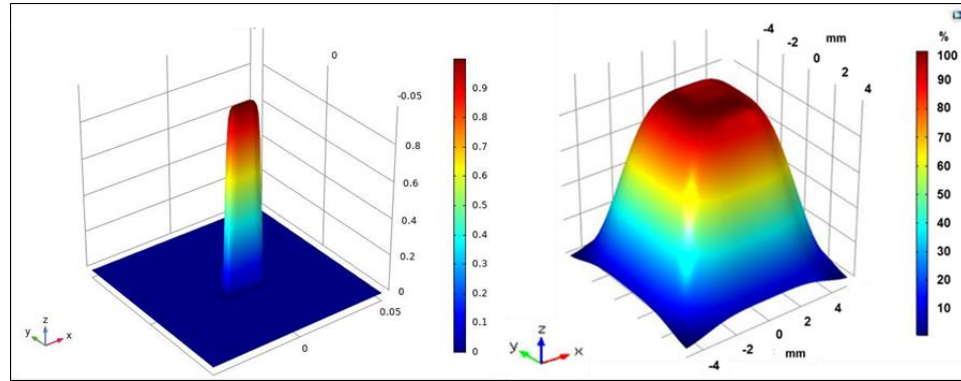
Fig. 3.19 Derived energy distribution used for simulation (20 mm x 5 mm and 4 mm x 4mm spots)

The boundary conditions followed in simulation are defined and presented in Figure 3.20. All the faces of the flat plate were considered in convective-forced heat exchange mode, whereas, at laser source vicinity, radiative mode was considered according to the boundary conditions applied. For the convective boundary conditions, the heat transfer coefficient considered based on predefined convective heat flux conditions available in COMSOL. The fluid present in the surrounding vicinity was chosen as air, whereas, for the radiation boundary conditions, the emissivity of the surface of the material was assigned as $\epsilon = 0.33$. The computational domain for the analysis was discretized with quadratic element, while, discretization of the temperature field uses second order basis functions or shape functions to solve for the degrees of freedom, which are considered, the solution vectors of the concerned solution field. Figure 3.21 shows the domain geometry with boundary conditions utilized and the tetrahedral user-defined meshing adopted for the computation. Thus, the transient thermal model generated with the necessary material property data and boundary conditions help run with time-dependent solver (PARDISO) available in COMSOL Multiphysics.

Description	Boundary	Boundary condition	Variable
Laser source	4	Heat Flux	Q
Radiation	4	Surface-To-Ambient	ε
Convection cooling	1 ,2,5,6	Convective Cooling	h
Insulation	3	Insulation	-
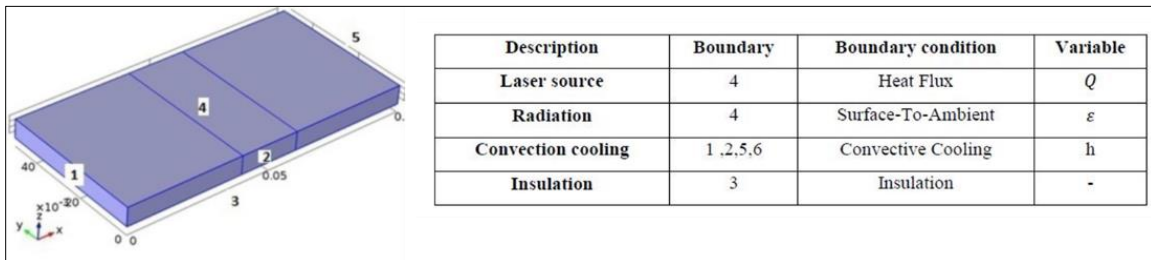
Fig. 3.20 Illustrating the boundary conditions of the flat plate used for simulation

The transient study was simulated to run for the time range of 0 to t with time intervals necessary for the solver to achieve the initial convergence. The average duration for running the simulation varies and depends mainly on the interaction time and the cooling time of the left out bulk part of the material. The governing equation to solve for the temperature distribution $T(x,y,z,t)$ across the steel substrate during the laser–material interaction is given by the equation (3) [151]. where ρ - density of the substrate material, C_p - specific heat capacity of the substrate material, k - thermal conductivity of the substrate material, h - convective heat transfer coefficient, σ - Stefan–Boltzmann constant ($\sigma = 5.67 \times 10^{-8}$ W/m^2 K^4), ϵ - emissivity of the substrate surface, T_{amb} - ambient temperature and Q - boundary heat source generated by the laser beam interaction.
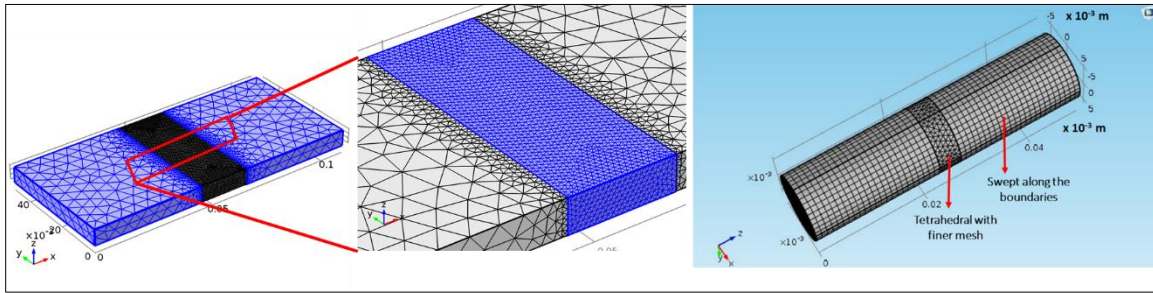
Fig. 3.21 Tetrahedral user-controlled mesh used for simulation

3.6.2 Theoretical modelling and governing equations for simulation of high speed laser surface hardening of cylindrical steel components

As optimizing the process involve cumbersome experimentation with numerous trails varying the processing conditions, it was felt pertinent to first simulate the process without traversing the laser beam spot using commercial FEM software COMSOL Multiphysics 5.5. The temperature dependent thermal properties of the material (EN31 Steel) were defined in the simulation utilizing interpolation functions that faithfully replicates the thermal properties as shown in Figure 3.2 and Table 3.2. The temperature dependent material properties help in coupling the non-linear behavior of the material in analysis and thereby precision in predicting heat affected zone dimensions and thermal transients. The first task undertaken was to simulate the process determining laser dwell time (duration of the laser beam exposed without any linear

traverse along the length of the cylindrical rod) required to produce a uniform quasi-stationary ring of 12 mm diameter. It should facilitate in producing a 4 mm wide laser treated layer across its circumferential periphery of steel rod with uniformly distributed hardened case (without any trace of melting). A transient laser-heat source model was created using a time-dependent spatial distribution of the energy input at the surface, calculated by multiplying the beam profile with the absorptivity of the material as per equation (1) and the term Q_0 represents the laser power density, which is applied as a boundary heat source in the thermal model.

As the laser beam used in our case has a square profile of 4 mm x 4 mm area with top hat energy distribution, a model is developed by superimposing an array of Gaussian heat sources with spatial distribution as represented in Figure 3.18(b). The dimensions of simulated square beam constructed in a way that all Gaussian beams appropriately overlap in area leading to the equivalent area of actual laser beam spot used for the experiments. The modelled energy distribution for the square spot laser beam consisted of nine superimposed circular Gaussian sources in a two-dimensional array with radius $r_b = 1$ mm and has an equivalent power share as shown in Figure 3.18(b). The total power density of the laser heat source was modified with summation of all individual nine beam sources (measured intensity of each source considered) as reported earlier for flat plat FEM analysis. Thus, the final modelled laser beam profile with its energy distribution shown in Figure 3.19(b) for 4 mm x 4 mm laser spot.

For generation of requisite transient thermal model in COMSOL Multiphysics, a heat-transfer-in-solids module available with software has been utilized and simulated on to a solid cylinder with a diameter of 12 mm and a length of 50 mm. All the faces of the cylinder considered in convective-forced heat exchange mode, whereas, at laser interaction region with material, radiative mode considered according to the boundary conditions applied. For the convective boundary conditions, the heat transfer coefficient considered based on predefined convective heat flux conditions available in COMSOL. The fluid present in the surrounding vicinity was chosen as air, whereas, for radiation boundary conditions, emissivity of the surface of the material was assigned as $\epsilon = 0.33$. The computational domain for the analysis discretized with quadratic element, while, discretization of the temperature field uses second order basis functions or shape functions to solve for degrees of freedom, which are considered, solution vectors of the concerned solution field. Figure 3.21(b) shows the domain geometry with

boundary conditions utilized and the tetrahedral user-defined meshing adopted for the computation. The average duration for running the simulation varies and depends mainly on the number of rotations of cylindrical rod and the cooling time of the left out bulk part of the material. In simulation, the end time t is the laser dwell time (LDT) is considered as experimentally defined one which constitutes the total duration of laser-on time for single-spot processing. It is the total duration of the laser beam exposed for producing the apparent ring spot of the laser without linear movement of the laser beam on the cylindrical rod. In case of processing with linear traverse along the length of the rod, laser dwell time was considered as the ratio of total time of laser beam covering entire length of processed rod to that of number overlapped apparent ring spots produced with 4 mm width. Moving mesh method was used in simulation with its velocity being used similar to that of linear speed. Experimentally, LDT for single spot processing was varied by laser-on duration exposure and in case of processing along the rod, it was governed by the linear speed.

3.7   Statistical modelling using response surface methodology

As statistical modelling of laser surface hardening process on simple geometries like flat plate are well reported in literature, statistical modelling on high-speed processing, especially with quasi-stationery laser is not known. Hence, the work on developing suitable statistical mathematical modelling for high-speed laser hardening of cylindrical rod, especially applicable for bearing element such as roller with complete elimination of softening, has been taken up and presented in this thesis work. Experiments for high-speed laser-surface hardening process of cylindrical rod conducted by utilizing three-factor with three-level BBD design as shown in Table 3.5(a) available in *Design Expert* software. The significance of the developed model assessed by analysis-of-variance ANOVA technique [152-154]. All fifteen experiments conducted as per matrix designed were analyzed and checked for the significance of all the three parameters and assess their interaction with responses and their interaction for adequacy [see Tables 3.5(b)]. As the aim of the study is to develop the statistical mathematical model by adopting RSM methodology, all three responses (Total Case Depth (TCD), Mean Hardness – Cross-sectional (MHC) and Differential Hardness – Longitudinal (DHL) were analyzed and co-

related with their parametric effects to generate regression equations. The quality of the laser-hardened layer obtained assessed by evaluating its critical responses.

Table 3.5 (a) Process parameters and (b) the experimental design levels used for the Box-Behnken design of experiment.

S no.	Factor	Units	Levels		
			-1	0	+1
1	Laser Power	W	2500	3000	3500
2	Linear Speed	mm/s	8	10	12
3	Rotary Speed	RPM	1600	1800	2000

	Factors		
Run	Laser Power (W)	Linear speed (mm/s)	Speed of rotary axis (RPM)
1	-1	-1	0
2	1	-1	0
3	-1	1	0
4	1	1	0
5	-1	0	1
6	1	0	-1
7	-1	0	1
8	1	0	-1
9	0	-1	-1
10	0	1	-1
11	0	-1	1
12	0	1	1
13	0	0	0
14	0	0	0
15	0	0	0

Figure 3.22 illustrate the schematic of these responses analyzed from the resulting laser-hardened layer obtained along its length and cross-section processed. As hardened depth near the surface of the treated layer can be easily demarcated macroscopically from the unaffected core

due to chemical reaction of etching associated with hard martensitic transformation (brighter being martensitically transformed region and darker being unaffected core), its boundary temperature can be realized to be Ac_1 ($T_{C1} = 735$ ^{0}C). Thus, TCD representing total hardened case-depth evaluated, considering the boundary temperature of A_{C1} in the contour, and an average of five readings along its processed length reported. MHC evaluated is a measure of average of all hardness values measured along its entire hardened cross-sectional depth with distance between indents being 50 μm. DHL is a qualitative feature determining hardness difference measured along its length of surface of the rod, obtained at a depth of 20 μm from the surface. Since the laser spot used was a square beam of 4-mm side, it was pertinent to consider hardness measurement up to 5 mm along the treated length with reporting of values obtained at central region. As significance of DHL is critical to evaluate hardness distribution uniformity along its longitudinal direction with minimization of its differential. Indeed reducing DHL to as minimum as possible is the principal aim to eliminate softening effects associated with induced temperatures and thermal diffusion effects of overlapping spiral tracks during high speed processing. Indeed, if linear speed increase beyond a limit that result in peak temperature at any point of surface below A_{C1} will drastically soften the case. Thus, response of DHL that depend on temperature distribution along its length determine the effective control of high-speed laser processing involving quasi-stationary laser beam.

Fig. 3.22 Schematic showing total case depth, mean hardness cross-sectional and differential hardness longitudinal

Multiple regression was fitted with response data by analyzing statistical significance test on the model coefficients and lack-of-fits. The developed regression model in each case was steered to the design space with statistical analysis for higher F-value and smaller P-value.

Perturbation plots along with surface and contour plots drawn in each case for all three responses (TCD, MHC and DHL) along with their corresponding interaction effects. Finally, numerical optimization using desirability approach [155] carried out that steer to establish optimal combination of parameters that fulfil multi-objectives of the process such as maximizing TCD and MHC and minimizing DHL. Thus, the predicted values obtained from the all the three responses with optimization approach validated from final experimental tests conducted and compared.

Table 3.6 depicts three responses (TCD, MHC, DHL) considered to evaluate the quality of the hardened layer obtained on the treated surface of the steel cylindrical solid rod using laser processing parameters constituting laser power, linear speed and rotary axis speed varied at three levels as per the design of experimentation of RSM approach. Analysis of Variance (ANOVA) in stepwise mode performed to identify the significance of each parameter's effect on the three output responses. Furthermore, its significance on linear and quadratic effects of the parameters and their interactions with model adequacy checked. The multiple regression model developed was based on the collection of statistical technique with defined polynomial expressions reported from various studies reported in literature [154]. The coefficients of the model predicted through regression analysis based on the three chosen responses. The sequential F-test, lack-of-fit test and other adequacy measures used to assess the fit of the model. The p-values were computed by means of ANOVA of the model and each term in the model, if do not exceed the level of significance ($\alpha=0.05$), then, it was considered adequate within the confidence interval of ($1-\alpha$). A p-value > 0.05 suggests no significant effect. The F-value is the ratio of the model mean squared divided by the residual mean squared, i.e. the variation explained by the model relative to that unexplained. The appropriate models fitted to the three responses based on the p-value < 0.05. Moreover, lack of fit is insignificant in the best model.

Table 3.6 Experimental input parameters and their responses obtained after laser surface hardening treatment.

	Factors and levels			Responses (Experimental)		
Exp. No	Laser Power (W)	Linear speed (mm/s)	Speed of rotary axis (RPM)	TCD (μm)	MHC (HV$_{0.5}$)	DHL (HV$_{0.5}$)

1	2500	08	1800	210	780	176
2	3500	08	1800	350	859	188
3	2500	12	1800	120	680	82
4	3500	12	1800	200	707	83
5	2500	10	1600	175	701	89
6	3500	10	1600	260	802	107
7	2500	10	2000	102	671	156
8	3500	10	2000	230	787	160
9	3000	08	1600	310	832	163
10	3000	12	1600	202	690	58
11	3000	08	2000	270	825	191
12	3000	12	2000	150	705	86
13	3000	10	1800	210	728	144
14	3000	10	1800	207	725	143
15	3000	10	1800	201	695	121

3.8   Processing of tapered roller bearing elements

Development of various methods by controlling process parameters and conditions in laser surface transformation hardening process on tapered roller bearing elements (AISI 52100 steel) to improve life and load bearing capacity anticipated to result in size reduction of the bearing by enhancing strength and fatigue life. Challenges for implementing laser surface treatment process on tapered roller bearing elements constituting inner racer, outer racer and rollers lies in obtaining uniform case depth across the required contact surface with enhanced hardness higher than core (which is already conventionally hardened and tempered to $800HV_{0.5}$) with vast reduction in post-process machining requirements applicable in industrial production environment. Additionally, the developed process should not deteriorate aspects such as strength, residual stress, retained austenite and surface roughness. Typical dimensions of the tapered roller bearing elements chosen for the current study are exhibited with deign criterion in Figure 3.23. The outer racer element is with outer and inner diameter of 55 mm and 44 mm respectively and with 12^0 taper angle and 13 mm width. Inner racer element with outer and inner diameter of 43.4

mm and 30 mm respectively and width of 17 mm. Roller is with 6 mm diameter and 12 mm length. All the bearing elements were made from 52100 bearing steel and prior treated with spheroidization and conventionally hardened and tempered.
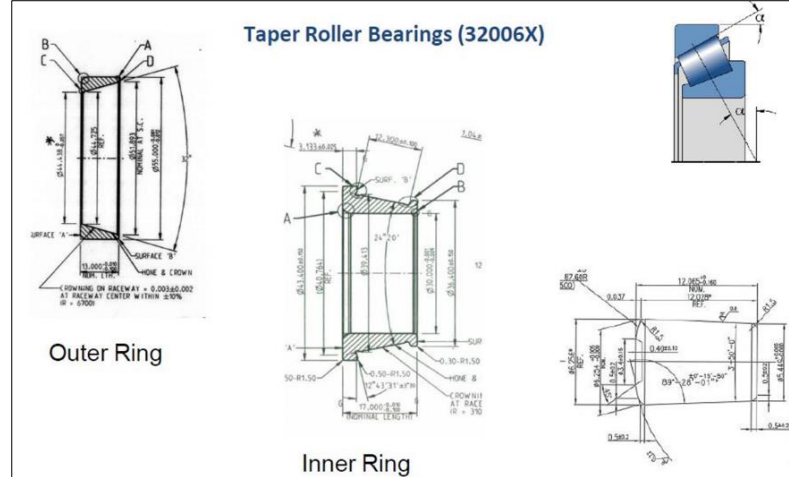
Fig. 3.23 Tapered Roller Bearing Elements

3.8.1 Experimental setup

The laser surface transformation hardening process is carried out using a 1000 μm Fibre coupled 6 kW diode laser integrated to 6+2 axis robot. The setup include an optical module to tailor multi-mode laser beam to a rectangular spot of 20 mm x 5 mm. An additional 25 mm wide nozzle jet to supply argon gas at a pressure of two bar employed to shield the treated layer against atmospheric contamination. Appropriate optimized parameters (mentioned in Table 3.7) with calibration of Lasertronic-Lompocpro system employed to enable measurement of surface temperatures during laser processing at different conditions. In order to employ different thermal processing conditions that induce definite processing temperatures and different cooling rates different laser processing modes and setups represented in Figures 3.25-3.26, 3.30 employed. Required hardening areas of tapered roller bearing elements (outer and inner racer, roller) mentioned in Figure 3.24. Typically, the surface treatment is performed on outer surface of the inner ring, an inner surface of the outer ring and the entire peripheral surface of the roller as mentioned in Figure 3.24.
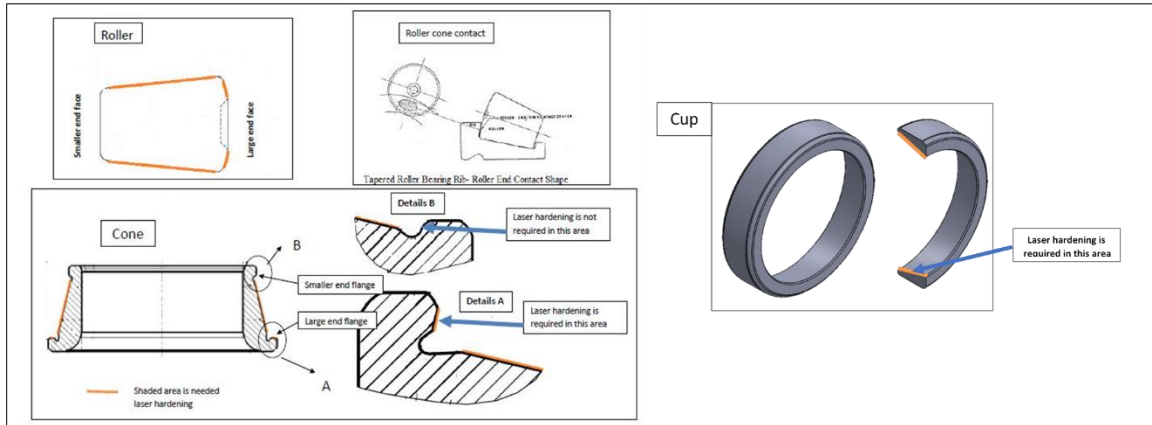
Fig. 3.24 Required Hardening areas of tapered roller bearing elements

Table 3.7 Process Parameters for Laser Hardening of TRB components

Laser processing setup conditions

Laser	Fiber Coupled Diode Laser
Workstation	6-Axis Robotic System
Laser Wavelength	915-980 nm
Fiber	1000 μm
Surface-temperature Measurement System	Lasertronic Lompocpro 7.6 with E-Maqs camera
Laser Beam Spot	20 mm * 5 mm (Rectangular)
Working Distance	300 mm

Laser parameters used for experiments

Laser Power	2600 W- 3200 W
Scanning Speed	15-20 mm/s
Surface Temperature	1000 ^{0}C - 1400 ^{0}C

Ramping and pulsing parameters

Programming mode	Continuous and Pulsed mode of hardening
Laser Intensity	50-95 %
Pulse width (ms)	10-70 s

3.8.2 Design of fixturing setups and conditions

Initially, LSH experiments were performed using magnetic fixture to hold both inner and outer racers with concentricity and minimal runout. The fixturing setups with magnetic fixture for both the racers are represented in Figure 3.25. Due to excess heat accumulation during laser processing, demagnetization of fixture resulted in detachment of racers while processing. To overcome the detachment issues, brass fixture fabricated for holding the racers, due to its higher thermal conductivity. The fixturing setups with brass fixture for both the racers represented in Figure 3.26. Due to distortion caused by usage of brass fixture, LSH experiments were done using same experimental setup mentioned for flat plates employing different thermal processing conditions to induce definite processing temperatures and cooling rates as mentioned in Chapter 6. Experiments were conducted with a fixed laser power, different laser processing modes and setups (with and without fluid contact around the racer using appropriate fixturing setup) represented in Figure 3.30 are employed. A new methodology incorporating appropriate fixturing setup to provide fluid flow below the steel sample (sufficient heat-sink effect) during laser hardening treatment is adopted. Additionally, different laser pulsing parameters and programming pattern were also designed and attempted to reduce ovality in bearing elements processed with retention of core, minimization of distortion and transition zones interfaces. The process was also optimized in such a way that the resulting treated layer induce higher compressive residual stresses and thereby increase in fatigue life of the bearing.
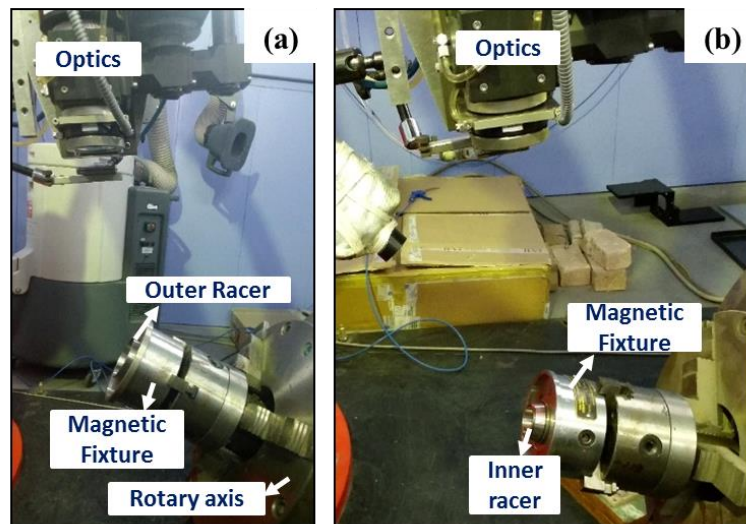
Fig. 3.25 Experimental setup processed using magnetic fixture (a) Outer racer (b) Inner racer
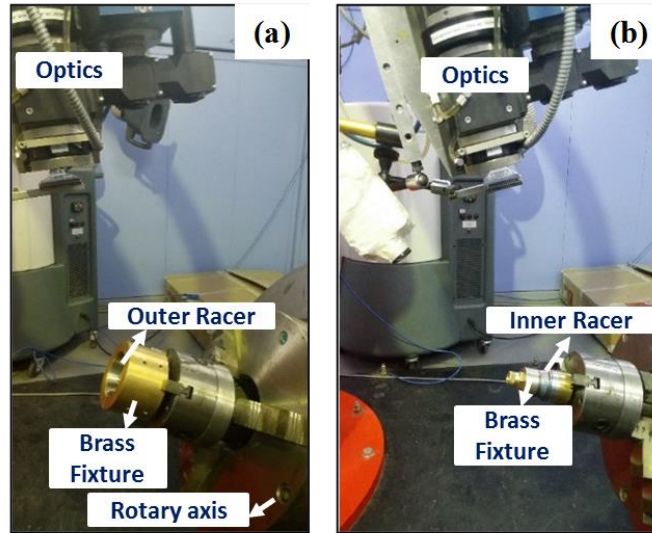
Fig. 3.26 Experimental setup processed using brass fixture (a) Outer racer (b) Inner racer

Laser beam is traversed across the surface of the part/component in order to achieve phase transformation on the surface with few hundreds of microns depth with elimination of softness in core due to associated tempering effects by virtue of increase in heat transfer coefficient. The surrounding immersed water facilitate to quick dissipation of heat from the treated surface and thereby enhance cooling rate to enable higher hardness improvement on surface compared to that of the part processed without fixturing setup with further plausible reduction in distortion substantially. Even though fixture fabricated to hold and rotate the outer ring of the bearing while carrying out laser surface treatment, which is made of brass, chosen due to its excellent thermal conductivity (115 W/m-K), distortion persisted when compared to that processed with water-cooled fixture. Using magnetic fixture, the racers were hardened but tempering effects could not be minimized and high distortion persisted. A constant heat input with a fixed laser power of 3800W and scanning speed of 12 mm/s was employed under both continuous wave (CW) and pulsed wave (PW) modes based on preliminary trials conducted that ensured minimum surface temperature of $1250 \pm 10\ {}^{0}C$ measured from the camera based temperature monitoring device.

Outer Racer: AISI 52100 bearing steel outer racer element with outer and 55 mm inner diameter and width of 13 mm (the region to be hardened) has been chosen for the study. Prior to laser surface irradiation on unground surface of racers and rollers, parts subjected to conventional hardening and tempering (CHT) treatment resulting in tempered martensitic microstructure with

84

dispersed globular carbides. Figure 3.27 shows 2D drawing of the fixturing setup assembly used for laser processing outer racer. It comprises of a bottom cover, a top cover, and a middle cover having a hollow cylindrical structure. As laser processing has to be done on the inside diameter of the outer racer, fixture has been designed such that complete external body of the outer racer will be in contact with fluid (water/oil). The outer ring of the bearing encapsulated between the top cover and middle cover, wherein the top cover and middle cover fastened with bolt and nut assembly. The outer surface of the outer ring is surrounded with the fluid (water/ heat dissipating fluid) to facilitate heat dissipation during the laser surface treatment. Further, a gasket is disposed between the top cover and the middle cover to prevent any leakage of the fluid from the assembly. The assembly of the top cover and the middle cover fixed to the bottom cover by fastening means. Further, the fixture assembly is designed as detachable one to fix to the rotary axis, which rotates the fixture at a pre-determined speed and simultaneous exposure of its inner surface to laser beam takes place for laser irradiation. The shape of the profiled laser beam is complementary to the profile of the inner surface of the outer ring. The sectional thickness of the top-cover and the hollow depth of bottom cover were optimized to 5 mm and 30 mm that enabled sufficient encapsulation of water in to the fixture (up to 1-ltr capacity) so as to enable adequate heat sink effect. Although En-9 steel material used in construction of fixture parts, copper coating was provided to their surfaces to help facilitate in laser heat reflection. The critical allowance for butting both middle and top covers was kept at 200 µm with press fit tapering that enables appropriate butting with no-leakage of fluid during laser processing (heat generated during processing) and minimized warpage.
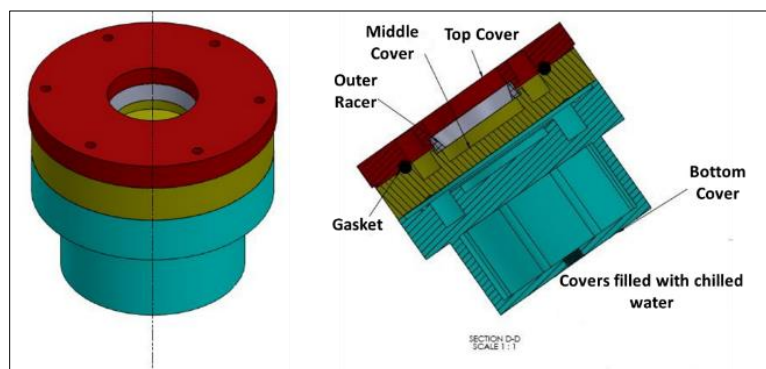
Fig. 3.27 Water cooled fixturing setup for outer racer and its cross-sectional view

Inner Racer: Referring to Figure 3.28 (a), when the outer surface of an inner ring of the bearing is to be surface treated, fixturing setup is detachably setup needs to be connected to the rotary unit. The fixture assembly is designed in a way to securely hold inner ring of the bearing with encapsulation of fluid in the hollow parts of the system. The fixture assembly comprises a lead screw, a top cover, a bottom cover, and a nut to butt inner ring. The lead screw is circumscribed by bottom cover at a lower operative end. Further, the inner ring is mounted on the top of the bottom cover circumscribing the lead screw. The top cover is mounted on top of the inner ring circumscribing the middle portion of the lead screw. Further, the arrangement of top cover, inner ring and bottom cover is secured by fastening a nut (not shown in figure) to the free end of the lead screw. Furthermore, a circumferential clearance is provided between the both top and bottom covers butted to the inner ring with respect to the surface of the lead screw. An orifice in configured on the top cover to supply fluid (water/ heat dissipating fluid) to fill the assembly with inner ring butted that facilities in efficient heat dissipation during the surface treatment of the outer surface of the inner ring. A washer arranged between the top cover and the nut provided to prevent fluid leakage. The inner ring is connected to the rotary that rotates at a pre-determined speed and simultaneously, only outer surface of the inner ring is exposed to the profiled laser beam. Processing trials were unsuccessful with this type of fixture as the amount of water (up to 0.5-ltr capacity) encapsulated was low and thereby inefficient heat dissipation. The fixture was then modified in design as well as setup as illustrated in Figure 3.28 (b). This modified fixturing setup is in such a way that outer surface of inner racer is processed with external flow of fluid dipped with 90% in normal/chilled water. The inner surface of racer is completely with water due to its hollow fixturing setup enabling sufficient water flow. This enabled sufficient encapsulation of water in to the fixture facilitate adequate heat sink effect.

Roller: Figure 3.29 illustrates another fixturing setup designed to hold the roller of the bearing. The fixturing setup comprises a holder assembly, a body cover, and a cap. The holder assembly is enclosed with a cylindrical hollow body cover and encapsulated between the cap and body cover, and is securely fastened by a bolt and nut assembly. The holder assembly is a magnetic assembly with projection of tapered tip that facilitate in fixing the roller self-centered. The profile of the extended tapered tip is complementary to the side face diameter of the roller element providing easy alignment of the roller element with the holder assembly. In an operative configuration, when the surface of the roller element is to be surface treated, the assembly is

connected to the rotary unit that rotates the assembly at a pre-determined speed, against the laser being impinged on the surface of the roller. The central axis of the roller is aligned with the axis of the rotary unit to provide uniform surface treatment of the rolling element. The shape of the profiled laser beam impinged on the rolling element is complimentary to the profile of the rolling element of the bearing. The roller is always processed with external fluid flow by dipping 90% of roller in normal or chilled water. Figure 3.30 shows the experimental setup utilized with water-cooled fixturing setups for laser surface hardening of tapered roller bearing elements constituting outer racer, inner racer and roller.
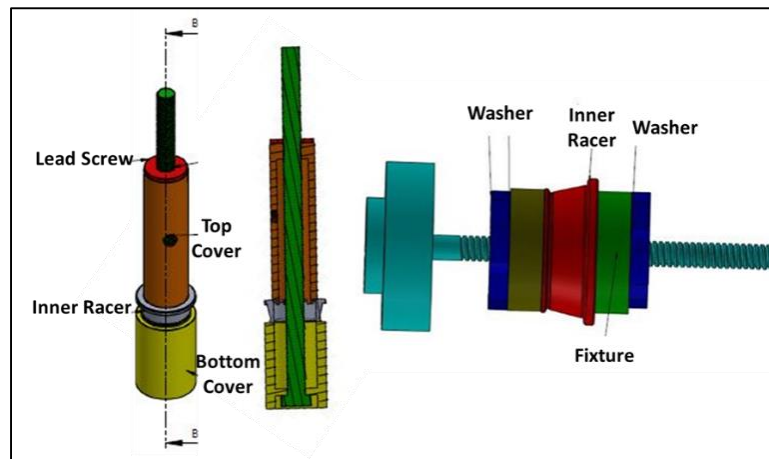
Fig. 3.28 Water cooled fixturing setup for Inner racer and its cross-sectional view (a) internal water storage (b) external water flow
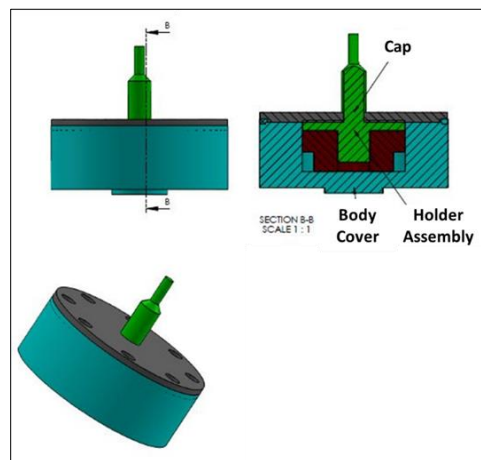
Fig. 3.29 Fixturing setup for roller and its cross-sectional view

87
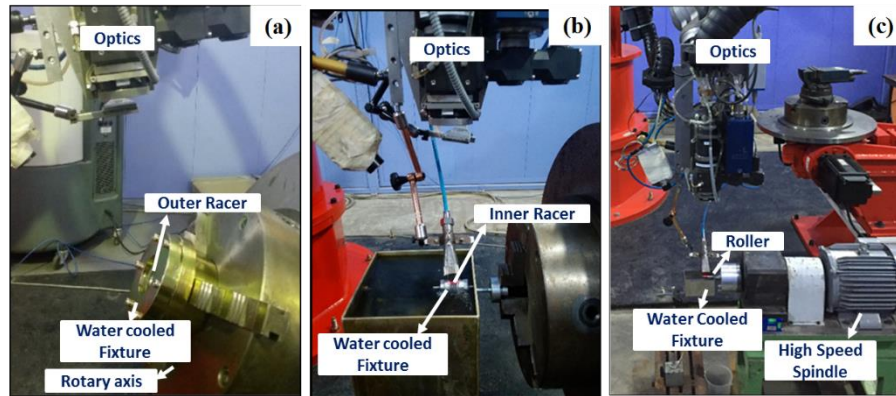
Fig. 3.30 High Power Diode Laser experimental setup processed using water-cooled fixture

(a) outer racer (b) inner racer (c) roller

3.9   Characterization of laser treated layers

After the experimentation and generation of laser-treated samples, characterization of the treated-layers has been carried out utilizing various tools depicted in Table 3.8. The sectioning of the laser-treated tracks was carried out with EDM wire cut machine to avoid induced deleterious stress effects on the metallographic samples. After sectioning of the treated layer samples, they were mounted in metallographic bakelite mounts using hot-press, although, in some cases cold mounting with thermo-setting resins were also used. These metallographic mounts were grinded and polished utilizing the semi-automatic grinder/polishers by adopting standard procedures. Laser treated surfaces as well as cross-sectional samples were etched in appropriate chemical etching solutions prepared for the purpose and analysed for microstructure, hardness and other properties. The techniques used for characterization and the description are given in the following paragraphs.

Table 3.8 Details of various characterization testing facilities used for the present study

	Facility	Purpose	Manufacturer
1)	Optical Microscope with Image Analyzer	Microscopy (50X - 500X) with Image analysis	Olympus Corporation, Japan
2)	Opto-Digital Microscope with Image Analyzer	Microscopy (5X – 20k X) with image analysis	Olympus Corporation, Japan

3)	SEM equipped with EDS attachment	Microstructure, surface morphology and composition	Hitachi, Japan & Thermo Electron Inc., USA
4)	FE-SEM attached with EBSD unit	Microstructure analysis with EBSD at higher magnification	Gemini 500 (M/s Carl Zeiss)
5)	XRD System	Phase analysis in microstructure	Bruker AXS, Germany
6)	Micro-XRD system	Phase analysis in microstructure and residual stresses	RIGAKU Corp., Japan
7)	Residual Stress Analyzer	Residual stress analysis	PANalytical B.V., The Netherlands
8)	Surface Profilometer	Surface roughness & wear profile	MAHR, Germany
9)	3D Non-contact Optical Profilometer	Surface topology and worn profile	Zygo Corporation, USA
10)	Automatic Hardness Tester	Vickers hardness measurement	Leica GmbH, Germany
11)	Ball-on-disc wear and friction monitor	Sliding wear testing at high (Hertzian) contact pressures	DUCOM, India
12)	Instron Universal testing machine for Tensile testing	Tensile properties	KUT 40, NA
13)	Micro-tensile testing equipment	Tensile properties	Walter-Bai Testing Industiestrasse, Switzerland
14)	Zeiss Prismo Coordinate measuring machine (CMM)	Roundness measurements	Zeiss, US

3.9.1 Case profile analysis

Figure 3.31 represents a typical case profile across the depth of laser treated layers of bearing steel with identification of various regions of interest marked in the schematic. For microstructural delineation, cross-sectional metallographic mounts of laser-treated and untreated bearing steels were etched with a 2%-Nital solution. The nomenclature of various regions of the treated layer delineated due to chemical etching of the treated sample are, namely, HZ (Hardened Zone) region indicating near-surface hardened region obtained due to laser irradiation with temperature above AC_1,($T > 735^0C$). SSZ (Super-Soft Zone) region below HZ with temperature

being varied between 735^0C and 350^0C; TCZ (Tempered Core Zone) region below SSZ with temperature falling between 350^0C and 150^0C. Finally, Unaffected Core Zone (UCZ) whose temperature will fall below 150^0C with unchanged microstructure that of substrate. The demarking of these regions could also be visualized with severe darkening of SSZ and partial darkening of TCZ regions plausibly obtained due to preferential chemical reaction associated with Nital etching.
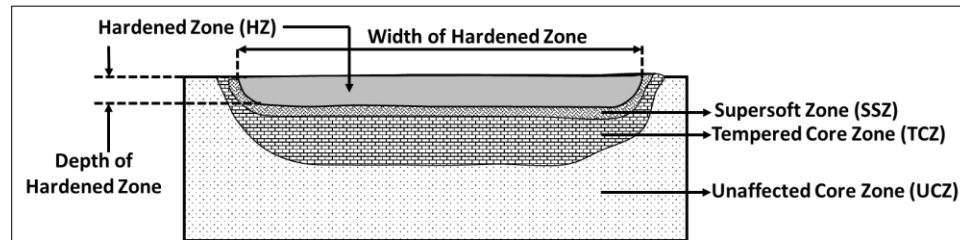
Fig. 3.31 Schematic illustration of laser hardened layer characteristics

3.9.2 Microstructure

Optical microscopy, Opto-digital Microscopy and Scanning Electron Microscopy (SEM): For microstructural delineation, cross-sectional metallographic mounts of laser-treated and untreated specimens were etched with a 2%-Nital solution. These etched samples were ultrasonically cleaned prior to microstructural analysis utilizing Stereo/Optical and Opto-digital Microscopes and High resolution Scanning Electron Microscope SEM (mentioned in Table 3.8). Different characteristic features of the laser hardened layer (as depicted in Figure 3.31) has been evaluated for understanding the influence of processing parameters on laser treated layers of bearing steel.

The image analysis subsystem attached to Opto-digital and optical microscopes used to quantitatively analyze various characteristics of the layers like case dimensions, %-phase content etc. wherever possible. High magnification microstructure analysis and elemental compositional changes in laser-treated layers were carried out utilizing high resolution SEM and FE-SEM. As the major advantage of these microscopes lie in providing better resolution (up to 5 nm for SEM and 1.5 nm for FE-SEM) and large depth of focus, microstructural analysis has been carried out by employing both secondary electron emission (SE) and back-scattered emission (BSE) techniques. It is pertinent to mention here that in case of multi-phase microstructure, BSE mode

was preferred which facilitates in better contrast and resolution of the image. EDX detectors attached to SEM and FE-SEM was used to analyze compositional variation (elemental distribution) in microstructure as well as as-treated surfaces by adopting various methodologies like line scanning, spot-analysis and area mapping. For evaluating size of carbides, martensite and austenite in untreated bearing steel microstructures, quantitative methods, had been used with importing of SEM micrographs in Image-analysis system attached to optical microscope.

3.9.3 Hardness analysis

Microhardness testing at 500gf load on untreated as well as laser-treated samples of bearing steel as well as processed bearing elements with different processing conditions carried out with an automatic digital Vickers micro-hardness testing facility (Lieca GmbH, Germany) mentioned in Table 3.8. The system is equipped with various indentor (Vickers and Knoop) and can be used with loads ranging from 1 – 2000gf and variable objective lens (10 – 100X). Hardness measurements were carried out across the depth as well as surface of the treated layers. An average of five readings reported for the purpose. A minimum of three times of indentation diagonal distance was always maintained between two indents every time when hardness measurements were undertaken in the samples.

3.9.4 Phase and residual stress analysis

Conventional XRD: X-ray diffraction analysis for identification and quantification of phases was carried out using XRD system (Bruker AXS, Germany). XRD technique utilizes the patterns obtained from the scattered electrons diffracted from lattice plane of the exposed surface. Each of the crystal plane will diffract with different intensity depending on orientation in the plane. The apparatus is equipped with auto divergence and convergence slit assemblies for constant area analysis, apart from normal fixed slits. The instrument was fine-tuned to high-resolution mode to detect even very low concentration phases and enable accurate positional measurements of Bragg peaks. A Cr target with low scanning speed ($2\theta{:}0.01^0/s$) utilized for the analysis of all laser-treated and untreated bearing steel specimens. Austenite, martensite and carbide phases identification and their analysis on untreated, unpolished and polished (after removal of oxide layer formed due to laser hardening) laser-treated surfaces have been carried out with XRD system. Quantification of various phases as well as phase-induced properties such as strain rate,

size, dislocation density etc. were also evaluated to select specimens, whenever required, by employing standard formulae.

Micro-focused X-ray Diffraction (Micro-XRD): Since the interest is to study the amount of martensite, austenite and carbides specifically in localized areas, micro-focused XRD equipment was used that will facilitate in assessing with more precision and accuracy. The x-ray beam in this case can be focused down to a spot as small as 10μm in diameter. Micro-XRD scan with a beam spot size of 100 μm was done using D/MAX RAPID II (RIGAKU) curved imaging plate X-ray diffraction system using Cr- Kα radiation. Scans were done on both untreated and laser treated layers (in different zones as per Figure 3.31). By comparing the diffraction patterns obtained, the amount of martensite, austenite and carbides were also obtained with scanning individually in specific HZ, SSZ, TCZ and UCZ regions of the laser treated layers and untreated bearing steel. From the XRD patterns, the volume percent of austenite, martensite and carbides were determined as per ASTM 975 [156] by "direct comparison" x-ray diffraction technique, which is proportional to the volume fraction of that phase. By using multiple peaks and averaging them, the error introduced because of preferred orientation in the sample could be reduced effectively.

Few laser treated as well as untreated bearing steel samples, residual stress estimation were valuated utilizing X-ray diffraction based residual stress analyzer (PANalytical BV, Netherlands). Prior to residual stress measurement, bearing steel samples (both in untreated and laser treated conditions) were polished utilizing colloidal silica as per standard metallographic practice. The diffraction of Cr Kα radiation at a diffracting angle of 106^0 martensite peak angle in [200] α-Fe crystallographic lattice plane of the steel sample surface has been utilized for measuring strain in the lattice. The residual stress has been computed by the software interfaced with the system by utilizing $Sin^2 \Psi$ technique with assumptions of elastic modulus (Es) and Poisson ratio (ν) being 210 GPa and 0.3 respectively. The analysis carried out three times to get reliable estimation. To evaluate the residual stresses in specific laser treated zone, the cross-sectioned specimens were fine polished and the residual stress measurements were performed using micro-focus X-ray diffractometer (Rigaku Rapid II D/MAX High-intensity micro focus system) operated with Cr-kα radiation and $Sin^2\Psi$ based analysis software integrated to the system with martensite peak angle in [200]α plane at 106^0 [157]. The region of interest was

limited by a special collimator to 100 μm^2 area, which is smaller than the depth of the laser hardened layer. The X-ray diffraction stress analyzer was performed in the cross-sectioned surface of treated layers and the residual stress was measured along the depth from the hardened layer to the end of substrate. An average of five readings was reported in each case at different regions of interest in surface and subsurface of laser treated layers processed under different conditions.

3.9.5 Surface topology / morphology

Surface roughness and topographic analysis of laser treated surfaces processed under different conditions were analyzed by employing contact surface Profilometer (MAHR, Germany) and 3-D non-contact optical Profilometer (Zygo Corporation, USA). The contact surface Profilometer was used for measuring roughness, surface waviness and contours of various laser-treated and untreated bearing steel samples. The measurement is based upon diamond stylus (2-μm radius) with inductive pickup for generating various profiles scanned with appropriate filers. Various roughness parameters (like Ra, Rz, Rmax, Wa, Rpv etc.) as per ISO and DIN standards and characteristic curves such as amplitude density curve, PW profile representation etc. could be obtained with the analysis carried out with software attached to the system. The 3D optical non-contact Profilometer is also used to scan the sample for generating 2D/3D image of the surface. Under optimum conditions, the system could facilitate scanning for the surface with vertical displacements of even less than 1 nm.

3.10 Performance evaluation of laser treated bearing steels and elements

3.10.1 Ball-on-disc Sliding wear testing

As one of the principal goals of the work is to evaluate the dry and lubricated sliding wear performance of laser-hardened bearing steels processed under different operating modes and different thermal processing conditions, conventional ball-on-disk Tribometer in rotating mode was employed with requisite testing conditions mentioned in Table 3.9. The schematic illustration of ball-on-disk Tribometer with setup is shown in Figure 3.32. Table 3.9 shows sliding wear test conditions used for the study. ISO VG 68 lubricant was used for lubricated wear

testing experiments. A 6 mm diameter 100Cr6 hardened spherical steel ball (950-1050 $HV_{0.5}$) under a load of 100N was used as stationary counter-body which can induce Hertzian contact pressure of 2.96GPa calculated as per standard equations 4-5, sliding against a laser-treated flat disk of 10 mm × 10 mm. Tests were conducted at room temperature (25 °C) under a controlled humidity of 70%. A total sliding distance of 90 m in unlubricated and 2000 m in lubricated conditions with the fixed sliding velocity of 0.05 m/s was adopted for all tests. The sliding coefficient of friction and wear depths were determined using online friction monitor and depth-sensor attached to the Tribometer and corresponding data was collected online during the wear test with the aid of WindCom 2010 software integrated to the Tribometer. Wear testing experiments were carried out at least three times, and the average results have been reported with inclusion of extreme values (highest and lowest) in the bar representing deviation obtained due to uncertainty in measurement. Wear depth profile in the transverse direction was measured using white light interferometer. Total wear volume was obtained by multiplying average area under depth profiles (evaluated utilizing non-contact Profilometer) with wear track length. Specific wear rate, K, was evaluated by using the relationship mentioned in equation 6 as per ASTM G99. Worn scar dimensions as well as wear volume loss of ball were also analysed as per standard equations.
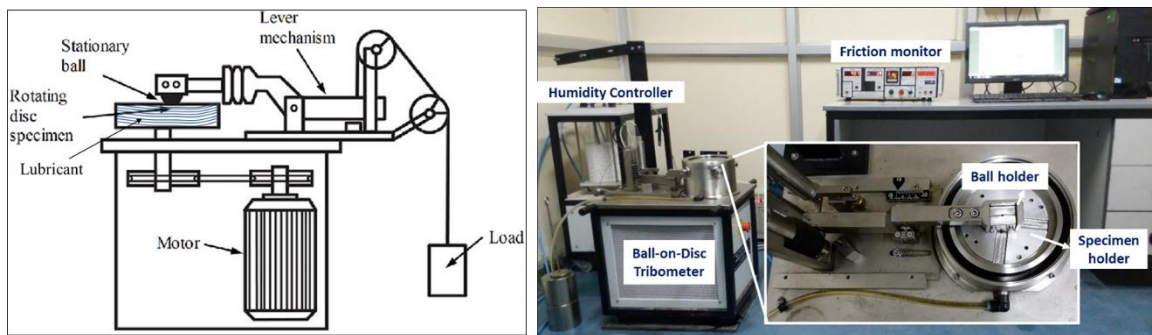
Fig. 3.32 (a) Schematic illustration of Ball-on-Disc Tribometer and (b) test setup

Table 3.9 Sliding wear test conditions

Test Conditions	

Material	Laser treated and un-treated bearing steel
Ball material	6 mm Dia. 52100 Spherical steel ball
Normal load	100 N
Duration of test	0.5 h (dry), 8 h (lubrication)
Sliding velocity	0.05 m/s
Condition & Ambient atm.	25-32 °C with 60-70% RH
Wear Track Diameter	5 mm
Sliding distance	90 m (dry), 2000 m (lubrication)
Lubricant	ISO VG 68 Hydraulic oil

$$\text{Contact radius (a): } \sqrt[3]{\frac{3F}{8}\left[\frac{(\frac{1-V_1^2}{E1})+(\frac{1-V_2^2}{E2})}{(\frac{1}{d1}+\frac{1}{d2})}\right]} \dots\dots\dots\dots\text{Eq. 4}$$

$$\text{Maximum Hertzian contact pressure } (P_{max}): \left(\frac{3F}{2\pi a^2}\right)\dots\dots\dots\text{Eq.5}$$

$$\text{Wear Rate} = \frac{\text{wear volume}}{\text{load} * \text{sliding distance}} \frac{\text{mm}^3}{\text{N} * \text{m}} \dots\dots\dots\dots\dots\dots\dots\text{Eq. 6}$$

Apart from testing conditions, factors like contact temperatures, tribo-chemical reactions, microstructural transformations, properties of transformed microstructures during wear itself greatly affect the wear performance of the surface modified layers. In order to investigate these effects on wear behavior, understanding mechanisms involved in the wear process itself becomes vital. As a consequence, study of worn-surface morphology, wear debris, subsurface microstructural changes, variation in compositional and phase changes of worn surfaces and wear particles has been carried out to understand wear mechanisms involved in sliding wear of untreated as well as laser-treated bearing steels. In order to assess mechanisms of wear involved in sliding wear testing of untreated as well as laser-treated (different conditions) steel, analysis of worn surface morphologies was analyzed using characterization tools such as SEM and EDS. Worn surface morphology analysis facilitated in understanding possible regime of wear like oxidation, abrasion etc.

3.10.2 Mechanical properties evaluation by tensile testing (micro and sub-sized)

Further to co-relate the mechanical properties like tensile strength, yield strength and elastic modulus of diode-laser hardened samples under CW mode and untreated bearing steels, ensile testing of few select samples were carried out utilizing micro-tensile testing equipment as shown in Figure 3.33(a-b). For this purpose, 0.5 mm thick specimen coupons with design specifications as shown in Figure 3.33(d) from various treated / untreated bearing steels are fabricated by EDM cutting. The region of cutting was chosen carefully (as shown in Figure 3.33(c)) from the diode-laser treated track to generate micro-tensile testing coupons. All specimen coupons were subjected to surface grinding to 0.2 Ra μm surface finish and static tensile testing of the specimens has been carried out on samples with a strain rate of 4.5×10^{-4} s^{-1} and an average of three test results have been reported. Few select tensile tests were also carried out on round specimens processed utilizing high-speed laser surface hardening processing using quasi-stationery beam approach as per ASTM E8M. Tensile testing was conducted using the INSTRON 5985 universal testing machine of 250kN capacity at a crosshead speed of 0.5 mm/min at room temperature. Schematic of the tensile specimen and process setup utilized for the purpose is given in Figures 3.34-3.35.

Micro-Tensile test setup

Micro-Tensile test specimen holder

Plate Dimension = 200x35x4 mm

Micro-Tensile sample marked on processed area for wire cutting (from Top 500 μm hardened layer)

Micro tensile test specimen (All dimensions in mm)
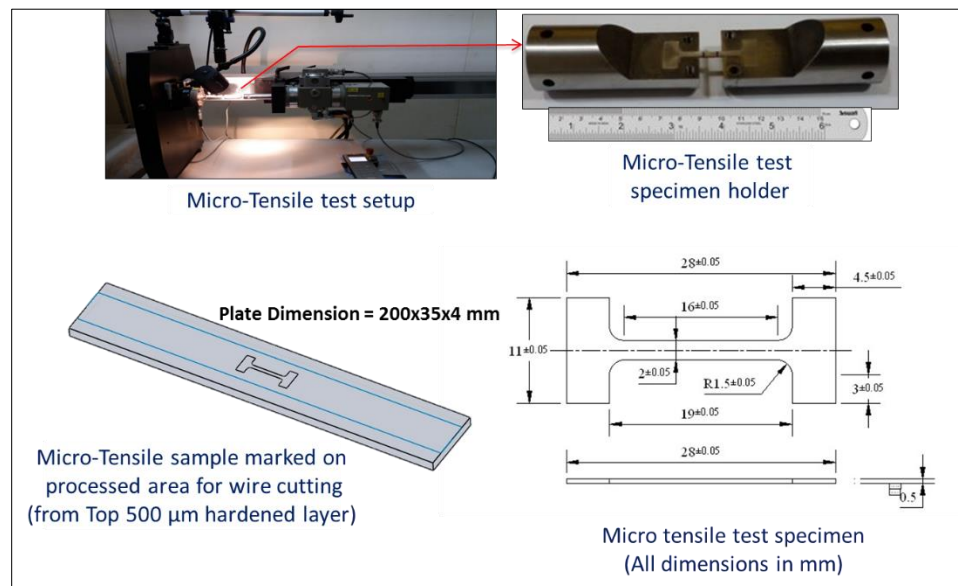
Fig. 3.33 (a) Micro-tensile test setup (b) test specimen holder (c) schematic illustration of specimen coupon generated for micro-tensile testing (d) design drawing of micro-tensile testing specimen coupon
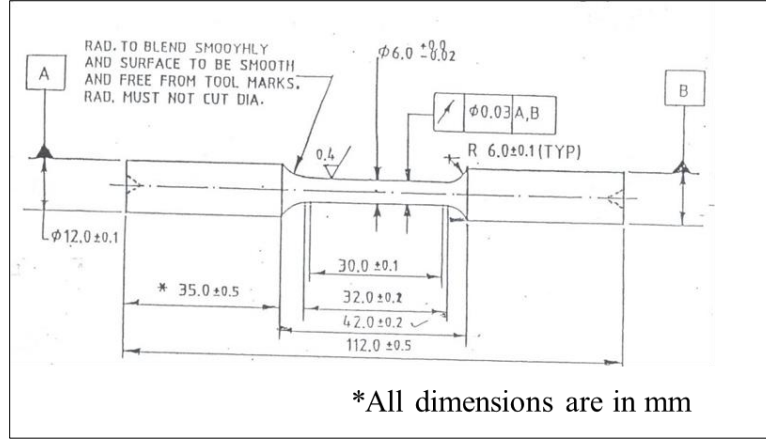
Fig. 3.34 Round tensile specimen as per ASTM E8M
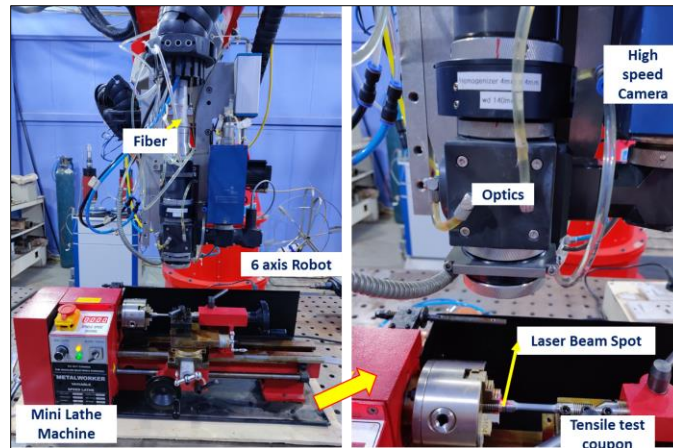
Fig. 3.35 Process setup

3.10.3 Roundness measurements on bearing elements utilizing coordinate measuring machine

Roundness measurements on bearing elements such as outer racers, inner racers and rollers were carried out by employing Zeiss Prismo Coordinate measuring machine utilizing calypso software at room temperature. The probe used in the present study was a ruby ball with a diameter of 1.5 mm and a measuring range of 700 mm x 900 mm x 500mm. The resolution of this equipment is close to + 0.1 μm and the experimental repeatability was found to be within +

0.6 μm. Variations in the coordinates of points located on the outer and inner faces of the ring before and after the LSH treatment were measured. The spacing in radial direction between measuring points was 0.5 mm for both inner and outer faces of the ring such that 26 equally spaced circumferential locations have been considered for measuring. Curvature analysis has been done on data extracted from CMM measurements using SolidWorks software to gain information about the amount of curvature on both laser treated and untreated surfaces of the bearing elements.

CHAPTER 4

Study on the influence of various prior-treatment conditions on laser surface hardening of bearing steel and their tribological performance evaluation

4.1   Introduction

As the main objective of the work is to assess influence of different thermal processing conditions employed in developing laser surface hardening process on bearing steel and bearing elements on their performance evaluation leading to life enhancement, understanding the effect of prior-treatment condition of bearing steel becomes foremost important. In of this, the first task taken up was to assess influence of different prior-treatment conditions on laser surface hardening of AISI 52100 bearing steel. Thus assessment of various prior-treatment conditions such as as–received hot-rolled (UT), spheroidization treatment (SPH), conventionally hardened and tempered (CHT) and combination these on laser surface hardening of bearing steel is subject of this work presented in this chapter. Subsequent to laser surface hardening treatment, analysis of microstructure, hardness and assessment of their tribological performance by subjecting to ball-on-disc sliding wear testing and their comparison with untreated counterparts is comprehensively explained in the present section. The as-received hot-rolled (UT) steel samples were subjected to Spheroidization treatment (SPH) as well as conventionally heat treated (SPH+CHT) and some directly heat treated (UT+CHT) without spheroidization. Laser surface hardening (LSH) was performed for all samples with a fixed laser power and scanning speed that can yield significant hardening effect without melting. The role of spheroidized carbides and prior treatment microstructure on improving the wear resistance of laser surface hardened bearing steel has been studied and compared with non-spheroidized counterparts.

4.2   Experimental Methodology

As previously explained in the previous chapter, material considered for this study was hot rolled (UT) 4mm thick flat plate of AISI 52100 bearing steel. Figures 3.5(a) and 3.6 provide schematic illustration of spheroidization and conventional heat treatment processes employed. The experimental procedure adopted is shown in Figure 4.1. In order to study the influence of spheroidization process with subsequent heat treatments on microstructure and tribological properties, three process variants (#1, #2, and #3) were used in this work and compared with non-spheroidized samples of similar process variants. In process #1, hot rolled plates (UT) subjected to Conventional Hardening and Tempering process treatment (UT+CHT). In process #2, hot rolled plates were subjected to laser surface hardening treatment (UT+LT) (process setup and parameters for LT are mentioned in later). In process #3, hot rolled plates conventionally hardened and tempered were subjected directly to laser surface hardening treatment without any spheroidization (UT+CHT+LT). Similarly, few hot rolled plates were subjected to Spheroidization annealing (SPH). These SPH samples were subjected to similar process variants as mentioned in process 1-3 and the nomenclature for these samples are termed as SPH+CHT; SPH+LT and SPH+CHT+LT respectively.
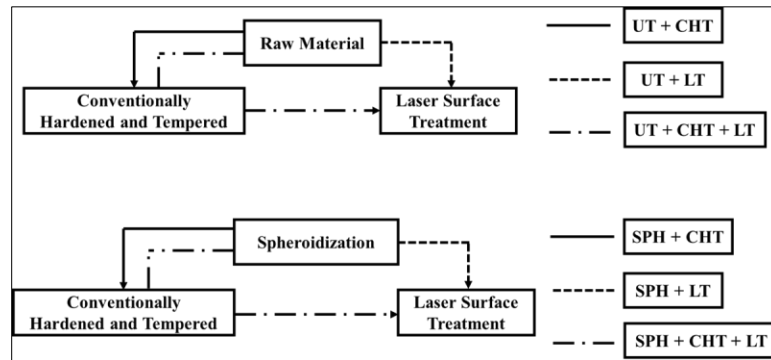
Fig. 4.1 Research Methodology

All the specimens with and without spheroidization treatment (UT and SPH) subjected to grinding and polishing prior to laser surface transformation hardening treatment. Laser surface hardening on all specimens were carried out employing the fiber-coupled diode laser (Laserline GmbH, Germany) integrated to 6+2 axis Robotic workstation (Model: RV40-RSV, Reis Robotics, Germany). The setup includes an optical module to tailor the multi-mode laser beam

into a rectangular spot of 20 mm X 5 mm, as shown in Figure 3.9(a). Experiments performed three times with laser surface hardening being carried out each time on fresh UT, SPH and CHT plates. Laser surface hardening (LT) was performed with a fixed laser power of 3 kW and scanning speed of 20 mm/s. These processing parameters have been chosen based on preliminary study conducted with assessment of surface temperature using EMaqs camera based temperature monitoring system. A power density of 30 W/mm^2 and interaction time of 250 ms, determined by the chosen parameters was found to be sufficient enough to induce surface hardening effect in steel with temperature falling well below solidus temperature of the bearing steel.

4.3   Microstructural and hardness distribution analysis

Figure 4.2 depicts near surface microstructures of untreated (UT) and treated (non-spheroidized with different methods of treatment) bearing steel whose prior-treatment condition microstructure primarily composed of lamellar pearlite and small amounts of grain boundary carbide (cementite). Different processing treatments involved conventionally hardened and tempered (CHT), laser surface hardened treatment (LT) and double hardened involving conventionally hardened and tempered and laser surface hardening treatment (CHT + LT). Thus, the nomenclature used for these treatment conditions are UT, UT+CHT, UT+LT and UT+CHT+LT as represented in Figure 4.2. Similar processing conditions with spheroidization treatment (SPH) as base material are identified with nomenclature constituting conventional harden and tempered treatment, laser surface hardening treatment and combination of both are considered as SPH, SPH+CHT, SPH+LT and SPH+CHT+LT. Figure 4.3 illustrate untreated spheroidized (SPH) base steel microstructure and treated surface microstructures of bearing steel processed under different condition. The corresponding X-ray diffraction patterns of these untreated and treated (in both CHT and LT conditions) with and without SPH prior-treatment condition are illustrated in Figure 4.4.
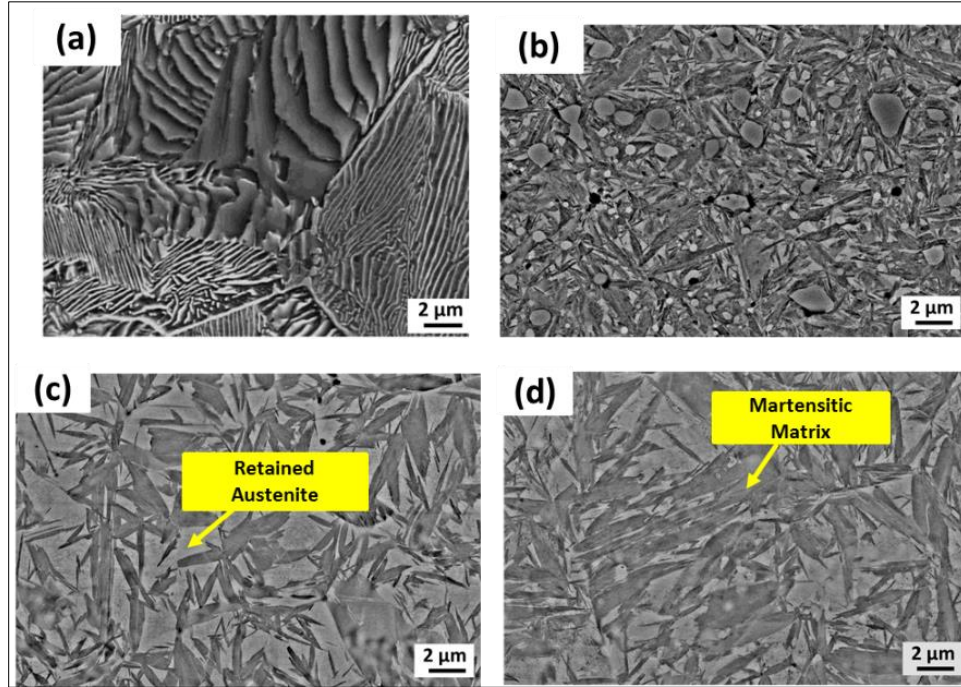
Fig. 4.2 Microstructures on the surface of bearing steel: (a) UT (b) UT+CHT (c) UT+LT and (d) UT+CHT+LT

Figure 4.2(b) shows the microstructure of UT steel after conventional hardened and tempered treatment (UT+CHT). It clearly reveals the tempered martensitic structure (dark needle like structure) with some amount of retained austenite (light constituent) and un-dissolved iron carbides (as per phase and metallographic analysis). When the steel tempered at low temperatures (< 520 K) to relieve the internal stresses, retained austenite decomposes and precipitation of transition carbides of iron takes place from the supersaturated martensite [159]. Indeed, the XRD pattern of the UT+CHT sample showed ferrite (α-Fe), retained austenite (RA) and cementite (Fe_3C) peaks. The Fe_3C (IC) peaks are very low in intensity, in-spite of its greater proportion in the microstructure due to low atomic scattering factor of carbon when compared to Fe [160]. The diffraction peaks are also substantially broader in the UT+CHT steel as compared to UT steel indicating the presence of large micro-strain (due to dislocations) [161]. Figure 4.2 (c-d) illustrate micrographs of surface of UT specimens after laser surface hardening (UT+LT) and laser hardening after conventional hardened and tempered condition (UT+CHT+LT). It is clear from these micrographs and the corresponding phase analysis that UT+LT results in highest amount of retained austenite of 42% among all the microstructures. With increasing

austenitization temperature, the amount of dissolved iron carbides and the carbon concentration in the austenite also increases, which causes a decrease in Ms and an increase in RA content. Indeed laser processing with prior treated condition (UT+CHT+LT), resulted in higher carbon and prior-carbides dissolution during austenitization, associated with high heating rate (high austenitization temperature) followed by their precipitation (determined by the subsequent cooling rate). Furthermore, marginal reduction in RA could be observed in UT+CHT+LT as compared to that of UT+LT, plausibly due to retardation of carbide dissolution in austenite with the already hardened structure. Indeed, dislocation density increase with crystallite size reduction as observed (as per XRD peak analysis) in martensite matrix of UT+CHT+LT as compared to that of UT+LT. The refinement in martensitic matrix (size) with strain state (peak broadening) was also observed to be reducing in the order of UT+CHT+LT to UT+LT to UT+CHT.

Figure 4.3(e) shows the microstructure after spheroidization treatment (SPH). Lamellar cementite completely disappeared with emergence of Spheroidized Alloy Carbides (SAC) with globular morphology as well as few undissolved iron carbide (IC) with irregular non-spheroidal morphology in the matrix of ferrite. During the spheroidization, the microstructure evolution can be simply classified into three stages. First, during austenitization, associated with the ferrite to-austenite transformation, some cementite lamellae will dissolve into austenite, and some cementite lamellae will fragment [162]. In the meantime, due to the Gibbs-Thomson effect, carbon will diffuse from the regions of cementite with larger curvature (such as the cementite lamellae edges, edges of holes in cementite lamellae, and sub boundaries of cementite) to the surrounding flat surfaces of cementite [163]. As a result, the cementite lamellae will gradually split up into ribbon-like or cylindrical pieces, which will finally evolve into granular undissolved cementite. With increase of austenitizing time, these undissolved cementite will coarsen [164]. Second, during the cooling process after austenitization, divorced eutectoid transformation will occur [165]. Most of cementite will directly nucleate at the existing undissolved cementite during the divorced eutectoid transformation, which will form globular cementite. At last, during the subsequent cooling to 690 ^{0}C, cementite will coarsen again, which is driven by the decrease of interfacial energy [166-167]. Thus, SPH microstructure [Figure 4.3(e)] constitute nearly full ferritic matrix with the distribution of globules of carbides. Here, these globular alloy carbides were composed of chromium rich ones as analysed from EDS, termed as globular alloy carbides (GAC) of MC or M_3C (M being Fe, Cr). Figure 4.3(f) shows the CHT treatment of SPH steel

specimens resulted in obtaining a final microstructure of tempered martensite with 1-2 µm sized dispersed spheroidal carbide particles (GAC) and few pockets of retained austenite (RA). With CHT treatment, these GACs are more or less retained, although few elongated course carbides and fine granular iron carbides (IC) still present. Apparently, initial spheroidization of cementite (as shown in Figure 4.3(e)) was observed to be beneficial to obtain nano carbides [168] which is visible from SPH+CHT microstructure when compared to non-spheroidized microstructure (as shown in Figure 4.2(b)). As similar to that of UT processed microstructures, RA increased in hardened microstructures of CHT, LT and CHT+LT as analysed from both XRD as well as microscopy analysis. The amount of retained austenite was highest to the tune of 32% in SPH+LT and lowest in SPH+CHT in the order of austenitization temperature involved in the process of treatment. Indeed, it could be attributed to significant dissolution of cementite and refining of prior austenite grain in SPH as compared to that of UT as base structures. Cementite dissolution will increase the content of C in austenite, and thus leads to the increase of austenite stability and the decrease of the martensite start temperature, which is beneficial to increase the content of retained austenite after quenching and tempering [169].
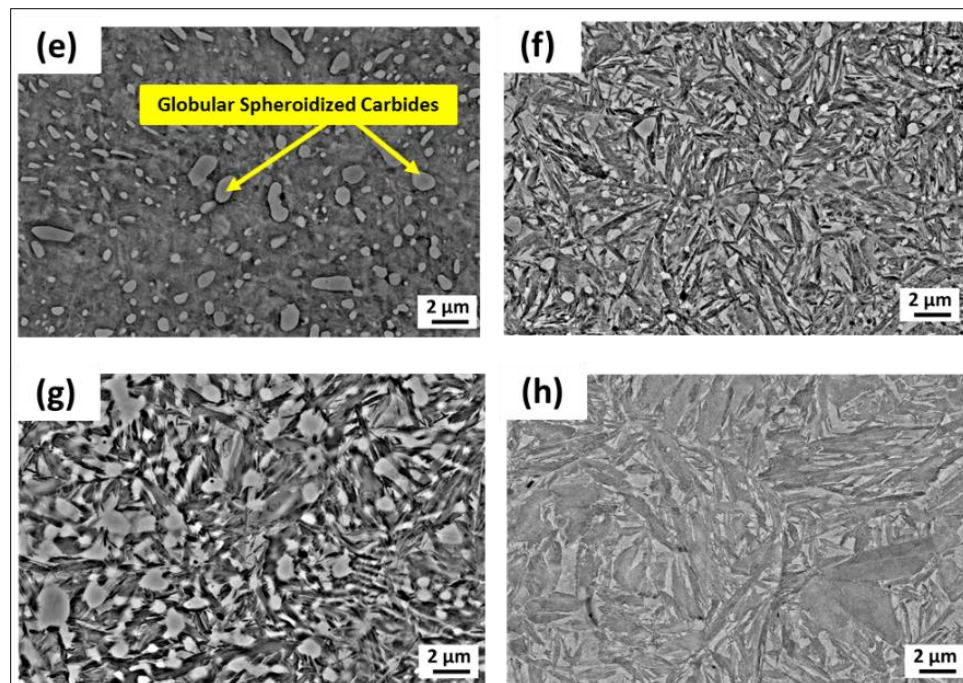
Fig. 4.3 Microstructures on the surface of bearing steel: (e) SPH (f) SPH+CHT (g) SPH+LT and (h) SPH+CHT+LT

Microstructures of hardened layers, conventionally hardened and tempered or laser treated, depicted in Figure 4.3(f-h) clearly reveal that amount of GAC od MC/M$_3$C types dissolved in the martensitic matrix varied in different degree with retention of retained austenite (γ-Fe) and martensite refinement. Higher the degree of austenitization or austenitization processing temperature, higher was the RA retention followed by dissolution and precipitation of GAC. Indeed, comparative XRD analysis (Figure 4.4), further corroborated the fact that, RA content increased from 14-15% in SPH+CHT to 32% in SPH+LT, with the exception of marginal decrease in SPH+CHT+LT. Furthermore, incomplete dissolution of prior-carbide globules associated with the coagulation of alloy carbides into clusters is still visible in SPH+LT (Figure 4.3(g)) and this could be due to the absence of tempering treatment. Indeed laser processing with prior treated condition (SPH+CHT) resulted in higher carbon and prior-carbides dissolution during austenitization, and followed by their precipitation, resulted in refinement with nano-carbides in martensite/austenite matrix as shown in Figure 4.3(h). The transformation of highly stressed martensite with twinned plates in laser processed ones along with CHT is evident on account of high cooling rates associated with laser processing cycle and high level of carbon diffusion in austenite with SPH treatment. Thus contributing to highest grain refinement in SPH+CHT+LT with maximum GACs discernible in the microstructure. Indeed, the microstructural variations formed due to different prior-treatment conditions were found to be consistent with their phase formation of martensite/ferrite/austenite/carbides and grain refinement assessed with XRD results.

The carbide peaks (IC or GAC) were very low in intensity; in-spite of its greater proportion in the SPH structure because of the atomic scattering factor of carbon being very low as compared to Fe [160]. It was observed that the retained austenite persists in the microstructure even after tempering at 513 K for 240 min. It may be possible that the tempering time used was not sufficient to convert all the retained austenite into martensite. The diffraction peaks are also substantially broader in the CHT steel samples as compared to the UT and SPH steel indicating the presence of large micro-strain (due to dislocations) [161]. This is typical for the as-quenched and tempered structure. The transformation of highly stressed martensite with twinned plates in laser processed ones is evident on account of high cooling rates associated with laser processing cycle. Furthermore, XRD analysis corroborates this effect as evident from the peak broadening

accompanied with peak shifting towards left side of the diffraction angle in all laser-processed surfaces depicted in zoomed part of Figure 4.4. Indeed, XRD analysis also corroborated the fact, previously explained in microstructure analysis, that RA increased from 15% in SPH+CHT to 21% and 32% in SPH+CHT+LT and SPH+LT and further increased to 38% and 42% in UT+CHT+LT and UT+CHT samples respectively. These higher amounts of RA (>30%) [170], is highly undesirable in typical bearing components as a major cause for premature failure which leads to negative influences, such as excessive dimensional growth and greatly affects the fatigue and impact strength of the components. Another distinguishable feature to be noted is the variation in carbides globules/granules in microstructures with different conditions of laser treated samples. Indeed quantification of these coarse globular carbides from XRD quantitative analysis as well image analysis (from SEM micrographs) indicated 6 – 7 % Vol. % in SPH+CHT increased to 9 – 11% Vol. % in SPH+CHT+LT sample due to higher cooling rates which enhances carbide precipitation.
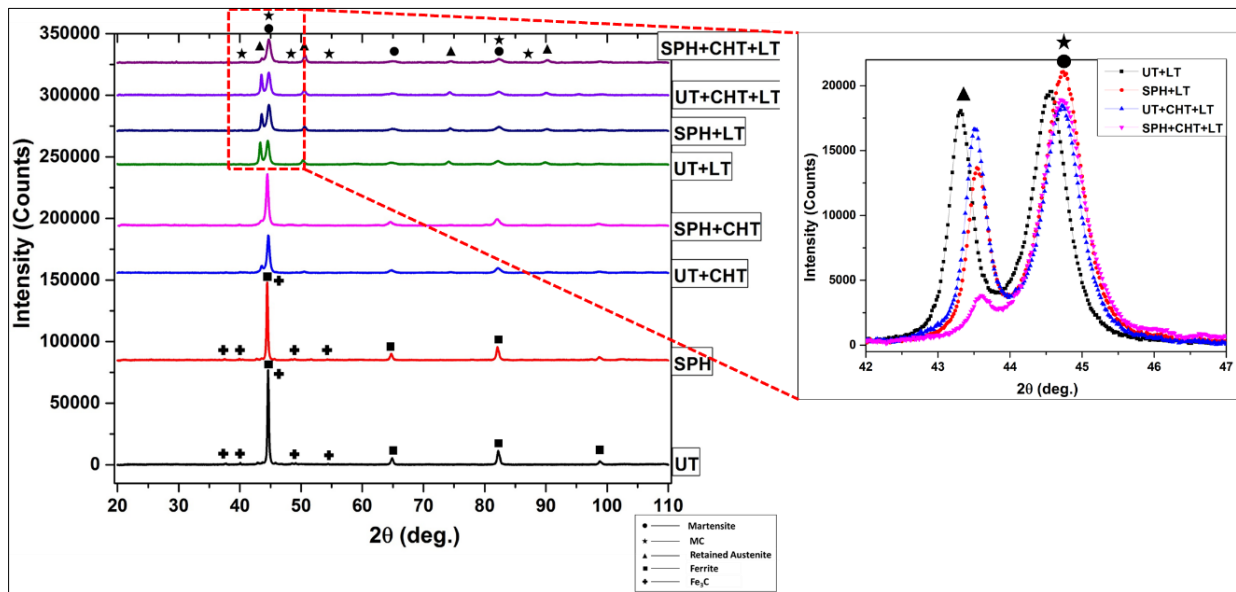
Fig. 4.4 X-ray diffraction patterns obtained on surface of laser-treated steel surface processed on different substrate conditions using Cu Target along with zoomed view

Figure 4.5 shows the hardness values obtained in all untreated and hardened layers processed with various prior-treatment conditions of bearing steel. It is clear that the SPH sample has lowest hardness of 190 – 210 $HV_{0.5}$ and SPH+CHT+LT, highest with 870 – 910 $HV_{0.5}$. Indeed, hardness obtained in the hardened layer is governed by the prevailing microstructural

factors of martensite density, amount of carbides, grain refinement and amount of retained austenite, as explained earlier. Reduction in hardness of bearing steel with SPH, as compared to that of UT, is the direct consequence of lamellar carbide transformation to soft ferrite. Hardness in treated layer of CHT or LT or combination of both without prior-spheroidization treatment increased from 670 – 680 $HV_{0.5}$ in UT+CHT to 790 – 830 $HV_{0.5}$ in UT+CHT+LT, in convergence with martensite density and grain refinement. Indeed, relatively higher improvement in hardness of UT+CHT+LT as compared to that of UT+LT could be attributed to maximum refinement in martensite matrix with precipitation of more nano-alloy carbides in the former. Although cooling rate associated with laser cycle is same in both conditions, presence of higher amounts of precipitated carbides due to CHT help facilitate more solid-solution strengthening coupled with microstructural refinement and thereby hardness.

Another striking feature one can observe from the Figure 4.5 is 20-25% improvement in hardened microstructures of steel with prior-SPH than non-SPH (UT). This clearly corroborates the fact that additional diffusion of carbon in austenite of spheroidized bearing steel help facilitate in strengthening of matrix with presence of nano-alloy carbides and high-stressed martensite. Apparently, strengthening of martensite/austenite matrix enhances with peak surface temperature during heating cycle of laser processing mode following by high cooling rate [171]. Thus high hardness could be observed in LT processed samples of SPH than UT that is envisaged to improve wear resistance. Indeed, samples (UT, SPH) processed directly with laser hardening treatment, without any prior spheroidization treatment, showed less extent of improvement in hardness when compared to those with CHT treated condition. Overall, hardness distribution in the treated layer observed to be well convergent with the strength of microstructure formed.
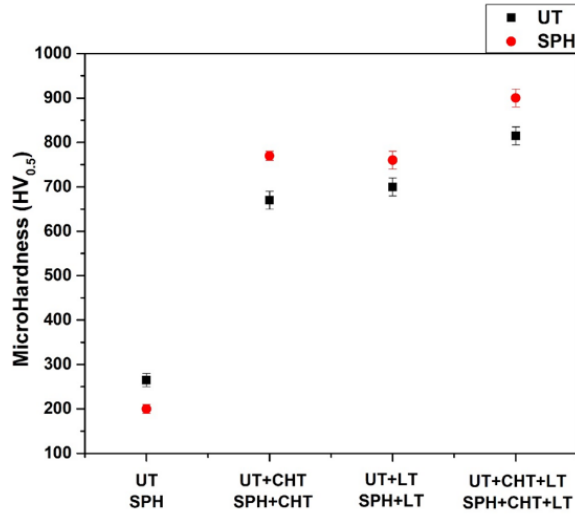
Fig. 4.5 Avg. microhardness distribution of bearing steel under different conditions

4.4　Mechanical properties evaluation by micro-tensile testing

To comprehend further the variation in mechanical properties with microstructure of laser-hardened bearing steels, few micro-tensile tests were also conducted on SPH+CHT and SPH+CHT+LT specimens and analysed. For the purpose, 0.5 mm thin tensile specimen coupons with 16 mm gauge length were subjected to monotonic static tensile testing at a constant strain rate of 4.5×10^{-4} s^{-1}. In case of laser-hardened specimen coupons, samples were carefully machined by EDM in such a way that only hardened layer thickness be retained. The testing was carried out until failure and the average of three tensile test results reported. Table 4.1 depict YS, UTS and %EL values of laser hardened and conventionally hardened specimens. Nearly 14% and 8% improvement in YS and UTS values of SPH+CHT+LT sample as compared to that of SPH+CHT counterparts could be obtained due to refined high strength martensitic/austenitic matrix with dispersion of uniformly distributed nano-carbides and alloy carbides (MC).

Table 4.1 Summary of Micro-Tensile Behavior of SPH+CHT and SPH+CHT+LT samples

Sample ID	Yield Strength (MPa)	UTS (MPa)	Elongation (%)
SPH+CHT+LT	1493	1683	0.89
SPH+CHT	1276	1544	0.82

4.5 Sliding wear behavior and performance evaluation

Sliding wear tests were conducted using a conventional ball-on-disk Tribometer in rotating mode under lubricated conditions. Sliding wear test conditions and Hertzian contact pressures are mentioned in Table 3.9. A total sliding distance of 1000 m in lubricated conditions with the fixed sliding velocity of 0.05 m/s adopted in each case. A detailed wear resistance assessment with evaluation was carried out to study the effect of spheroidization and subsequent heat treatments on coefficient of friction (COF) as well, as depicted in Figure 4.6. These graphs elucidate the development of friction coefficient with the time of sliding contact. The COF reduced vastly in oil lubricated condition on all samples as evident from the observed 0.08 COF in laser treated surfaces of prior spheroidized and conventionally treated sample of SPH+CHT+LT and 0.082 COF in non-spheroidized and prior conventionally treated sample (UT+CHT+LT) in steady state conditions under mixed lubrication regime. Marginal reduction in COF of laser treated surfaces as compared to UT and SPH substrates could be attributed to microstructural homogeneity, increase in hardness and more specifically high compressive residual stresses possible [172]. It can be observed that SPH with subsequent hardening treatment (samples of SPH+CHT+LT, SPH+LT and SPH+CHT) exhibited lower friction coefficient as depicted in Figure 4.6(a) than non-spheroidized counterparts followed by hardening treatment (samples of UT+CHT+LT, UT+LT, UT+CHT) as evident from Figure 4.6(b)).
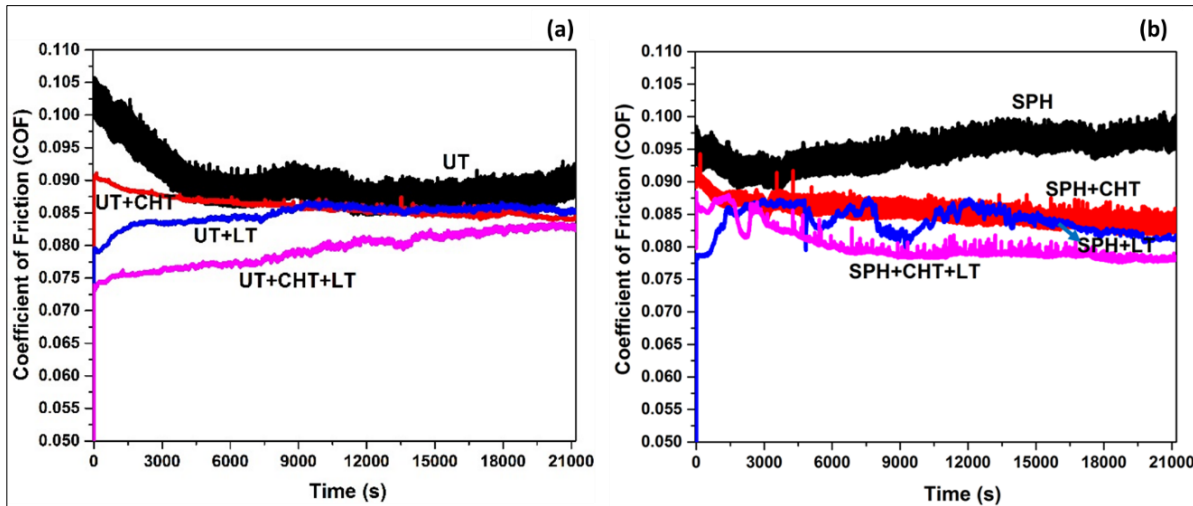
Fig. 4.6 Variation of COF under lubricated conditions (a) non-spheroidized samples (b) spheroidized samples under different heat treatment conditions

As friction coefficient is a tribo-system property, it depends not only on the strength of the microstructure but also on the contact stress, lubricating environment condition, tribo-chemical reaction etc. and its effect with progression of wear in sliding contact. In fact, regular replenishment of lubricating oil and measured film thickness as per Dowson and Higginson formula envisaged mixed lubrication regime ($1<\lambda<3$) throughout the duration of test. Indeed, maintenance of friction coefficient within the range of 0.075 – 0.105 throughout the test period in all cases, irrespective of change in microstructure of the steel with different treatments (UT, SPH, CHT, CHT+LT etc.) corroborate the regime of testing.

However, close observation of variation in friction coefficient with duration of test in UT and hardened UT cases (Figure 4.6(a)) indicate considerable influence of steel microstructure. With the exception of bare UT specimen, all of them exhibited similar trend of progressive sluggish increment in friction coefficient with time. This elucidates that part of the applied load is carried by trapped lubricant and part of it by asperities that protrude above the oil film thickness. Thus wear took place particularly in those regions of material contact (asperities) with smoothening of the surface due to mild abrasive wear. Indeed this wear rate was found to depend not only on the surface roughness but also the strength of the microstructure and tribochemical wear due to chemically active anti-scuffing additives to the oil. Indeed, low strength (shear and fatigue) pearlitic microstructure in UT with absence of globular carbides facilitated in reduction of friction coeffiecnt during initial running-in period (before stabilization) up to 3200 seconds with mild wear as against abrasive wear with smoothening effect in case of other treated surfaces. Indeed, this progressive improvement in friction coefficient with time was found to be higher with higher strength of the matrix microstructure.

In case of SPH surfaces (with and without hardening treatment), again with the exception of untreated specimens, friction coefficient either remained constant with minor fluctuations or reduced with time indicating comparable wear in more or less similar martensitic matrix with presence of globular carbides (presence of globular carbides entail greater asperities and roughness). Indeed, retention of soft pearlitic matrix with globular carbides in SPH compensated

abrasive wear of matrix with contact load and polishing of hard globules and thereby initial marginal increment in friction coefficient with progression of wear.

The lower friction levels for the spheroidized samples with subsequent process #1, #2 and #3 can be attributed to the presence of alloy carbides with high hardness that entail anti-wear performance. This positive effect during the process of wear test as they can protrude during initial wear slightly due to higher load and thereby reduce contact and facilitate in enhancing load-bearing capacity [173-174]. Thus increasing the density of the hard phases in laser treated layers presumably improved the wear behaviour of the bearing steel [173]. Effective prevention of direct contact of two bodies with oil lubrication reduces the COF owing to the presence of lubricating film that facilitates in reducing the contact stress [173, 175-177]. The variability of COF in the initial running stage is due to mixed-lubricated sliding effect associated with surface roughness and with progression of wear, it decreases, owing to annihilation of surface asperities and smoothing [177]. Apparently, further decrease in COF is associated with formation of effective low-shear oil film as reported by the study conducted by Anoop and Co-workers [176].

Figure 4.7 illustrating comparative specific wear rates evaluated from the standard empirical relationship (Equation 3) shows maximum improvement of wear resistance in SPH+CHT+LT sample. The wear rate (value multiplied by 10^{-6} mm^3/N-m) reduced to 0.13 in SPH+CHT+LT), 0.81 in SPH+LT) and 1.24 in SPH+CHT as compared to that of SPH specimen (2.16), indicating two-to-three fold improvement in SPH+CHT+LT sample. In specimens hardened without spheroidization treatment (UT based), specific wear rate reduced to 0.26 in UT+CHT+LT, 1.42 in UT+LT and 1.52 in UT+CHT as compared to that of UT specimen (2.00), indicating one-to-two fold improvement in UT+CHT+LT processed sample. Thus highest improvement in wear resistance of SPH+CHT+LT sample could be attributed to highest solid-solution strengthened microstructure produced with refined martensite matrix and high amount of nano carbides associated with highest cooling rate experienced by laser treatment cycle. Indeed, the wear resistance was higher in all spheroidized samples as compared to non-spheroidized counterparts hardened with similar processing conditions. This is convergent with the hardness improvement observed in the microstructures.
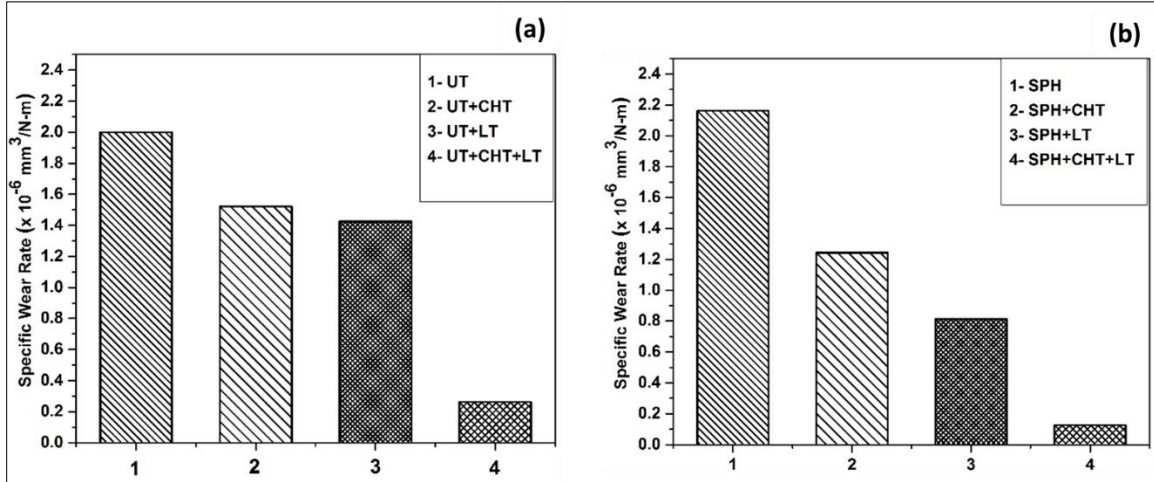
Fig. 4.7 Sliding wear resistance of (a) non-spheroidized samples (b) spheroidized samples under different heat treatment conditions under lubrication conditions

The extent of improvement in wear resistance due to laser treatment was more in SPH+CHT condition, which could be attributed to maximum hardness improvement of 880 - 910 $HV_{0.5}$ as against 200 - 210 $HV_{0.5}$ in SPH substrate. Furthermore the extent of improvement is higher in SPH+CHT+LT sample than UT+CHT+LT [as shown in Figures 4.7(a-b)) one owing to refined solid-solution strengthened martensitic matrix structure with higher amounts of sub-micron and nano-sized alloy carbides (GAC and IC) observed in the prior spheroidized microstructure. Indeed, higher the amount of refined alloy carbides coupled with refined martensitic matrix, higher would be its contribution in reducing wear. This high strength martensitic microstructure resulted in effective prevention of direct contact of two bodies with oil lubrication. In similar studies involving sliding wear test evaluation of steels with different martensitic structures, greater amounts of martensite with refinement exhibited greater wear resistance reported [178].

4.6 Assessment of wear mechanisms

Further to understand mechanisms of wear, SEM worn surface morphologies of (shown in Figure 4.8 & 4.9 (a-d)) UT, SPH and subsequent three different process variants (#1, #2, and #3) are considered and analyzed. They elucidate altogether different mechanisms involved in the wear process. As the hardness is very low in UT (260 ± 20 $HV_{0.5}$) and SPH (200 ± 10 $HV_{0.5}$)

samples, very large wear debris particulates seen in the Figure 4.8(a). Large wear particles detachment indicates severe deep pits and craters formation on the surface. These pits, in turn, retain large volumes of the lubricant and bring the surfaces closer to each other and more irregularities come into direct contact. As a result, increase in friction coefficient as previously explained. With process variant #1 of UT and SPH samples, material removal appear smoother (with removal of virgin rough surface asperities associated with grinding furrows) coupled with plowing of few pockets of debris particles in both UT+CHT and SPH+CHT samples. The worn-out surface of the SPH+CHT samples shows a smoother preface compared to the UT+CHT samples. Mild adhesion and delamination wear observed in UT and SPH samples processed with variant #2 as against no such grooving and delamination in UT and SPH laser treated layers processed with variant #3.

The worn scar width reduced by half (when compared with that of UT and SPH counterpart) with surface grinding furrows being still visible in UT+CHT+LT and SPH+CHT+LT processed one. This evidently attributes to the formation of fine carbide particles because they lead to less surface damage during wear testing [179]. Indeed, the high strength martensitic microstructure comprising refined martensite and nano-sized alloy carbides (higher hardness with compressive stress in SPH+CHT+LT surface) acts more elastically in mixed lubrication regime and thereby resist wear particles detachment. The maximum hardness and therefore the yield stress is high enough, the contact is close to an elastic state. Very small particles formed in this case as shown in Figure 4.9(d) and the surface topology changes only slightly. Indeed, the smoothening of grinding furrows visible in SPH+CHT+LT surface (Figure 4.9(d)) suggest a vast reduction in contact load and thereby wear as reported in several works involving the study of sliding wear under the contact of hard steel surfaces in mixed lubrication regimes [175, 180].
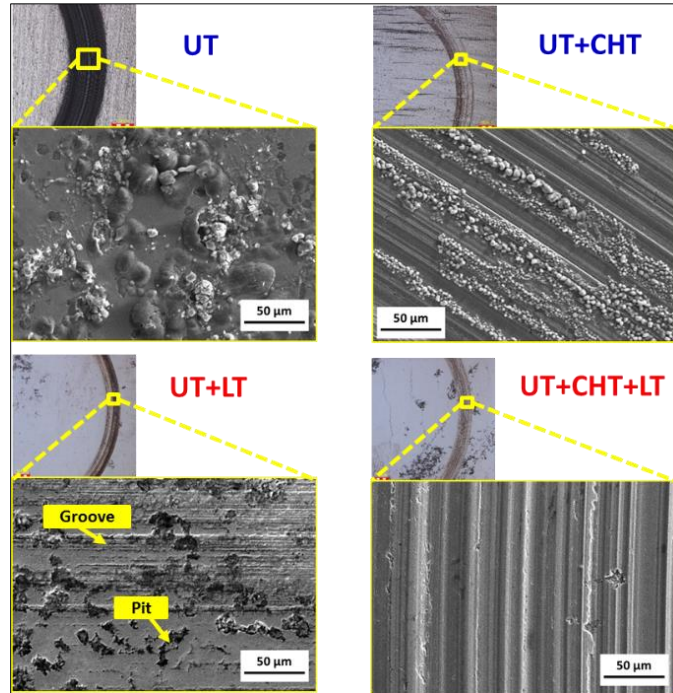
Fig. 4.8 Surface morphological analysis utilizing SEM of Worn out regions of the sliding wear test specimens under lubricated conditions (a) UT (b) UT+CHT (c) UT+LT (d) UT+CHT+LT
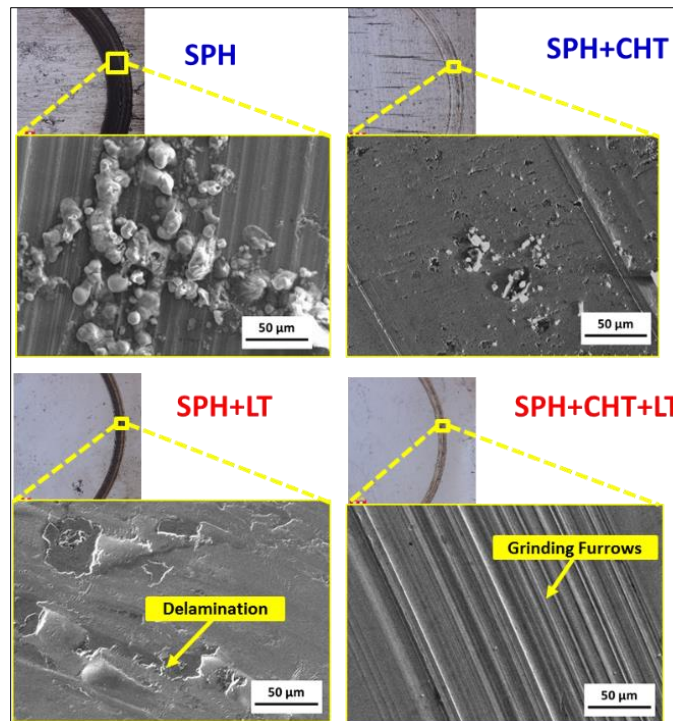
Fig. 4.9 Surface morphological analysis utilizing SEM of Worn out regions of the sliding wear test specimens under lubricated conditions (a) SPH (b) SPH+CHT (c) SPH+LT (d) SPH+CHT+LT

4.7   Summary

The study clearly demonstrated the effect of spheroidization and its subsequent prior treatment condition, with and without conventionally hardened and tempered condition, on microstructure, hardness distribution and sliding wear performance vis-à-vis laser hardened counterparts. Hardness in laser-treated layer increased with microstructural refinement, in the order of UT+LT < SPH+LT < UT+CHT+LT < SPH+CHT+LT. Volume fraction of retained austenite decreased in the order of UT+LT > UT+CHT+LT > SPH+LT > SPH+CHT+LT. Spheroidization treatment lead to globular alloy carbide formation that invariably helped in improving the strength of the matrix microstructure coupled with reduction in retained austenite content.

Wear resistance improved in the order of UT+LT < SPH+LT < UT+CHT+LT < SPH+CHT+LT convergent with strengthening of martensite matrix and formation of nano carbides. Maximum reduction in friction co-efficient and specific wear rate was observed in SPH+CHT+LT sample due to its highest strengthening of martensitic matrix with maximum refinement and highest amount of dispersed nano-carbides coupled with optimum control of retained austenite. Thus, the study demonstrated the requirement of spheroidization treatment as well as conventional hardened and tempering treatment prior to laser surface hardening to enhance load-bearing capacity of a bearing steel with considerable improvement in wear resistance.

CHAPTER 5

Comprehensive study on control of laser heat input (different modes of processing) in laser surface hardening of bearing steel and their assessment of sliding wear performance

5.1 Introduction

Further to the previous study demonstrating efficacy of spheroidization treatment and conventionally hardened and tempered treatment requirement to obtain maximum wear resistance, the next step was to explore further improvement in high cooling rate by imparting appropriate laser heat input with any possible mechanisms of modulation of laser power. Thus prior treated condition of both SPH and CHT has been chosen for further experimentations due to its superior properties in terms of hardness and tribological properties. Additionally, any improvements in laser hardened layer by virtue of retention of core strength of prior hardened bearing steel and control of distortion and/or deformation with reduction of heat affected zone that are found in previous study are required to be explored by altering the thermal processing conditions. Indeed, precisely control peak temperatures with increase in cooling rates are reported in various works involving laser surface hardening of steel. Keeping these aspects, next study to assess efficacy of laser surface hardening treatment utilizing Pulsed Wave (PW) mode on SPH+CHT condition has become tantamount. Thus, the present chapter to comprehensively investigate and compare Continuous wave (CW) and Pulsed wave (PW) modes of processing on laser surface hardening of prior hardened bearing steel has become principle subject of the work.

Influence of the different processing modes (CW & PW) on microstructure, hardness and wear behavior of AISI 52100 bearing steel are discussed in the current chapter. Laser surface

treatment of bearing steel was carried out utilizing the high power diode laser integrated to robotic workstation. The effect of various processing variables, namely pulse duration, pulse frequency, laser spot size, laser power and scanning speed on case depth, hardness and microstructure of the treated layers has been discussed in detail in this chapter. Results from unlubricated and lubricated sliding wear tests conducted with a ball-on-disc test rig on laser treated (processed under different operating modes) and SPH+CHT bearing steel have been compared to assess improvement in wear resistance due to laser treatment.

5.2   Experimental Methodology

In the present work, 4-mm thick bearing steel grinded plate with prior-microstructure comprising predominantly martensite with dispersed globular carbides as shown in Figure 3.7 mainly of type (Fe, Cr)C, and through-thickness hardness ranging 750-800 $HV_{0.5}$ (obtained by conventionally through hardened and tempered treatment) was used for the purpose. Figure 3.10 illustrates the different modes of laser scanning operations used for LSH treatment. The laser surface transformation hardening treatment was carried out by employing continuous wave (CW) and pulsed (PW) modes using a 1.5 mm fiber coupled diode laser integrated to 6+2 axis robot. The setup include an optical module to tailor the multi-mode laser beam to a rectangular spot of 20mm x 5mm as shown in Figure 3.9 (a). In-situ high-speed camera based surface temperature monitoring and controlling system with E-Maqs (Lasertronic-Lompocpro 7.6, Fraunhofer IWS, Germany) was used for measuring surface temperatures during processing. Table 3.4 elucidates the LSH process parameters utilized for the study.

5.3   Determination of processing windows for laser treatment

Initially, a feasibility study has been carried out to select an appropriate fixed peak laser power (3200 W) and scanning speed (20 mm/s) under CW mode that can yield a min. hardened case depth of 300µm without any trace of surface melting. The results obtained in terms of case depth and surface temperature with variation in heat input (150 – 200 J/mm) showed hardened case ranging from no-hardened zone to maximum of 600-µm case with skin melting effect. The surface temperature measured using E-Maqs [details mentioned in Chapter-3] was found to be in

the range of 650^0C (in 150 J/mm sample) to beyond 1450^0C. Thus appropriate fixed peak laser power of 3200 W and 20 mm/s scanning speed [energy density of 32 J/mm^2 as per Eq. 5.1] could be finalized for actual experimentation under both continuous wave (CW) and pulsed wave (PW) modes to assess its effect on case depth, surface hardness and microstructural variations of the treated layers. A pulse duration with power-on time of 90ms and power-off time of 10ms with 90% duty cycle yielding 10 Hz frequency has been chosen in case of PW mode of processing. The same peak laser power of 3200W and scanning speed of 20 mm/sec was used for PW mode of processing in order to realize similar heat-input condition vis-à-vis CW mode of processing. Basically, the maximum output laser power that could be realized (associated with the lasing phenomena of the laser source) in practical sense due to different modes of CW and PW laser irradiation processes will be distinguishably different, although the laser source is pumped with fixed current (depending on laser output power fixed). In PW mode, due to closing of the shutter (mechanical modulation with switching) of the diode laser source for few milliseconds, the peak (maximum) laser power that will be realized at the end of the pulse will be shorter (at the end of 90 ms) than that realized in case of CW mode. Thus the mechanical resistance offered by the pulsing of the shutter in PW mode entails lower peak laser power realization on the impinging surface. As the power-off time (in PW mode) was just 10ms, there would be only marginal reduction in the peak laser power (actual peak power realized at the end of pulse).

$$\text{Laser energy density} \left(\frac{J}{mm^2}\right) = \text{Laser power(W)}/\left[\text{processing speed}\left(\frac{mm}{s}\right) * \text{Laser spot width (mm)}\right]\ldots\ldots\ldots\ldots\ldots\ldots\ldots\text{Eq. 5.1}$$

5.4 Influence of different processing modes on laser treated layer characteristics

Figure 5.1 represents a typical case profile across the depth of laser treated layers of bearing steel obtained in CW and PW modes with identification of various regions of interest marked in the optical macrograph along with microstructures obtained from different zones. Indeed, PW mode of processing with pulse duration of 90 ms ensured sufficient power absorption resulting in hardened depth with marginal variation. The nomenclature of various regions of the treated layer delineated due to chemical etching of the treated sample, namely, HZ (Hardened Zone) region indicating near-surface hardened zone obtained due to laser irradiation

with temperature above AC_1, ($T > 735^0C$); SSZ (Super-Soft Zone) region below HZ with temperature being varied between 735^0C and 350^0C; TCZ (Tempered Core Zone) region below SSZ with temperature falling between 350^0C and 150^0C and finally, Unaffected Core Zone (UCZ) whose temperature will fall below 150^0C with unchanged microstructure that of substrate. The demarking of these regions could be visualized with severe darkening of SSZ and partial darkening of TCZ regions delineated because of preferential chemical reaction associated with Nital etching. Delineation of especially softened regions, SSZ and TCZ has been considered based on the microstructural changes involving carbide nucleation in TCZ and growth of carbides in SSZ as similar to the reported studies involving laser softening of martensitic steels [181]. Apparently, these critical austenitization and tempering temperature assumptions referred are in agreement with the temperatures reported in a recent study on the prediction of microstructural design in bearing steels with hardness distribution [182]. The bright top surface region constituting HZ indicates complete austenitization without any melting involved, as no undulations could be visualized on surface.
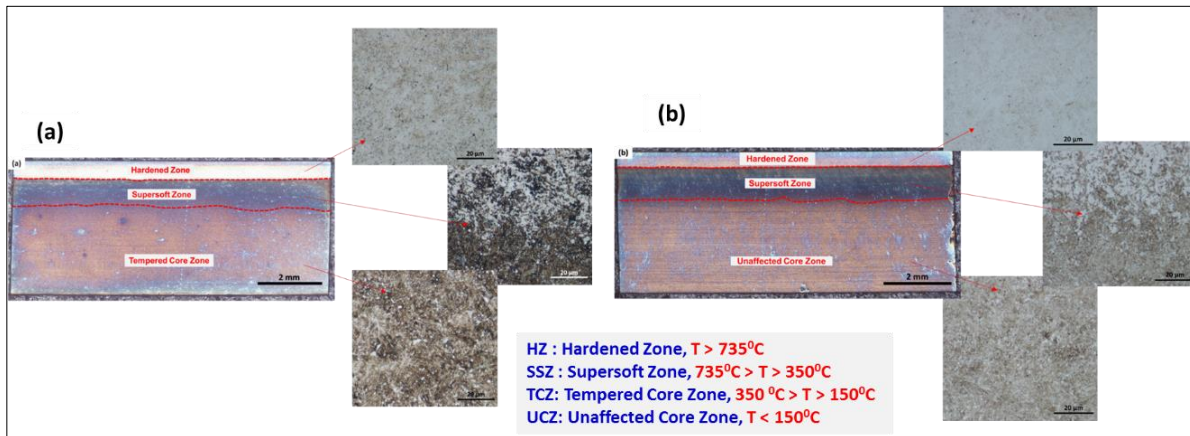
Fig. 5.1 Cross-sectional macrographs of laser treated bearing steel processed under different modes (a) CW (b) PW

The HZ depths for CW and PW modes were noted to be 450 ± 10 μm and 320 ± 20 μm respectively. It is clear from the Figure 5.1 that higher austenitization enhanced HZ depth in CW, compared to that of PW one, plausibly due to raise in peak temperature in the CW mode of thermal cycle. Whereas, SSZ depths (850 ± 50 μm) remained more or less similar in the treated layers, plausibly, on account of similar thermal diffusion effects. It is clear that, higher tempered

martensitic transformation depth could be observed in the TCZ zone of CW mode as compared to that of PW mode. The high cooling rate possible in PW mode facilitated in reducing tempering effect and thereby retaining core structure. Similar effects, although with different steels were observed in laser hardening studies reported elsewhere [183, 184].

5.5 Influence of different processing modes on microstructure, phase analysis and hardness of treated layers

Further to the case depth evaluation, microstructure analysis on the surfaces as well as through their depths by FESEM and Micro-XRD (Figures 5.2 and 5.3) characterization provide insight into the understanding of the effect of processing conditions on structural transformations. As the steel was subjected to conventional through hardening and tempering treatment (CHT), the microstructure (depicted in Figure 3.3) displayed tempered martensitic matrix with dispersion of MC alloy carbides (M being Fe and Cr) and pockets of austenite. It is clear that precipitation of globular alloy carbides (MC) along with different amounts of retained austenite (γ-Fe) and martensite phases varied with laser processing conditions.

XRD analysis of the treated surfaces as shown in Figure 5.3 indicated higher broadening of α-Fe (martensite) peaks in PW layer than in CW layer. The size and morphologies of globular precipitates (observed to be complex carbides of Fe and Cr from EDS analysis), previously observed in untreated core microstructure, was found to get modified with mode of processing on account of vast variation in laser treatment cycle condition and its associated cooling rate effects. The microstructural refining effect (martensite matrix) was found to be greater in HZ region of PW layer (depicted in Figure 5.2(b)) than that observed in HZ region of CW (depicted in Figure 5.2(a)) processed layer. Similar effects of microstructural refinement with variation in heat input conditions were reported in the study conducted by R. Akhtar and co-workers and attributed to peak temperature variation [185].

Apparently, retained austenite content was observed to be lower (depicted in Figure 5.4) in PW processed layer than in CW layer. This is expected as thermal cycle of PW mode of processing experiences low period of austenitization and higher cooling rate during laser treatment cycle. Conversely, CW mode of processing experiences relatively lower cooling rate with increased duration in austenitization, thereby facilitating higher carbon diffusion into the

prior austenite grains and globular carbides. Thus coarsening of microstructure with enlargement of prior-austenite grains and globular carbides could be observed in hardened region microstructure of CW layer as evident from Figure 5.2(c). However, comparing microstructures of core regions below the transition zones of PW (depicted in Figure 5.2(h)) and CW (depicted in Figure 5.2(g)) layers showed wide variation on account of variation in thermal cycle the prior-hardened steel experiences. The tempering (softening) effect on martensite matrix with dissolution of prior carbides is clearly evident in the core region of CW processed layer. This could be attributed to higher thermal diffusion effect the region experiences on account of higher peak temperature influenced by the laser treatment cycle. Thus weakening of martensite matrix with dissolution of carbides and austenite could be anticipated in the microstructure of core region of CW processed layer than PW one. Similar effects of softening associated with laser treatment cycle were reported by Sangwoo So and co-workers and attributed to thermal diffusion effects [186-188]. It can also be seen that (Figure 5.4) higher volume fraction of carbide phase is present in PW mode compared to that of CW due to higher cooling rates which enhances carbide precipitation. EDS analysis in region 1&2 of Figure 5.2 showed higher chromium content in PW mode as compared to that of CW processed sample as listed in Table 5.1.

Table 5.1 EDS analysis of different spots marked in Fig. 5.2

Condition	Position in figure	Elemental distribution (wt. %)		
		C	Cr	Fe
CHT	1 ((Globular Carbides)	5.07	2.09	92.84
	2 (Matrix with nano carbides)	2.66	1.68	95.66
	3 (Matrix without carbides)	4.48	1.60	93.92
CW	1	6.23	2.64	91.14
	2	3.91	2.02	94.07
	3	4.06	1.47	94.47
PW	1	4.31	2.88	92.80
	2	5.81	1.74	92.07
	3	3.36	1.94	94.69
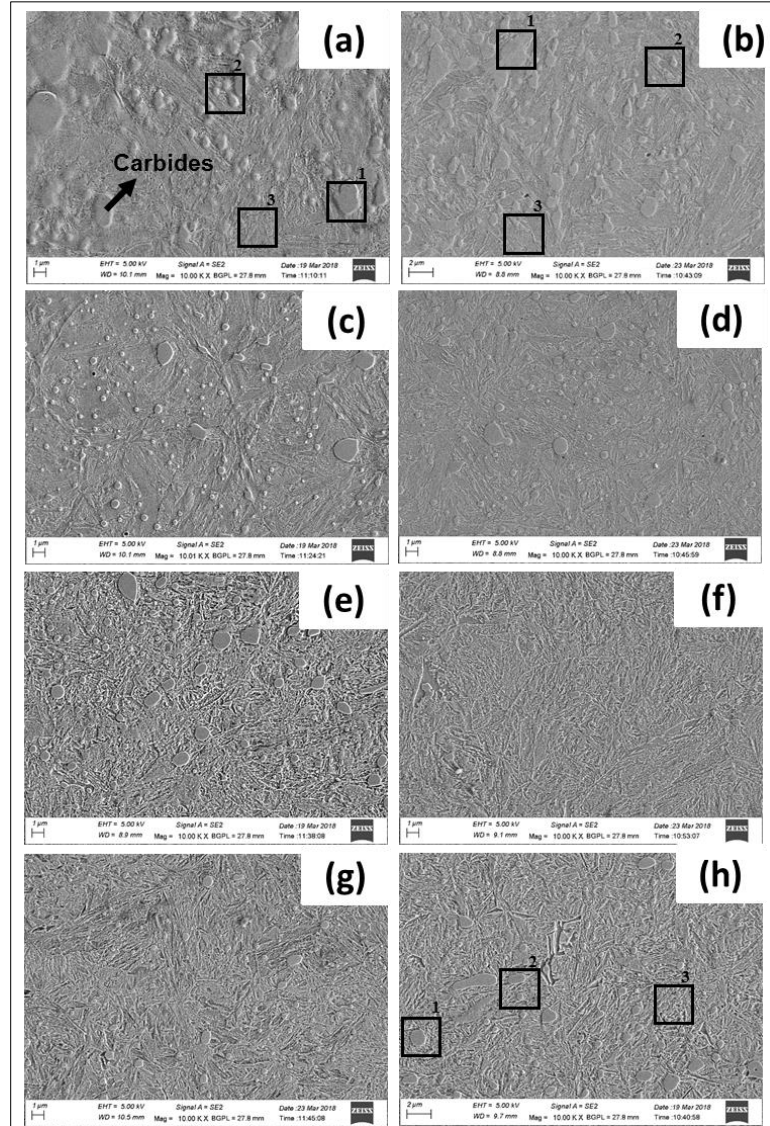
Fig. 5.2 Cross-sectional FESEM micrographs within the laser-hardened layers of bearing steel processed under different modes: (a) HZ zone at 50 μm from surface processed under CW mode; (b) HZ zone at 50 μm from surface processed under PW mode; (c) HZ zone at 130 μm from surface processed under CW mode; (d) HZ zone at 130 μm from surface processed under PW mode; (e) SSZ zone at 520 μm from surface processed under CW mode; (f) SSZ zone at 520 μm from surface processed under PW mode; (g) TCZ zone processed under CW mode; (h) UCZ zone processed under PW mode.
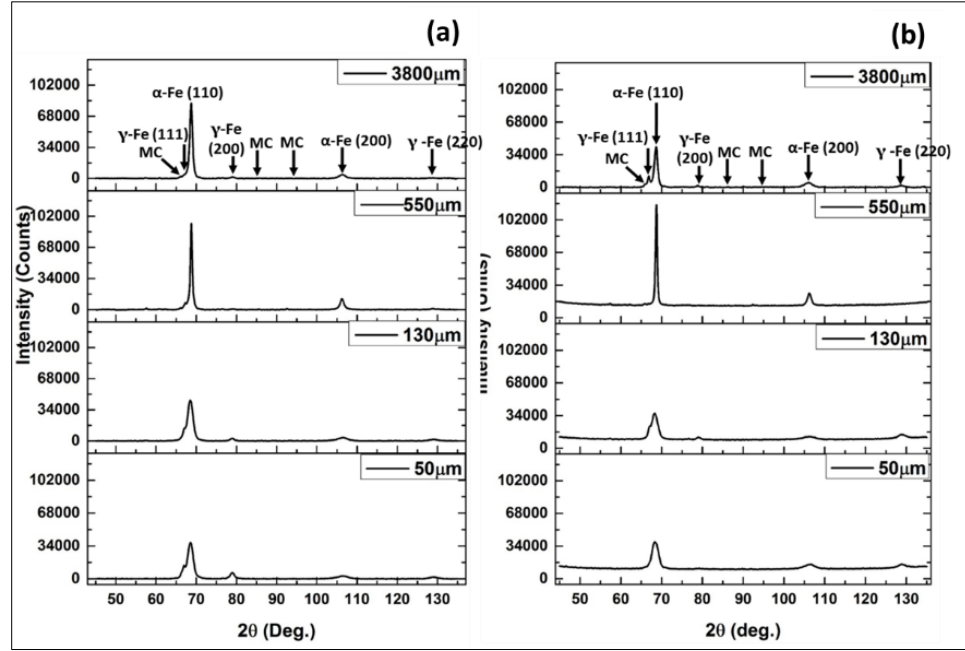
Fig. 5.3 Cross-sectional Micro X-ray diffraction profiles of laser hardened bearing steel (a) CW (b) PW.
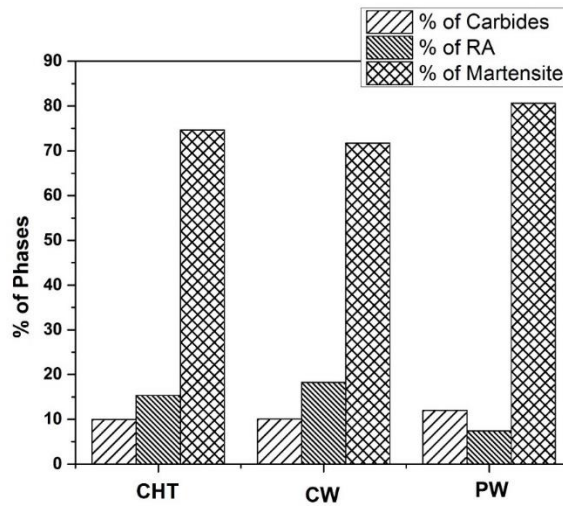
Fig. 5.4 Depicts the volume fraction of various phases present in the samples processed at different operating modes

Figure 5.5 shows hardness distribution of transverse cross-sectional laser treated layers. Hardness in HZ region of laser treated layers increased in the order from 940 ± 10 $HV_{0.5}$ in CW mode to 1000 ± 20 $HV_{0.5}$ in PW mode, in convergence with refinement in martensitic matrix and globular carbides observed in its microstructures. Various studies on laser hardening of bearing

steels concurred with the trend observed and attributed to higher dissolution of carbon from prior globular carbides in prior austenite grains [189]. Thus strengthening of martensite/austenite matrix enhances with peak surface temperature during heating cycle of laser processing mode following by cooling (cooling rate increases in the order CW<PW). At the interface region (SSZ), there is substantial dip in hardness (as low as 490 ± 20 HV$_{0.5}$) which could be attributed to high heating temperature and thermal diffusion experienced in the region with maximum partitioning of cementite particles inter-located at austenite/martensite plates. Hardness distribution in the HZ region of CW mode is less (940 ± 10 HV$_{0.5}$) compared to PW mode, due the difference in cooling rates and thus, affecting the hardness distribution in both surface and core regions. Comparing hardness in UCZ of layers processed with PW and CW modes, hardness reduced to significantly low (640 ± 20 HV$_{0.5}$) in CW layer, well below that of substrate due to higher tempered martensitic transformation observed in the microstructure as previously reported [181]. Thus PW mode of processing facilitates in less tempering effect in the core region and thereby facilitating in higher retention of core hardness.
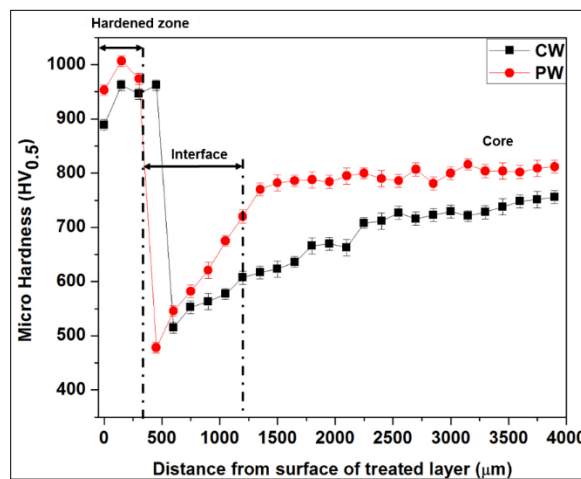
Fig. 5.5 Cross-sectional hardness profiles across the depth of treated layers of bearing steel processed under different operating modes (a) CW (b) PW

5.6   Effect of different processing modes on sliding wear behaviour of bearing steel and their comparison with conventionally treated counterparts

Although life of bearings depends on rolling contact fatigue resistance, assessing wear performance by employing laboratory scale testing with ball-on-disc Tribometer under lubricating as well as dry conditions (in special conditions of usage) has proven as one of the realistic performance evaluation as reported by several works [190]. As real-time testing of bearings under actual or simulated condition consume long duration, assessing their life performance under sliding conditions in short duration, give valuable quick reference for their performance evaluation. Thus, sliding wear resistance performance evaluation utilizing ball-on-disc wear test rig involving Hertzian contact pressures of about 2.96 GPa has been tested and reported to compare wear performance under both unlubricated and lubricated conditions. Results in terms of specific wear rate as well as coefficient of friction were compared with laser-hardened surfaces (under both CW and PW modes of processing) and untreated counterparts. Figures 5.7 & 5.8 illustrate effect of laser treatment (under both CW and PW modes) on wear depth, specific wear rate as compared to that of untreated substrate (conventionally hardened and tempered) to assess sliding wear performance. Furthermore, to realistically assess wear performance under different conditions, both un-lubricated and lubricated conditions were employed. It is clear from wear depths evaluated from the worn profiles at the end of testing cycle of 90m in dry condition and 2 km in lubricated condition that laser surface-hardening treatment showed two-to-five fold improvement, depending upon the treated surface as compared to untreated counterpart, both in lubricated and dry conditions. The worn track depth reduced to a maximum of 68 µm (in un-lubricated dry condition) and 06 µm (in lubricated condition) in laser treated specimen processed with PW mode as against 135 µm (in un-lubricated) and 12 µm (in lubricated) in laser treated specimen processed with CW mode. Comparing wear depths of LSH specimens processed under PW mode with untreated CHT condition, tested under dry conditions, it is evident that wear resistance improved by a factor of six.
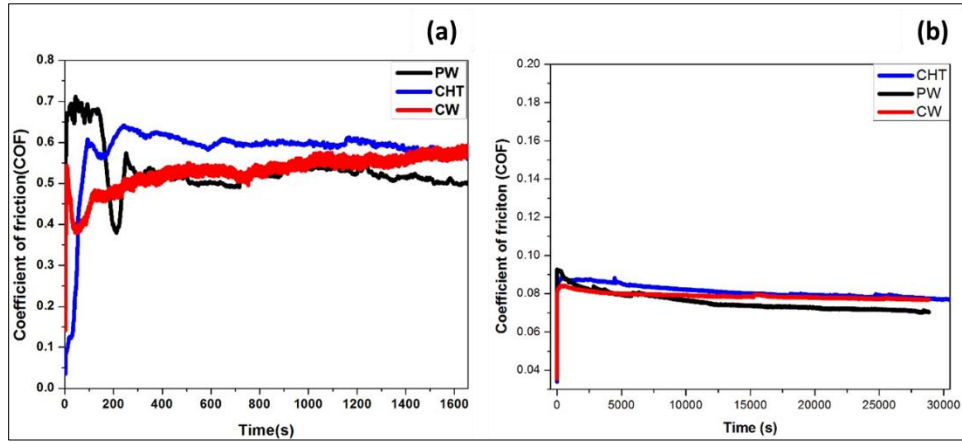
Fig. 5.6 Variation of COF under different operating modes and prior-treated sample (a) Unlubricated (b) lubricated conditions
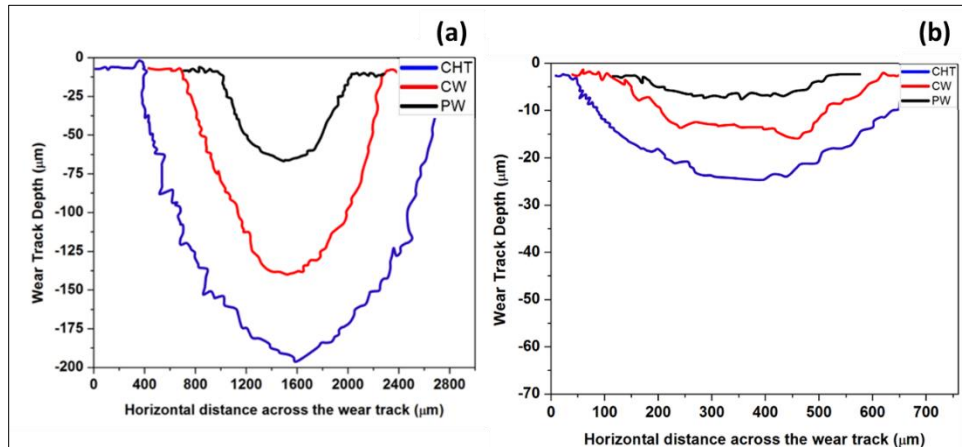
Fig. 5.7 Vertical cross-sectional profile of the worn track of 52100 CHT steel and laser treated samples processed with different operating modes (a) Unlubricated (b) lubricated conditions
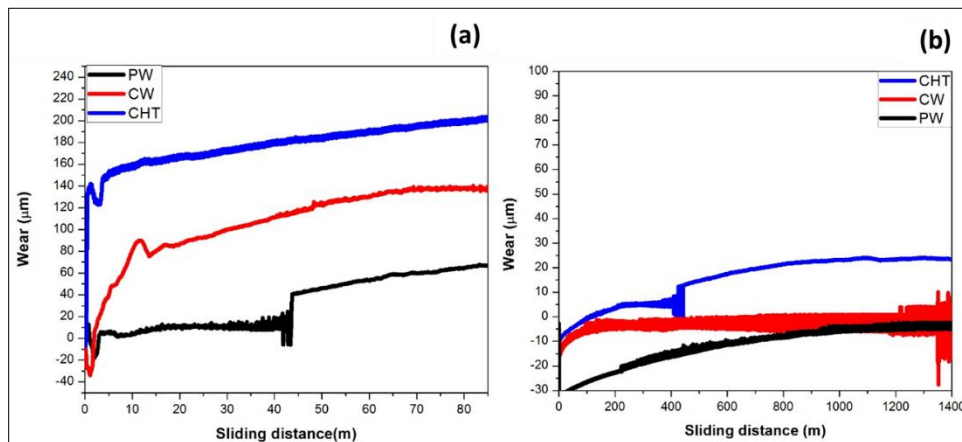
Fig. 5.8 Variation of wear under different operating modes and CHT substrate sample (a) Unlubricated (b) lubricated conditions

Figure 5.9 illustrating comparative specific wear rates evaluated from the standard empirical relationship (Eq. 3.1) shows that maximum improvement in wear resistance (an order of 10 and 7) in both dry and lubricated conditions happened in PW mode of LSH. The wear rate (value multiplied by 10^{-6} mm^3/N-m) reduced to 0.55 (in unlubricated) and 0.035 (in lubricated) in PW mode and 1.48 (in unlubricated) and 0.1566 (in lubricated) in CW mode LSH-treated specimens, as compared to that of untreated specimens (3.53 (in unlubricated) and 1.125 (in lubricated)), These results indicated two-to-three fold improvement in lubricated condition and four-to-five fold improvement in unlubricated conditions. This improvement in wear resistance could be attributed to high strength microstructure (refined martensite matrix and carbide density with modified morphologies) formed in laser treated layers associated with enhanced cooling rates experienced by laser treatment cycle. Indeed, the order of wear resistance was PW>CW>CHT, in conjunction with strength of surface determined by hardness. The extent of improvement in wear resistance due to laser treatment was more in lubricating condition than in unlubricating dry environment owing to effective prevention of direct contact of two bodies with oil lubrication. Lowest specific wear rate was observed on the surface processed with PW condition which could be attributed to maximum hardness improvement of 950 - 1020 HV$_{0.5}$ as against 780 - 790 HV$_{0.5}$ in unaffected substrate. Furthermore the extent of improvement is higher in PW sample than CW one, owing to refined solid-solution strengthened martensitic matrix structure with higher amounts of sub-micron and nano-sized alloy carbides observed in the microstructure. Indeed, higher the amount of refined alloy carbides coupled with refined martensitic matrix, higher would be its contribution in reducing wear. In similar studies involving sliding wear test evaluation of steels with different martensitic structures, greater amounts of martensite with refinement exhibited greater wear resistance reported [191].
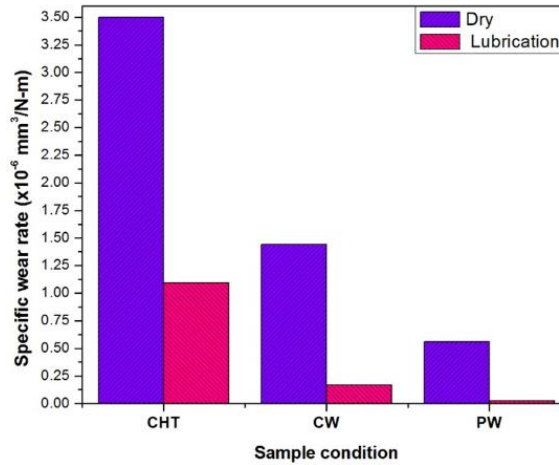
Fig. 5.9 Sliding wear resistance of laser treated (CW and PW) and untreated under dry and lubrication conditions

A detailed assessment with evaluation was carried out to study the effect of laser operating modes on coefficient of friction (COF) as depicted in Figure 5.6. It is clear from the graphs that COF changes with sliding distance and reaches a peak value in the transient period, generally termed as running-in period, and later attain steady state as known to be common in dry conditions [191]. The COF reduced vastly in oil lubricated condition on all samples as evident from the observed 0.5 - 0.56 COF in laser treated surfaces in unlubricated conditions to 0.075-0.08 COF in lubricated ones under steady state conditions. Marginal reduction in COF of laser treated surfaces as compared to untreated substrate could be attributed to microstructural homogeneity, increase in hardness on surface and more specifically high compressive residual stresses [192]. Untreated steel surface, although prior hardened with martensitic transformation, showed a residual stress level of -30 ± 15 MPa owing to surface grinding operation being carried out prior to measurement. With laser treatment under CW mode of processing, the induced compressive stresses on the treated surface enhanced to -330 ± 10 MPa. This could be attributed to the levels of strains induced in the layer associated with martensitic transformation. Indeed, vast reduction in α-Fe X-ray peak intensity accompanied with broadening observed in XRD graph (Figure 5.3) corroborate the effect. In case of PW processed condition, further enhancement in compressive residual stress levels (-530 ± 40 MPa) could be observed as compared to that of CW condition. Indeed high cooling rates that prevail in PW mode facilitate

highly stressed martensitic transformation coupled with enhanced refined carbide precipitation and reduced retained austenite [193].

Comparing friction coefficients with compressive residual stress obtained in HZ of laser treated layers processed with different operating modes, lowest coefficient of friction obtained in PW one and associated with highest compressive residual stress. These results corroborate the effects observed in various reported findings [192-197]. Indeed, alloy carbides with high hardness can possess anti-wear performance during the process of wear test as they can protrude during initial wear slightly due to higher load and thereby reduce contact and facilitate in enhancing load bearing capacity [194, 198]. Thus increasing the density of the hard phases in laser treated layers presumably improve the wear behavior of 52100 bearing steel [192]. Effective prevention of direct contact of two bodies with oil lubrication reduces the COF in lubrication conditions [191]. The variability behavior of the COF in the initial running stage is found to be due to boundary-lubricated sliding with surface roughness and with progression of wear, it decreases owing to annihilation of surface asperities and smoothing [199]. Apparently, further decrease in COF associated could be due to formation of effective low-shear oil film [200].

5.7 Worn surface analysis

SEM analysis of worn surfaces (Figures 5.10 and 5.11) could provide further insight into analyzing material removal mechanisms involved during wear at different investigated conditions of sliding. In general, the material removal mechanisms in sliding wear under dry conditions involved asperity removal with deformation, adhesion, fatigue, and abrasion. It is clear from worn surface morphologies slid in dry conditions (Figure 5.10) that mild abrasion played a predominant role in untreated substrate with pits and delaminated oxide layer as against mild adhesion with oxide layer de-lamination in laser treated surfaces. Indeed, deeper scoring lines are visible in untreated substrate worn morphology as against elongated mild oxide layers with fragmented particles (delamination) in laser treated worn surfaces. Thus the strength of microstructure determined the mechanism of wear involved. Apparently, the deep grooves formed in untreated substrate surface are clearly visible with entrapment of wear debris along with few localized micro-cracks and plastic flow lines. In laser-treated specimens, the worn surfaces are comparatively smoother and there was no evidence of scoring lines except in some

isolated regions (see Figure 5.10(c)). In addition, micro cracks and plastic deformation were not observed in laser treated specimens. Indeed high strength microstructure presumably resisted plastic deformation and thereby prevent severe adhesion and as such hard martensitic structure can impart greater resistance to crack nucleation.

However, if we compare worn surfaces between CW processed and PW processed ones, there is some evidence of pitting and wear debris on the worn surface of CW processed samples (Figure 5.10(b)) with no groove formation. The wear debris observed in Figures 5.10(b, c) could probably due to the transfer of material from the ball to the specimen as a result of the ball being softer than the specimen. Indeed, elongation of oxide layers was higher with relatively less delamination (lower amounts of fragmented debris particles) in PW processed worn surface as compared to that of CW processed counterpart. This could be attributed due to relatively high strength martensitic structure (refined martensite with high density micro-sized and nano-sized alloy carbides) of PW processed surface. Indeed the large sized wear debris in CW-processed one envisages high flash temperature (Figure 5.10(b)). On the whole, higher the strength (hardness) of the treated microstructure, higher was the wear resistance.

SEM morphologies of worn surfaces shown in Figure 5.11 of surfaces tested under lubrication condition elucidate altogether different mechanisms involved in the wear process. Under lubrication conditions, the effective film formed present at contact area help facilitate reduced asperity contact and thereby lowering of contact stress [201]. Indeed vast reduction in coefficient of friction attributes to this factor. Comparing the worn surface morphologies of surfaces, it is clear that mild delamination with few pockets of debris particles could be observed in untreated substrate as against no such delamination in laser treated counterparts. Indeed, the grinding furrows are still visible in both CW and PW processed worn surfaces indicating low effect of contact stress with better lubricity. Furthermore, smoothening of grinding furrows was more in CW-processed worn surface than PW-processed one indicating high wear effect. Indeed, effective oil film thickness formed during wear that depend on the contact stress and strength of microstructure facilitated high wear resistance [201].
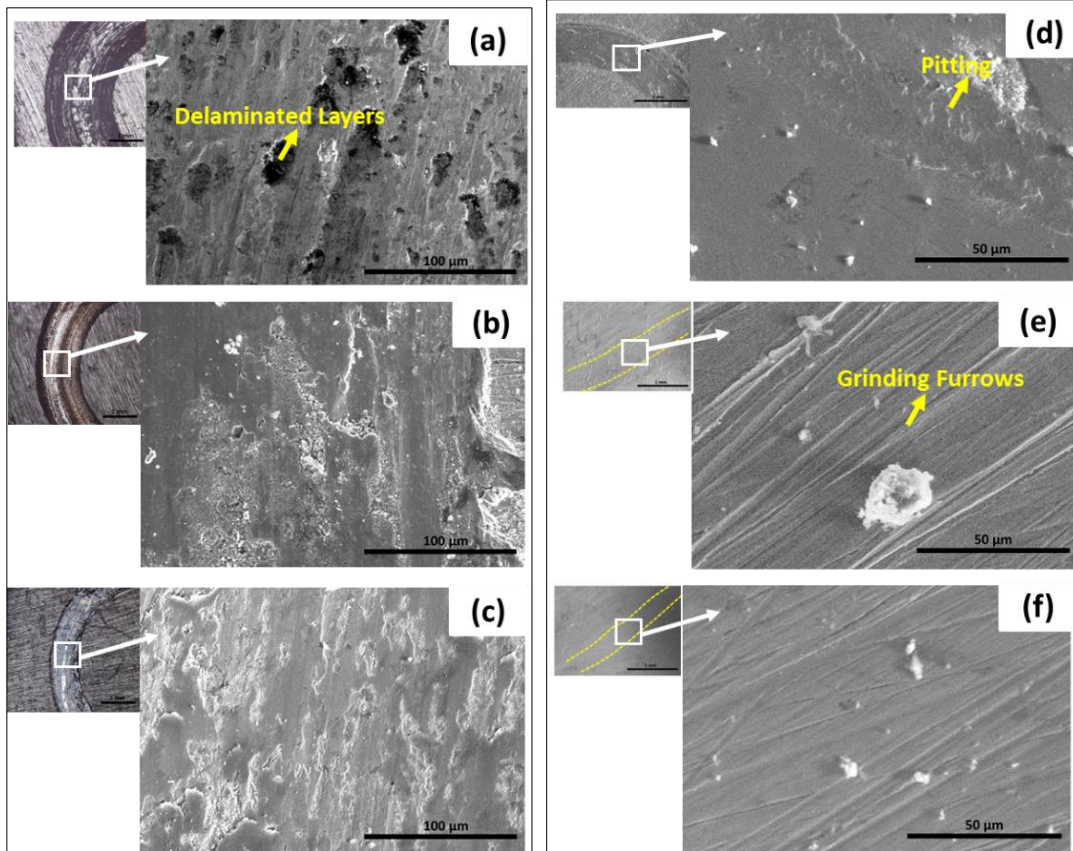
Fig. 5.10 Surface morphological analysis utilizing SEM of Worn out regions of the sliding wear test specimens under unlubricated conditions (a) CHT (b) CW (c) PW

Fig. 5.11 Surface morphological analysis utilizing SEM of Worn out regions of the sliding wear test specimens under lubricated conditions (d) CHT (e) CW (f) PW

5.8   Summary

The study described in this chapter demonstrated the effect of pulsed-wave (PW) mode of hardening on surface hardening of 52100 bearing steel with prior through-hardened condition is investigated and case depth, hardness, microstructure analysis and tribological properties on treated layer are analysed. Under optimum processing conditions, PW mode of processing facilitated in enhanced microstructural refinement with partially dissolved carbide globules with marginally reduced case depth as compared to that of CW processed mode. The study demonstrated that the retained austenite content was observed to be lower and higher volume fraction of carbide phase in PW processed layer than in CW layer as PW mode experiences low

period of austenitization and higher cooling rate during laser treatment cycle. Hardness as high as 1000-1020 $HV_{0.5}$ could be achieved in PW-processed case with retention in core hardness as compared to that of CW-processed counterpart whose hardness achieved was 880-900 $HV_{0.5}$ along with significant reduction in core hardness due to tempering effect.

The study also demonstrated the feasibility of improving sliding wear resistance in PW mode laser processed bearing steel under prototypic laboratory load conditions. The hardened layers in PW mode produced by rapid cooling were harder than CW mode processed and untreated bearing steel substrate. Sliding wear testing results showed five-fold and three-fold improvements in un-lubricated and lubricated conditions in laser processed layer as compared to that of untreated one. Comparing friction coefficients with compressive residual stress obtained in HZ of laser treated layers processed with different operating modes, lowest coefficient of friction obtained in PW one and associated with highest compressive residual stress. The Surface processed with PW mode of processing had the highest compressive residual stress and thereby exhibited best wear resistance performance.

CHAPTER 6

Investigation of different thermal processing conditions that induce varied heat transfer coefficients and cooling rates in laser surface hardening of bearing steel

6.1   Introduction

The previous work on the effect of Pulsed-Wave (PW) mode on surface hardening of bearing steel with prior through-hardened condition investigated and compared with Continuous (CW) mode clearly demonstrated the efficacy of applying pulsed mode of laser processing for improved microstructure on account of its enhanced cooling rate with significant retention in core strength. This paved the way to explore possible improvement in heat transfer rate and/or cooling rate in laser treatment cycle by adopting other mechanisms of processing conditions and setups. The current study is aimed to comprehensively assess influence of different thermal processing conditions (combined effect of processing mode and heat-sink condition with fluid contact) in diode laser hardening of prior-treated bearing steel entails high importance. Additionally, detailed effect of these conditions on hardness, residual stress, microstructure and tribological behavior of the laser-treated layer help envisage its adoption for implementation of laser surface hardening process on thin-sectioned steel parts and components. Results from both unlubricated and lubricated sliding wear tests conducted with a Ball-on-disc test rig on laser treated (both in continuous wave and pulsed wave mode under with/without fluid contact conditions) and untreated bearing steel have been compared to assess improvement in wear resistance due to laser treatment.

6.2   Experimental Methodology

In view of the above, subsequent experiments were carried out using a 20-mm X 5-mm multi-mode rectangular diode laser spot on ground samples of prior treated bearing steels were subjected to laser treatment as mentioned in Chapter 3. The surface temperature was monitored during laser processing by employing high-speed camera based Lompocpro system integrated to the high-power diode laser workstation in order to understand the influence of different thermal processing conditions on the surface temperature effects on characteristics of treated layers. Indeed temperature measured with in-situ high-speed camera-based system indicated surface temperatures of $1260^0C \pm 10^0C$ and $1210^0C \pm 8^0C$ (sampling deviation) when processed under CW and CW-UF modes. Assuming that the fluid contact beneath the sample is sufficient with heat-sink effect, synonymous to higher thickness, the heating rate may decrease and thereby reduce surface temperature. Measurement of surface temperatures in pulsed wave mode of laser processing was done utilizing two-color pyrometer integrated to LASCON LPC03 controller software indicated surface temperatures of $1180^0C \pm 10^{\ 0}C$ and $1110^0C \pm 8^0C$ on laser treated surfaces processed in PW and PW-UF modes. Assessed temperatures were found to be overestimated by above 15% as per analytical model depicted by Nath and Co-workers [202-203] study owing to the utilization of Nd: YAG laser whose output power effects will be different to that of pulsing using diode laser. However, as the pulsing parameters are chosen are limited in variation, more specifically low laser-off time (10 ms) with 90% duty cycle, the significant variation could not be realized in surface temperatures estimated from the analytical model.

The method of processing constitute scanning of the laser at the centre of the plate under optimum processing parameters and prior-treatment conditions (CHT) with/without fluid contact and modes of laser (CW, PW). It is clear that measured distortion angle after LSH vastly changed with processing method adopted (schematic shown in Figure 6.1). It reduced from 4^0 in case of CW mode to 1^0 in case of PW-UF mode a shown in Table 6.1. The fluid flow contact beneath the steel surface has vastly reduced the distortion of the plate both in CW and PW processing modes and responsible for enhancement in heat-transfer rates. The distortion was also found to reduce with the change in mode of laser processing (PW) associated with possible reduction in peak surface temperatures.
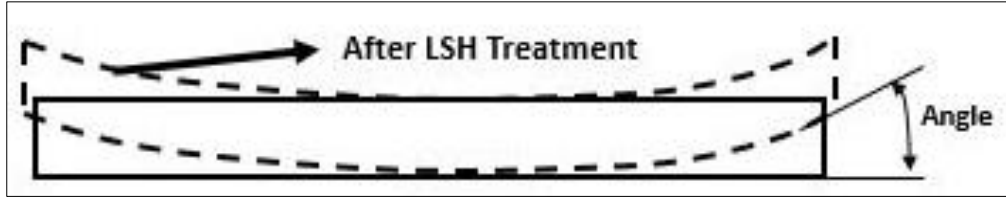
Fig. 6.1 Schematic illustration with distortion analysis of LSH treatment carried out on bearing steel plate processed under different conditions

Table 6.1 Distortional analysis of LSH treatment carried out on bearing steel plate processed under different conditions

Sample Condition	Angle (deg.)
CHT	0
CW	4
CW-UF	2
PW	3.5-3
PW-UF	1

6.3   Case depth, microstructure, hardness and phase analysis

Figure 6.2 depicts variation in case depth with different zones of interest evaluated due to different thermal processing conditions involved in the study. It is well known that carbon diffusion associated with heating rate during austenitization above Ac_1 or Ac_m (in turn peak temperature) and cooling rate (influenced by fluid contact condition and mode of processing) govern the case depth and hardness distribution in treated layer depth [204]. Although carbon diffusion time reduces with fluid contact beneath the sample surface, the cooling rate enhances and as a result high stressed martensitic transformation envisaged as compared to that of steel processed without fluid contact beneath the sample. Apart from the demarcation of these hardened (HZ) and softened (SSZ and TCZ) by virtue of etching effect, range of hardness variation measured within these regions also facilitated in bifurcating these regions through the depth of the sample. A 25 - 30% reduction in hardness (570 - 720 $HV_{0.5}$) to that of base has been considered for TCZ region (Stage-I tempering) and with further softening (hardness < 570 $HV_{0.5}$), SSZ region (Stage-II softening) has been considered. These considerations for SSZ and

TCZ regions are found to be in good agreement with that reported in studies involving tempering of hypereutectoid steels [205].

The HZ depth was highest in CW mode among all the treated layers processed under different conditions. The demarcation of various zones within the treated layer determined by the hardness distribution were also found to be convergent with the surface temperatures measured by E-Maqs high-speed camera-based system and thermocouple embedded at the bottom of the laser treated steel sample wherein no fluid contact involved. It is clear that in the treated layer processed under CW mode, the temperature measured at the bottom of the sample was still about 250 ^{0}C (measured with the help of thermocouple) indicating softening effect associated with martensitic tempering. The high heating rate with relatively longer soaking duration (related to the low thickness of the steel sample) attributed to this effect and as a result huge TCZ depth of about 2.3 mm could be noted with hardness variation between 600 to 650 HV$_{0.5}$. This depth got reduced to as low as 400 μm in PW mode and further to 150 μm in CW-UF and PW-UF modes. Thus the variation in terms of pulsed mode of processing and fluid contact beneath the sample bottom surface facilitated core hardness retention to greater depth owing to reduced carbon diffusion time and high cooling rate effects. In a similar study involving laser hardening with various thickness of steel, higher thickness induced low carbon diffusion distance and thereby, no softening associated with martensitic tempering could be induced to greater depths [206].
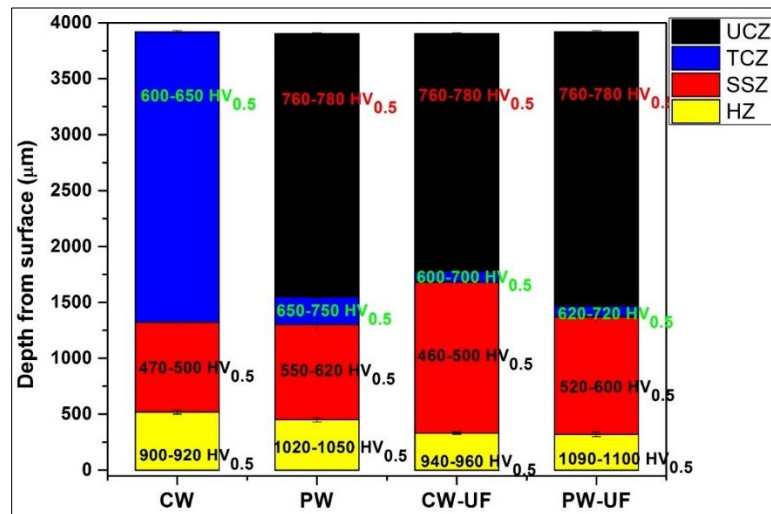
Fig. 6.2 Bar graph representing depth from surface and hardness in various zones of laser treated bearing steel processed under different conditions (a) CW (b) PW (c) CW-UF (d) PW-UF

In contrast SSZ depth enhanced in PW, CW-UF, and PW-UF modes. Hardness in such zones (SSZ) was observed to be as low as 460 - 550 $HV_{0.5}$, with the highest depth in CW-UF mode of processing. Indeed, this zone could have experienced temperature in the range of 730 – 350 ^{0}C and thereby soften to a maximum extent of hardness reduction. On the whole, the HZ depth in the treated layer was highest in CW mode to the tune of 485 μm and got reduced with the employment of other processing conditions. This could be attributed to the factors such as high heating rate, effective carbon diffusion time and rate of cooling associated with thermal processing condition, as reported by other studies involving laser hardening due to pulsed mode and thickness related heat sink effects [204, 206]. From close observation of SSZ depth formation, one can evidently visualize its significant variation with thermal processing condition involved. The SSZ depth was highest to the tune of 1.2 mm in case of CW-UF and as a result maximum lowering of the bulk strength, although with retention of core hardness. Additionally, the hardness improvement achieved in HZ region of CW-UF was lowest (940-960 $HV_{0.5}$) among all the laser-treated layers processed with retention of bulk property.

Further to the case depth evaluation, microstructure analysis on the surfaces as well as through thickness depths by FE-SEM and XRD characterization provided insight into the understanding of the effect of processing conditions on structural transformations. Figures 6.3 and 6.4 exhibited representative high magnification FE-SEM micrographs and their corresponding X-ray diffraction patterns of laser treated surfaces processed under different conditions. It is clear that precipitation of globular alloy carbides (MC) happened in different degree along with varying amounts of retained austenite (γ-Fe) and martensite phases with laser processing condition. Indeed laser processing (in all processed modes) resulted in higher carbon and prior-carbides dissolution during austenitization, associated with high heating rate (high peak temperature), followed by their precipitation (determined by the subsequent cooling rate) and thereby higher amount of globular alloy carbides are discernible as compared to that of untreated CHT. Indeed quantification of these coarse globular carbides from XRD quantitative analysis as well image analysis (from FE-SEM micrographs) indicated 9 - 12 Vol.% in laser treated surfaces as against 6 - 7% Vol.% in CHT. However, the distribution of globular carbides is inhomogeneous in all laser treated microstructures, plausibly, due to irregular thermal diffusion effects associated with differential thermal gradients in laser treatment cycle and non-uniform distribution of prior-carbide globules in CHT microstructure. Due to incomplete dissolution of

prior carbide globules associated with short laser treatment cycle, some partially dissolved as well as coagulated irregularly shaped carbide globules are still observed in laser treated HZ layers. A closer examination of microstructures at high magnification of laser treated surfaces indicated presence of two different types of alloy carbides, one dense and coarser one with size varying between 1 - 6 μm in nearly-spherical and elongated morphologies, another nano-sized ones with irregular morphologies. EDS analysis indicated qualitative variation in Cr content between coarse globular carbides and nano-carbides with relatively higher Cr-content in the former.

Spheroidized carbides greatly influence austenitization kinetics during the heating period of laser treatment cycle followed by martensitic transformation during the cooling cycle. Coagulation of alloy carbides into clusters is also visible in some cases, and this aspect was found to be higher in CW condition that can be attributed to high heating rate with improved austenitization duration. The transformation of highly stressed martensite with twinned plates in laser processed ones is evident on account of high cooling rates associated with laser processing cycle. Furthermore, XRD analysis corroborates this effect as evident from the peak broadening in all laser-processed surfaces depicted in Figure 6.4. Higher the heating rate, higher the dissolution of Cr in prior globular carbides (Cr has higher diffusivity and solubility than C) and as a result coarsening of globular carbides could be observed with increasing peak temperatures in the order of PW-UF to PW to CW-UF to CW. Indeed, with an increase in cooling rate in the order of CW to CW-UF to PW to PW-UF, refinement, and stress in martensite twins (increase in C%) are evident from the qualitative analysis of α-Fe X-ray diffraction peaks presented in zoomed part of Figure 6.4. Correspondingly, hardness in HZ region of treated layers increased in the order from 900 $\pm$10 $HV_{0.5}$ to 1100 $\pm$20 $HV_{0.5}$ as evident from the presented values in Figure 6.2. Various studies on laser hardening of bearing steels also concurred with the trend observed and attributed to higher dissolution of carbon from prior globular carbides in prior austenite grains [207]. Thus strengthening of martensite/austenite matrix enhances with peak surface temperature during the heating cycle of laser processing mode following by cooling rate (cooling rate increases in the order CW<CW-UF<PW<PW-UF).

Another aspect that can be observed is variation in retained austenite phase of surface microstructures with processing modes. The retained austenite (RA) content in the

microstructures was evaluated by optical microscopy (with appropriate etching resulting in dark-coloured areas as martensite and light-coloured areas as RA) and more accurately by adopting standard X-ray Diffraction method. As evident from micrographs (marked in Figure 6.3), RA content increased from 15% in CHT to 20% and 18% in PW and PW-UF and further increased to 23% and 22% in CW and CW-UF mode respectively. With increasing austenitization temperature (in CW mode), the amount of dissolved carbides and the carbon concentration in the austenite also increases, which causes a decrease in Ms and an increase in RA content [208]. It is well known that PW mode of processing with similar peak powers, when compared to CW mode, depending on the pulsing parameters, facilitate in reduction of prior-austenite grain size, but at the same time, if the heat dissipation rate is sluggish owing to sufficiently low thickness of steel plate, it may result in suppression of driving force for prior-austenite growth in asymptotic behaviour [209]. Thus facilitating a significant reduction in RA content in microstructure processed in PW and PW-UF when compared to the CW and CW-UF processed sample. Similar aspect was reported by Jeremy Epp and co-authors in their study involving heat treatment of bearing steel and attributed to the effect of lower austenitization soaking duration [210].
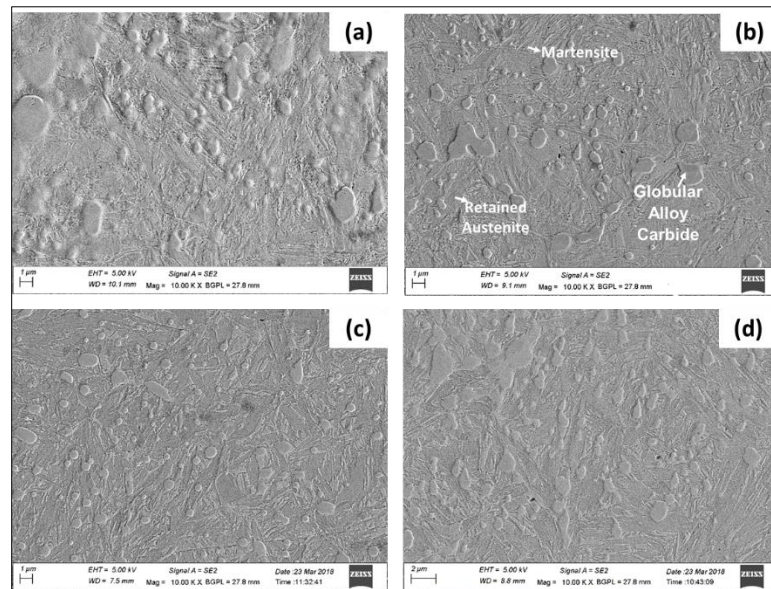
Fig. 6.3 FE-SEM micrographs of LSH treated steel on near surface region processed under different conditions (a) CW (b) PW (c) CW-UF (d) PW-UF

Further to understand the influence of thermal profile through the depth of treated layer associated with laser treatment cycle, microstructure analysis through the depth of treated layer

processed under CW-UF and PW-UF (exhibiting maximum hardness improvement) modes are presented in Figure 6.5. High magnification FE-SEM microstructures at different depths, namely, near surface HZ region (Figure 6.5(a)), region at 200 μm below the surface (Figure 6.5(b), intermediate region at 1000 μm below the surface representing SSZ (Figure 6.5(c)) and central TCZ region (Figure 6.5(c)) provide further insight into understanding of microstructures with depths of the laser treated layer. It is well known, that microstructural variation through the depth of treated layers follows the transformations induced due to the laser treatment cycle. The microstructure at depth in PW-UF mode experiencing maximum peak temperature (Figure 6.5(b)-right) exhibited refined martensite/austenite matrix with dispersion of uniformly distributed nano-carbides (higher amounts as compared to the surface region) and alloy carbides (MC). Indeed high austenitization duration would have facilitated high carbon martensite formation at this region and refinement in terms of nano-carbides in martensite/austenite matrix, thus contributing to maximum hardness improvement in the hardened layer depth (HZ region). The microstructure in CW-UF mode experiencing maximum peak temperature (Figure 6.5(b)-left) exhibited coarser globular alloy carbides with higher amount of retained austenite when compared to PW-UF mode.
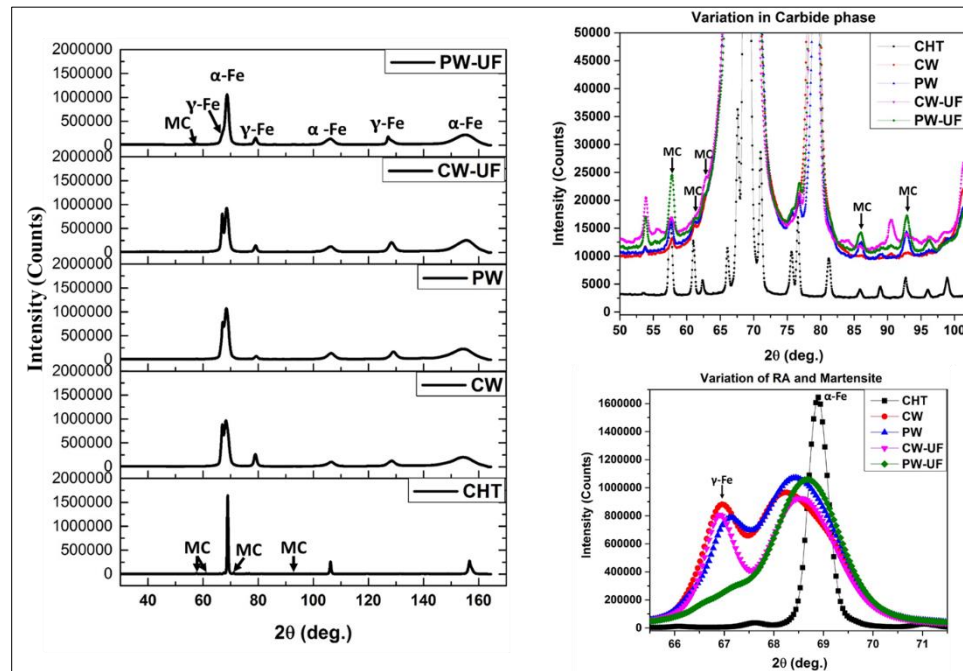
Fig. 6.4 Micro X-ray diffraction patterns obtained on surface of laser-treated steel surface processed with different conditions using Cr Target along with zoomed views
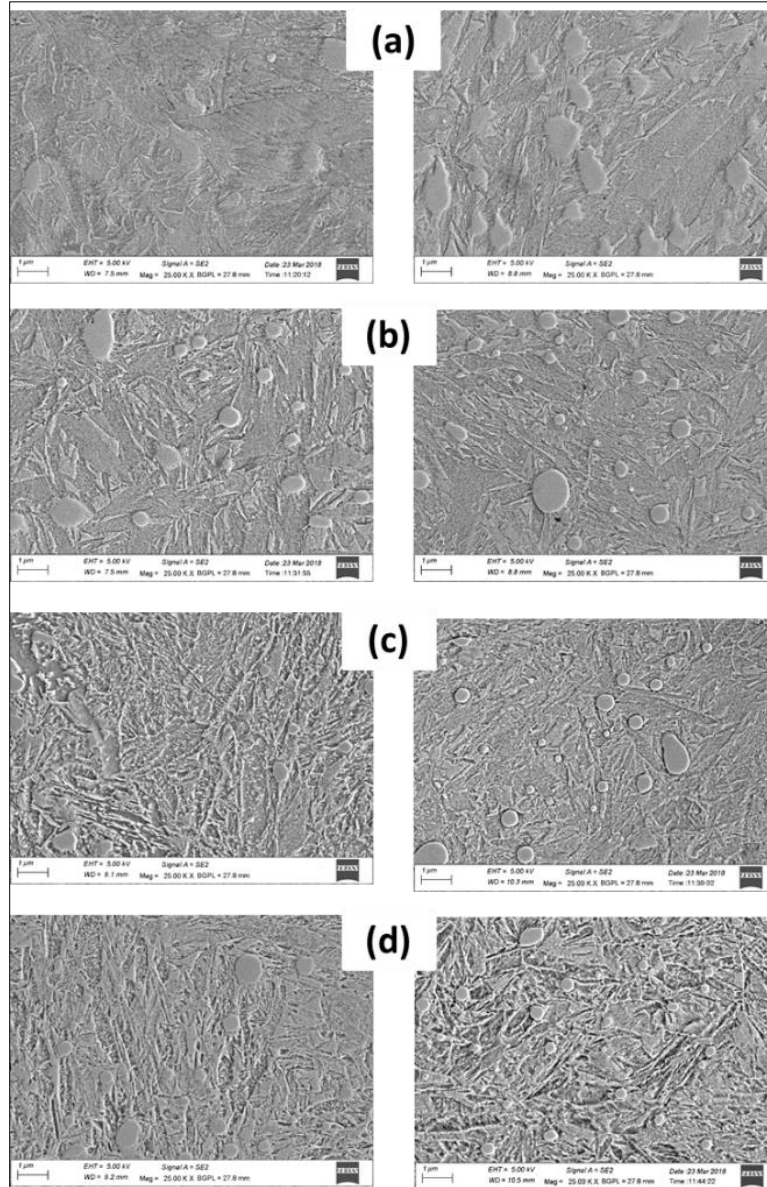
Fig. 6.5 FE-SEM micrographs of LSH treated steel at (a) HZ (Surface), (b) HZ (peak), (c) SSZ and (d) TCZ regions processed under CW-UF (left) and PW-UF (right) modes

Microstructures in SSZ and TCZ regions depicted in Figures 6.5(c & d) both in PW-UF and CW-UF modes indicate drastic change in matrix microstructure with presence of undisturbed residual globular alloy carbides on account of martensite decay as temperature experienced in the regions are well below lower critical A_{c1} temperature. As a result, drastic reduction in hardness to a tune of 480 $HV_{0.5}$ and 550 $HV_{0.5}$ in CW-UF and PW-UF modes respectively (as previously explained) is observed in SSZ region experiencing highest tempering temperature with

maximum partitioning of cementite particles inter-located at austenite/martensite plates along with their coarsening. With further increase in case depth below SSZ region (Figure 6.5(d)) microstructure exhibited undisturbed residual globular carbides along with partitioning of acicular carbides in the matrix of tempered martensite/austenite (associated with martensite decomposition). The amount of martensitic decay in this region is low on account of low temperatures prevailing (as compared to the high temperature in SSZ). The mechanism of formation of such microstructures in SSZ and TCZ could well be explained by two stages of heat affected zone softening models associated with tempering temperature transformation kinetics reported by classical literature [208]. Although both stages of softening (initial stage-I in SSZ and later stage-II in TCZ) involve distinguishably different tempering times with initial SSZ being longer and later in TCZ being shorter. The softening in SSZ microstructure involve significant population of carbide nucleation with coarsening and ferrite recrystallization (generally above 400-450^{0}C), whereas, TCZ involving shorter tempering temperature and duration result in carbide nucleation [211].

6.4 Residual Stress analysis

As residual stress induced on the treated surface is vital for assessing improvement in various properties such as fatigue, wear resistance, etc., residual stress measurements were carried out on bearing steel laser-treated surfaces at different thermal processing conditions after fine polishing. Figure 6.6 illustrates residual stress measurements of laser treated surfaces with an average of five readings being undertaken. It is clear that induced residual stress levels were compressive due to microstructural transformation associated with laser hardening treatment under all thermal processing conditions. The initial low value of -30 ± 15 MPa in untreated (prior hardened and tempered) surface could be due to grinding and polishing carried out on sample prior to residual stress measurements. With laser treatment in CW and CW-UF mode, the evaluated residual stress levels of treated surface enhanced to -330 ± 10 MPa and -450 ± 10 MPa respectively. Furthermore, with enhanced cooling rate condition in laser processing modes of PW and PW-UF, residual stress levels of the treated surface increased to -530 ± 40 MPa and -570 ± 15 MPa respectively. Improvement in residual stress levels due to laser surface hardening treatment could be attributed to the extent of strain induced martensitic transformation in the treated surface. Indeed vast reduction in α-Fe X-ray diffraction peak accompanied with peak

broadening and peak shifting (shown in Figure 6.4) towards the left side of diffraction angle corroborate the enhancement of compressive residual stress level on account of thermal conditions prevailing in laser processing mode. The maximum cooling rate in PW-UF condition induced high strains in martensitic plates to the extent of compensating the tensile stresses induced due to high retained austenite and globular alloy carbides as observed in microstructures previously. Thus, higher compressive residual stress condition of laser treated surface processed under PW-UF mode envisaged greater improvement in wear resistance as well as fatigue strength and thereby life. In a similar study involving assessment of residual stress in laser treated medium carbon alloy steel, compressive residual stresses as high as -450 MPa was observed and attributed to the strain induced carbon martensitic transformation, although with a low-carbon content [212-214].
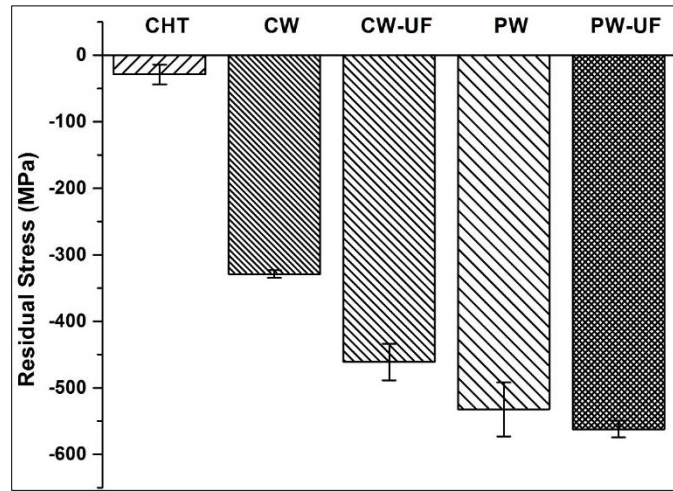
Fig. 6.6 Surface residual stress levels obtained on laser-treated steel surface processed with different conditions

Figure 6.7 represents the residual stresses evaluated across the depth of laser treated layers processed under different conditions indicating fluctuation, owing to plausible variations in phases of martensite, globular MC carbides, retained austenite, precipitated cementite and ferrite with depth. The residual stress levels were highly compressive in HZ region of PW-UF mode sample with maximum of -630 ± 20 MPa being reached at 200 μm depth (highest peak temperature) and then sudden drop to + 680 ± 15 MPa (tensile) at the commencement of SSZ region owing to martensite decay associated with nucleation and coarsening of carbides as well

143

as recrystallization of ferrite. With further increase in depth of the laser treated layer, gradual reduction in tensile stress level improved and finally exhibited compressive stress level near TCZ region and unaffected core in CW-UF, PW and PW-UF processed samples, whereas, in CW processed sample, tensile nature has been observed throughout its depth. The stress distribution across the depth of the laser treated layer was found to be conversant with the phase transformations induced in the microstructures explained earlier. Similar residual stress distribution effects in the laser treated layers on the surface as well as through their depth were reported by several studies [215-216] involving laser hardening treatment of steels and found to alter based on thermal processing conditions. Indeed, the factor of precipitation of nano-carbides at boundaries of martensitic plates due to prevailing high cooling rates facilitated for greater improvement in compressive residual stress levels, despite with higher amounts of retained austenite and alloy carbides that generally induce tensile stress, as compared to residual stress levels reported in the literature.
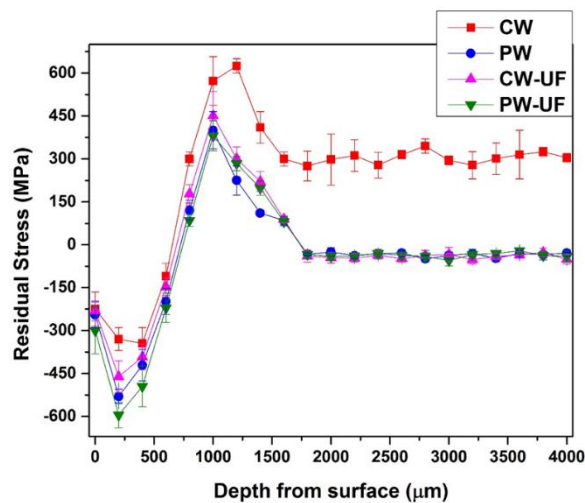
Fig. 6.7 Residual stress depth profiles at the centre of the hardened track obtained on laser treated steel samples processed with different conditions

6.5 Sliding wear behavior and performance evaluation

Figure 6.8 illustrates the effect of laser surface transformation hardening treatment (under different conditions) on wear behavior (measured in terms of wear depth) in comparison to that of the untreated substrate to assess sliding wear performance conducted under both un-lubricated and lubricated conditions. It is clear from wear depths evaluated from the worn profiles obtained

144

at the end of the testing cycle of 90m in dry condition and 2000m in the lubricated condition that, laser surface-hardening treatment showed two-to-five fold improvement, depending upon the treated surface, as compared to untreated counterpart, both in lubricated and dry conditions. The wear depth reduced to a maximum of 50 μm (in un-lubricated dry condition) and 05 μm (in lubricated condition) in LSH treated specimen processed with PW-UF mode and to 65 μm in un-lubricated dry condition) and 07 μm (in lubricated condition) in LSH treated specimen processed with PW mode as against 100 μm and 125 μm (in un-lubricated) and 9 μm and 10 μm (in lubricated) in LSH treated specimen processed with CW-UF and CW modes respectively. Comparing wear depths of LSH specimens processed under PW-UF mode with untreated CHT condition, tested under dry conditions, it is evident that wear resistance improved by a factor of six. The wear depth on the counter body side of a hardened steel ball of 6-mm diameter was found measurably low (scar diameter as low as 10-15 μm) and more or less similar in all laser-processed conditions when tested under lubricating conditions. In case of sliding testing under dry conditions, the counter body wear (hardened bearing steel ball) was also found to be proportionately increasing in worn scar width and depth with laser-treated sample processing under PW mode of processing with fluid contact to CW mode of processing without any fluid contact.
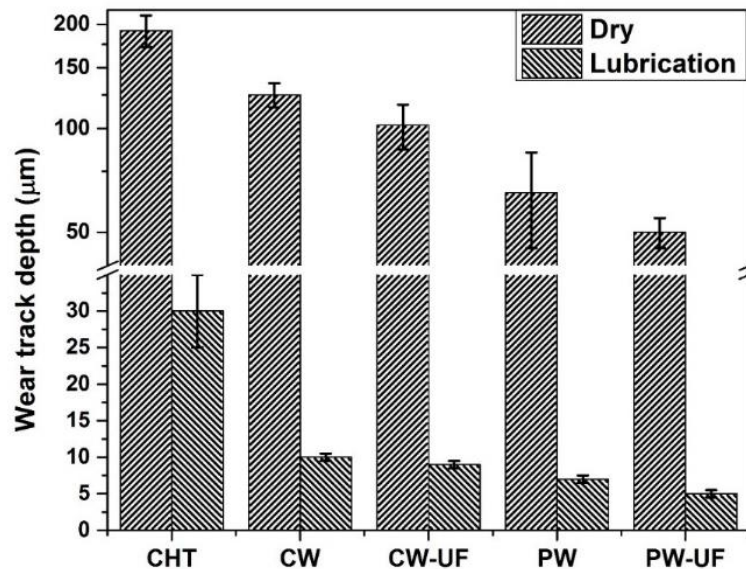
Fig. 6.8 Worn track depth of laser treated bearing steel processed under different conditions
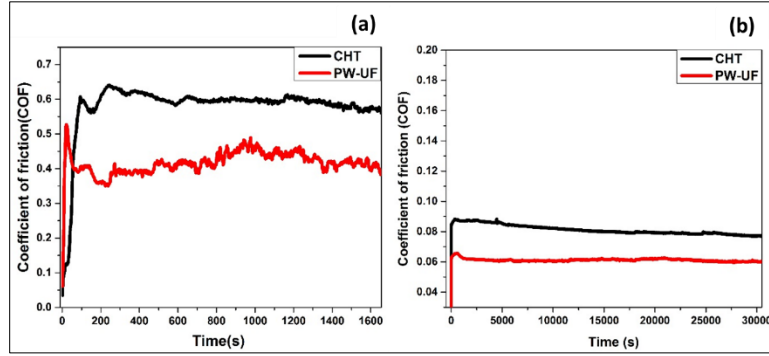
Fig. 6.9 Variation of COF under PW-UF operating mode and prior-treated sample (a) Unlubricated (b) lubricated conditions

An attempt has been made to correlate residual stress induced on surfaces with sliding wear resistance evaluated in terms of specific wear rate when subjected to ball-on-disc wear testing under lubricated conditions. The detailed study under the lubricating condition of wear testing was considered more relevant as an application such as bearing demands tribological performance improvement in lubricated condition. Figure 6.9 and 6.10 illustrates a comparison of specific wear rate and Mean COF with residual stress levels observed in untreated substrate and laser treated surfaces processed under different thermal processing conditions. Crosschecking the weight loss results calculated for both ball and disk followed similar trend as reported in specific wear rate analysis. As the wear regimes fall under mixed lubricated condition, part of the load is carried by metal contact (contacting asperities) and a part by dragging lubricating fluid. It is clear that wear resistance improved in the order of residual stress condition in treated surface [217]. It increased in the order of CW to CW-UF to PW to PW-UF by improvement in compressive residual stress levels of the treated layer. The specific wear rate and COF_{mean} reduced to a maximum in both PW and PW-UF modes of processing, consistent with the vast improvement in hardness and residual stress conditions. COF_{mean} reduced from 0.085 in CHT surface to 0.065 in laser treated surface processed under PW-UF condition owing to the presence of lubricating film that facilitates in reducing the contact stress [17-20]. Although hardness enhancement with laser processing condition followed wear resistance improvement, it is more relevant to correlate with residual stress level as it can contribute more effectively for applications such as bearings wherein rolling contact fatigue property improvement is tantamount. Indeed, a high level of induced compressive residual stresses can delay fatigue crack nucleation and growth, thereby enhance plastic deformation resistance, and fatigue life.

146
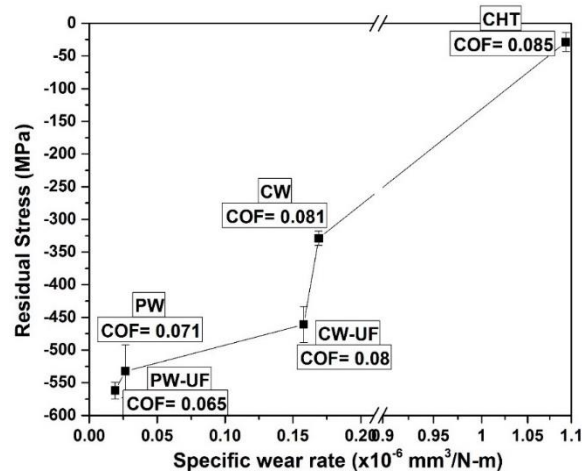
Fig. 6.10 Comparison of Surface residual stress levels with specific wear rate and COF$_{mean}$ (under lubrication conditions) obtained on laser-treated steel surface processed with different conditions

A detailed assessment with evaluation was carried out to study the effect of laser processing modes and conditions on the coefficient of friction (COF) during wear testing as depicted in Figure 6.9. These graphs elucidate the development of friction coefficient with the time of sliding contact. COF in unlubricated dry condition varied in the range of 0.55-0.65 in CHT surface and got reduced to 0.4-0.5 in laser treated surface processed under PW-UF condition. Similarly, friction coefficient reduced from 0.08 in CHT surface to 0.06 in laser surface modified surface processed under PW-UF condition when tested under lubricating sliding contact. Thus conditions of sliding wear testing could vastly vary friction coefficient, with high in the former unlubricated condition than later.

The development of friction with time (shown in Figure 6.9) in both sliding contact conditions showed the presence of initial running-in periods in varying levels as wear happens initially with virgin material contact with surface asperities playing a predominant role before getting stabilized in steady-state condition with the progression of wear. In dry unlubricated sliding contact condition, the initial wear was high with friction owing to virgin material contact (no oxidation happens due to low temperature) with the removal of irregularities and asperities carrying most of the load [224]. With time, these irregularities get worn out, and an oxide film forms (with an increase in flash temperature [225]) and thereby reduce friction with time and stabilizes in steady state with wear progression. The formation oxide-bearing film at the end of

147

running-in period help facilitates in the drop of friction coefficient towards a steady state value as evident from the graph of Figure 6.9(a). The running-in periods were found to be as short as 100 and 200 s (maximum friction coefficient of 0.55 and 0.65) respectively in CHT and laser treated PW-UF surfaces when tested under dry conditions. With the progression of wear, these friction coefficient reduced by 10% in both untreated and laser-treated surfaces with final steady state values being maintained to 0.6 in CHT surface and 0.4 in PW-UF laser treated surface. Indeed, high residual stress condition of the laser-treated surface (under PW-UF condition) with refined high-strength martensitic microstructure and nano alloy carbides help facilitated in the reduction of friction, a factor associated with a reduction in abrasive wear due to elastic nature of the microstructure.

Similar trends in the development of friction coefficient could be observed in a test involving lubricating sliding contact under mixed lubrication regime, although, the friction coefficient was lower by an order owing to the presence of lubricating film that facilitates in reducing the contact stress [218-221]. The running-in periods associated with initial boundary lubrication condition wherein viscous dragging forces of the fluid film increases until its rupture with progression of time, friction coefficient increases. This is evident from the graphs presented in Figure 6.9(b), wherein friction coefficient increased to a maximum of 0.088 after 1200 s in untreated CHT surface and 0.067 after 1200 s in laser-treated surface processed under PW-UF condition. The prolonged running-in periods observed in lubricating sliding contacts, as compared to dry sliding condition, could be due to a significant reduction in contact stress associated with a lubricating oil film. Apparently, a similar reduction in friction coefficient in steady state was observed in laser treated surface processed under PW-UF as compared to untreated CHT counterpart, a similar factor observed in dry sliding contact testing condition, and attributed to high-strength martensitic microstructure with presence of nano-sized alloy carbides, increase in hardness on surface and more specifically high compressive residual stresses [219].

6.6 Worn surface analysis

The material removal mechanisms in sliding wear under dry conditions with steel contact involve asperity removal with plastic deformation, adhesion, fatigue, and abrasion. It is clear from worn surface morphologies of surfaces slid in dry conditions [Figure 6.11(a, b)] that severe

adhesion and mild abrasion with delamination played a predominant role in CHT substrate with formation of pits and plastically deformed and delaminated oxide film (evidenced from EDS analysis indicating patches of oxides of Fe and Cr) as against mild adhesion with smeared oxide layer delamination (absence of pits) in laser treated surface. Indeed, deeper scoring lines are visible in untreated substrate worn surface as against smoothened film with elongated mild oxide layer patches (smeared debris) along with few pockets of fragmented debris particles (deformation) in laser treated worn surfaces. Thus, the strength of contacting surface microstructure coupled with test conditions determined the mechanism of wear involved. The deep grooves formed in untreated substrate surface are clearly visible with entrapment of wear debris along with few localized micro-cracks and plastic flow lines. In laser-treated specimen, the worn surfaces are comparatively smoother, and there was no evidence of scoring lines except in some isolated regions (see Figure 6.11(b)). In addition, micro cracks and plastic deformation were not observed in the laser treated specimen. Indeed high strength microstructure with higher compressive residual stress presumably resisted plastic deformation and thereby prevented severe adhesion and as such hard martensitic structure can impart greater resistance to crack nucleation.
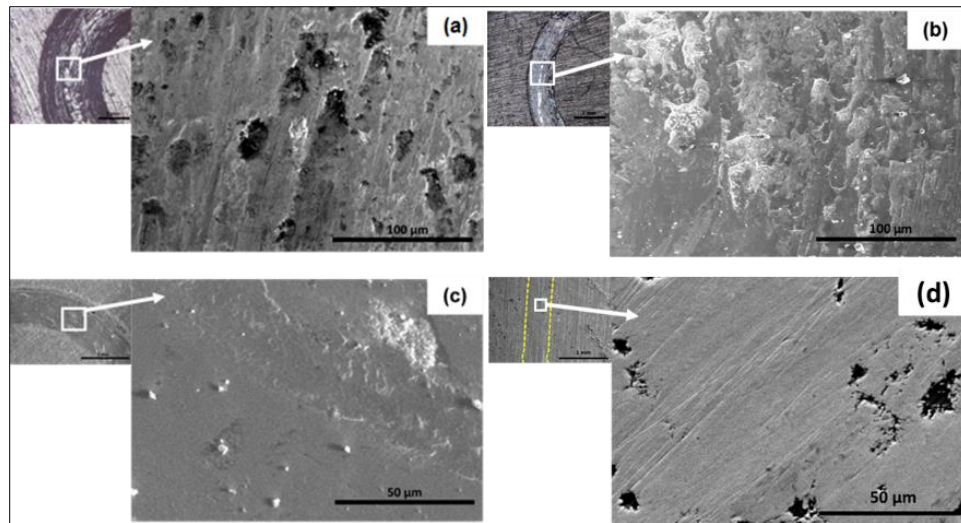
Fig. 6.11 Surface morphological analysis utilizing SEM of Worn out regions of the sliding wear test specimens under (a,b) dry and (c,d) lubricated conditions (a,c) CHT (b,d) PW-UF

Further, to understand mechanisms of wear in lubricating conditions, SEM worn surface morphologies of (shown in Figure 6.11(c, d)) two extreme conditions, (involving untreated

149

(CHT) and laser treated under PW-UF mode) were considered and analyzed. They elucidate altogether different mechanisms involved in the wear process. It is clear that worn surfaces are far smoother and largely undisturbed with shallow scars when compared to that of worn surfaces tested in unlubricated conditions (evident from the low mag micrographs). Indeed, the presence of lubricating film facilitated in bearing the load with reduced asperity contact and thereby lowering contact stress by an order [222]. Apparently, vast reduction of friction coefficient from 0.4-0.6 in dry condition to 0.06-0.08 in lubricated condition attributes to this factor (graphs presented in Figure 6.9). Comparing the worn surface morphologies of CHT and PW-UF surfaces tested under lubrication condition, it is clear that the material removal was smoother (with removal of virgin rough surface asperities associated with grinding furrows) coupled with plowing of few pockets of debris particles in untreated substrate as against no such grooving and delamination in laser treated counterpart. The worn scar width reduced by half (when compared with that of CHT counterpart) with surface grinding furrows being still visible in PW-UF processed one. Indeed, the high strength martensitic microstructure comprising refined martensite and nano-sized alloy carbides (higher hardness with compressive stress in PW-UF surface as compared to that of CHT) acts more elastically in mixed lubrication regime and thereby resist wear particles detachment. Indeed, the fine debris particles visible in both worn surface morphologies (Figure 6.11(c,d)) suggest a vast reduction in contact load and thereby wear as reported in several works involving the study of sliding wear under the contact of hard steel surfaces in mixed lubrication regimes [218, 223].

6.7 Summary

The study conducted on diode laser-based surface hardening treatment with different thermal processing conditions involving continuous-wave and pulsed-wave modes with and without fluid contact on bearing steel successfully demonstrated their effects on retention of core hardness, microstructural transformation and induced residual stress levels. The amount of fluid confined and the pulsing parameters greatly influence factors such as softening, component distortion and case profile uniformity of real parts such as bearing components for processing. The microstructural changes induced on the surface as well as subsurface due to different thermal processing conditions were found to be conversant with phase transformations obtained.

The hardness in the treated layer surface increased with increase in cooling rate associated with the thermal processing condition of laser treatment cycle. It increased in the order of CHT<CW<PW<PW-UF, convergent with the amount of refinement in martensite and carbides observed in the microstructure. The study also co-related well with the improvement in sliding wear resistance in convergence with the enhancement of residual compressive stress levels observed in the treated surfaces. A two-to-three fold improvement could be visualized in wear resistance of the laser treated surface processed under pulsed mode with fluid contact beneath the steel sample when compared to conventionally hardened counterpart owing to the vast improvement in hardness (1050 - 1100 $HV_{0.5}$) and compressive residual stress levels (-550 to -650 MPa).

Indeed the strength of laser treated layer microstructure improved with enhancement in hardness, compressive residual stress level, and microstructural refinement with the distribution of alloy nano-carbides in a martensitic matrix. A three-fold improvement in sliding wear resistance in un-lubricated dry condition and three-to-four fold improvement in lubricated condition achieved with the pulsed mode of laser processing under fluid contact. Indeed, the coefficient of friction reduced (in both lubricated and unlubricated conditions) with the implementation of thermal processing condition involving pulsed mode under fluid contact. Although wear mechanisms involved are similar in laser treated and untreated surfaces when tested under similar conditions, great reduction in wear realized in laser treated surfaces, owing to high resistance to shear and plastic deformation induced by high strength martensitic microstructure. In this way, a deeper understanding of the process envisioned with understanding on the effect of different thermal processing conditions during laser transformation hardening treatment. The study also facilitated to develop the novel method of laser surface transformation hardening with pulsed-wave mode of processing under fluid contact beneath the thin-sectioned steel for effective retention of bulk properties with reduced distortion and improvement in tribological performance.

CHAPTER 7

Finite Element Analysis with Temperature Distribution and Experimental Validation of Laser Surface Hardening Processes

7.1   Introduction

Further to the previous detailed study on understanding of different thermal processing conditions on resulting surface hardened layers on bearing steel and their characterization, it was felt pertinent to simulate temperature distribution in laser surface hardening process and validate experimentally. Hence, FEM analysis of the process on simple flat and round samples with variation in processing modes and conditions and their experimental validation has become the subject of the present work presented in this section. COMSOL Multiphysics software has been used to simulate the process on steel flat and rod samples with assessment of various processing conditions and types such as (a) different modes of laser processing – CW and PW, (b) effect of pulsing parameters in single pulse processing and (c) optimization of high-speed quasi-stationery beam processing on cylindrical rod on thermal contours and case profile analysis. Simulating the process by FEM help facilitate in understanding evolution of thermal history in laser surface hardening process with ease of optimization on bearing steel and bearing elements to be implemented for actual development of the process as explained in later sections of the work. The experimental results of case depth profiles as well as hardness distribution contours in the treated layers of flat specimen validated well with the temperature distribution simulated with FEM model.

In order to develop a suitable methodology for processing of bearing element such as roller, a quasi-stationary laser beam processing technique approach proposed utilizing high-

speed rotation has been simulated by FEM and validated with actual experimentation. Indeed, the developed quasi-stationery high-speed process helped to obtain a uniform hardened layer along the entire work piece surface with complete elimination of deleterious inter-pass softening effects in the overlapped regions and melting. The simulated model developed validated with actual experimentation on En-31 steel rod employing a fiber-coupled diode laser system integrated to high-speed rotating mini lathe. Two principal quality-determining factors of laser surface hardened layer, namely, total hardened case depth and hardness distribution across and along its depth and length of the rod are correlated and compared. The most important output factor - differential hardness – a measure of variation in hardness distribution obtained longitudinally along the processed rod length - was analysed in terms of its variation with processing parameters such as laser power, linear speed and rotary axis speed. The simulated thermal history with temperature distribution and thermal contours simulated facilitated in co-relating the hardened surface profile with hardness distribution. Indeed the temperature distribution profiles simulated along the treated layer longitudinally and through-thickness, processed with high rotary axis speed and appropriate linear speed exhibited uniform treated layer with complete elimination of inter-pass tracking softening effects with surface temperature being above critical temperature throughout the processed length.

7.2   Simulation of temperature profiles by different modes of laser surface hardening on thin plate of bearing steel

To precisely control peak temperatures and enhance cooling rate, laser surface hardening utilizing Pulsed Wave (PW) mode on surface hardening of bearing steel investigated and compared with Continuous wave (CW) mode. Influence of different processing modes (CW & PW) on temperature distribution are predicted through FEM simulation and validated with experimental results. Using COMSOL Multiphysics analytical model, laser beam was constructed (as shown in Figures 3.13 and 3.19) which resembles the actual High Power Diode Lasers (HPDL) source used in the experimentation of laser surface hardening process. In the present work, 4-mm thick En-31 bearing steel grinded plate utilized for the purpose. The laser surface transformation hardening treatment was carried out by employing continuous wave (CW)

and pulsed (PW) modes using a 1.5 mm fiber coupled diode laser integrated to 6+2 axis robot. The setup include an optical module to tailor the multi-mode laser beam in to a rectangular spot of 20mm x 5mm as shown in Figure 3.8. In-situ high-speed camera based surface temperature monitoring and controlling system with E-Maqs (Lasertronic-Lompocpro 7.6, Fraunhofer IWS, Germany) is used for measuring surface temperatures during processing. Table 7.1 elucidates the LSH process parameters utilized for experimentation. The thermophysical properties data used in the finite element model were temperature dependent properties corresponding to the bearing steel. The governing equations, laser-energy distribution profile, meshing strategy and study configuration formulated for the laser-material interaction are, as previously mentioned in Chapter 3. The process parameters such as laser power and scanning speed used for experimentation are considered as inputs to the Finite element model.

Table 7.1 LSH process parameters utilized for experimentation

Laser setup	
Laser type	Fiber-Coupled Diode Laser (915-980 nm)
Workstation	8-Axis Robotic System
Fiber	1.5 mm
Diode laser Beam Spot (FWHM)	20 x 5 mm
Working Distance	300 mm
Modes of Processing (CW & PW)	
Laser Power	2500-3500 W
Scanning speed	20 mm/s
Pulse Duration	90 ms
Pulse Frequency	20 Hz
Duty cycle	90 % (PW)

Both for actual experimentation and simulation, laser power, ranging from 2500 - 3500W, with fixed scanning speed of 20 mm/s were chosen for both continuous wave (CW) and pulsed wave (PW) modes. These process parameters chosen to ensure maximum austenization in the steel with temperature falling just below melting. A pulse duration with power-on time of

90ms and power-off time of 10ms with 90% duty cycle yielding 10 Hz frequency was considered for PW mode of processing. The same peak laser powers ranging from 2500 - 3500W and scanning speed of 20 mm/sec was used for PW mode of processing in order to realize similar heat-input condition vis-à-vis CW mode of processing. Basically, the maximum output laser power that could be realized (associated with the lasing phenomena of the laser source) in practical sense due to different modes of CW and PW laser irradiation processes will be distinguishably different, although the laser source is pumped with fixed current (depending on laser output power fixed). In PW mode, due to closing of the shutter (mechanical modulation with switching) of the diode laser source for few milliseconds, the peak (maximum) laser power that will be realized at the end of the pulse will be shorter (at the end of 90 ms) than that realized in case of CW mode. Thus the mechanical resistance offered by the pulsing of the shutter in PW mode entails lower peak laser power realization on the impinging surface. As the power-off time (in PW mode) was just 10ms, there would be only marginal reduction in the peak laser power (actual peak power realized at the end of pulse).

The evaluated temperature solution field has been utilized to get requisite surface temperature plots and the hardened case profile predicted using the temperature gradients. Figure 7.1 represents the temperature evolution with respect to time at a particular point on the model surface by varying laser power. The simulation carried out in CW and PW modes with similar peak laser power of 2500W resulted in peak temperatures of $1050^0C \pm 10^0C$ and $900^0C \pm 10\ ^0C$ respectively. With increase in laser power to 3000W, peak temperatures increased to $1250^0C \pm 10^0C$ and $1010^0C \pm 10\ ^0C$ respectively for CW and PW modes and with further increase in laser power to 3500W, peak temperatures reached $1380^0C \pm 10^0C$ and $1200^0C \pm 10\ ^0C$ respectively. It can be observed that the peak temperature decreased in PW mode of processing even though processed with similar peak laser powers due to thermal cycle of PW mode experiences low period of austenization and higher cooling rate. Conversely, CW mode experiences relatively lower cooling rate with increased duration in austenization resulted due to higher peak temperatures as shown in Figure 7.1(c) processed with laser power of 3000W. Indeed temperature measured with in-situ high-speed camera-based system indicated surface temperature of $1395^0C \pm 10^0C$ (sampling deviation) when processed under CW mode. Measurement of surface temperatures in PW mode of laser processing was done utilizing two-color pyrometer integrated to LASCON LPC03 controller software indicated surface temperature

of $1225^0C \pm 8\ ^0C$ on laser treated surfaces processed in PW mode processed with laser power of 3500W. The comparison shows that the simulation temperature results are in good correlation with the experimentally measured values with error less than 5%.
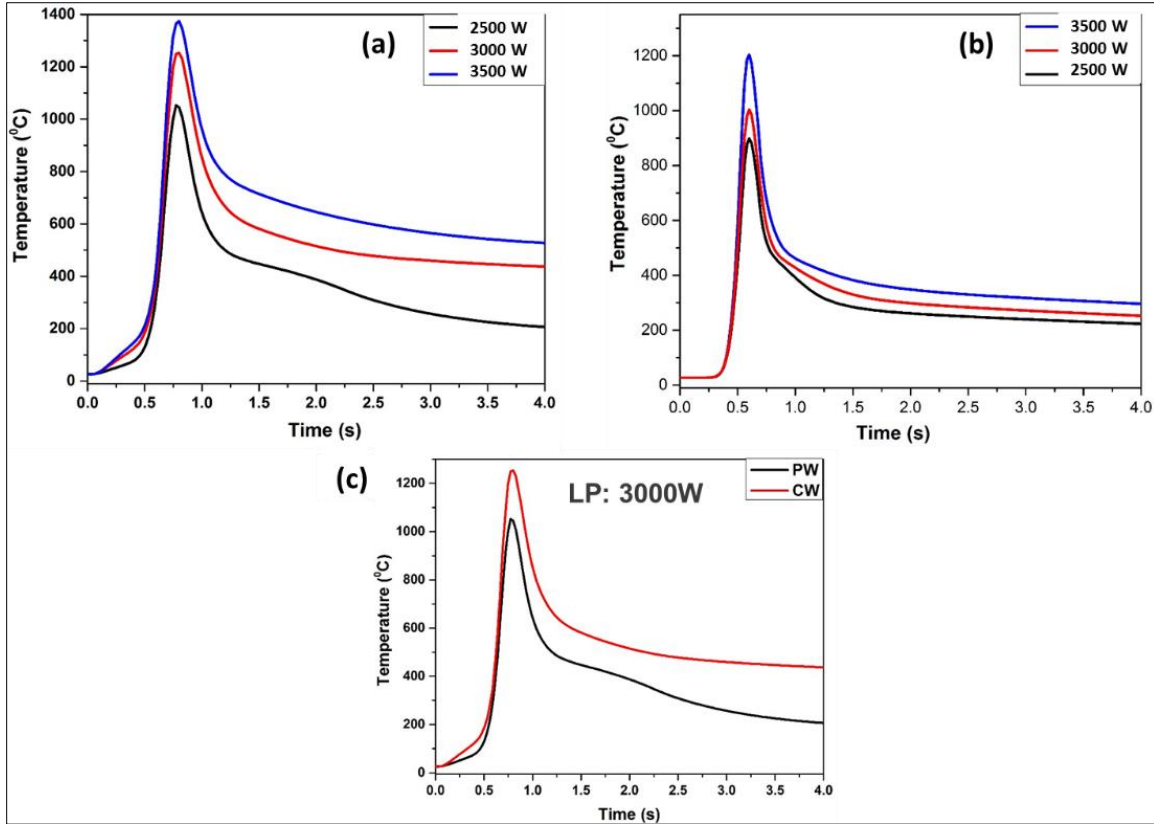
Fig. 7.1 Temperature distribution from simulation analysis at different laser powers in (a) CW and (b) PW modes and comparison

It is clear that the temperature distribution processed under CW mode with laser power of 3000W, the temperature measured at the bottom of the sample (prior hardened steel) was still about 250 ± 10^0C (measured with the help of thermocouple) indicating softening effect associated with martensitic tempering. The high heating rate with relatively longer soaking duration (related to the low thickness of the steel sample) attributed to this effect. Temperature measured at the bottom of the sample from simulation was about 420 ± 10^0C and 200 ± 10^0C in CW and PW modes respectively processed with similar laser power of 3000W. No significant tempering effect in the core region could be realized in PW processed sample that realizes retention of core properties.

The hardening region is predicted by displaying the data range from A_{c1} - 735^0C (critical austenitization temperature for bearing steel) to the maximum surface temperature. With the help of the corresponding temperature gradients obtained from the model, the hardened zone was predicted. The hardened region obtained from the micrograph and the hardened region predicted by the transient thermal model for both the modes of processing are compared and presented in Figure 7.2. The comparison between the experimental and simulation data processed with laser power of 3500W are shown in Table 7.2. The hardened zone (HZ) depths from experimental for CW and PW modes were noted to be 830 $\pm$ 10 μm and 590 $\pm$ 10 μm respectively and from simulation analysis, 836 $\pm$ 10 μm and 630 $\pm$ 10 μm respectively. It is clear that higher austenization duration enhanced HZ depth in CW, compared to that of PW one, plausibly due to raise in peak temperature in the CW mode of thermal cycle. Overall, the HZ depth in the treated layer was highest in CW mode to the tune of 836 μm and reduced with the PW mode. This could be attributed to the factors such as high heating rate, effective carbon diffusion time and rate of cooling, as reported by other studies involving laser hardening due to pulsed mode and thickness related heat sink effects [226, 227]. The data obtained from simulation results utilizing the COMSOL FE model were found to be in good correlation with the experiment results. The average percentage of error between the experiments and simulation results was found to be less than 2 %.
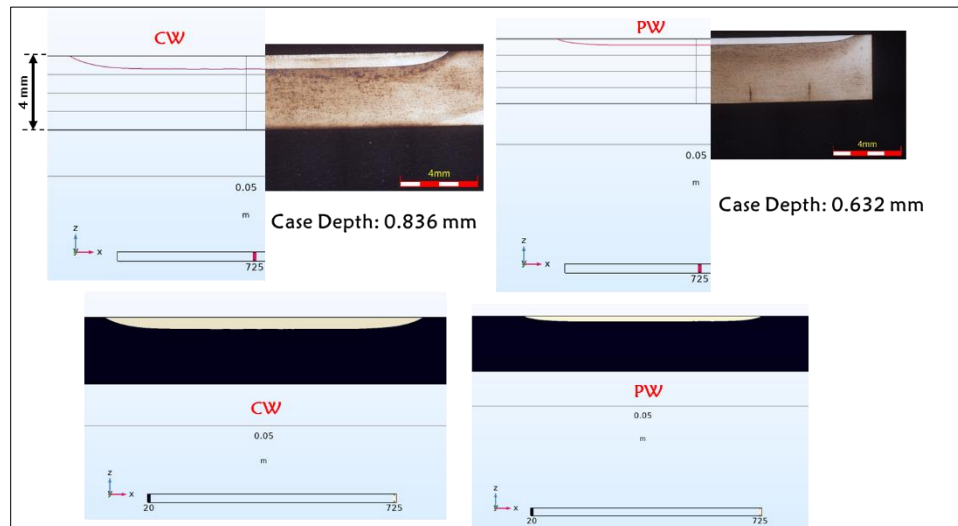
Fig. 7.2 Comparison of predicted hardened regions with the actual micrograph processed with laser power: 3500W (a) CW (b) PW

Table 7.2 Validation of hardened depth and temperatures with experimental and simulation processed with laser power: 3500W

Modes of processing	Hardened depths (µm)			Peak Temperature (˚C)		
	Modelled	Experimental	Error (%)	Modelled	Experimental	Error (%)
CW	830 ± 10	836 ± 10	<1	$1380\ ^0C \pm 10\ ^0C$	$1395\ ^0C \pm 10\ ^0C$	1.07
PW	$590 + 10$	630 ± 10	<1	$1200\ ^0C \pm 10\ ^0C$	$1225\ ^0C \pm 8\ ^0C$	2

7.3 Experimental and numerical modelling of single-pulse laser surface- hardening process

In this study, a 3-D thermal analysis assisted by systematic experimental study using fiber coupled high power diode laser was employed to predict temperature histories in hardened zone (HZ) and heat affected zone (HAZ) in laser transformation hardening of 4mm thick En-31 prior hardened steel flat plate. The laser surface transformation hardening treatment was carried out by employing pulsed (PW) mode using a 0.6 mm fiber coupled to the diode laser integrated to 6+2 axis robot. Temperature profiles and case depth distribution contours are analyzed both experimentally by variation in laser power and pulse duration and by simulation using COMSOL Multiphysics 5.5. In the transient thermal model, a Laser beam with rectangular profile of dimension 20 mm x 2 mm was employed in pulsed mode. Table 7.3 elucidates the LSH process parameters utilized for experimentation. The thermal model had been run for the same and the hardened zone and heat-affected zone were assessed with the help of the temperature gradients.

Table 7.3 Process parameters for Single Pulse Laser Surface Hardening

Laser setup	
Laser type	10 kW Fiber-Coupled Diode Laser (915-980 nm)
Workstation	8-Axis Robotic System
Fiber	0.6 mm
Diode laser Beam Spot (FWHM)	20 x 2 mm
Working Distance	300 mm
Process Parameters	
Laser Power	1750-2500 W
Pulse Width	50-80 ms

Two sets of experiments have been conducted (i) by fixing laser power of 2 kW and varying pulse duration - Pulse-On time ranging from 50 to 80 ms and Pulse-Off time ranging from 50 to 20 ms with total single pulse duration of each one fixed at 100s and (ii) by fixing pulse duration of Pulse-On time of 50 ms, Pulse-Off time of 50 ms and varying laser power from 1750-2500W. The nomenclature used to identify various regions of the treated layer, delineated due to chemical etching of the treated sample, are, namely, HZ (Hardened Zone) region; SSZ (Super-Soft Zone) region; TCZ (Tempered Core Zone) region and Unaffected Core Zone (UCZ). These were predicted based on the critical austenization and tempering temperatures' distribution of En-31 steel that were previously mentioned in Chapter 5 section 5.2. Analyzing the results of the samples allows one to investigate the effects of the laser power and the pulse duration on the HZ depth and widths based on the temperature distribution in different zones from simulation. To examine the influence of the laser treatment on the micro-hardness on the surface as well as subsurface of the laser treated layers, a Vickers Microhardness Tester was employed at 500 g load after polishing and light etching.

7.3.1 Effect of varying pulse duration

Figure 7.3 shows the temperature distribution on the surface and case depth for the peak laser power of 2 kW at varying pulse duration i.e., Pulse-On time (50-80 ms), Pulse-Off time (50-20 ms) respectively but with total single pulse duration of 100ms remaining constant. The depth and widths of HZ, SSZ and TCZ predicted based on the temperature distribution contour and compared with actual measured values from macrographs. Delineation of different zones based on temperature distribution are clearly discernible from macrographs. It is evident that with increase in pulse duration resulted in increase of depth and widths of HZ and peak hardness corresponding to pulse interaction time. With increase in pulse width, case depth was found to increase as a direct consequence of the enhanced heat input. It can be seen that, the average heating rate [as shown in Figure 7.3] significantly increased with the increase of pulse duration. Higher the pulse duration time, higher the peak temperature observed. Maximum peak temperature of $1460 \pm 10\ ^0$C was observed in sample processed with Pulse-On time of 80 ms and got reduced to $1100 \pm 10\ ^0$C in the sample processed with Pulse-On time of 50 ms. This could be attributed to higher thermal diffusion, the region experiences with higher peak temperature of laser treatment cycle and lower rise in temperature for individual shorter duration laser pulse and the higher cooling time [228]. At this maximum laser pulse interaction time of 80 ms, the HZ depth up to which temperature is raised to 1460 ^{0}C is ~740 μm (simulation) and ~705 μm (experimental) and HZ width is raised to ~2260 μm (simulation) and ~2220 μm (experimental) as shown in Table 7.4. It shows that the hardening depth and width reduced when the surface temperature lowered from $1460 \pm 10\ ^0$C to $1100 \pm 10\ ^0$C due to decrease in pulse interaction time. The widths and depths of SSZ and TCZ increased with increase in pulse width. Further, since the increase in heating rate increases with pulse duration, more homogenization possible and as a result higher hardness. Indeed thermal diffusion period during austenitization reduces with pulse width and as a result, reduction in case depth envisaged with decrease in hardness. Similar results were reported by Miokovic et al. for laser heating cycle of 0.5–2.5 Hz frequencies [226]. The agreement between the experimental and simulated depths and widths of hardening by varying pulse duration is reasonably good with error falling less than 10%.
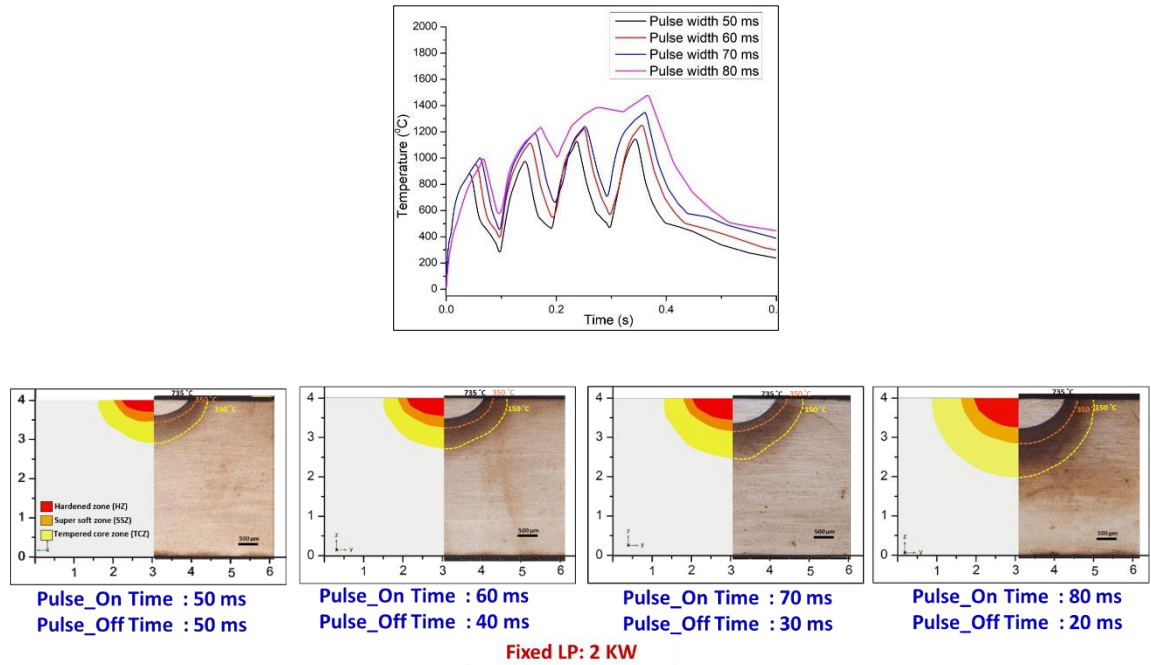
Fig. 7.3 Effect of varying Pulse Duration on thermal profiles and case depth

Table 7.4 Validation of hardened depth and widths experimental and simulation

Pulse width (ms)	Hardened depths (µm)			Hardened widths (µm)			Peak Hardness (HV$_{0.5}$)	Peak Temperature (°C)
	Modelled	Experimental	Error (%)	Modelled	Experimental	Error (%)		
80	744	705	5.2	2264	2220	1.9	880 ± 10	1462
70	541	520	3.8	1981	1950	1.5	870 ± 10	1346
60	472	500	5.6	1824	2000	8.8	865 ± 5	1227
50	300	380	2.6	1665	1690	1.4	860 ± 5	1100

7.3.2 Effect of varying laser power

Figure 7.4 shows the temperature distribution on the surface and case depth for the fixed pulse duration of Pulse-On time of 50ms, Pulse-Off time of 50ms and varying laser power from

161

1750-2500 W. With increase in laser power, the case depth and widths increased. In fact, laser power directly effects the depth of heat penetration into the steel substrate, as it is directly proportional to the heat input [229]. Maximum peak temperature of 1350 ± 10 ^{0}C was observed in sample processed with laser power of 2500 W and it reduced to 1080 ± 10 ^{0}C when processed with laser power of 1750 W. This could be attributed to high thermal diffusion the region experiences associated with higher peak temperature of laser treatment cycle. Higher peak hardness of 920 ± 5 HV$_{0.5}$ observed in sample processed with maximum laser power of 2500 W as shown in Table 7.5. The agreement between the experimental and simulated depths and widths of hardening by varying laser power were reasonably good with error falling less than 5%.

From the above work, results indicated that with increase in laser power and fixed pulse duration, depth and width of hardened zone and hardness distribution improved in the treated layers. The HZ and HAZ dimensions predicted from the model were found to be in good correlation with the experimental data. Another set of experiments by fixing laser power and varying pulse duration i.e. pulse on and off time, higher improvement in depth and width of hardened zone with marginal improvement in hardness observed in treated layers and the same reflected from simulation thermal analysis.
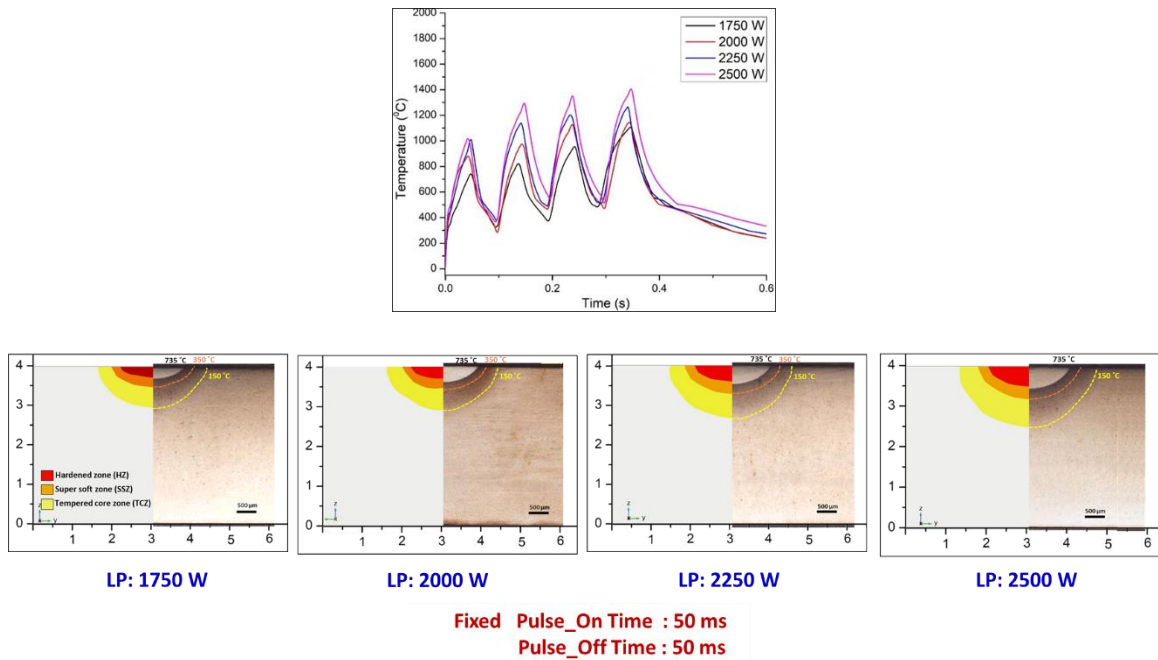
Fig. 7.4 Effect of varying Laser Power on thermal profiles and case depth

Table 7.5 Validation of hardened depth and widths experimental and simulation

LP (W)	Hardened depths (µm)			Hardened widths (µm)			Peak Hardness (HV$_{0.5}$)	Peak Temperature (°C)
	Modelled	Experimental	Error (%)	Modelled	Experimental	Error (%)		
1750	277	300	7.6	1603	1550	3.3	865 $\pm$ 5	1080
2000	300	380	2.6	1665	1690	1.4	860 $\pm$ 5	1100
2250	406	450	9.7	1823	1870	2.5	880 $\pm$ 10	1250
2500	506	500	1.1	1979	2060	3.9	920 $\pm$ 5	1350

7.4 Finite element analysis of temperature distribution during high speed laser surface hardening of cylindrical steel components

Many studies attempted to optimize laser surface-hardening process utilizing high speed processing; none of them used FEM technique to correlate the temperature distribution with the critical responses such on hardness distribution behavior along the treated layer to minimize deleterious softening effects. The response in terms of differential hardness across the treated layer critically helps us to determine the tempered regions formed across the treated layer and assert even smaller variation in hardness within the treated layer across its length and depth. Thus, this aspect needs effective investigation to obtain homogenous hardened case. Indeed, uniform hardness distribution across the treated layer envisages minimization of the response - differential hardness - across the treated layer with maintenance of constant surface temperature, well above critical austenitization temperature as reported earlier [230]. If the response is too high, as in case of helical processing, non-uniform variation in temperature distribution leads to non-uniform hardness distribution across the treated layer. In the present study, the influence of critical laser processing parameters constituting laser power, linear speed and rotary axis speed on treated layer depth and hardness distribution along the treated layer depth and length obtained

on cylindrical solid steel rod was analysed. Using COMSOL Multiphysics 5.5, FEM model was developed to simulate its thermal history and validate with the experimental results.

7.4.1 Simulation of stationary virtual laser beam by high-speed rotation

As the first task was to obtain a uniform laser-treated track of 4 mm width (equal to beam spot size) across its circumference, appropriate laser dwell time (LDT) needs to be optimized by simulating the model with different durations at an appropriate fixed parameters of Laser Power (LP) and rotary axis speed (RAS). Thus, the quasi-stationary beam with virtual ring dimensions of 12-mm diameter is obtained by determining LDT leading to hardened case covering the entire periphery. Keeping in view, the 16 mm^2 laser beam spot and the energy density consideration, LP and RAS were fixed at 2500W and 2000 RPM respectively. The single-spot processing with variation in LDT was simulated employing the FEM model developed with COMSOL Software. The LDT was chosen in a way that entire gamut of processing effects, ranging from no-hardening zone to commencement of melting was considered. The temperature solution field so obtained by transient thermal model on surface as well as subsurface across its cross-sectional thickness of the cylindrical rod had been utilized to predict the hardened region that could be realized in the sample run. Figure 7.5 illustrate cross sectional temperature contours at the center of the laser track obtained from simulation with variation in LDT ranging from 30 – 700 ms. A minimum 30 ms was required to complete one rotation of the laser spot enveloping the entire periphery of the 12 mm diameter rod. The demarcation for hardening and melting of the steel rod was visualized from the critical austenitization and melting temperatures of the steel (A_{c1} - 735^{0}C and T_m= 1493^{0}C).

It is clear from the simulated cross-sectional thermal contours depicted at Figure 7.5, at different LDTs, hardened case profile evolved depending on the surface temperature fluctuation along its circular periphery associated with heat accumulation due to high-speed rotation. All simulated temperature contours (radial direction) presented in the figures were taken at the center of the laser spot. An LDT of 30 ms constituting one single complete rotation (Figure 7.5(a)) could not raise the surface temperature (at any point) beyond Ac_1 (maximum surface temperature, Ts_{max} is 185^{0}C and minimum surface temperature, Ts_{min} is 130^{0}C) and as a result no hardening case be realized both in radial as well as lateral direction from simulation as well as experimental cross sectional case depth profile. With increase in LDT to 150 ms (Figure 7.5(b))

enabling five rotations, Ts_{max} increased to 925^0C and thereby emergence of hardened case is discernible, although not covering entire periphery. As the Ts_{min} was 580^0C, non-uniformity in hardened case development persisted. Indeed, heat accumulated was not sufficient to raise beyond Ac_1 at certain regions indicating no hardening effect. Similar non-uniformity in case depth could be observed from experimental case depth analysis. Only quarter portion of the cylinder hardened case depth can be observed from the Figure 7.5(b). Apparently, the cross-sectional case profile at the region of Ts_{max} indicated in Figure 7.5(b) showed a hardened case width of nearly 4 mm equating with the laser spot size dimensions. This evidently corroborates the model developed by applying the strategy (previously explained) for laser-beam profile-energy distribution converged well with actual applied one. With further increase in LDT to 310 ms (shown in Figure 7.5(c)), hardened case profile could entirely cover the periphery with maximum hardened case depth being 550 µm with Ts_{max} of 1250^0C and minimum case depth being 300 µm for Ts_{min} of 900^0C. This could be attributed to the sufficient heat accumulation and transfer through the cross-section of the steel rod (diameter of the rod being 12 mm) at LDT of 310 ms. The experiment result depicting case depth profile along its radial direction showed a case depth of 305 – 470µm. Luca Giorleo et al., [231] observed similar influence in their study involving high speed laser surface hardening process on cylindrical rods of different diameters modeled via the FEM approach and developed analytical model for predicting the temperature difference. It is analogous to the reported result on rod processed with 10mm diameter with rotational speed of 2100 RPM, the maximum surface temperature being about 1330°C and the temperature difference at the end of the process is 290°C form the simulation analysis. In fact, simulation results as per predicted analytical model of Luca et al., showed almost similar temperature differences by substituting our current parameters. With further increase in LDT to 700 ms, melting could be observed at some region owing to Ts_{max} reaching 1620^0C (T_m of steel being 1493^0C) as evident from the thermal contour depicted in Figure 7.5(d). Thus indicating a requirement of minimum 300 ms LDT with 2000 RPM rotational speed to obtain a virtual quasi-stationery laser beam of 12 mm diameter to obtain a continuous hardened case depth covering the entire periphery. However, if one can observe the hardened case depth distribution along its entire radial direction, a difference of 150 µm persists in all almost all cases. This could be attributed to the prevailing temperature gradient (difference between Ts_{max} and Ts_{min}) of 300 – 350^0C associated with practical limitation of the processing factors such as uniform rotation of

the rod with elimination of runout, surface finish, dynamic beam focusing etc. associated with rod material and its geometry.

Further, to decipher the evolution of hardened case profile, thermal profiles across different depths for a representative case of LDT with 310 ms depicted in Figure 7.6. It is clear that a minimum of more than ten rotations will enable effective laser dwell time to raise the surface temperature to nearly 1300^0C as evident from the peak temperature depicted in the graph Figure 7.6(c). From the figure, it is clear that even at a depth of 0.5 mm, the peak temperature realized was just below 700^0C indicating limitation of heat accumulation with temperature below critical austenitization range. Thus the surface temperature could be maintained in between critical austenitization and melting temperatures (Ac_1 and T_m) throughout its periphery across its 4 mm track width. As the temperature range maintained was well within 900^0C – 1250^0C, elimination of tempering as well as melting was possible. From the Figure 7.6(c), it is clear that a minimum three rotations amounting to 90 ms required to reach austenization temperature (A_{C1}) on that particular point of the surface. Thus with an LDT of 310 ms (shown in Figure 7.5(c)), hardened case profile could entirely cover the periphery with maintenance of austenitization temperature throughout its surface. Indeed, the effective thermal diffusion time (austenitization duration), a period involving LDT with subtraction of initial duration required for reaching A_{C1}, was observed to be 220 ms for covering the entire periphery of the rod with treated hardened case. Apparently, effective thermal diffusion time (austenitization period) evaluated form the graph was observed to about 220 ms. Indeed, the experiment result depicting case depth profile along and across its radial and lateral directions (Figure 7.6(b)) conducted with LDT of 310 ms on the steel rod showed a case depth of $305 - 470\mu$m. The result matched well with the FEM model developed with error falling within 8% indicating validation of the model. Convergent with the case profile dimensions revealed by macrograph, hardness distribution in the treated layer was also found to be in the range of $800 - 860$ HV$_{0.5}$ as against $220 - 240$ HV$_{0.5}$ of substrate with complete elimination of tempering effects. Thus, high-speed rotation of a square laser beam with top-hat energy intensity profile could facilitate processing with quasi-stationary beam with near virtual ring as reported in very few reports [231].

(a)

(b)

(c)

(d)
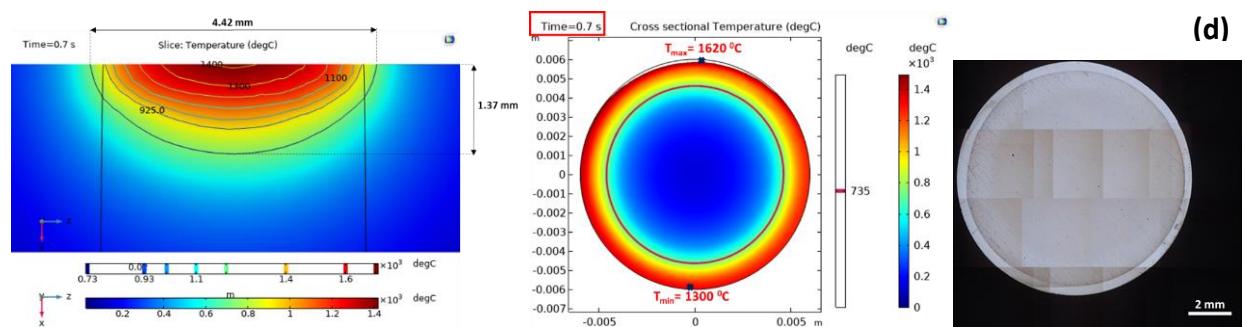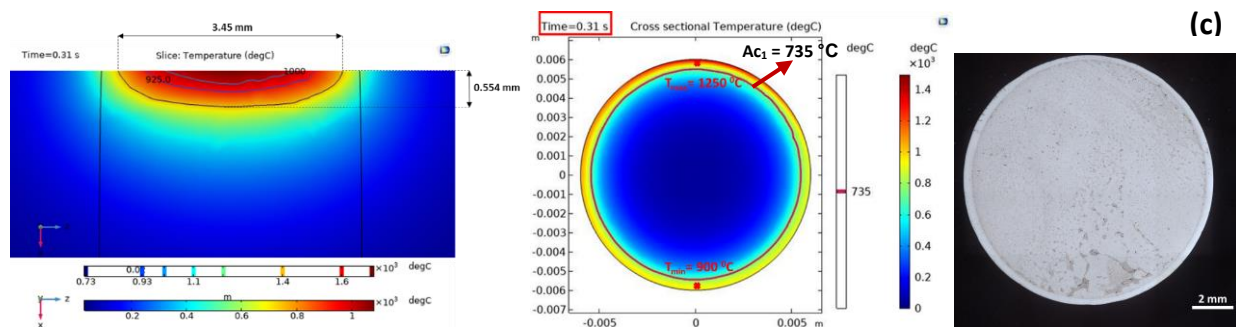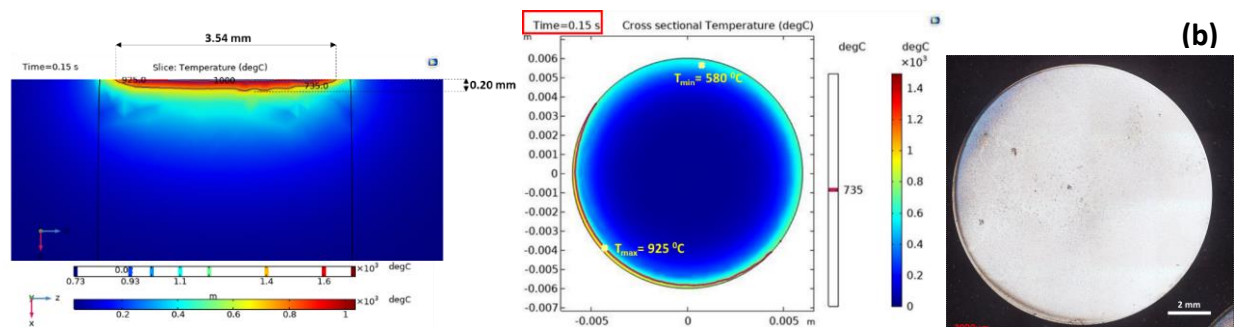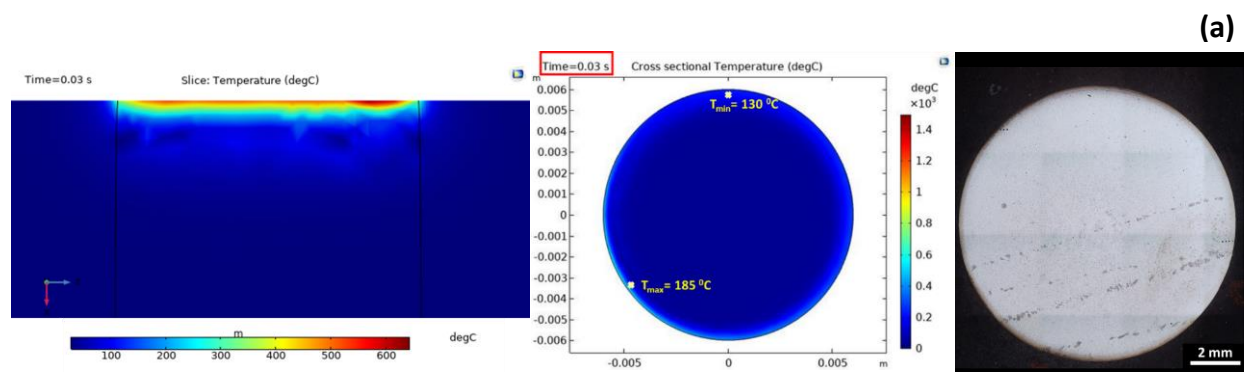
Fig. 7.5 Traverse and longitudinal cross sectional temperature contours with case depth profiles by varying dwell time with fixed laser power: 2.5kW (a) 0.03s; (b) 0.15s; (c) 0.31s; (d) 0.7s
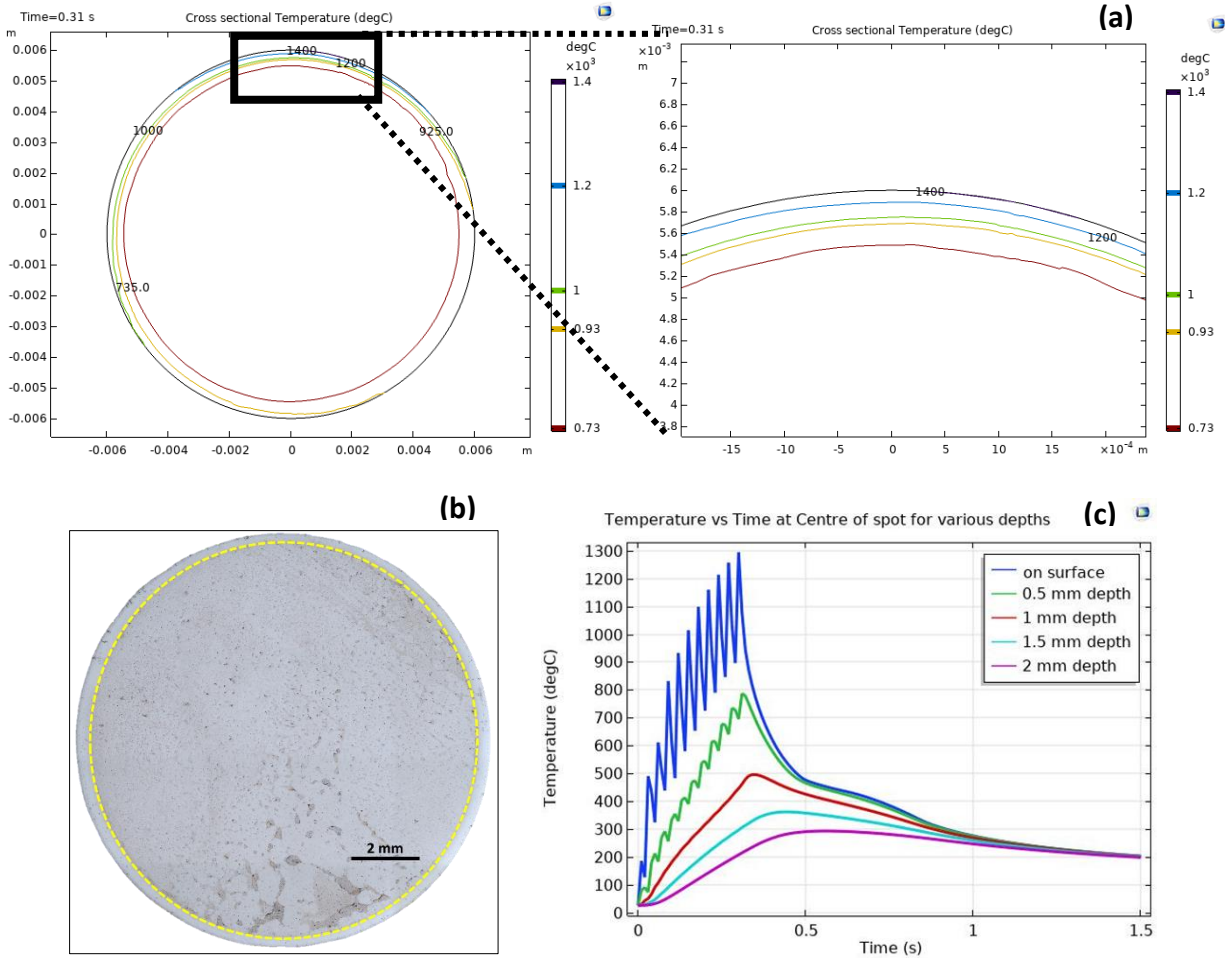
Fig. 7.6 Simulated and experimental cross sectional temperature contours obtained in the sample steel rod specimen processed with a fixed laser power: of 2.5kW, rotary axis speed of 2000 RPM and a LDT of 310 ms: (a) Various temperature contours obtained radially at center of laser spot ranging from surface to the depth of A_{C1} (b) Actual A_{C1} contour line (dotted line) obtained from the experimental result of the metallographically etched sample and (c) Simulated point graph at laser spot center with thermal profiles determined at different depths of the treated layer

7.4.2 Experimental details and characterization

Further to the FEM model developed and validated for high-speed laser processing with stationary square beam on solid cylindrical steel rod, experiments were carried out for processing

across its length by traversing the beam with Robot manipulation with pre-determined linear speed. Experiments were conducted on 12-mm diameter cylindrical steel rod with 50 mm length (En-31 steel whose chemical composition and base microstructure and hardness reported elsewhere [232]) with same setup as explained previously. Critical processing parameters such as laser power, linear speed and rotary axis speed were varied in specific range while other minor processing parameters and conditions being were kept constant. The model developed was also to ascertain influence of these process variables on the resulting quality of the hardened layer with their range of variation chosen based on optimized parametric condition developed on modelled single-spot quasi-stationary beam process and validated. Thus, a range of 2500 – 3500 W for laser power was chosen, restricting maximum surface temperature reachable to 1450^0C as per simulation. As the limitation of the rotary axis was 2000 RPM, two lower rotary axis speed levels constituting 1600 RPM and 1800 RPM were considered for experimental trials to assess its effect on hardness distribution across its processed length. Further to the optimum LDT of 310 ms required for single spot stationary beam processing (minimum hardened case depth of 300 μm), similar residual time for laser beam movement through the lateral traverse direction (along the length of the rod) has been considered. Calculation of this dwell time indicated requirement of linear speed lesser than 13 mm/s. As a result, 8–12 mm/s range in linear speed was considered for the experimentation.

The quality of the laser-hardened layer obtained can better be assessed by evaluating its case profile and its uniformity with hardness distribution. Thus, three important quantitatively determining quality factors, namely, Total Case Depth (TCD), Mean Hardness – Cross-sectional (MHC) and Differential Hardness – Longitudinal (DHL) were determined and evaluated. Figure 3.22 illustrate the schematic of these results analysed from the laser-hardened layer obtained along its length processed. Additionally, the surface hardened layer profile across its periphery was also assessed macroscopically in radial direction to assess case-profile uniformity. In order to analyze hardened case profile, samples after laser surface treatment were sectioned in both longitudinal and transversal cross sections using an EDM wire cutting machine and metallographic specimen mounts were prepared and then subjected to grinding and polishing employing standard metallographic procedures. These metallographic specimens were etched with 2%-Nital solution to reveal case profile and macrostructure. The macrostructures was observed using Opto-digital microscope at low as well as high magnifications as deemed fit.

Micro hardness distribution in the laser hardened layer across its longitudinal and cross-sectional directions was measured utilizing a diamond-indentor based Vickers Micro-hardness Tester (Walter UHL, VMHT 104) employing a 500 g load.

Hardened depth near the surface of the treated layer could be easily demarcated macroscopically from the unaffected core due to chemical reaction of etching associated with hard martensitic transformation (brighter being martensitic transformed region and darker being unaffected core). The critical boundary temperature determining Ac_1 ($T_{C1} = 735\ ^0C$) be realized in the macrostructure of the etched specimen as similar to that depicted in Figure 7.6 for processed sample using quasi-stationary beam with 310 ms LDT. Thus, TCD representing total hardened case-depth was evaluated, considering the boundary temperature of A_{C1} in the contour, and an average of five equidistant-readings along its processed length (same spatial position for all processed samples) was reported. MHC evaluated is a measure of average of all hardness values measured along its entire hardened cross-sectional depth with distance between indents being 50 μm. DHL is a qualitative feature determining hardness difference measured (between maximum and minimum) along its length of surface of the rod, obtained at a depth of 20 μm from the surface. Since the laser spot used was a square beam of 4 mm side, it was pertinent to consider hardness measurement up to 5 mm along the treated length with reporting of values obtained at central region. As significance of DHL is critical to evaluate hardness distribution uniformity along its longitudinal direction with minimization of its differential. Indeed reducing DHL to as minimum as possible is the principal aim to eliminate softening effects associated with induced temperatures and thermal diffusion effects of overlapping spiral tracks during high speed processing. Indeed, if linear speed increase beyond a limit that result in peak temperature at any point of surface below A_{C1} will drastically soften the case. Thus, response of DHL that depend on temperature distribution along its length determine the effective control of high-speed laser processing involving quasi-stationary laser beam. Indeed, the hardened case profile that evolve due to quasi-stationery beam process adopting high-speed rotation is analogous to the processing of the steel rod with a ring-shaped laser beam (equivalent to the diameter of the rod). As a result, TCD that will be obtained in longitudinal direction of the processed rod will be similar to that of quasi-stationary beam processing but with variation in hardness distribution because of varied overlapping effects associated with the dynamics of the moving laser beam and its linear speed.

7.4.3 Validation of experimental results with FEM Model

Further to understand the influence of processing parameters on the quality of the laser surface hardened layer in terms of case depth and hardness distribution along its longitudinal surface, transient thermal model developed using COMSOL, explained previously, for stationary beam processing has been extended by traversing the laser beam along its length. The FEM model was developed coupling temperature-dependent properties of steel under designated boundary conditions with movement of laser beam using moving mesh. The transient evolution of the temperature distribution on surface during the treatment process by varying laser power, linear speed and rotary axis speed are shown in Figs. (7.7 and 7.8). Only central region of the rod was considered to plot thermal profiles to avoid deleterious effects of laser power acceleration and deceleration during starting and ending of the process during laser processing. The red line delineation indicates the Ac_1 critical austenitization temperature limit of 735^0C for EN31 steel. Indeed, it is known that drop in surface temperature at any point along its length below A_{C1} will lead to softening.

The validation of the temperature distribution history obtained through simulation of the treated layer co-related quantitatively with resulting experimental output of total hardened layer depth termed as TCD, measured at specific central region of treated layer along its length. As previously defined for stationery beam process explained previously, TCD was determined from the simulated thermal contour with delineation of boundary of A_{C1} temperature. The hardness distribution in the treated layer was qualitatively assessed across its depth and along its length in terms of Mean Hardness Cross-sectional - MHC and differential hardness longitudinal − DHL. **Table 7.6** depicts comparison of experimental output parameters (evaluated from macrostructure analysis and hardness measurements of metallographic samples of the processed sample rods) with simulated temperature contours in terms of surface, peak and critical transformation temperatures. The TCD was evaluated from the depth of the simulated layer obtained with position of the demarked A_{C1} temperature contour line, whereas, DHL was co-related with the temperature differential - ∇T evaluated from the difference in temperature of maximum and minimum at the surface during processing along with the frequency of points on the surface attaining temperature below that of A_{C1}. MHC was co-related with maximum temperature attained through the case layer depth simulated. The criteria for assessing these quality

parameters are convergent with various reported studies involving correlation of defining temperature contours in the simulated layers of steel, more specifically, A_{C1} boundary, peak and critical austenitization temperatures in single-track processing employing wider beam spots and temperature differential in multi-track processing with overlapping [232-236]. Indeed, TCD assessed from the FEM simulated temperature distribution profiles correlated well with the experimental values with error falling below 8%.

7.4.3.1 Effect of laser power

The transient evolution of the temperature distribution field sweeping the surface at different laser powers (2500-3500 W) during the surface treatment process are shown in Figure 7.8. It clearly illustrates variation in surface temperature distribution along the central region of the length of the rod (25mm) with variation in laser power employed. Indeed, maximum surface temperature (T_{Smax}) and minimum surface temperature (T_{Smin}) was fluctuating between 1045^0C and 920^0C and thereby leading to a temperature differential (∇T) of 125^0C in case of the rod processed with laser power of 3500 W. With decrease in laser power to 2500W, T_{Smax} and T_{Smin} was fluctuating between 900^0C and 750^0C with a temperature difference of 150^0C. Despite with reduction in laser power from 3500 W to 2500 W, ∇T enhanced marginally from 125^0C to 150^0C, indicating no significant influence on uniformity in hardness distribution. Apparently, it is evident from the surface contour profiles, there is no point going down below A_{C1} indicating complete elimination of any tempering effect throughout its treated surface length. Thus the steel rod processed with high rotary axis speed of 2000RPM and low linear speed of 8 mm/s could eliminate deleterious softening effect that generally occur when processed with low rotary axis speed. In a similar study involving simulation of temperature history and its validation employing multi-pass laser hardening process on steel, the temperature differential in austenitization temperatures at surface visualized hardness distribution in the overlapped region [235, 237-239]. From the experimental values of TCD and MHC depicted in Table 2 for varying laser power, it is clear that TCD increased from 170 µm to 330 µm and MHC increased from 768 $HV_{0.5}$ to 864 $HV_{0.5}$ with laser power from 2500W to 3500W. This is obvious since increase in heat input increases heat penetration and thereby deeper shift into the A_{C1} as well as increase in maximum temperature point through the depth of the hardened layer. Indeed, assessing TCD from the simulated thermal history with identification of A_{C1} boundary matched well with

experimental values with error falling within 8%, as similar to that previously observed in stationary laser beam processing. Apparently, simulated contour profiles corroborated that maximum austenitization temperature through the depth of the layer increased from 900^0C to 1045^0C with increase in laser power from 2500W to 3500W. Similar effects of case depth and hardness distribution through its case depth with heat input were observed in a reported study involving high speed laser surface hardening of steel rod involving apparent spot technique [231].

The effect of laser power on longitudinal hardness distribution along the length of the rod surface determined in terms of DHL was minimal as evident from its value ranging from 55-63 $HV_{0.5}$, depicted in Table 7.6. This effect could be attributed, not only to the marginal difference in ∇T (125 – 150^0C) observed from the simulated contours, but also maintenance of surface temperature always above A_{C1} throughout its processed length. Apparently, with increase in laser power from 2500W to 3500W, $T_{S\text{-min}}$ increased from 750^0C to 920^0C accompanied with higher regularity in surface contour profiles as evident from Figure 7.7. Furthermore, this factor of retaining surface temperature, well above A_{C1}, throughout its process length, indicates effective control of thermal heat dissipation and rate of cooling necessitated with high speed rotation and thickness of the steel rod. It appears that the chosen parameters utilized for 4 mm wide laser spot entails minimal heat dissipation effects and thereby minimal influence of laser power on hardened case.

This can further be explained by considering that increase in laser power increases thermal diffusion time into the steel rod but at the same time restricts its rapid self-quenching effect, governed by the diameter of the rod and thereby case depth and its hardness distribution. In similar studies involving co-relation of simulated thermal history (maximum austenitization and surface temperatures) with actual hardness distribution results of steel, increase in laser power directly enhanced hardness with minimized variation and attributed to enhanced effective thermal diffusion time and cooling rate [232, 240]. Overall, the influence of laser power on experimentally defined DHL qualitatively matched well with simulated thermal profile. Increase in laser power reduced the temperature difference leading to a lowering of DHL, analogous to the effect of thermal diffusion distance in the overlap region of multi-pass laser hardening process [235].

Table 7.6: Experimental results of TCD, MHC and DHL obtained in laser treated layers processed with different processing conditions vis-à-vis comparison with simulated thermal history parameters

Laser Power (W)	Rotary axis speed (RPM)	Linear speed (mm/s)	Experimental			Simulation				Error
			TCD (µm)	MHC ($HV_{0.5}$)	DHL ($HV_{0.5}$)	TCD (µm)	T_{s-max} (^0C)	T_{s-min} (^0C)	Temp diff. (^0C)	TCD
2500	2000	8	170	768	63	181	900	750	150	6.1%
3000			270	825	58	295	945	800	145	8.0%
3500			330	864	55.25	350	1045	920	125	5.7%
3500	1600	8	370	832	163	381	1100	700	400	2.8%
3500	1800		350	859	89	365	1050	700	350	3.9%
3500	2000	12	150	705	79	159	980	780	200	5.6%
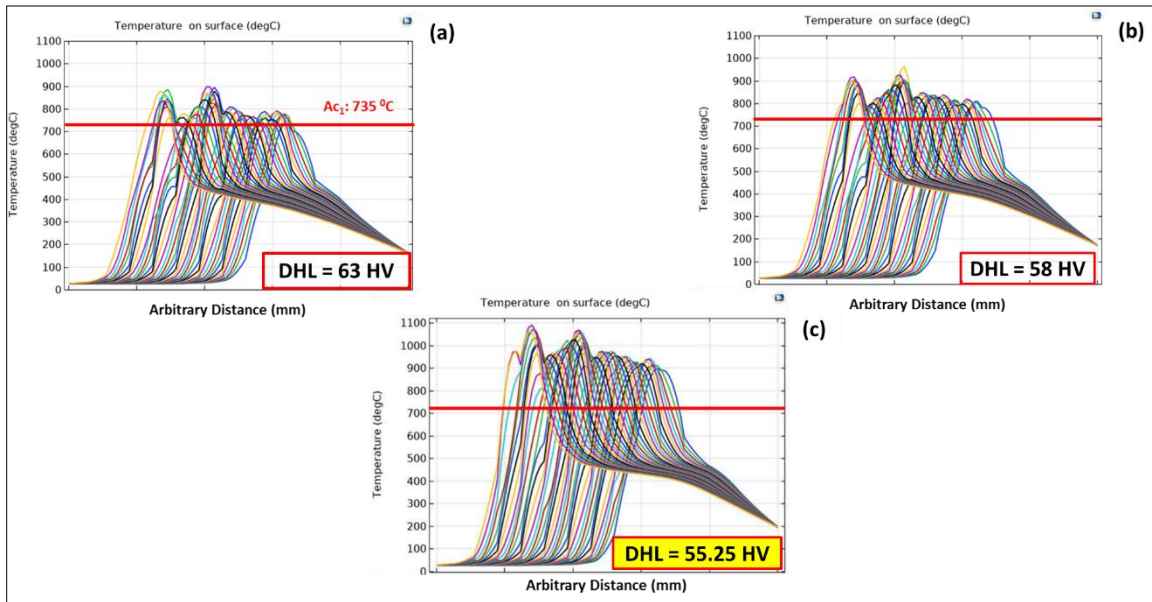
Fig.7.7 Temperature profiles on surface of the cylindrical rod at different locations by fixing Rotary Axis Speed: 2000 RPM, linear speed: 8mm/s & varying laser power (a) 2500 W (b) 3000 W (c) 3500 W

7.4.3.2 Effect of linear speed and rotary axis speed

To validate the proposed model, quantitative prediction of surface temperature distribution along the length of treated rod and thermal diffusion length governed by A_{C1} boundary with variation in RPM and linear speed was simulated with thermal history and co-related with their respective experimental values of TCD and DHL. Figures 7.8 and 7.9 illustrate transient evolution of the temperature distribution field as well as surface contours sweeping the surface at different rotary axis speeds (1600 – 2000 RPM) and linear speeds (8 and 12 mm/s) during the surface treatment process.
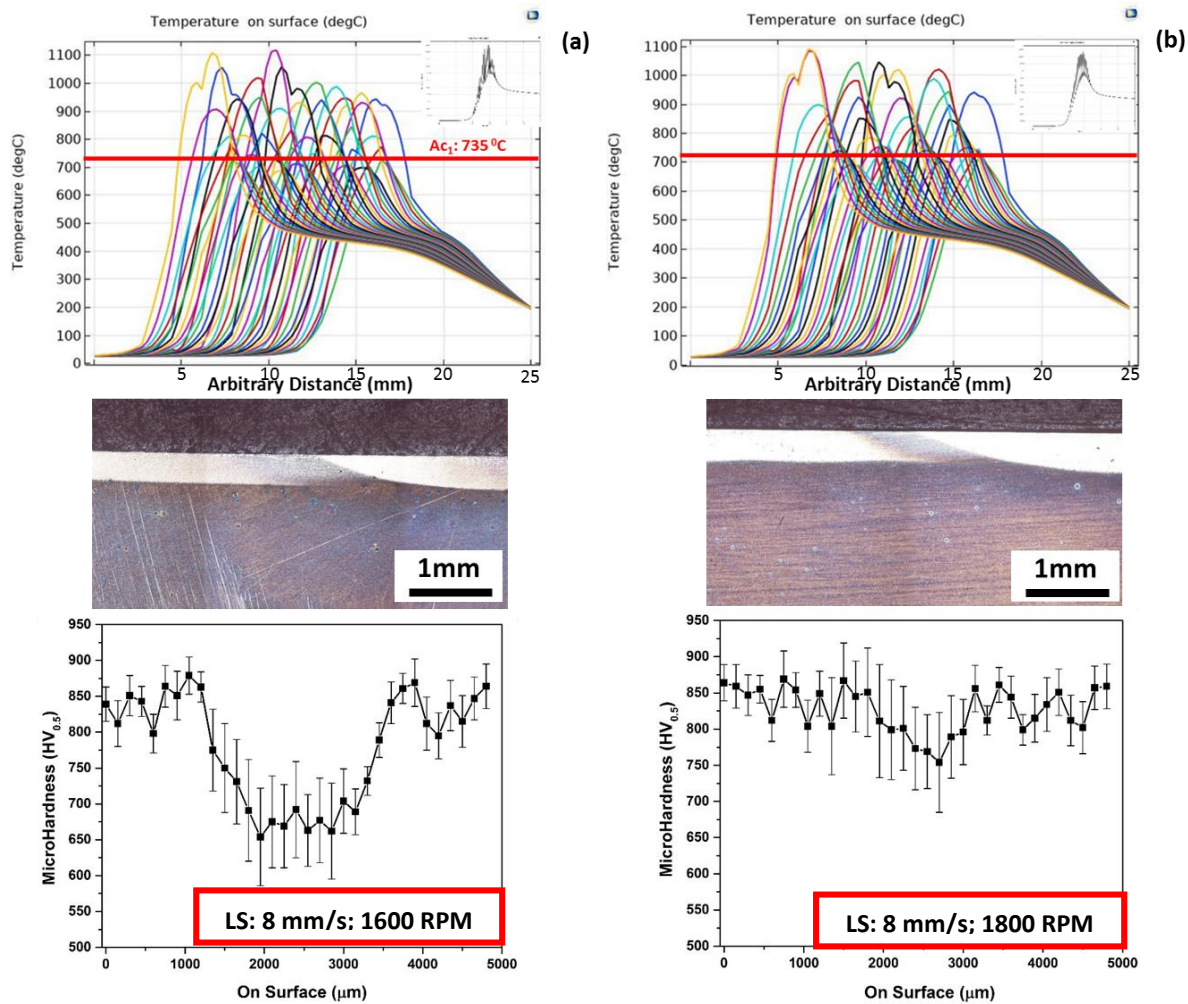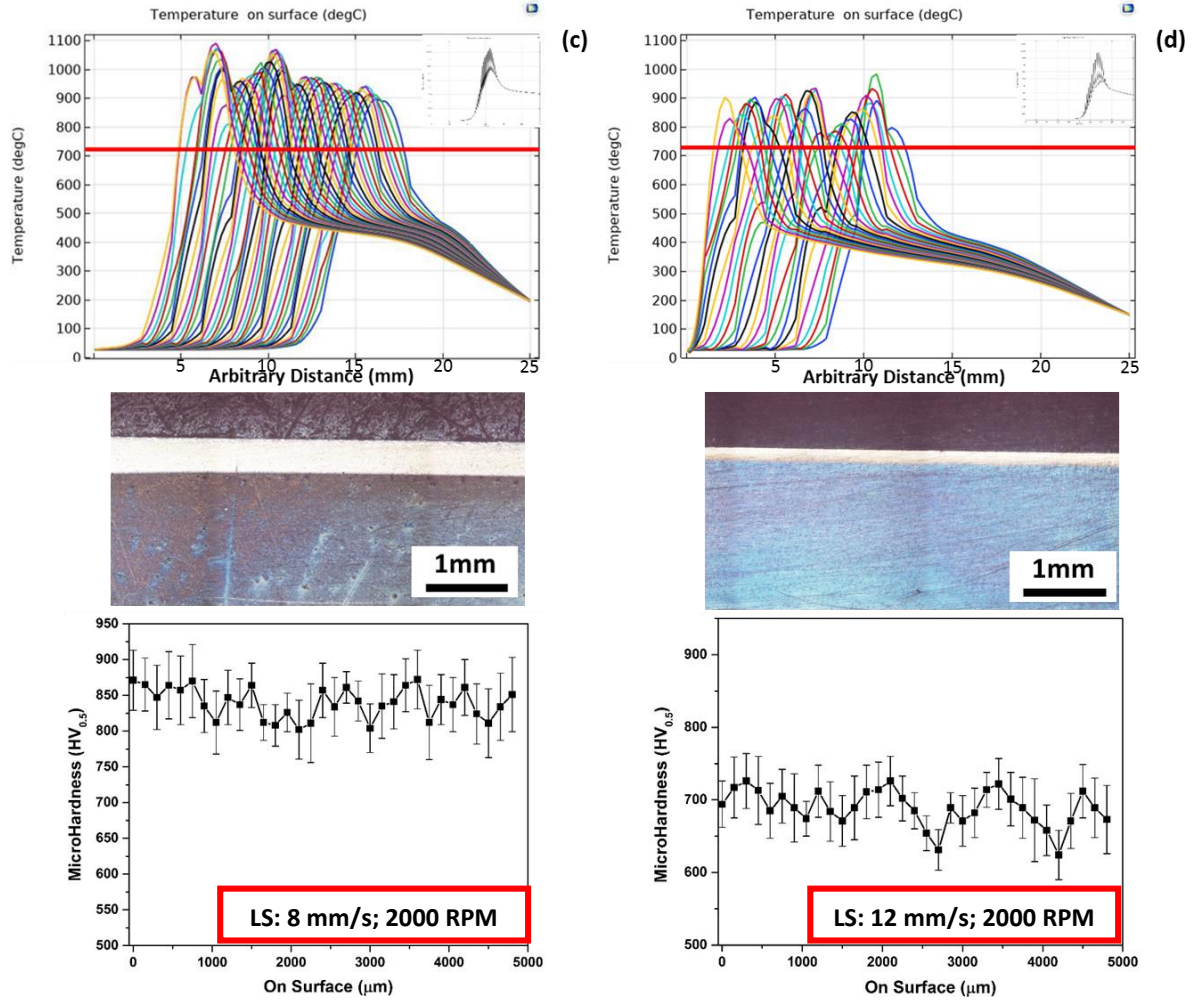
Fig.7.8 Temperature profiles on surface of the cylindrical rod at different locations by fixing LP:3.5 kW, Linear speed: 8mm/s & varying rotary axis speeds (a) 1600 RPM (b) 1800 RPM (c) 2000 RPM (d) 2000 RPM @ 12 mm/s; cross-sectional macrographs; surface hardness distribution

Figure 7.8 (a-c) indicate variation in surface temperature distribution along the central region of the length of the rod (25mm) processed by fixing laser power of 3500 W, linear speed of 8 mm/s and varying rotary axis speeds from 1600-2000 RPM. It is known that drop in surface temperature at any point along its length below A_{C1} will lead to softening and its extension determined by the thermal diffusion distance governed by rotary axis speed. It is clear that greater uniformity in temperature distribution persisted on the surface processed with 2000 RPM (Figure 7.8c)) when compared to those processed with 1600 and 1800 RPMs. Indeed maximum surface temperature (T_{Smax}) and minimum surface temperature (T_{Smin}) was fluctuating between

1045^0C and 920^0C and thereby leading to a temperature differential (∇T) of 125^0C in case of the rod processed with 2000 RPM. Whereas, in case of 1600 RPM and 1800 RPM rotary axis speeds (thermal contours of Figure 7.8 (a) and (b)), one-third of their peak points were falling below 735 ^{0}C envisaging significant tempering effect associated with insufficient overlapping of circular scanning tracks. Indeed, large DHL values to the tune of 163 HV$_{0.5}$ and 91 HV$_{0.5}$ were observed in both of the processed samples. Thus, higher the ∇T, greater was the non-uniformity in hardness distribution along its length associated with the frequency of surface temperature falling below the critical austenitization level leading to tempering effects. Thus with increase in rotary axis speed from 1600 to 2000 RPM, DHL reduced from 163 HV$_{0.5}$ to 56 HV$_{0.5}$ in conjunction with reduction in ∇T from 400^0C to 125^0C. As such, from the contour graph (Figure 7.8(c)), it is clear that no point on the surface exhibited fall in temperature below A$_{C1}$, thereby eliminating any softening effect. The trend in variation of experimentally determined values of DHL with variation in speeds of linear and rotary axes were convergent with estimated ∇T values from the simulated profiles envisaging FEM model validation. Thus, least DHL of 55.25 HV$_{0.5}$ could be realized in treated layer processed with 2000 RPM and 8 mm/s linear speed, convergent with minimal temperature differential of 125^0C indicating good co-relation between the predicted FEM-model with experimental results. Thus, optimum processing condition with high rotary axis speed entails elimination of overlapping softening effects in high-speed laser surface-hardening process. Similar influence of controlling surface temperature uniformity along the length of the laser quenched cylindrical rod was found to be governed by the evolving thermal history simulated, although temperature maintenance was carried out by controlling scanning speed [236].

The cross-sectional macrographs of hardened rod coupons depicted in Figures 7.8 (a-d). In Figure 7.8(a), a larger tempered region could be observed in hardened depth of steel rod (in longitudinal direction) due to the influence of insufficiently lower rotary axis speed of 1600 RPM. With increase in rotary axis speed to 1800 RPM (Figure 7.8(b)), significant reduction in tempered softened zone (determined by reduction in hardness) could be observed. This could be comparable with the thermal contours, wherein, one-third of their peak points were falling below 735°C envisaging significant tempering effect associated with ineffective thermal diffusion of circular scanning tracks. On the other hand, a minimum variation of heat-treated depth of

material be observed with negligible tempered region in treated case processed with a higher rotary axis speed of 2000 RPM, as shown in Figure 7.8(c). Similar aspect of negligible tempered region was observed with reduced case depth when processed with higher scanning speed of 12 mm/s and rotary axis speed of 2000 RPM. The measured surface hardness for various conditions are presented in Figures 7.8(a-d). In lower rotary axis speeds conditions of 1600 and 1800 RPM, significant variation of surface hardness be observed due to temperatures at those particular points falling below A_{C1} and thereby entailing subsequent tempering effects. In hardness profiles of Figures 7.8(a-b), the tempering effect (Ts < A_{C1}) could easily be identified due to generation of tempered martensite structure (clear contrast variation in cross-sectional macrograph be noted) that results in a significant hardness reduction. In Figures 7.8(c-d), a uniform hardness distribution along its treated surface (longitudinal) is discernible. In this case, it is clear that no point on the surface exhibited fall in temperature below A_{C1}, thereby eliminating any softening effect contributing to a minimum variation in surface hardness.

Furthermore, comparing surface temperature profiles predicted from FEM model for rod processed with linear speeds of 8 mm/s and 12 mm/s (Figures 7.8 (c) and (d)), despite no softening effect, non-uniformity in hardness distribution on surface increased with increase in linear speed that could be attributed to enhancement in thermal diffusion distance. Indeed, temperature differential ∇T got increased from $125^{0}C$ in rod processed with 8 mm/s to $200^{0}C$ in rod processed with 12 mm/s. As no drop in temperature below A_{C1} realized at any point on the surfaces, no softening effect observed due to elimination of overlapping tempering effect. As such, T_{Smax} and T_{Smin} temperatures for the case processed with 8 mm/s ($1045^{0}C$ and $920^{0}C$) were high as compared to that processed with 12 mm/s ($980^{0}C$ and $780^{0}C$). Total case depth also doubled (330 ± 10 μm as per experimental value) in case of the rod processed with 8 mm/s linear speed to that processed with 12 mm/s (150 ± 10 μm as per experimental value). This is obvious due to increase in linear speed reduces laser interaction time and thereby high heat penetration into the steel substrate (analogous to the ring-shaped laser beam scanning). In other words, enhancement in surface temperature with reduction in linear speed will obviously enhances the case depth. Similar effects of case depth with laser scanning speed were reported in studies involving laser surface hardening process and their co-relation with simulated FEM models [232-233, 240-241]. Indeed, experimental DHL values of $56HV_{0.5}$ and $79 HV_{0.5}$ for the cases of 8 mm/s and 12 mm/s corroborated the evolution of thermal history as per FEM model and

validated. On the whole, coupling FEM model with experimental validation help facilitated in understanding influence of processing parameters on the resulting quality of the hardened layer in high-speed laser hardening process.

Figure 7.9 exhibits surface temperature contours simulated at different locations of the steel rod developed with FEM model and processed with optimized parameters (obtained from experimental result of min. DHL) constituting laser power of 3500 W, linear speed of 8 mm/s and rotary axis speed of 2000 RPM. Indeed, uniform thermal effect (color contrast variation) with surface temperature maintained within the range of 920^0C– 1045^0C throughout its processed length validate the FEM model for optimizing the process with complete elimination of softening of the treated layer. The cross-sectional macrographs in longitudinal as well as in radial direction of the rod experimented with optimized parameters, depicted in Figure 7.10, also matched with the hardened case profile in both longitudinal and radial directions. Indeed, measured total case depth values along axial and longitudinal direction varied between 330 – 360 μm and 325 – 450 μm respectively. Furthermore, cross-sectional hardness profile of treated sample rod, depicted in Figure 7.10(c), illustrated a hardness variation of 840 – 870 $HV_{0.5}$ within its depth of 360 μm as against its unaffected core whose average hardness was 230$HV_{0.5}$. The differential hardness along its treated layer surface showed minimal variation along its length and depth and co-related well with the simulated temperature differential maintained. Similar control in temperature uniformity along the length of the laser hardened cylindrical rod has been reported by Sagar V. Telrandhe et al., [242] but they maintained temperature uniformity by controlling heat input instead of rotary axis speed. Indeed, error difference in case depth within 8% could be realized between the simulation and experimental validation. Overall, qualitatively, excellent agreement could be visualized between the actual experimental values determining case and hardness profiles with that of predicted ones of the developed FEM model.
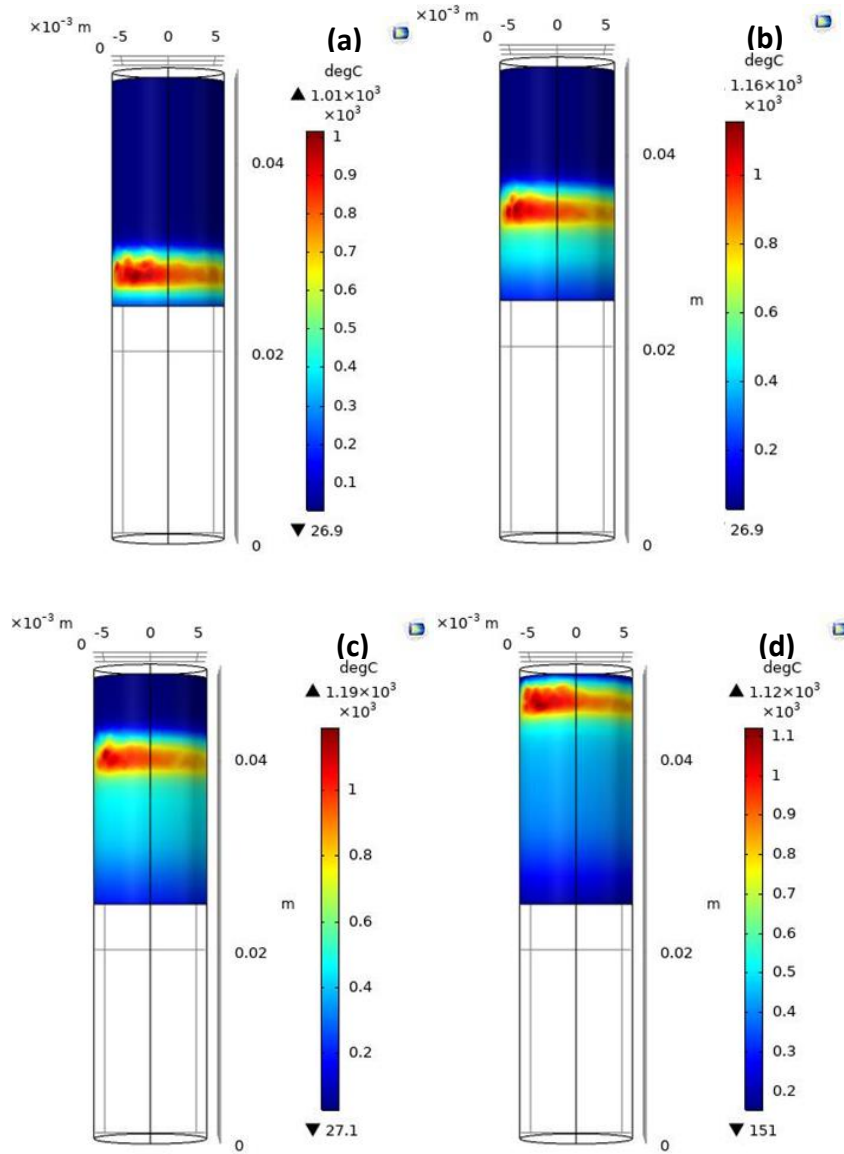
Fig.7.9 Surface temperature contours at different locations (a) 29mm (b) 35mm (c) 41mm (d) 47mm @ LP:3.5 kW, Linear speed: 8mm/s; 2000 rpm
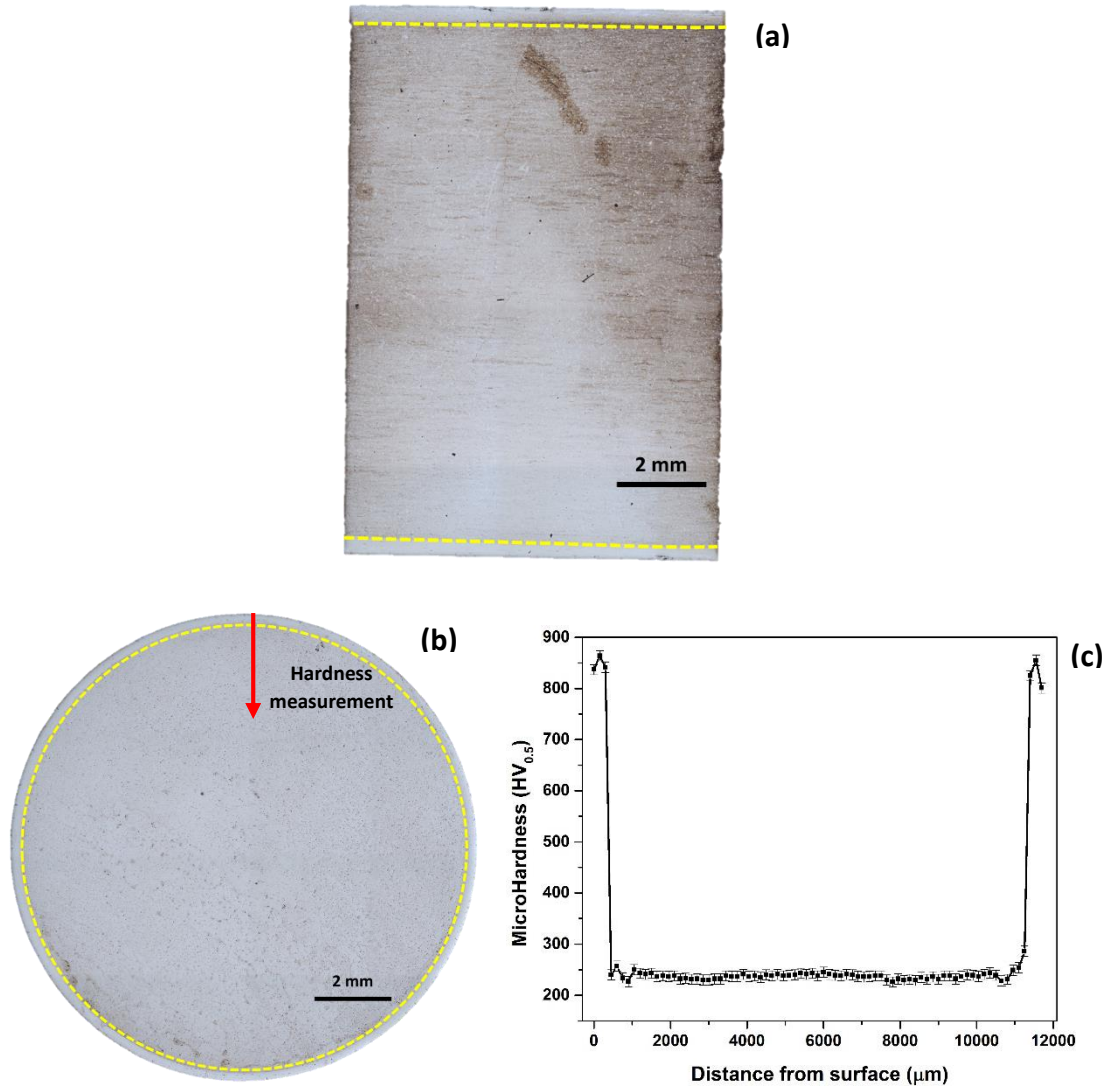
Fig.7.10 (a) Longitudinal and (b) Cross-sectional Macrographs and (c) hardness distribution profile along the depth of the steel rod processed at Laser power - 3.5 kW, Linear speed – 8 mm/s and Rotary Axis Speed - 2000 RPM

7.5   Summary

From the simulation and experimental studies conducted by employing different modes of laser surface hardening on thin sectioned plates, better control in heating cycle and surface temperature with retention of core properties was observed in sample processed with PW mode of processing when compared to CW mode. Using COMSOL Multiphysics, the hardened depth and temperature developed with various modes of processing by varying laser power predicated well and validated with the experimental data.

In the study involving simulation and experimental validation on the effect of varying pulse duration and laser power, case profiles matched well the simulated temperature contours, as far as HZ and HAZ depths and widths concerned. From the above work, results indicated that with increase in laser power and fixed pulse duration of Pulse-On time of 50 ms and Pulse-Off time of 50 ms, depth and width of hardened zone and hardness distribution has improved in the treated layers. The HZ and HAZ dimensions predicted from the model were found to be in good correlation with the experimental data. Another set of experiments by fixing laser power and varying pulse duration i.e. pulse on and off time, higher improvement in depth and width of hardened zone with marginal improvement in hardness observed in treated layers same reflected from simulation thermal analysis.

The FEM model was utilized to optimize the high-speed quasi-stationery laser surface hardening process on solid cylindrical steel rod of En-31 with 12 mm diameter.. Effect of three critical processing parameters, namely, Laser Power, Linear Speed and Rotary Axis Speed on the quality of laser hardened layer in terms of total case depth (TCD) and hardness distribution, namely - Mean Hardness - Cross-sectional (MHC) and Differential Hardness − Longitudinal (DHL) were investigated and assessed. Following conclusions are drawn:

(a) There exists an optimum processing parameter range over the investigated range of processing conditions (2.5-3.5 kW laser power, 8-12 mm/s linear speed and 1600 − 2000 RPM rotary axis speed) determined by the cylindrical steel rod diameter and laser spot dimensions, over which a uniform hardened layer could be achieved with high-speed rotation with complete elimination of softening effect associated with overlapping of circumferential tracks.

(b) There exists an optimum laser dwell time determined by thermophysical properties, diameter of the steel rod and the laser spot dimensions (multi-mode square beam of 4 mm x 4 mm) that limit the case possible to harden with uniform hardness distribution possible.

(c) The simulated temperature distribution as per FEM model facilitated in quantitatively assessing its case depth with hardness distribution influenced by the critical processing parameters of laser power, linear speed and rotary axis speed. Indeed optimum processing conditions indicate usage of 2000 RPM with laser power and linear speed being in the

range of 2.5 -3.5 kW and 8-12 mm/s respectively required to maintenance surface temperature above critical austenitization range through its treated depth with complete elimination of softening due to inter-track tempering and melting.

(d) Indeed evaluation of temperature differential from the temperature distribution contours of the numerically simulated FEM model helped to assess hardness distribution in the treated layer surface along its processed length.

(e) Within the range of parameters experimented on the steel rod (1600 – 2000 RPM, 8 -12 mm/s Linear Speed and 2.5 – 3.5 kW Laser Power), depth of treated layer and its uniformity in hardness distribution is influenced by rotary axis speed, linear speed and laser power, necessarily in that order.

(f) Assessing temperature history by FEM model with evaluation of surface temperatures, maximum/minimum surface temperatures, temperature differential and temperature distribution in longitudinal as well as axial directions through the rod length and thickness help facilitated in validating the simulated model with experimental results in terms of hardened case depth and hardness distribution through its treated case (in both transversal and radial directions) with quantitative assessment of simulated thermal history with optimum conditions entailing differential hardness of 56 – 58 HV with an error difference of less than 8% in case depth.

(g) In conclusion, it is clear that FEM model developed with simulation of the process help facilitated effectively in optimizing the process to obtain maximum hardened layer throughout its processed length with greater uniformity in hardness distribution and complete elimination of deleterious softening and melting effects.

It is believed that the numerical approach of FEM model proposed and its validation with experimentation is an appropriate way to optimize the laser surface hardening process for assessing the hardened layer profile and optimizing the process for applying on simple flat and round geometrical configuration and bearing elements such as rollers.

CHAPTER 8

Statistical Analysis and Multi Objective Optimization of High Speed Laser Surface Hardening Process of Cylindrical Components by Means of RSM and Desirability Approach

8.1   Introduction

Although in the previous section, simulation with validation of FEM model of cylindrical rod of bearing steel proved successful, the dynamics of the effect of critical processing parameters on the resulting hardened case profile and hardness distribution remained as a challenge to understand comprehensively. Indeed, the dynamic spatial changing of the laser-beam spot interaction with steel rod and laser beam intensity profile makes the process very difficult to understand and thereby envisaging the need to conduct numerous experimentation with wide range of variation in processing parameters and analyses. This paves the way to develop suitable mathematic model with statistical analysis and multi-objective optimization approach. In pursuance to understand these complex phenomena of laser surface hardening of bearing steel cylindrical rod and get quick response on the influence of critical processing parameters on the quality of laser-hardened layer, a statistical method presented in this section with an aim to optimize the process utilizing response surface methodology (RSM). The three-factor with three-level Box-Behnken design available in RSM was used to develop the regression model with a multi-objective optimization technique to optimize the process parameters such as laser power, linear scanning speed and rotary axis speed on attaining maximum case depth, maximum mean hardness along hardened layer depth and minimum differential hardness across the longitudinal section of the hardened layer on the solid bearing steel rod.

8.2   Design of experimentation using Box-Behnken methodology

To validate the developed mathematical model, experiments were conducted on a 12 mm diameter cylindrical EN31 bearing steel rod of 50 mm length (chemical composition and base microstructure and hardness reported in Chapter 3) with same setup as explained previously. Critical processing parameters such as laser power, linear speed and rotary axis speed were considered as variables, while, other minor processing parameters and conditions kept constant. As the aim of the model was to ascertain influence of these process variables on the resulting quality of the hardened layer, its variation was chosen based on the optimized parametric condition developed on single-spot quasi-stationary beam process modelled and validated previously (reported in Chapter 7). Thus, a range of 2500 – 3500 W for laser power and 1600 – 2000 RPM for rotary axis speed has been chosen for developing the statistical model. Further to the optimum LDT of minimum 0.31 s required for single spot stationary beam processing (minimum hardened case depth of 300 μm), similar residual time for laser beam movement through the lateral traverse direction (along the length of the rod) has been considered. Calculation of this dwell time indicated requirement of linear speed lesser than 13 mm/s. As a result, 8 – 12 mm/s range in linear speed was considered for the RSM design of experimentation. Table 3.5 illustrate the range of these three factors with three-level design considered for development of the RSM model.

As it is well known that quality of the laser-hardened layer obtained can better assessed by its case depth and hardness distribution, three different responses constituting Total Case Depth (TCD), Mean Hardness – Cross-sectional (MHC) and Differential Hardness – Longitudinal (DHL), as previously explained in chapter 7 were evaluated. Figure 3.22 illustrate the schematic of these three responses analysed from the resulting laser hardened layer obtained along its length processed. Additionally, the surface hardened layer profile across its periphery was also assessed macroscopically in radial direction to assess case-profile uniformity. In order to analyze hardened case profile, samples after laser surface treatment were sectioned in both longitudinal and transversal cross sections using an EDM wire cutting machine and metallographic specimen mounts were prepared and then subjected to grinding and polishing employing standard metallographic procedures. These metallographic specimens were etched with 2%-Nital solution to reveal case profile and macrostructure. The macrostructures was

observed using Opto-digital microscope at low as well as high magnifications as deemed fit. Micro hardness distribution in the laser hardened layer across its longitudinal and cross-sectional directions was measured utilizing a diamond-indentor based Vickers Micro-hardness Tester (Walter UHL, VMHT 104) employing a 500 g load.

As hardened depth near the surface of the treated layer can be easily demarcated macroscopically from the unaffected core due to chemical reaction of etching associated with hard martensitic transformation (brighter being martensitcally transformed region and darker being unaffected core), its boundary temperature can be realized to be Ac_1 ($T_{C1} = 735$ ^0C) as depicted in Figure 7.6. Thus, TCD representing hardened case depth was evaluated considering the boundary of A_{C1} and average of five readings along its processed length was reported. MHC evaluated is a measure of average of all hardness values measured along its entire hardened cross-sectional depth with distance between indents being 50 μm. DHL, a qualitative feature that determines hardness distribution uniformity along the surface of rod, is a measure of difference between maximum and minimum micro-hardness values obtained along the treated layer at a depth of 20 μm from the surface and a length of 5 mm. Since the laser spot used was a square beam of 4 mm side, it was pertinent to consider hardness measurement up to 5 mm along the treated length with reporting of values obtained at central region. As significance of DHL is critical to evaluate hardness distribution uniformity along its longitudinal direction with minimization of its differential. Indeed reducing DHL to as minimum as possible is the principal aim to eliminate softening effects associated with induced temperatures and thermal diffusion effects of overlapping spiral tracks during high speed processing. Indeed, if linear speed increase beyond a limit that result in peak temperature at any point of surface below A_{C1} will drastically soften the case. Thus, response of DHL that depend on temperature distribution along its length determine the effective control of high-speed laser processing involving quasi-stationary laser beam.

As the aim of the study is to develop the statistical mathematical model by adopting RSM methodology, all three responses (TCD, MHC and DHL) were analysed and co-related with their parametric effects to generate regression equations. Multiple regression was fitted with response data by analyzing statistical significance test on the model coefficients and lack-of-fits. Experiments were carried out by utilizing three-factor with three-level BBD design available in

Design Expert software. The significance of the developed model was analysed by analysis-of-variance ANOVA technique [243, 244]. All fifteen experiments conducted as per matrix designed were analysed and checked for the significance of all the three parameters and assess their interaction with responses and their interaction for adequacy. The developed regression model in each case was steered to the design space with statistical analysis for higher F value and smaller p-value. Perturbation plots along with surface and contour plots were drawn in each case for all three responses (TCD, MHC and DHL) along with their corresponding interaction effects. Finally, numerical optimization using desirability approach [245] was carried out that steer to establish optimal combination of parameters that fulfil multi-objectives of the process such as maximizing TCD and MHC and minimizing DHL. Thus, the predicted values obtained from the all the three responses with optimization approach was validated from final experimental tests conducted and compared. Furthermore, results were compared with FEM model developed for the process by induction of laser movement in the already developed FEM model employing quasi-stationary single spot laser processing.

8.3 Statistical Analysis of Results

Table 3.6 depicts three responses (TCD, MHC, DHL) considered to evaluate the quality of the hardened layer obtained on the treated surface of the steel cylindrical solid rod using laser processing parameters constituting laser power, linear speed and rotary axis speed varied at three levels as per the design of experimentation of RSM approach. A sum of fifteen experiments were conducted as per the matrix arrived by 3-factor with 3-level Box Behnken design. Analysis of Variance (ANOVA) in stepwise mode was performed to identify the significance of each parameter's effect on the three output responses. Furthermore, its significance on linear and quadratic effects of the parameters and their interactions with model adequacy checked. The multiple regression model developed was based on the collection of statistical technique with defined polynomial expressions reported from various studies reported in literature [246]. The coefficients of the model were predicted through regression analysis based on the three chosen responses. The sequential F-test, lack of fit test and other adequacy measures were used to assess the fit of the model. The p-values were computed by means of ANOVA of the model and each term in the model if do not exceed the level of significance (α=0.05) then it was considered adequate within the confidence interval of (1-α). A p-value > 0.05 suggests no significant effect.

The F-value is the ratio of the model mean squared divided by the residual mean squared, i.e. the variation explained by the model relative to that unexplained. The appropriate models had been fitted to the three responses based on the p-value < 0.05. Moreover, lack of fit is insignificant in the best model.

ANOVA analysis for all the three responses presented in Tables 8.1-8.3 illustrate the efficacy of regression model developed. Indeed, these statistics for each response of TCD, MHC and DHL evaluated and assessed indicate their individual, interactive as well as quadratic effects of all three parameters. In statistical analysis, a model with a higher F value (>1) and smaller p-value (< 0.05) is considered as significant [246]. As evident from the F and P values for the developed regression model for each response is less than 0.01% with lack of fit value being greater than 0.05, the developed model interpreted the experimental data with more than 99.5% accuracy. It is also obvious from the R^2 and Adjusted R^2 values in all three cases fell between 88.97 − 96.44 %, pretty close to 1, discrepancy could be minimized from the predicted model and experimental data. Thus, the regression model developed for all three responses determining the quality of laser hardened layer in terms of case depth and hardness distribution based of process parameters could visualized excellent predictability. Analysis for each individual response on the evolved model was explained at later sections. The interactive perturbation, surface and contour plots obtained for each response was also co-related with their effects on the treated layer quality in terms of the chosen output responses. As the goal of this multi-objective optimization is to find the conditions on the variables (independent) that entail optimum combination of parameters that fulfil multi-objectives, desirability function was approached to solve the optimization problem. At the end of the development of the model, validation experiments conducted and compared with their corresponding predicted values.

8.4   Development of Mathematical model for TCD

Table 8.1 represents ANOVA results for the response TCD with variation of all three influencing parameters constituting laser power, linear speed and rotary axis speed. Indeed, it is clear that all three parameters significantly influence on TCD linearly as F value being greater than 1.0 and P value falling below 0.05. Indeed, high values of F, especially for individual parameters of laser power and linear speed suggest that they induce maximum effect on TCD.

No significant effect on TCD visualized with interactive effects of all the parameters along with quadratic effects of both laser power and linear speed, as F and P values fell beyond the required limits. Thus, first order of all three parametric terms, second order of linear speed considered for predicting the TCD response effectively. The final regression model to determine total case depth in terms of actual variables formulated by:

TCD (μm) = +1101.05357 + 0.10825 * Laser Power - 172.46429 * Linear Speed - 0.12187 * Rotary Axis Speed +7.16071 * Linear Speed^2………Eq.7

Table 8.1: ANOVA analysis for TCD

Source	Adj. SS	DOF	Adj. MS	F-value	P-value	
Model	58630.13	4	14657.53	67.68	< 0.0001	Significant
Laser Power	23436.12	1	23436.12	108.22	< 0.0001	
Linear Speed	27378.00	1	27378.00	126.42	< 0.0001	
RPM	4753.13	1	4753.13	21.95	0.0009	
Linear Speed x Linear Speed	3062.88	1	3062.88	14.14	0.0037	
Residual	2165.61	10	216.56			
Lack-of-fit	2123.61	8	265.45	12.64	0.0753	Not Significant
Pure Error	42.00	2	21.00			
Total	60795.73	14				

R^2: 96.44 %; Adj. R^2: 95.01%

As evident from the mathematical model and values of R^2 (96.44%) and Adjusted R^2 (95.01%) being pretty close to 1, the built regression model agree well with experimental data for TCD. Discrepancy could be reduced to a maximum extent with 99.5% accuracy in prediction with excellent goodness of fit. The high F values of both laser power and linear speed indicate their significant influence on the effect of total case depth formation in the process. Rotary axis speed induce less significance in TCD formation. Indeed, this elucidates that laser power and linear speed directly affect case depth formation, with laser power effect being more pronounced than linear speed. In fact, laser power directly effects the depth of heat penetration into the steel substrate with direct proportionality as against negative effect of linear speed on heat penetration

into the material [247-249]. Furthermore, perturbation plot for TCD depicted in Figure 8.1 illustrate to compare the effect of all three factors in the central point in the design space. Indeed, TCD plotted by varying only one parameter over its range, while keeping other factors constant, exhibited sensitivity with input variable. Thus, the developed model exhibited good agreement between the determined and obtained response of TCD within the experimental range. Indeed, the lack of fit F value of 0.0753 implies that it is not significant relative to the pure error. Similar effects was also observed in various reported studies involving RSM model development on different laser surface processing methodologies [245, 247, 250].
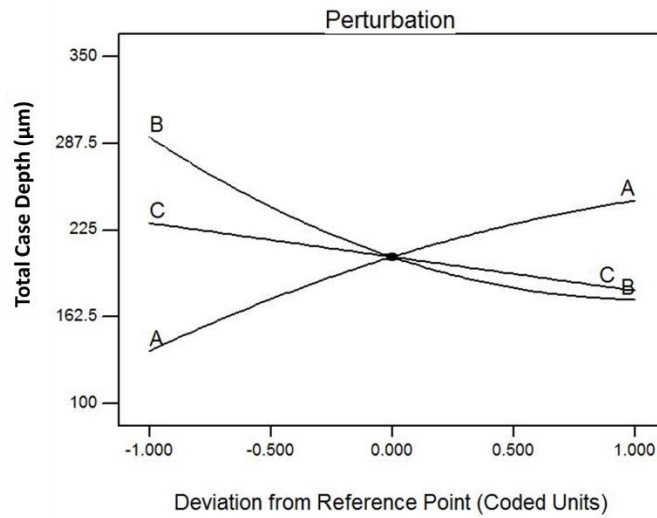
Fig. 8.1 Perturbation plot of TCD

The two-dimensional and three-dimensional surface and contour plots presented in Figure 8.2 display the interaction effect of all three parameters (laser power, linear speed and rotary axis speed) on TCD for the selected range. It is obvious from the interactive surface and contour plots of laser power with linear speed (Figure 8.2 (a and b)) and rotary axis speed (Figure 8.2 (c and d)) that with increasing laser power and decreasing linear speed and rotary axis speed, TCD increases. With highest laser power and lowest linear speed, maximum TCD obtained. Indeed heat input increases with increase in laser power and decrease in linear speed and rotary axis speed. The influence of rotary axis speed was quite sluggish in case depth formation, as compared to that of linear traverse speed. This envisages that the LDT varied in radial direction (evaluated from the conversion factor of rotary axis speed to linear speed on 12 mm diameter steel rod) is far lower by two orders of magnitude as compared to that of LDT varied in linear

traverse direction. As a result, influence of rotary axis speed term is lesser on case depth formation than linear speed. Indeed the surface and contour plots implying interactive effects of linear speed with rotary axis speed depicted in Figure 8.2 (e and f) corroborate its ineffective influence on TCD. In few of the reported studies involving optimization of laser surface treatment process employing RSM technique, model developed exhibited influence of parameters associated with heat input and thermal diffusion time on output response of case formation [251]. Overall, the regression model developed for TCD proved adequacy in predicting results in conjunction with experimental values.
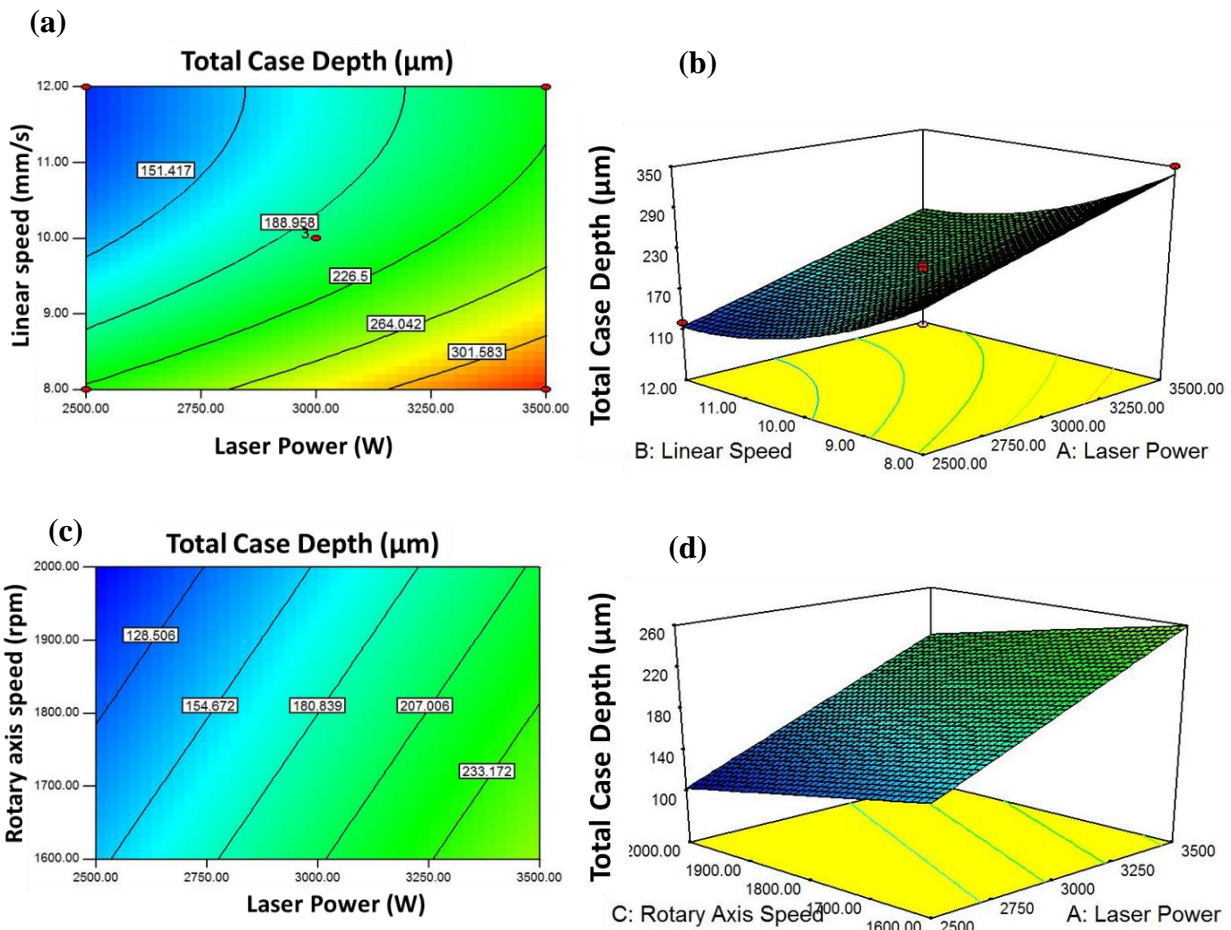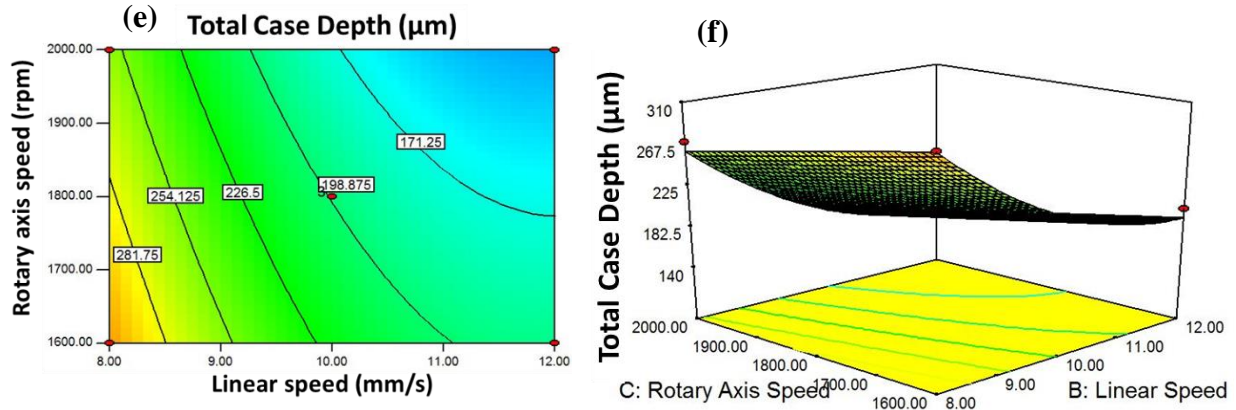
Fig. 8.2 The interaction effect between laser power, linear speed and rotary axis speed on response TCD (a,c,e) surface plots (b,d,f) contour plots.

8.5   Development of Mathematical model of MHC

Table 8.2 represents ANOVA results for the response MHC with variation of parameters constituting laser power and linear speed. Indeed, it is clear that both parameters of laser power and linear speed significantly influence on MHC linearly as F value being greater than 1.0 (30.61 for laser power and 77.51 for linear speed) and P value falling below 0.05. Indeed, high values of F, especially for individual parameters of laser power and linear speed suggest that they induce maximum effect on MHC, as similar to that observed in case of TCD. Quadratic term of linear speed was next most influential on MHC as evident from their respective F and P values. The final regression model to predict mean hardness distribution across the depth of laser treated case in terms of actual variables is as follow:

MHC ($HV_{0.5}$) = +1556.17857 + 0.080750 * Laser Power - 181.58929 * Linear Speed + 7.47321 * Linear Speed^2 ……….…….Eq.8

Table 8.2: ANOVA analysis for MHC

Source	Adj. SS	DOF	Adj. MS	F-value	P-value	
Model	49401.67	3	16467.22	38.65	< 0.0001	Significant
Laser Power	13041.13	1	13041.13	30.61	0.0002	
Linear Speed	33024.50	1	33024.50	77.51	< 0.0001	

192

Linear Speed * Linear Speed	3336.04	1	3336.04	7.83	0.0173	
Residual	4686.73	11	426.07			
Lack-of-fit	4020.73	9	446.75	1.34	0.4983	Not Significant
Pure Error	666.00	2	333.00			
Total	54088.40	14				

R^2: 91.34 %; Adj. R^2: 88.97%

As the empirical model indicated F and P values of 38.65 and 0.0001, within the desired limits, it is valid for prediction. The "Lack of Fit F-value" of 1.34 implies no significance relative to the pure error and this implies 49.83% chance with such large value be due to noise. The value of (R^2: 91.34 %) indicate that 91.34 % of the variability in the results could be observed by the model for MHC along the depth of treated layer. The adjusted R^2 (Coefficient of Determination) value being 88.97 % indicates the significance of the model. Indeed linear speed and laser power indicate significant influence on MHC as evident from their F and P values. As hardness distribution through the depth of the treated layer depends on extent of temperature gradient induced with amount of martensitic transformation, heat input (laser power) and thermal diffusion time (linear speed) terms influenced MHC values. Indeed, the very low parametric range, in terms of thermal diffusion time, was considered for rotary axis speed parameter in the design space, no significant influence realized. Linear speed parameter induced highest influence on the MHC, due to the fact, that reduction in linear speed allows more laser energy penetration into the steel substrate leading to enhanced supercooling and thereby higher hardness through its depth. In a similar study involving optimization employing statistical modelling of hardness distribution in laser surface hardening of steel, linear speed parameter induced highest influence and attributed degree of supercooling [252]. In fact, all individual, quadratic and interactive terms connected with rotary axis speed showed no significant influence on MHC. The result corroborate the lack of influence on MHC response due to rotary axis speed parameter being considered in low parametric range, as similar to that explained in TCD formation.
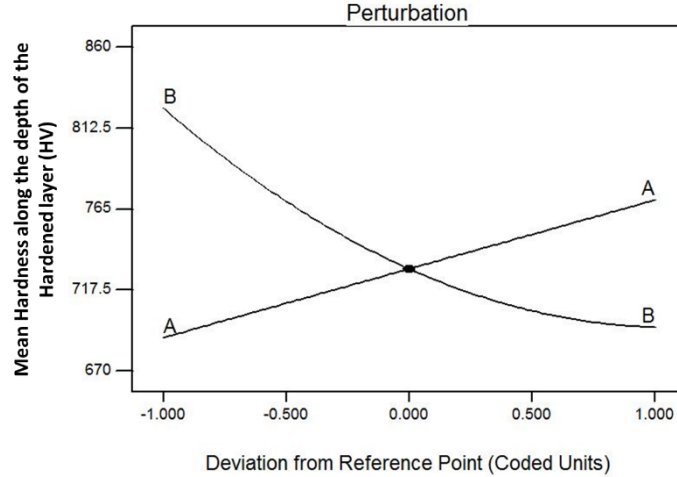
Fig. 8.3 Perturbation plot of MHC (HV$_{0.5}$)

Furthermore, the perturbation plot depicted in Figure 8.3 elucidates dominant negative significant influence of linear speed and moderate positive influence of laser power on MHC with no influence of rotary axis speed. The impacting influences of all these process parameters are considered at the center point in the designed space. It is clear that the laser power has direct positive effect while the linear speed has negative effect on the response of mean hardness along the depth of treated layer. The rotary axis speed did not influence on the response of MHC, plausibly due to its sluggish influence associated with parametric range chosen in the design window. As effective thermal diffusion time associated with speed plays an important role for showing significant effect of all the parameters on the response MHC, rotary axis speed effect chosen in its design space being as low as 30 – 375 ms, its non-significant effect could be perceived on MHC response. In fact, as previously explained, linear as well as quadratic effect on linear speed parameter influenced most on MHC response. The two-dimensional and three-dimensional surface and contour plots presented in Figure 8.4 display the influence of interaction effect of parameters (laser power and linear speed) on MHC for the selected range. It is clear from the plotted graphs (Figure 8.4 (a-b)) that by increasing laser power coupled with reducing linear speed, maximum mean hardness along the depth of treated layer could be realized as evident from the curvature of the plot. Either increasing laser power or decreasing linear speed increases the heat input with prolonged interaction time to enhance the temperature gradient with higher degree of supercooling (higher martensitization) and thereby higher mean hardness through the depth of the treated layer [252]. Similar effects was also observed in various

reported studies that average hardness value in the treated layer increases by reducing the scanning speed due to the increase of the martensitic phase in the microstructure [252]. Indeed, the developed empirical model adopting RSM for MHC has proven its efficacy with high accuracy in prediction.
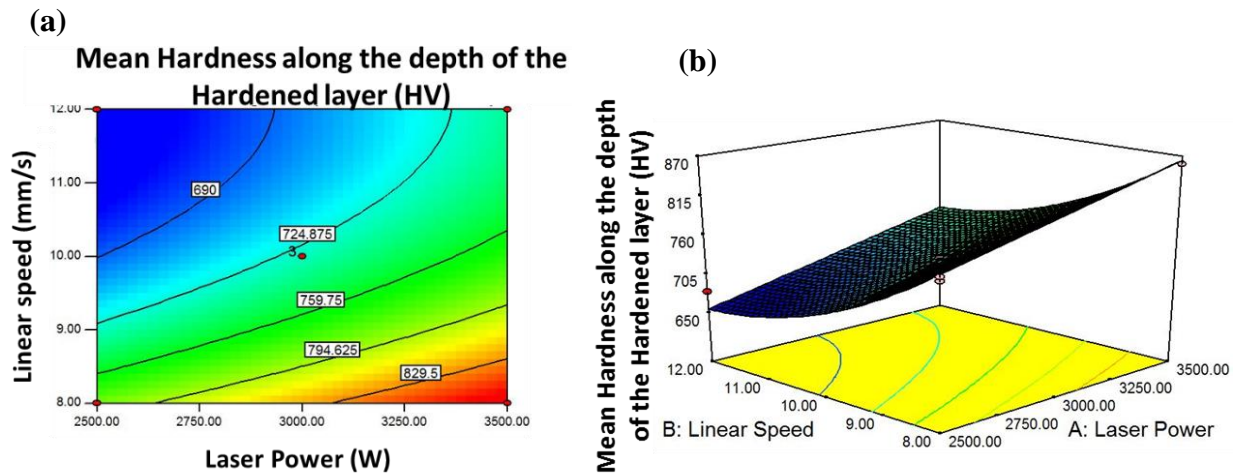
Fig. 8.4 The interaction effect between laser power and linear speed on response MHC (a) surface plot (b) contour plot

8.6   Development of Mathematical model of DHL

Table 8.3 illustrates ANOVA test results for the response DHL, a term assessing the quality of the laser treated surface layer associated with the distribution of hardness along the treated length of the steel rod, with variation in parameters of linear speed and rotary axis speed. It is clear from the coded values of F and P that only linear speed and rotary axis speed induce significant influence on the response of DHL. Among the parameters of linear speed and rotary axis speed, rotary axis speed parameters influence is most significance as its first order linear term got maximum F and minimum P value amongst all of their effects. All other linear (for laser power), quadratic and interactive effects of parameters in the designed space induce no significant influence in determining DHL as their P values are falling beyond the desired limit of less than 0.05. The final regression model to predict differential hardness longitudinal in terms of actual variables is as follow:

DHL $(HV_{0.5})$ = +481.80000 + 10.81250 * Linear Speed - 0.25562 * Rotary Axis Speed ……Eq.9

Table 8.3: ANOVA analysis for DHL

Source	Adj. SS	DOF	Adj. MS	F-value	P-value	
Model	24651.25	2	12325.63	98.40	< 0.0001	Significant
Linear Speed	3741.13	1	3741.13	29.87	0.0001	
RPM	20910.12	1	20910.12	166.93	< 0.0001	
Residual	1503.15	12	125.26			
Lack-of-fit	1165.15	10	116.52	0.69	0.7202	Not Significant
Pure Error	338.00	2	169.00			
Total	26154.40	14				

R^2: 94.25 %; Adj. R^2: 93.29%

The "Lack of Fit" F and P values of 0.69 and 0.7202 implies that Lack of Fit is not significant relative to the pure error and there is only 72.02% chance that it could occur due to noise. Indeed, the values of R^2 (94.25 %) and Adjusted R^2 (93.29%) indicate that the variability in the results could be observed by the coded model and its significance. As compared to the significant influence of laser power on responses of TCD and MHC on the regression model, DHL did not depend on its resulting effect. This is obvious due to the utilization of wide laser spot of 4 mm x 4 mm with its uniform energy distribution and the window of chosen parametric range. However, the interaction time associated with rotary axis speed is so sensitive (negative influence) to develop gradient in peak temperatures at surface as it principally depend on the overlapping of circular tracks with short duration dissipating heat laterally. As a result, the influence of rotary axis speed on DHL is significant as predicted by the regression model. Indeed, higher the rotary axis speed, higher the temperature gradient along the lateral direction and as a result higher will be the resulting DHL value. In contrast to the influence of rotary axis speed, effect of linear speed was found to significant in positive sense. Thus, higher the linear speed, higher will be the temperature gradient produced in the hardened layer in lateral direction, associated with overlapping of circular tracks within the fixed rotary axis speed. Thus, entailing

increase in differential hardness across its surface length. Figure 8.5 illustrating perturbation plots elucidates almost linear converging plots with convergence at the center for both linear speed and rotary axis parameters. Thus minimal variation in hardness distribution along its length, a factor determining the uniformity of treated case along its length, could be achieved by minimizing linear speed and maximizing rotary axis speed that depend on the rod diameter and its thermophysical properties.   .
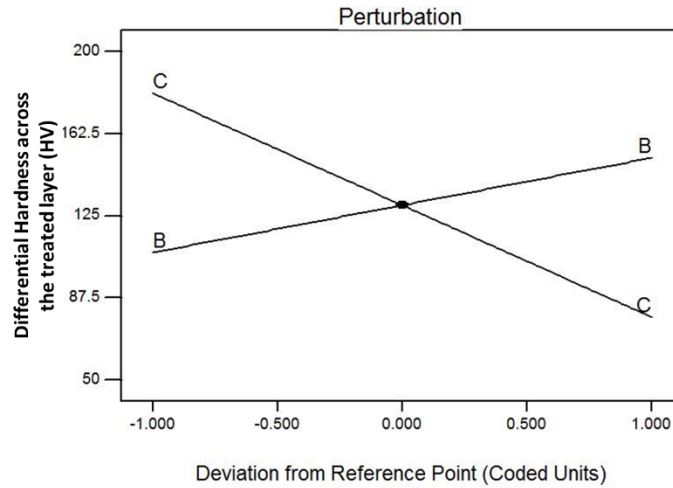
Fig. 8.5 Perturbation plot of DHL (HV$_{0.5}$)

From the perturbation plot in Figure 8.5, it is clear that linear speed has significant positive effect and rotary axis speed has maximum negative effect on the DHL response, with influence of laser power being void. As previously explained, DHL remained constant with variation of laser power parameter, principally attributable for not-to-significant variation in temperature gradient in lateral direction, convergent with FEM result. The trend of the parametric effect, as far as rotary axis speed is considered, is similar to the previously assessed for perturbation plots of TCD and MHC. Furthermore, the low F and high P values of the model, as similar to that of the MHC response reiterate lack of influence affecting the DHL response due to insensitivity of second order quadratic and interactive terms of all the three parameters chosen within the domain space. Indeed, the level of variation chosen for the parameters of rotary axis speed and linear speed in a way that envisages stabilization of heat input (martensitic transformation) for diameter of the steel rod and as result no effect on temperature gradient leading to alter DHL. Similar ANOVA analysis on lack of influence due to input energy variation on hardness was reported by Giorleo and co-workers involving parametric effect on

treated layer case utilizing apparent spot laser hardening technique [253]. In this way, the developed RSM model could help facilitate in understanding the influence of variables not effecting the response and thus predicting to the accuracy of the model. The two-dimensional and three-dimensional surface and contour plots presented in Figure 8.6 display the influence of interaction effect of parameters (linear speed and rotary axis speed) on DHL for the selected range. It is clear from the plotted graphs (Figure 8.6 (a and b)) that by increasing rotary axis speed coupled with reducing linear speed, minimal differential hardness along the longitudinal surface of the treated layer could be realized as evident from the curvature of the plot. Furthermore, to clarify such effects of DHL on the resulting quality of the laser-hardened layer, FEM modelling was carried out and explained later with correlating evolving temperature gradient along the length of the treated rod surface with variation in process parameters. Indeed, the developed model for DHL proved adequacy in predicting results to close approximation.
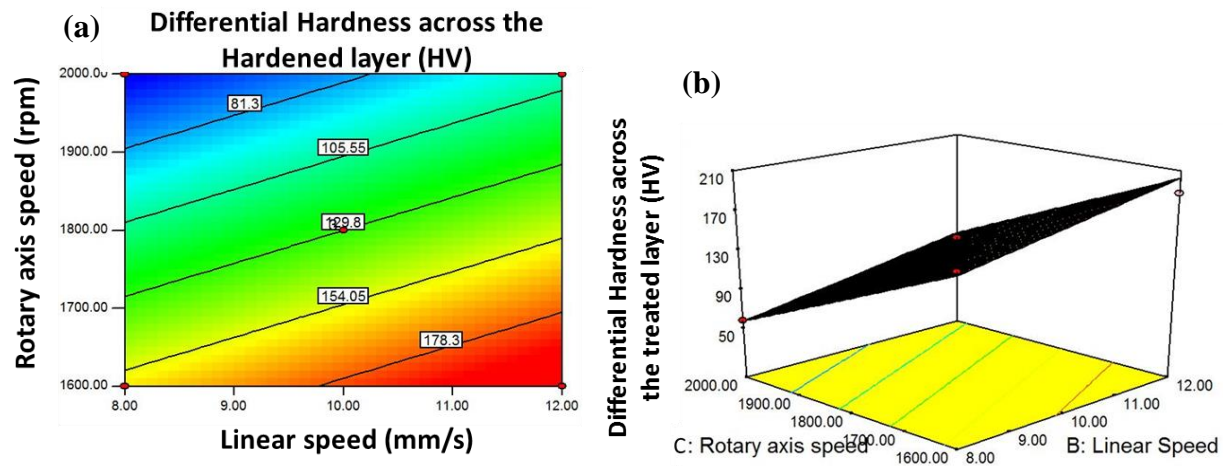
Fig. 8.6 The interaction effect between linear speed and rotary axis speed on response DHL (a) surface plot (b) contour plot

8.7   Numerical optimization using desirability approach

Since there are many quadratic and interaction terms influencing output responses (TCD, MHC and DHL) in the regression model, with independent parameters, it may not be suitable to find the optimum process parameters. Thus, necessitating application of a combined objective optimization technique to solve this problem. The goal of multi-objective optimization is to find

the conditions on the variables (independent) that steer optimal combination of parameters that fulfil multi-objectives to maximize TCD and MHC and minimize DHL. The desirability function is a numerical approach to solve a combined objective optimization problem [250, 252, 254]. This function satisfies all responses and searches for optimum parameters with desirability value '0' representing unacceptable design for the response selected and '1' representing perfect configuration. The optimization criteria (goal and factor range) for the optimization model enlisted in Table 8.4. As mentioned earlier, DHL, a true measure of hardened layer quality, is critical to evaluate hardness distribution uniformity along its longitudinal direction. Reducing DHL to as much minimum as possible is the principal aim to eliminate softening effects associated with induced thermal and diffusion effects of overlapping spiral tracks during high speed processing. In the optimization process, all the responses entail equal importance with highest being for DHL. The optimal parameter should satisfy the objectives that include maximizing TCD, MHC and minimizing DHL. Table 8.5 shows the solutions obtained for the given range and conditions. The two-dimensional contour plots for overall desirability are shown in Figure 8.7 that illustrate desirability of laser surface hardening conditions for a combined desirability value of 0.988.

Table 8.4: Criteria for optimization of parameters

Constraints	Goal	Lower limit	Upper limit	Importance
Laser Power (W)	Is in range	2500	3500	3
Linear Speed (mm/s)	Is in range	8	12	3
Rotary Speed (RPM)	Is in range	1600	2000	3
TCD (μm)	Maximize	102	350	3
MHC ($HV_{0.5}$)	Maximize	671	859	3
DHL ($HV_{0.5}$)	Minimize	58	191	5

Table 8.5: Optimum solutions obtained as per design criteria

Number	Laser Power	Linear Speed	Rotary Speed	TCD	MHC	DHL	Desirability	
1	3499.97	8.00	1956.70	338.913	878.564	57.9975	0.988	Selected

2	3500.00	8.00	1968.86	338.209	879.702	54.6983	0.987	
3	3401.02	8.00	1959.86	328.208	864.526	57.9989	0.975	

The optimal values for the intended high speed laser surface hardening process parameters on steel rod of 12 mm diameter are 3499.97 W laser power, 8 mm/s linear speed and 1956.70 rpm rotary axis speed. The resulting optimized hardened layer depth is 338.9 μm with cross-sectional mean hardness through its depth being 878.5 $HV_{0.5}$ and differential hardness about 57.99 $HV_{0.5}$. This RSM approach had been applied to conduct actual experiment and compare with results obtained. The values predicted by all the responses as per the optimization approach recommends the optimal process parameters. The predicted values were compared with optimal parameters that are tested. The results of validation tests and its comparison is depicted in Table 8.6. The percentage of error between the actual vale and the predicted value is less than 5%, which is in the acceptable range. Thus, results indicate that experimental values are in fine agreement with the predicted values, thereby concluding that the optimal parameters obtained by response surface methodology can be applied with high accuracy.
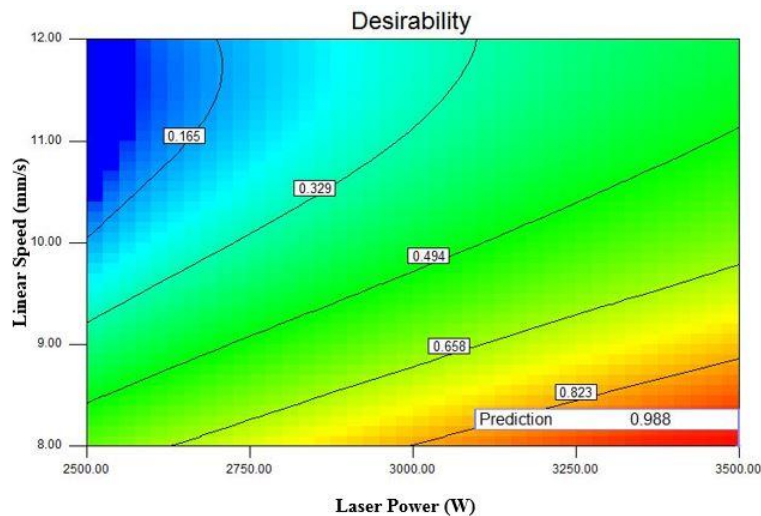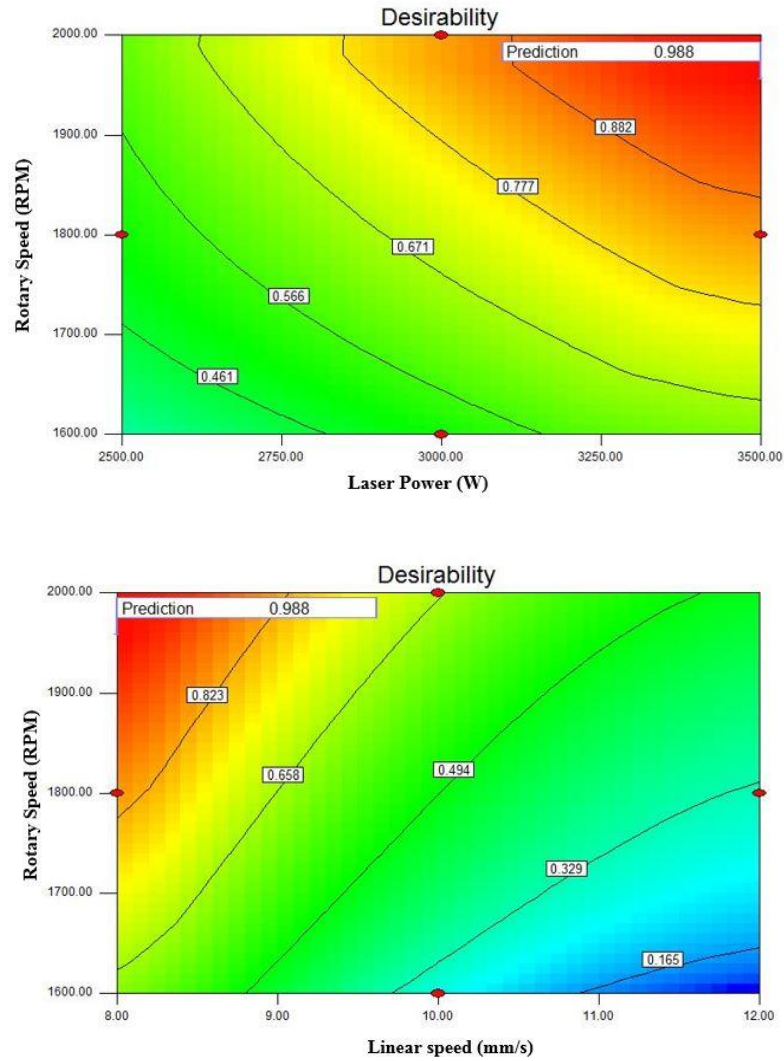
Fig. 8.7 Contour plots of overall desirability for high speed laser surface hardening process at desirability of 0.988, Laser Power: 3499.97 W, Linear Speed: 8.02mm/s, Rotary Speed: 1956.70RPM.

Table 8.6: Validation test results

Responses	Predicted	Desirability	Experimental	Error (%)
TCD	338.824	0.988	330	2.67
MHC	878.708	0.988	864	1.70
DHL	57.5726	0.988	55.25	4.20

8.8   Validation of experimental results with RSM and FEM

Further to understand the influence of processing parameters on quality of the laser surface hardened layer in terms of hardness distribution along its longitudinal surface, transient thermal model developed using COMSOL and explained previously for stationary beam processing has been extended by traversing the laser beam along its length. The FEM model was developed coupling temperature-dependent properties of steel under designated boundary conditions with movement of laser beam using moving mesh. To validate the proposed model, quantitative prediction of surface temperature distribution along the length of treated rod by utilizing optimized parameter from desirability approach were simulated and evaluated thermal history. Figure 8.8 indicate variation in surface temperature distribution along the central region of the length of the rod (25mm) at the optimized parameter i.e., laser power of 3500 W, linear speed of 8 mm/s and rotary axis speed of 2000 RPM. Only central region of the rod was considered to plot thermal profiles to avoid deleterious effects of laser power acceleration and deceleration during starting and ending of the process during laser processing. The red line delineation indicates the Ac_1 critical austenitization temperature limit of 735^0C for EN31 steel. Indeed, it is known that drop in surface temperature at any point along its length below A_{C1} will lead to softening and its extension determined by the thermal diffusion distance governed by rotary axis speed.
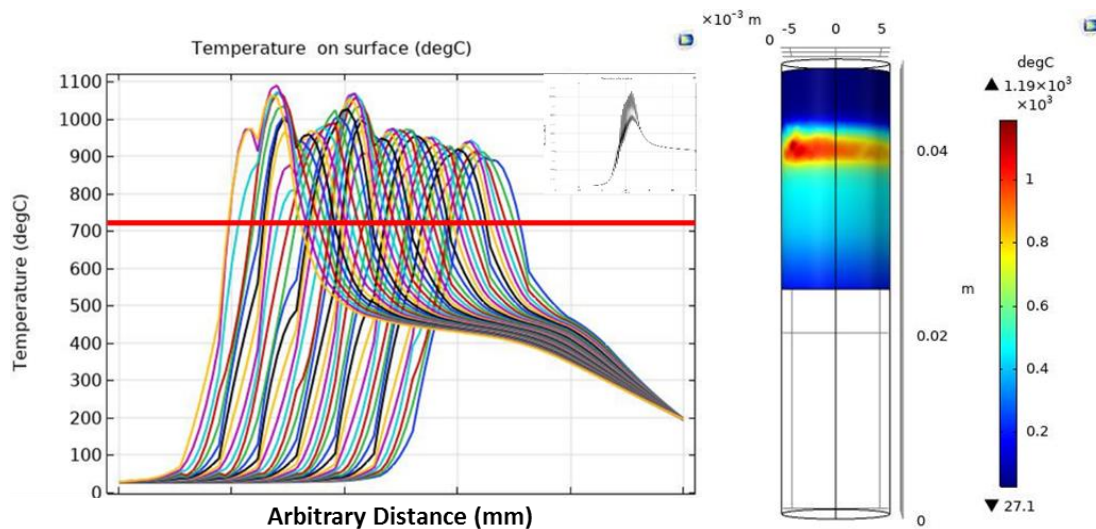
Fig.8.8 Temperature profiles on surface of the cylindrical rod at different locations and surface temperature contours at 35mm location by fixing LP:3.5 kW, Scan speed: 8mm/s & Rotary Speed: 2000 RPM

It is clear that greater uniformity in temperature distribution persists on the surface processed with 2000 RPM (Figure 8.8(a)). Indeed maximum surface temperature (T_{Smax}) and minimum surface temperature (T_{Smin}) was fluctuating between 1045^0C and 920^0C and thereby leading to a temperature differential (∇T) of 125^0C. Thus at higher rotary axis speed of 2000 RPM, DHL reduced to 56 $HV_{0.5}$ in conjunction with minimal ∇T of 125^0C. As such, from the point graph (Figure 8.8(a)), it is clear that no point on the surface exhibited fall in temperature below A_{C1}, thereby eliminating any softening effect. The experimental as well as RSM predicted values matched with their least DHL values of $56HV_{0.5}$ indicating good co-relation between both FEM and RSM models with experimental results. Thus, optimum processing conditions with high rotary axis speed entails elimination of overlapping softening effects in high speed laser surface hardening process. Figure 8.8(b) exhibits surface temperature contours simulated at center of the location of the steel rod developed with FEM model and processed with optimized parameters (obtained from RSM model as well) constituting laser power of 3500 W, linear speed of 8 mm/s and rotary axis speed of 2000 RPM. Indeed, uniform thermal effect (color contrast variation) with surface temperature maintained within the range of 1035^0C– 960^0C throughout its processed length validate the FEM model for optimizing the process with complete elimination of softening of the treated layer.
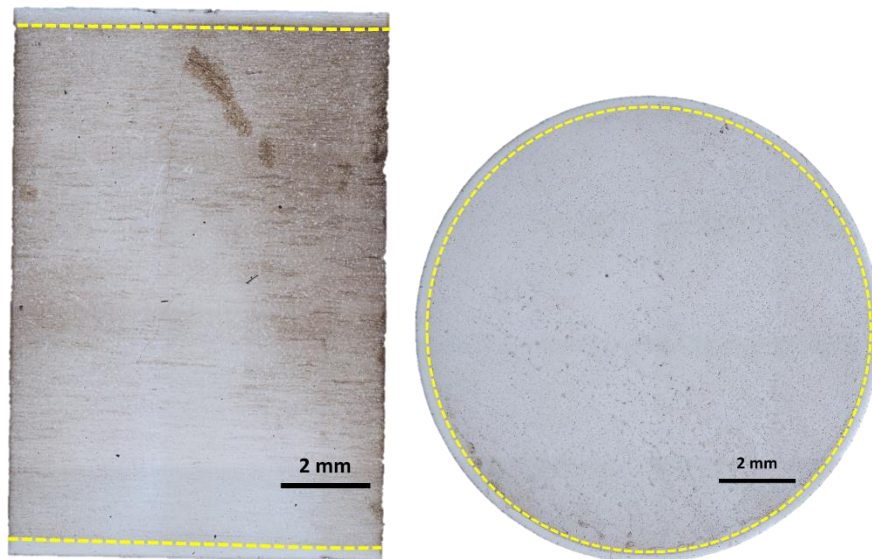
Fig. 8.9 Longitudinal and Cross-sectional Macrostructures processed at LP: 3.5 kW, Scan speed: 8mm/s; 2000 rpm

The cross-sectional macrographs in longitudinal as well as in radial direction of the rod experimented with optimized parameters obtained from RSM model, depicted in Figure 8.9, also matched with the hardened case profile in both longitudinal and radial directions. Indeed, measured total case depth values along axial and longitudinal direction varied between 330 – 360 μm and 450 – 325 μm respectively. Apparently, hardness values measured in the treated case profile also showed minimal variation along its length and depth and co-related well with the simulated temperature differential maintained. Similar control in temperature uniformity along the length of the laser hardened cylindrical rod has been reported by Sagar V. Telrandhe et al., [255] but they maintained temperature uniformity by controlling heat input instead of rotary axis speed.   Indeed, error difference in case depth within 5% could be realized between the simulation, design optimization and experimental validation. Overall, good agreement reached found between the actual experimental values with that predicted from optimization using developed RSM and FEM models.

8.9 Mechanical properties evaluation of laser hardened bearing steel employing high-speed quasi-stationery beam processing: Tensile testing

Further to quantify and qualify the proposed high-speed quasi-stationery laser processing of cylindrical rods developed and validated with FEM and RSM modelling, it was felt pertinent to assess strength of the processed bearing steel by subjecting to static tensile testing. The impact of high-speed laser surface-hardening process on the mechanical behavior of En31 steel, specimens of dimensions corresponding to Figure 3.34 were carefully prepared and machined after laser heat treatment to match the dimensions of a standard specimen according to the ASTM E8M standard. Table 8.7 depict comparative tensile properties of laser hardened and untreated substrate of bearing steel. It indicates that a significant increase in yield strength and tensile strength obtained in specimens processed with high-speed laser surface-hardening process as compared to that of untreated En31 steel. As the test coupons processed with optimized

parameter obtained from desirability approach, uniform hardness distribution obtained with minimal differential hardness resulted in improved, yield (22%) and tensile strength (17%) compared to that of untreated substrate. Yield strength would principally depend on the volume fraction of the harder phases like martensite or carbides present in a given microstructure, as laser surface hardened microstructure contains significantly greater amounts of martensite and carbides and as a result offers greater yield strength.

Table 8.7 Tensile test results

Treatment	YS (MPa)	UTS, (MPa)	% El	Fracture location
Untreated	420-425	640-645	27-28	Within gauge length
Laser Treated	550-555	775-781	1.5-2	

8.10 Summary

In this study, the RSM model is utilized to optimize the high-speed quasi-stationery laser surface hardening process on solid cylindrical steel rod with critical response variables affecting the process. Effect of three critical processing parameters, namely, Laser Power, Linear Speed and Rotary Axis Speed on the quality of laser hardened layer in terms of total case depth (TCD) and hardness distribution, namely - Mean Hardness - Cross-sectional (MHC) and Differential Hardness – Longitudinal (DHL) were investigated and assessed. Following conclusions are drawn:

1. There exists an optimum range of processing parameters determined by the cylindrical steel rod diameter and laser spot dimensions, over which a uniform hardened surface be obtained with case depth of few hundreds of micrometers high-speed rotation entailing complete elimination of softening effect that is inherent in conventional helical processing.

2. Optimization of the treated layer can be achieved by maximizing case depth (TCD) and mean hardness through depth (MHC) and minimizing differential hardness across the longitudinal direction of the treated layer (DHL).

3. According to regression model, linear quadratic and interactive terms of all three parameters exert effective influence on TCD, whereas linear and quadratic codes of laser power and linear speed influenced on MHC and combined effect of linear speed and rotary axis speed on DHL. Experimental results of the model with desirability approach exhibited good agreement with less than 5% error.

4. To achieve maximum case depth in 12-mm diametric En-31 steel rod with maximum hardness through its case depth and minimal differential hardness, the optimal parameters are a laser power of 3.5 KW, linear speed of 8 mm/s and rotary axis speed of 2000 RPM.

5. Combining the finite element method and the response surface methodology is an efficient way to optimize the process parameters and good agreement with less than 5% error found between the two methods.

It is believed that the type of approach combining FEM and RSM models proposed in this study is the most appropriate way to optimize the high-speed laser surface hardening process for improving the performance of laser-hardened layers on engineering steel components of cylindrical geometry.

CHAPTER 9

Application and development of laser surface hardening process on actual tapered roller bearing elements including process setup and assessment of their engineering advantages in comparison with conventional industrial practices

9.1 Introduction

Further to the comprehensive study on development of laser surface hardening process on prior spheroidized and conventionally hardened (SPH+CHT) bearing steel with control of processing parameters/conditions (different modes of processing and thermal processing conditions with external fluid contact and other approaches) and analyses of resulting hardened layers, it was felt pertinent to apply the process on actual taper roller bearing elements such as inner racer, outer racer and roller. Indeed numerical and mathematical simulation of the laser hardening process with FEM and RSM along with its validation with experiments on flat and round specimens help facilitated in quickly arriving at optimal processing conditions and parameters, given the geometry and thickness of the bearing steel. As the application of the process on actual bearing elements will be altogether a different aspect, it was felt pertinent to apply the process on actual bearing elements such as racers and rollers, which is the subject of this section. As, such steel bearing elements are used in any application with treatments of both spheroidization and conventional hardening and tempering with full martensitic structure of hardness $780 - 800\ \mathrm{HV}_{0.5}$ and enhancing further hardness on surface with retention of core strength by imparting laser surface hardening treatment help improve life of bearing. Thus the

aim of the current final study is to assess efficacy of the laser surface hardening treatment with different thermal processing conditions on actual bearing elements and explore their engineering advantages and life enhancing capability.

In the present work, laser surface hardening treatment of conventionally hardened (SPH+CHT) tapered roller bearing racers (both inner and outer racer) and rollers with methodologies proven by already explained works has been tested and assessed. The present work highlights these novel methods applied on treating outer periphery for inner racer, inner periphery for outer racer and outer surface of roller used in thin-sectioned tapered roller bearing assembly. The same high power diode laser integrated to a robotic workstation has been used for process experimentation and development. Although, well known Continuous Wave (CW) mode of laser processing could provide improved case-profile with higher hardness than conventionally processed heat treatment method, distortion effects and loss of core properties persisted. In order to overcome these effects, improvised fixturing setups was designed, fabricated and tested to fix bearing elements when subjected to laser surface hardening treatment under both Continuous Wave (CW) and Pulsed Wave (PW) modes at optimized conditions. Additionally, influence of PW processing parameters as well as variation in fluid flow contact conditions were also attempted and resulting case-profile uniformity, roundness, surface finish and distortion control of the treated racers has been studied and presented in this chapter. Improved pulsing conditions with a specific design of fixturing setup exhibited vast advantages over other methodologies with CW mode of processing and conventionally adopted surface hardening methods.

9.2   Design and development of fixtures/setups for processing racers and their engineering advantages

In order to quickly fix bearing elements such as racers (inner and outer racers) to the rotary axis of the diode laser processing system, fixture with magnetic chuck has been used for rotating the racer with impingement of 20 mm X 5 mm diode laser beam on the bearing contact surface of inner OD (for outer racer) and outer OD (for inner racer) of the racers and processed. Indeed, magnetic fixture helped quickly align racer to the axis of rotary with complete elimination of runout, which is vital for obtaining uniform case across its circular periphery. The

process carried out on racers with optimum parameters of laser power and rotating speed under continuous wane mode resulted in hardness improvement of 850-860 $HV_{0.5}$ with case depth of 0.5-0.6mm. Nonetheless, many a times, due to high heat input, demagnetization of fixturing setup resulted with detachment of racers while laser processing, sometimes also leading to non-uniformity in case depth. Another major drawback of the process setup observed was complete through-thickness softening of the core due to lower sectional thickness of bearing racer and a result loss of core strength. Hardness in the core has got reduced to 420-430 $HV_{0.5}$ from substrate hardness of 780-800 $HV_{0.5}$ indicating softening effect associated with martensitic tempering. To overcome these issues, brass fixture (that butts to racer) was used to hold the outer/inner racer to provide additional heat-sink affect. Although hardness in the case improved to the tune of 890 – 920 $HV_{0.5}$ as mentioned in Tables 9.1 and 9.2, retention of core was still an issue along with case uniformity, plausibly due to the difficult in ensuring proper contact with brass fixture. However, core hardness reduction in the racer processed with brass fixture was not that much to that processed with normal magnetic steel fixturing setup. Major drawback with huge distortion persisted with racers processed using brass fixture, which is critical in design of bearings. To maintain the dimensional stability and control in distortion and core retention, next step up utilizing water cooled fixtures were developed (Figs 3.27-3.29) and tested. Designing aspects of appropriate water-cooled fixtures (fluid contact to enhance heat transfer co-efficient) for both the racers are previously mentioned and explained in Chapter 3. Comparative analysis of case depth, hardness distribution, distortion and surface roughness in processed racers utilizing different types of water-cooled fixturing setup are explained in the following sections.

Tables 9.1 and 9.2 Case depth and hardness distribution of lasers treated outer and inner racers processed under different parameters and fixturing setups

Fixture for Outer racer	Laser Power (W)	Scan Speed (mm/s)	Case Depth (mm)	Hardness ($HV_{0.5}$)	
				Hardened region	Substrate region
Using Magnetic Fixture	2400 2000	10	0.5-0.67 0.32-0.4	850-860 805-810	420-430 430-450

| Using brass fixture | 3000 | 20 | 0.41-0.52 | 920-940 | 760-780 |
| | 2500 | | 0.39-0.4 | 860-880 | 760-780 |

Fixture for Inner racer	Laser Power (W)	Scan Speed (mm/s)	Case Depth (mm)	Hardness (HV$_{0.5}$)	
				Hardened region	Substrate region
Using Magnetic Fixture	2400	10	0.53-0.6	850-860	420-430
	2000		0.4-0.5	805-810	430-450
Using brass fixture	3000	20	0.55-0.57	920-940	760-780
	2500		0.39-0.4	880-900	760-780

9.3 Case depth and hardness distribution analysis of outer racers processed under different thermal processing conditions

Figure 9.1 represents typical hardened case profile across the treated layer obtained in PW mode with various regions of interest identified (mentioned in Chapter 5) and marked in the optical micrograph. The HZ depth was highest in CW mode as against reduced depth in other modes processed under fluid contact around the racer as shown in Figure 9.2 and values presented in Table 9.3. Its known that carbon diffusion associated with heating rate during austenization (in turn peak temperature) and cooling rate (governed by fluid contact condition and mode of processing) administer the case depth formation in the treated layer [256]. Although carbon diffusion time reduces with fluid contact beneath the sample surface, the cooling rate enhances and as a result, lesser treated layer depth be obtained as compared to that of racer processed without fluid contact around it. It is clear that in the treated layer processed in CW-mode, the peak temperature measured at the bottom of the sample was still about 250^{0}C (measured with the help of thermocouple) indicating sufficient softening effect associated with martensitic tempering. The high heating rate with prolonged soaking duration associated with low thickness of the racer attributed to this effect and as a result, huge TCZ depth of about 2.03

mm noted. This depth got reduced to as low as 0.7 mm in PW mode and further to 0.57-0.61 mm in CW-UF and PW-UF modes. Thus, variation in terms of pulsed mode of processing and fluid contact around the racer facilitated core hardness retention to greater depth owing to high cooling and high heat-transfer coefficient rates. In a similar study, involving laser hardening with various thicknesses of steel, higher thickness induced high heat transfer coefficient and thereby no softening associated with martensitic tempering could be induced to greater depths [257]. Similarly, SSZ depth reduced in PW, CW-UF and PW-UF modes due to enhanced cooling rates. Overall, the HZ depth in the treated layer was highest in CW mode to the tune of 0.82 mm and got reduced with employment of other processing conditions. Hardness in HZ region of treated layers increased in the order from 810 ± 10 $HV_{0.5}$ to 1080 ± 20 $HV_{0.5}$ (CW to PW-UF modes) as evident from the presented values in Figure 9.2. Hardness in SSZ zones were observed to be as low as 390-580 $HV_{0.5}$, with highest depth be seen in CW mode of processing. Indeed, this zone experiences temperature in the range of $735^0C - 350^0C$ and thereby soften to maximum extent of hardness reduction. Overall, retention in core strength successfully achieved in sample racer processed with PW, CW-UF and PW-UF with maximum in PW-UF due to enhanced heat transfer coefficient.
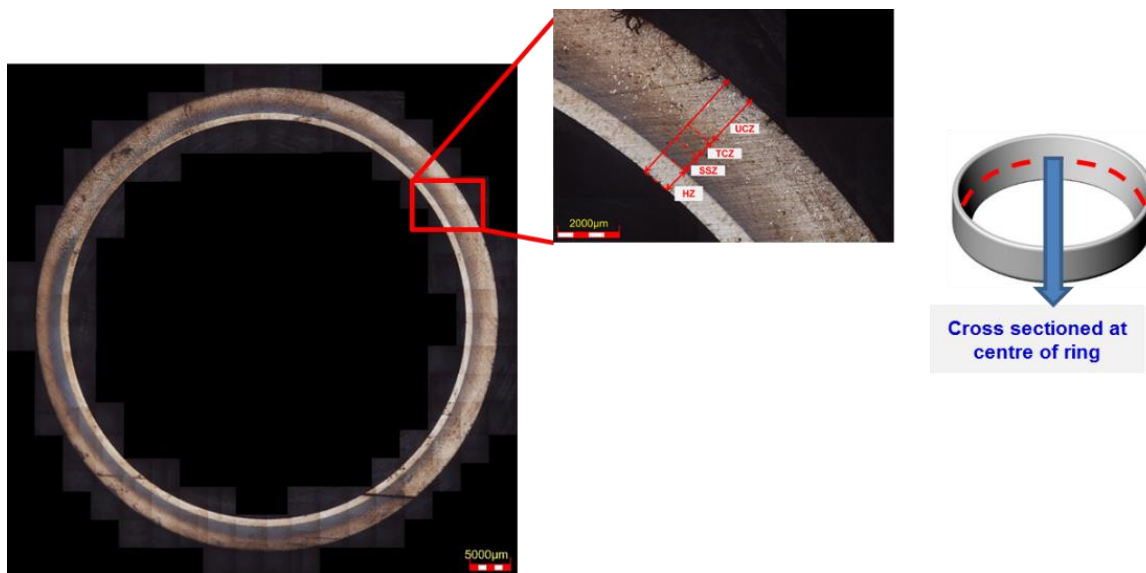
Fig. 9.1 Cross-sectional macrograph of laser treated outer racer processed in PW mode
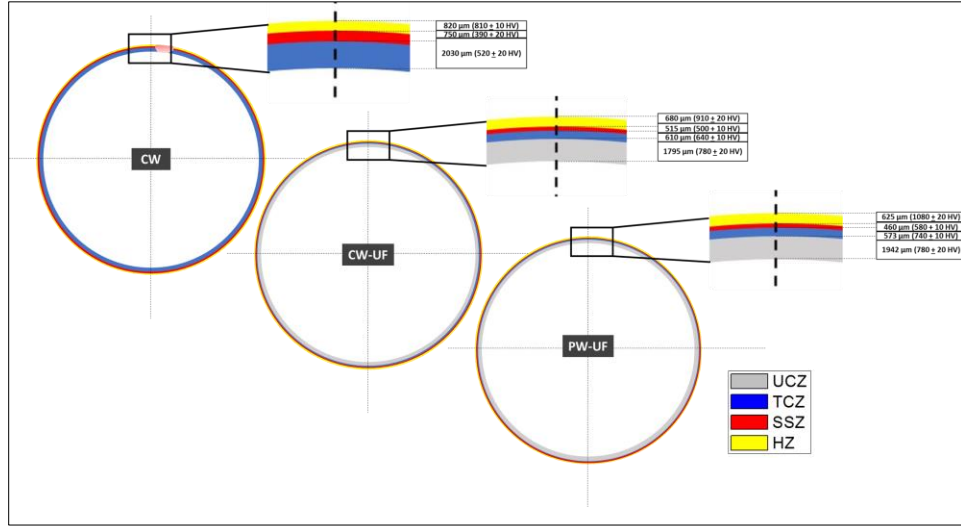
Fig. 9.2 Case depth and hardness distribution analysis of laser treated outer racer processed under different thermal processing conditions

Table 9.3 Case depth analysis of lasers treated outer racer processed under different thermal processing conditions

Component	Mode of Processing	Hardened Zone Depth (HZ)	Super Soft Zone (SSZ)	Tempered Core Zone (TCZ)	Unaffected Core Zone (UCZ)
Outer Racer	CW	820 μm	750 μm	2030 μm	-
	CW -UF	680 μm	515 μm	610 μm	1795 μm
	PW-UF	625 μm	460 μm	573 μm	1942 μm

9.4 Surface topographic analysis on outer racer processed under different thermal processing conditions

Figure 9.3 illustrates the topographic profiles as well as surface roughness parameters (mentioned in Table 9.4) of laser-treated and untreated outer racer surfaces obtained with a 3D Profilometer. It is clear from the topographic pictures that there is only a marginal increase in the average roughness (R_a). However, the PV values (alternatively R_t, a measure of maximum distance between highest and lowest peaks in the measured surface roughness profile) increased

to 18-20 µm compared to untreated steel. Surface topographic profiles (Figure 9.3(a)) with high PV values clearly indicated the presence of heavy undulations on treated surfaces and gave rise to relatively a rougher surface processed under CW mode when compared to other samples processed with PW and fluid contact.
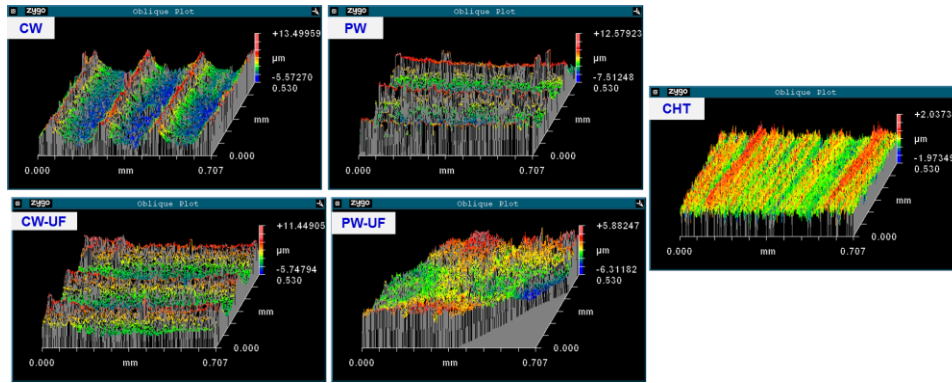
Fig. 9.3 Surface topographic profiles of laser treated and untreated outer racer processed under different thermal processing conditions

Table 9.4 Surface roughness parameters of lasers treated outer racer processed under different thermal processing conditions

Condition	Ra (µm)	PV (µm)	rms (µm)
CW	2.413	20.092	2.877
CW-UF	2.196	17.197	2.783
PW	2.036	19.072	2.525
PW-UF	1.166	12.194	1.482
Substrate (CHT)	0.310	4.011	0.394

9.5 Roundness and curvature analysis utilizing CMM on outer racer processed under different thermal processing conditions

Radial measurements had also been performed on the inner side (treated side) of the outer racer utilizing CMM and an average of three measurements measured at the centre of the racer have been reported (shown in Figure 9.4 and Table 9.5). Variation in radial direction in as-received sample was around 45-50 µm, given for grinding allowance after laser treatment. As

distortion depends on input hear energy, higher deviation could be observed in the sample processed under CW condition due to higher peak temperature whose deviation was around 615-620 μm. Whereas, the racers processed under CW-UF mode resulted in lesser deviation in radial direction around 130-140 μm. Furthermore, with enhanced cooling rate condition in laser processing modes of PW and PW-UF, radial distortion further minimized to 120-130 μm. and 60-70 μm respectively. This could be attributed to the reduced heating rate, effective carbon diffusion time and high rate of cooling factors associated with thermal processing conditions, as reported by other studies involving laser hardening effect due to PW mode and thickness related heat sink effects [258-259]. Apparently, maximum cooling rate in PW-UF condition induced least deviation in the curvature profile, almost equivalent to the as-received condition. Curvature contours presented in Figure 9.5 and extracted from CMM measurements on outer racer processed under different thermal processing conditions provide further insight into the understanding of distortion control possible with different thermal processing conditions. The size variation, ovality and expansion (maximum red in colour) was maximum in CW mode processed racer without fluid contact, when compared to the racer processed with other modes of PW with/without fluid contact conditions. Indeed high heat-transfer rate with high cooling rate possible in PW mode of processing with fluid contact significantly lowered distortion with core strength retention and high surface hardness.

Table 9.5 Roundness analysis utilizing CMM on outer racer processed under different thermal processing conditions

Condition	Roundness Value (μm) at central region of treated racer
PW-UF	69.1
PW	123.3
CW-UF	139.4
CW	614.6
Substrate (CHT)	45.8
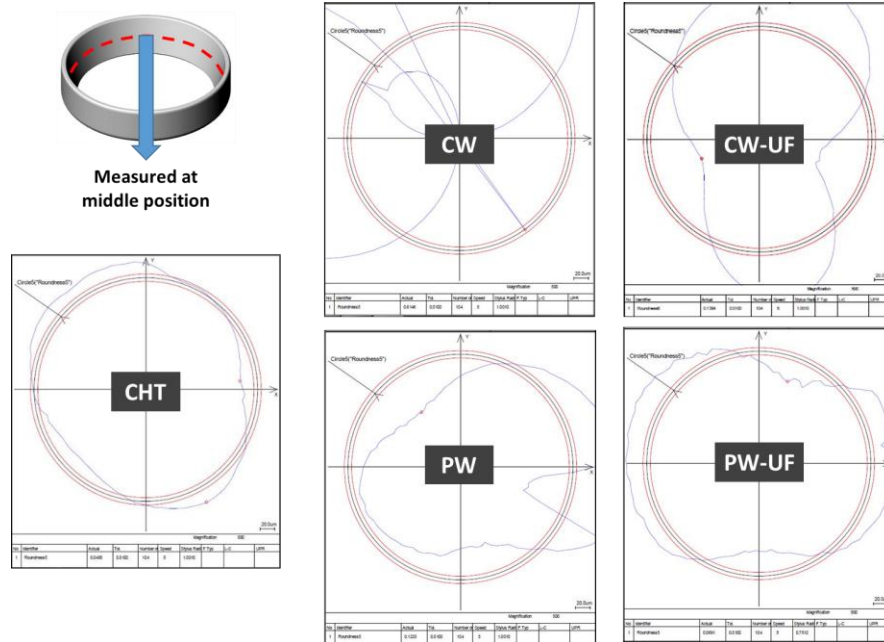
Fig. 9.4 Roundness measurements utilizing CMM on outer racer processed under different thermal processing conditions
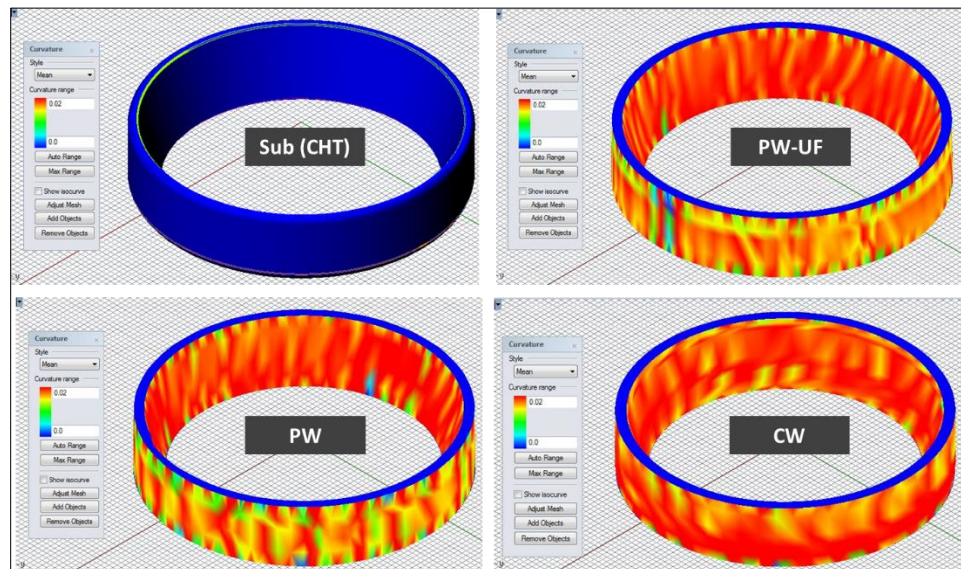
Fig. 9.5 Distortion (Curvature) analysis utilizing CMM data on outer racer processed under different thermal processing conditions

9.6 Case depth and hardness distribution analysis of laser treated inner racer processed with a different water-cooled fixturing setup

Figure 9.6 represents a typical case profile across the depth of laser treated layer of inner racer bearing element obtained in PW mode with external fluid-contact fixturing setup. The uniform hardened depth to a tune of 650 ± 10 μm is evidently discernible in longitudinal and cross-sectional sections of processed racer. The case obtained was fully matching across the contact regions required (design requirements). Further to understand the influence of thermal profile through the depth of treated layer associated with laser treatment cycle, microstructure analysis through the depth of treated layer processed under PW-UF (exhibiting maximum hardness improvement) mode is presented in Figure 9.6. SEM microstructures at different depths, namely, near surface HZ region (Figure 9.6(a)), intermediate region at 800 μm below the surface representing SSZ (Figure 9.6(b)) and UCZ region (Figure 9.6(c)) provide further insight into understanding of microstructures with depths of the laser treated layer. Its known that microstructural variations through the depth of treated layers follows the transformations induced due to the laser treatment cycle. The microstructure at a depth, in PW-UF mode, experiencing maximum peak temperature, exhibited refined martensite/austenite matrix with dispersion of uniformly distributed nano-carbides (higher amounts as compared to the surface region) and alloy carbides (MC). Indeed high austenitization duration would have facilitated in high-carbon martensite formation at this region and refinement in terms of nano-carbides in martensite/austenite matrix, thus contributing to maximum hardness improvement in the hardened layer (HZ region). Microstructures in SSZ region depicted in Figure 9.6(b) indicated drastic change in matrix microstructure with presence of undisturbed residual globular alloy carbides because of martensite decay as temperature experienced in the regions are well below lower critical A_{c1} temperature. As a result, drastic reduction in hardness to a tune of 520 ± 10 $HV_{0.5}$ be observed in SSZ region experiencing highest tempering temperature with maximum partitioning of cementite particles inter-located at austenite/martensite plates along with their coarsening. With further increase, in case depth below transition region (Figure 9.6(c)), as-received microstructure is discernible. Hardness in HZ region of laser treated layers increased to 1050 ± 20 $HV_{0.5}$, in convergence with refinement in martensitic matrix and globular carbides observed in its microstructures. Various studies on laser hardening of bearing steels concurred with the trend observed and attributed to higher dissolution of carbon from prior globular carbides in prior austenite grains [260]. Thus, PW-UF mode of processing facilitated in less tempering effect in the core region and thereby facilitating in higher retention of core strength.
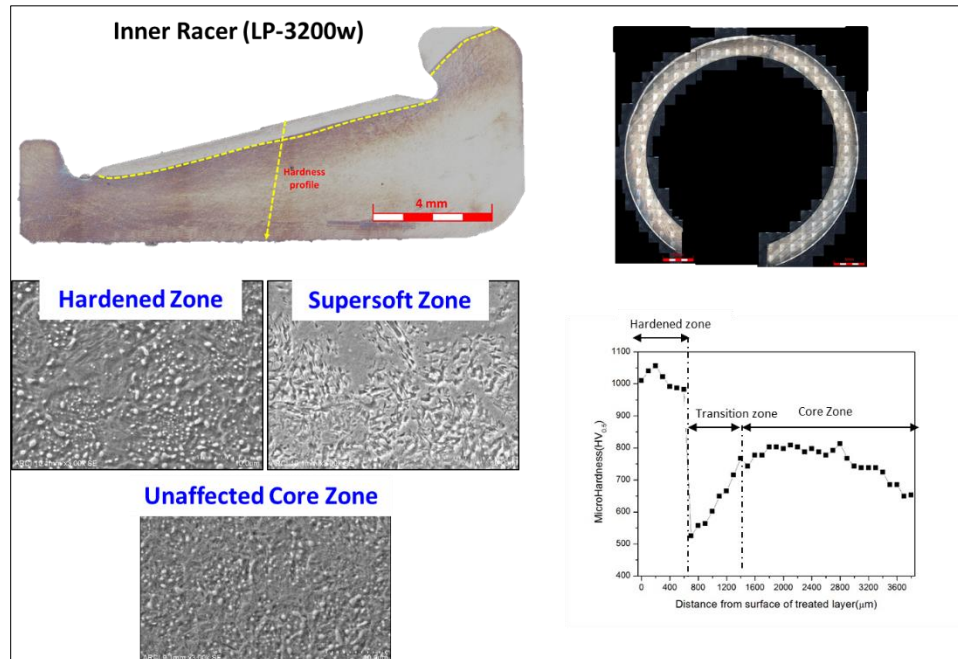
Fig. 9.6 Cross-sectional macrograph, microstructures and hardness distribution analysis of laser treated inner racer processed using water cooled fixture

9.7 Case depth and hardness distribution analysis of laser treated rollers processed using water cooled fixturing setup

Similar to the lines of successful design and development of fixturing setups for laser hardening of racers, appropriate water-cooling fixturing setup has been developed for processing of the roller of the chosen tapered roller bearing assembly. Figure 9.7 represents a typical case profile across the depth of laser treated layer of roller bearing element obtained in PW mode with external fluid-contact fixturing setup. The uniform HZ depth obtained in both longitudinal and cross-sectional be noted (1.0-1.5 mm). The case profile uniformity obtained was found to be matching across the contact regions required (design requirements) for the roller. Hardness in HZ region of laser treated layers of racer element increased to 1050 ± 20 HV$_{0.5}$, in convergence with refinement in martensitic matrix and globular carbides observed in its microstructure.
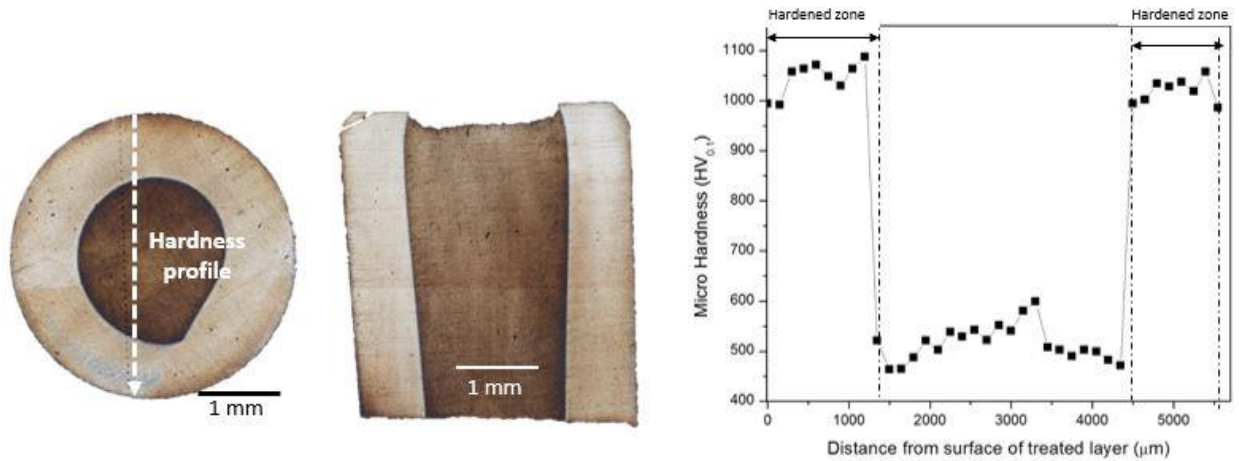
Fig. 9.7 Cross-sectional macrograph and hardness distribution of laser treated roller using water cooled fixture

9.8   Summary

The study conducted on laser surface hardening treatment with different thermal processing conditions successfully developed and demonstrated on actual tapered roller bearing elements with improvement in surface hardness and retention of core and thereby providing advantages when compared to conventional industrial practices. Designed and developed appropriate fixturing setups (analysing amount of fluid) for bearing elements to provide sufficient heat sink (fluid-chilled water) for increasing heat transfer coefficients and cooling rates. Roundness variations in bearing element such as outer racer was lowest when processed with PW-UF mode (60-70 µm) when compared to other processing modes. The hardness in the treated layer surface increased with increase in cooling rate associated with mode of laser processing in the order of CHT<CW<PW<PW-UF. Retention of core properties in bearing elements (outer racer, inner racer and roller) was successful by adopting laser pulsed mode and external flow of fluid condition. In this way, a deeper understanding of the process gained in comprehending the effect of different thermal processing conditions during laser transformation hardening treatment of bearing elements on case depth, hardness and dimensional variations.

CHAPTER 10

Conclusions and future scope of work

10.1 Conclusions

In the present research work, laser heat-input was controlled by varying laser processing parameters, different modes of processing (pulsed mode entails better control of temperature and thereby enhances cooling rates with greater uniformity), processing under different thermal conditions/setups yielding varied heat-transfer coefficients (involving external fluid contact) and cooling rates. To overcome the tempering effects in overlapped regions, when processing cylindrical bearing elements such as rollers, a quasi-stationary laser beam processing technique proposed and experimented with integration of a high-speed rotary axis to obtain a uniform hardened layer along the entire surface. An attempt was also made to develop and implement the developed laser surface hardening process on actual bearing elements of taper roller bearing with design and development of various fixturing and processing setups and studied their effects on distortion control and surface properties improvement with core retention.

Various work elements constitute: (a) Comprehensive study on the influence of prior-treatment conditions on laser surface hardening of bearing steel and their tribological performance evaluation; (b) Study on control of laser heat input (different modes of processing) and different thermal processing conditions with analysis of treated layer characteristics and assessment of their sliding wear performance; (c) Setting up of high-speed laser processing apparatus for surface hardening of cylindrical thin-sectioned steel parts/components using quasi-stationery laser beam approach; (d) Finite element analysis with development of a FEM model and statistical modelling with multi objective optimization employing RSM with desirability approach for high-speed laser surface hardening process on cylindrical part and (e) Application development of laser surface hardening process on actual tapered roller bearing elements with assessment of their engineering advantages in comparison with conventional methods.

From the preliminary study on influence of prior-treatment conditions on laser surface hardening of bearing steel and its tribological performance evaluation; following conclusions are drawn:

➢ Laser surface hardening of bearing steel with prior spheroidized and conventionally hardened and tempered condition showed improved properties in terms of hardness and sliding wear resistance.

➢ Spheroidized prior treated laser hardened bearing steel resulted in enhanced microstructural refinement with formation of nano alloy carbides in treated layers as compared to other conditions.

From the comprehensive study on control of laser heat input (different modes of processing) in laser surface hardening of bearing steel and their assessment of sliding wear performance, the following conclusions are drawn:

➢ Precise control in peak temperatures with improved cooling rates by adopting Pulsed Wave (PW) mode of processing overcome deleterious effects of large HAZ and retention of core.

➢ PW mode of processing facilitated in enhanced microstructural refinement with partially dissolved carbide globules with marginally reduced case depth as compared to that of Continuous Wave (CW) processed mode.

➢ The study demonstrated that the retained austenite content was observed to be lower and higher volume fraction of carbide phase in PW processed layer than in CW layer as PW mode experiences low period of austenitization and higher cooling rate during laser treatment cycle.

➢ PW mode of processing at optimum conditions resulted in 1000-1020 $HV_{0.5}$ with retention in core hardness as compared to CW mode processed counterpart whose maximum hardness achieved was 890-910 $HV_{0.5}$ along with significant reduction in core hardness due to tempering effect, whereas, hardness of untreated prior-hardened was in the range of $760 - 800$ $HV_{0.5}$.

➢ Sliding wear-testing results showed five-fold and three-fold improvements in un-lubricated and lubricated conditions of laser processed layer as compared to that of untreated one.

- ➢ Comparing friction coefficients with compressive residual stress obtained in HZ of laser treated layers processed with different operating modes, lowest coefficient of friction obtained in PW one and associated with highest compressive residual stress.
- ➢ The Surface processed with PW mode of processing had the highest compressive residual stress and thereby exhibited best wear resistance performance.

Comprehensive study has been carried out to investigate the influence of different thermal processing conditions that induce varied heat transfer coefficients and cooling rates on treated layer characteristics and sliding wear behaviour of laser surface hardened bearing steel. From the analysis of the results the following conclusions are drawn:

- ➢ The amount of fluid confined and the pulsing parameters greatly influence factors such as softening, component distortion and case profile uniformity of real parts such as bearing components for processing.
- ➢ PW mode of processing with fluid contact (PW-UF) induced largest compressive residual stress of -530 ± 10 MPa and exhibited best wear resistance performance.
- ➢ Hardness in the treated layer with microstructural refinement increased with increase in cooling rate in the order of CHT (780 ± 20 $HV_{0.5}$) < CW (910 ± 10 $HV_{0.5}$) < CW-UF ((950 ± 10 $HV_{0.5}$) < PW (1030 ± 10 $HV_{0.5}$) < PW-UF (1100 ± 10 $HV_{0.5}$).
- ➢ A two-to-three-fold improvement could be visualized in wear resistance of the laser treated surface processed under PW-UF steel sample when compared to CHT counterpart owing to the vast improvement in hardness and compressive residual stress level.
- ➢ The study also facilitated to develop the novel method of laser surface transformation hardening with pulsed-wave mode of processing under fluid contact beneath the thin-sectioned steel for effective retention of bulk properties with reduced distortion and improvement in tribological performance.

From the study on optimization of high-speed laser surface hardening process on cylindrical steel rod by adopting Response Surface Methodology and its correlation and validation with FEM model developed. Effect of three critical processing parameters, namely, Laser Power, Linear Speed and Rotary Axis Speed on the quality of laser hardened layer in terms of total case depth (TCD) and hardness distribution, namely - Mean Hardness - Cross-sectional

(MHC) and Differential Hardness – Longitudinal (DHL) were investigated and assessed, the following conclusions are drawn:

> An improvised system with integration of high-speed mini lathe and fixturing setup with diode laser system helped to generate a quasi-stationary annular laser beam for laser surface hardening of thin-sectioned cylindrical part.

> There exists an optimum range of processing parameters determined by the cylindrical steel rod diameter and laser spot dimensions, over which a uniform hardened layer could be achieved with high-speed rotation to achieve the uniform hardened case with complete elimination of softening effect associated with overlapped of circumferential tracks.

> Optimization of the process is achieved by maximizing case depth TCD and mean hardness through depth MHC and minimizing differential hardness across the treated layer length DHL.

> Combining the finite element method and the response surface methodology is an efficient way to optimize the process parameters and good agreement with less than 5% error found between the two methods.

> Assessing temperature history by FEM model with evaluation of surface temperatures, maximum/minimum surface temperatures, temperature differential and temperature distribution in longitudinal as well as axial directions through the rod length and thickness help facilitated in optimizing the process.

> The RSM methodology with BBD design established the empirical regression models for case depth and hardness distribution profiles across and along the axial and longitudinal directions of the laser-hardened layer obtained on the steel rod.

> According to regression model, linear quadratic and interactive terms of all three parameters of laser power, linear speed and rotary axis speed exerted effective influence on TCD, whereas linear and quadratic codes of laser power and linear speed influenced more on MHC and combined effect of linear speed and rotary axis speed on DHL. Experimental results of the model with desirability approach exhibited good agreement with less than 5% error.

> To achieve maximum case depth in 12 mm diameter En-31 steel rod with maximum hardness through its case depth and minimal differential hardness, the optimal parameters are laser power - 3.5 kW, linear speed - 8 mm/s and rotary axis speed - 2000 RPM.

➢ It is clear that by combining empirical model with RSM approach and FEM model with simulation of the process help facilitated effectively in optimizing the process to obtain maximum hardened layer throughout its processed length with greater uniformity in hardness distribution and complete elimination of deleterious softening and melting effects.

➢ The numerical approach of FEM model proposed and its validation with experimentation is an appropriate way to optimize the high-speed laser surface hardening process for assessing the hardened layer profile and optimizing the process for applying on engineering components of cylindrical geometry.

From the study conducted on laser surface hardening treatment with different thermal processing conditions successfully developed and demonstrated on actual tapered roller bearing elements with improvement in surface hardness and retention of core and thereby providing advantages when compared to conventional industrial practices, the following conclusions are drawn:

➢ Successfully developed and demonstrated laser surface hardening process on actual tapered roller bearing elements with improvement in surface hardness and retention of core and thereby providing advantages when compared to conventional industrial practices.

➢ Designed and developed appropriate fixturing setups for bearing elements to provide sufficient heat sink (fluid) for increasing heat transfer coefficients and cooling rates.

➢ Roundness variations in bearing element such as outer racer was lowest when processed with PW-UF mode (60-70 μm) when compared to other processing modes.

➢ Retention of core properties attained in bearing elements (outer, inner racers and rollers) when processed with pulsed mode and external flow of fluid condition.

10.2 Future Scope of Work

Present research involves control of laser heat-input by employing different modes of laser processing, different thermal processing conditions as well as by setting up of a high-speed laser processing setup for processing thin-sectioned bearing steel and application development

on actual bearing elements. The methodology adopted to overcome the tempering effects in overlapped regions, when processing cylindrical bearing elements such as rollers, a quasi-stationary laser beam processing technique proposed and experimented with integration of a high-speed rotary axis to obtain a uniform hardened layer along the entire surface is indeed successful and promising. The characterization of laser treated layers that include, case depth, microstructure, hardness, phase and residual stress, surface morphology, tensile properties as well as roundness measurements. The work also includes assessment of sliding wear behaviour of laser-treated and untreated steels employing high Hertzian contact pressures that simulate close-to-real bearing contact conditions and accompanied with assessment of wear mechanisms involved. Although an extensive study has been conducted in this regard, it is apparent that there are ample scopes for further work in this area.

Some suggestive directions for the possible future work given below:

➢ Testing and analysis of Rolling Contact fatigue (RCF) of Laser surface hardened layers and thereby assessing life of the bearing.

➢ Further analysis of laser treated layers using advanced characterization tools such as TEM, Nano-Indentation to assess influence of nano-carbides in improving strength of microstructure.

➢ Take up further studies to reduce deleterious retained austenite in laser treated layers with imparting of post laser-hardening treatments such as sub-zero treatment and also by imparting different treatments to bearing steel prior to laser hardening.

➢ Develop FEM model with experimental validation for high-speed laser hardening process employing different laser beam spots.

References

1. Chen L, Xie T, Xia X (2010) Rolling bearing application technology. China Machine Press, Beijing.

2. Chang H, Chen L (2007) Bearing assembly technology. Henan People's Publishing House, Zhengzhou.

3. Xie Y, Zhang S (2009) Research on development and present situation of tribology science and engineering application. Higher Education Press, Beijing.

4. Bhushan B (2007) Introduction to tribology. China Machine Press, Beijing.

5. A. P. Voskamp. Microstructural changes during rolling contact fatigue. PhD thesis, Technical University of Delft, 1996.

6. SKF. General Catalogue. Germany, 5000e edition, 2003.

7. T. S. Nisbet. Rolling Bearings. Number 04 in Engineering Design Guides. Oxford University Press, 1974.

8. H.K.D.H Bhadeshia, Mechanical bearings. Technical Report http://www.msm.cam.ac.uk/phase-trans/2010/types/index.html, University of Cambridge, Cambridge, U. K., 2010.

9. T. A. Harris and M. N. Kotzalas. Essential Concepts of Bearing Technology. Taylor & Francis, 2007.

10. Wilberth Solano Alvarez, "Microstructural degradation of bearing steels", PhD Thesis (2014).

11. M.-H. Evans. White structure flaking (WSF) in wind turbine gearbox bearings: effects of 'butterflies' and white etching cracks (WECs). Materials Science and Technology, 28:3–22, 2012.

12. E. N. Bamberger. Effect of materials – metallurgy viewpoint. In P. M. Ku, editor, Interdisciplinary Approach to the Lubrication of Concentrated Contacts, number SP– 237 in NASA, pages 409–437, Washington, D. C., USA, 1970. NASA.

13. E.V. Zaretsky E. V. Rolling Bearing Steels – A Technical and Historical Perspective, Materials Science and Technology, Vol. 29, No. 1, 2012, Institute of Materials, Minerals and Mining, London.

14. H. K. D. H. Bhadeshia. Steels for bearings. Progress in Materials Science, 57: 268–435, 2012.

15. W. J. Anderson, E. N. Bamberger, W. E. Poole, R. L. Thom, and E. V. Zaretsky. STLE life factors for rolling bearings. In E. V. Zaretsky, editor, Materials and Processing, pages 71–128, Park Ridge, IL, 1992. Society of Tribologists and Lubrication Engineers.

16. Murat Arbak, A. Erman Tekkaya, Feridun Ozhan, "Comparison of various preforms for hot forging of bearing rings", Journal of Materials Processing Technology 169 (2005) 72–82.

17. Lutz Nowag, Jens Solter, Ekkard Brinksmeier, "Influence of turning parameters on distortion of bearing rings", Prod. Eng. Res. Devel. (2007) 1:135–139.

18. E.V. Zaretsky, Rolling Bearing and Gear Materials, Tribology for Aerospace Applications, STLE SP-37, Society of Tribologists and Lubrication Engineers, 1997, p 325–451.

19. J. Dossett and G.E. Totten, ASM Handbook, Volume 4D, Heat Treating of Irons and Steels.

20. G. Krauss, Principals of Heat Treatment of Steels, ASM International, 1980, p 75–76.

21. J. Dossett, G.E. Totten, Introduction to Surface Hardening of Steels, (2013).

22. George, J. and Brock, R., "Polymeric engine bearings for hybrid and start stop applications," SAE Technical Paper 2012-01-1966, 2012.

23. Harris TA. Rolling bearing analysis. New York: Wiley; 2001.

24. Littmann WE, Widner RL. Propagation of contact fatigue from surface and subsurface origins. ASME J Basic Eng 1966;88:624–36.

25. Weinzapfel N, Sadeghi F. Numerical modeling of sub-surface initiated spalling in rolling contacts. Tribol Int 2013;59:210–21.

26. Lundberg G, Palmgren A. Dynamic capacity of roller bearings. Acta Polytech, Mech Eng Series 1952;2(4):1–32.

27. Cretu SS, Benchea MI. Compressive residual stresses effect on fatigue life of ball bearings. ASME international mechanical engineering congress and exposition; 2007.

28. T.E. Tallian, Failure Atlas for Hertz Contact Machine Elements (ASME Press, New York, 1992).

29. G. C. Pratt, "The seizure resistance of aluminium-based materials for engine bearings," Tribology, vol. 1, no. 2, pp. 109–114, 1968.

30. Q. Wang, "Seizure failure of journal-bearing conformal contacts," Wear, vol. 210, no. 1–2, pp. 8–16, 1997.

31. P Dinesh Babu, K R Balasubramanian and G Bhuvanasekharan, Int. J. of Surface Science and Engg, 5(2/3), 2011, pp.131.

32. J D Majumdar and I Manna, Sadhana, Vol.28, June/August 2003, pp.495.

33. Laser Institute of America, Handbook of Laser Materials Processing, Magnolia Publishing Inc., 2001

34. M Hua, Se Dao, T M Shao and H Y Tam, Journal of Materials Processing Technology, Vol.192-193, 2007, pp.89

35. Chengyun Cui, Jiandong Hu, Yuhua Liu, Kun Gao and Zuoxing Guo, Applied Surface Science, Vol.254, 2008, pp.6537

36. FAQ: What are the possible applications of laser surface engineering?, Weld. Inst. (n.d.). https://www.twi-global.com/technical-knowledge/faqs/faq-what-are-the-possible applications-of-laser-surface-engineering/ (accessed March 12, 2018).

37. E. Kennedy, G. Byrne, D.N. Collins, A review of the use of high power diode lasers in surface hardening, J. Mater. Process. Technol. 155–156 (2004) 1855–1860.

38. Design and Analysis of Experiments, 10th Edition. Douglas C. Montgomery. ISBN: 978-1-119-49244-3 June 2019.

39. William, M. Steen, and J. Mazumder. "Laser material processing." London, New York (1991): 108-144.

40. Ready, John F., and Dave F. Farson, eds. LIA handbook of Laser materials processing. Orlando: Laser Institute of America, 2001.

41. F. M. Kustas and M. S. Misra, "Application of ion implantation to improve the wear resistance of 52100 bearing steel", Thin Solid Films, Metallurgical and protective coatings, 122 (1984) 279-286.

42. Y. Chen, Y. Shi, H. Xie, Z. Wu, X. Jiang, T. Bell, H. Dong, Surf. Eng. 12 (2) (1996) 137.

43. K. Ram Mohan Rao, S. Mukherjee, P.M. Raole, I. Manna, "Low energy isothermal plasma-immersion ion implantation of nitrogen for enhanced hardness of AISI 52100 ball bearing steel", Surface and Coatings Technology 150 (2002) 80–87.

44. Yafeng Lian, Qunji Xue, Hanqing Wang, "The tribological behaviour of GCr15 bearing steel implanted with cerium", Surface and Coatings Technology 73 (1995) 98-104.

45. A. Erdemir and R. F. Hochman, "Surface metallurgical and tribological characteristics of TiN coated bearing steels", Surface and Coatings Technology, 36 (1988) 755 – 763.

46. Ali Erdemir, "Rolling-contact fatigue and wear resistance of hard coatings on bearing steel substrates", Surface and Coatings Technology, 54/55 (1992) 482-489.

47. W. Alma, A. Erdemir and R. F. Hochman, Proc. Conf. on Ion Plating and Implantation, Applications to Materials, American Society for Metals, Metals Park, OH, 1986, p. 169.

48. R. F. Bunshah, Thin Solid Films, 107 (1983) 21.

49. K. Komvopoulos, N. Saka and N. P. Suh, J. Tribol., 109 (1987) 223.

50. Ghulam Moeen Uddin, Awais Ahmad Khan, Muhammad Ghufran, Zia-ur-Rehman Tahir, Muhammad Asim, Muhammad Sagheer, Muhammad Jawad, Jawad Ahmad, Muhammad Irfan and Bilal Waseem, "Experimental study of tribological and mechanical properties of TiN coating on AISI 52100 bearing steel", Advances in Mechanical Engineering 2018, Vol. 10 (9) 1–10.

51. F.A.P. Fernandes, J. Gallego, C.A. Picon, G. Tremiliosi Filho, L.C. Casteletti, "Wear and corrosion of niobium carbide coated AISI 52100 bearing steel", Surface and Coatings Technology 279 (2015) 112-117.

52. Xiaoming He, Wenzhi Li, Hengde Li, "Tribological performance enhancement of amorphous hard carbon films on AISI 52100 bearing steel", Surface and Coatings Technology 71 (1995) 223-228.

53. A. Rahbar-kelishami, A. Abdollah-zadeh, M.M. Hadavi, R.A. Seraj, A.P. Gerlich, "Improvement of wear resistance of sprayed layer on 52100 steel by friction stir processing", Applied Surface Science 316 (2014) 501-507.

54. T.Y. Hsu (Xu Zuyao), Chen Yexin, and Chen Weiye, "Isothermal Martensite Formation in an AISI 52100 Ball Bearing Steel", Metallurgical Transactions A, Volume 18A, 1987, 1389-1394.

55. Chao Huang, Chaolei Zhang, Le Jiang, Yong Yang, Yazheng Liu, "Isothermal heat treatment of a bearing steel for improved mechanical properties", Journal of Alloys and Compounds 660 (2016) 131-135.

56. Ravindra kumar, J Alphonsa, Ram Prakash, K S Boob, J Ghanshyam, P A Rayjada, P M Raole and S Mukherjee, "Plasma nitriding of AISI 52100 ball bearing steel and effect of

heat treatment on nitrided layer", Bull. Mater. Sci., Vol. 34, No. 1, February 2011, pp. 153–159.

57. Xingliang Li, WenYue, ChengbiaoWang, Xiaocheng Gao, Song Wang, Jiajun Liu, "Comparing tribological behaviors of plasma nitrided and untreated bearing steel under lubrication with phosphor and sulfur-free organotungsten additive", Tribology International, 51 (2012), 47-53.

58. R. Ramesh, R. Gnanamoorthy, "Fretting wear behavior of liquid nitrided structural steel, En24 and bearing steel, En31", Journal of Materials Processing Technology 171 (2006) 61–67.

59. Karthikeyan Rajan, Vinod Joshi, Arindam Ghosh, "Effect of Carbonitriding on Endurance Life of Ball Bearing Produced from SAE 52100 Bearing Steels", Journal of Surface Engineered Materials and Advanced Technology, 2013, 3, 172-177.

60. Sukru Taktak, "Tribological behaviour of borided bearing steels at elevated temperatures", Surface & Coatings Technology 201 (2006) 2230–2239.

61. Sukru Taktak, Sukru Ulker, Ibrahim Gunes, "High temperature wear and friction properties of duplex surface treated bearing steels", Surface & Coatings Technology 202 (2008) 3367–3377.

62. Zhaoxi Cao, Tianqi Liu, Feng Yu, Wenquan Cao, Xiaodan Zhang, Yuqing Weng, "Carburization induced extra-long rolling contact fatigue life of high carbon bearing steel", International Journal of Fatigue 2019.

63. J. Chakraborty, D. Bhattacharjee and I. Manna, "Austempering of bearing steel for improved mechanical properties", Scripta Materialia 59 (2008) 247–250.

64. J. Chakraborty, D. Bhattacharjee and I. Manna, "Development of ultrafine bainite + martensite duplex microstructure in SAE 52100 bearing steel by prior cold deformation", Scripta Materialia 61 (2009) 604–607.

65. J. Chakraborty, P.P. Chattopadhyay, D. Bhattacharjee, and I. Manna, "Microstructural Refinement of Bainite and Martensite for Enhanced Strength and Toughness in High Carbon Low-Alloy Steel", Metallurgical and Materials Transactions A, Volume 41A, 2010, 2871-2879.

66. J. Chakraborty, I. Manna, "Development of ultrafine ferritic sheaves/plates in SAE 52100 steel for enhancement of strength by controlled thermomechanical processing", Materials Science and Engineering A, 548 (2012) 33-42.

67. Yuming Pan, Bingxu Wang, Gary C. Barber, "Study of bainitic transformation kinetics in SAE 52100 steel", Journal of Materials Research Technology, 2019.

68. E. C. Santos, K. Kida, T. Honda, H. Koike and J. Rozwadowska, "Fatigue strength improvement of AISI 52100 bearing steel by induction heating and repeated quenching", Materials Science, Vol. 47, No. 5, March, 2012.

69. Y.J. Cao, J.Q. Sun, F. Ma, Y.Y. Chen, X.Z. Cheng, X. Gao, K. Xie, "Effect of the microstructure and residual stress on tribological behavior of induction hardened GCr15 steel", Tribology International 115 (2017) 108-115.

70. A. Amanov, I.S. Cho, I.G. Park, Y.S. Pyun, "The migration of spheroidal cementite towards the surface in nanostructured AISI 52100 steel", Materials Letters 174 (2016) 142-145.

71. Yan-Li Song, Cheng Yu, Xia Miao, Xing-Hui Han, Dong-Sheng Qian, Xu Chen, "Tribological Performance Improvement of Bearing Steel GCr15 by an Alternating Magnetic Treatment", Acta Metall. Sin. (Engl. Lett.), 2017.

72. Matteo Villa, Karen Pantleon, Marcel A.J. Somers, "Enhanced carbide precipitation during tempering of sub-zero Celsius treated AISI 52100 bearing steel", Conference paper, April 2013.

73. D. Senthilkumar, "Influence of deep cryogenic treatment on hardness and toughness of En31 steel", Advances in Materials and Processing Technologies, 2018.

74. M. K. Chaanthini, Arul Sanjivi, "Improving Surface Hardness of EN31 Steel by Surface Hardening and Cryogenic Treatment", J. Inst. Eng. India Ser. D (2019) 100(1):37–42.

75. M.S. Devgun and P.A. Molian, "Experimental study of laser heat-treated bearing steel", Journal of Materials Processing Technology, 23 (1990) 41-54.

76. Iryna Yakimets, Caroline Richard, Gérard Béranger, Patrice Peyre, "Laser peening processing effect on mechanical and tribological properties of rolling steel 100Cr6", Wear 256 (2004) 311–320.

77. A. Basu, J. Chakraborty, S.M. Shariff, G. Padmanabham, S.V. Joshi, G. Sundararajan, J. Dutta Majumdar and I. Manna, "Laser surface hardening of austempered (bainitic) ball bearing steel", Scripta Materialia 56 (2007) 887–890.

78. S. Lei, Q.K. Liu, Y.P. Liu, H. Li. "Wear Behavior of Laser-hardened GCr15 Steel under Lubricated Sliding Conditions", Materials Science Forum Vol. 628-629 (2009) pp. 697-702.

79. Hong Zhou, Chengtao Wang, Qingchun Guo, Jiaxiang Yu, Mingxing Wang, Xunlong Liao, Yu Zhao, Luquan Ren, "Influence of processing medium on frictional wear properties of ball bearing steel prepared by laser surface melting coupled with bionic principles", Journal of Alloys and Compounds 505 (2010) 801-807.

80. R. Akhter, A. Hussain, W.A. Farooq and M. Aslam, "Laser Surface Hardening of GCr15 Bearing Steel Ring", Key Engineering Materials Vol. 442 (2010) pp. 130-136.

81. Donato Sorgente, Ottavio Corizzo, Antonio Ancona, Leonardo D. Scintilla, Gianfranco Palumbo, Luigi Tricarico, "Laser hardening of a AISI 52100 bearing steel with a discrete fiber laser spot", Proc. of SPIE Vol. 8963 1-10.

82. Peng-yu Lin, Yong-fu Zhu, Hong Zhou, Cheng-tao Wang and Lu-quan Ren, "Wear resistance of a bearing steel processed by laser surface remelting cooled by water", Scripta Materialia 63 (2010) 839-842.

83. Niroj Maharjan, Wei Zhou, Yu Zhou, Naien Wu, "Underwater laser hardening of bearing steels", Journal of Manufacturing Processes 47 (2019) 52-61.

84. WU Gan, WANG Rui, YANG Jang-ping, CHEN Xue-kang, CAO Sheng-zhu, GUO Wan-tu, SHANG kai-wen, Wei Bo, Wang Xiao-yi, Wang Lan-xi, "Study of laser nitriding on the GCR15 steel surface", Physics Procedia 18 (2011) 285–290.

85. L. Tricarico, A. Ancona, G. Palumbo, D. Sorgente, R. Spina, P.M. Lugara, "Discrete spot laser hardening and remelting with a high-brilliance source for surface structuring of a hypereutectoid steel", Materials and Design 115 (2017) 194-202.

86. F. Gutierrez Guzman, C. Sous, H. van Lier, G. Jacobs, "An energetic approach for the prognosis of thermally induced white etching layers in bearing steel 100CrMn6", Tribology International 143 (2020) 106096.

87. Y.K. Danileoko, A.M. Prokhorov, A.I. Pchelintsev, A.V. Sidorin, Heat hardening of steel by pulse-periodic laser radiation, Sov. J. Quantum Electron. 16 (12) (1986) 1611.

88. G. Habedank, J. Woitschig, T. Seefeld, W. Juptner, F. Vollertsen, R. Baierl, H. Bonas, P. Mayr, R. Schroder, F. Jablonski, R. Kienzler, Endurance limit of pulsed laser hardened component-like specimens—experiment and simulation, Mater. Sci. Eng. A 488 (2008) 358–371.

89. W. Wu, N.G. Liang, C.H. Gan, G. Yu, Numerical investigation on laser transformation hardening with different temporal pulse shapes, Surf. Coat. Technol. 200 (2006) 2686–2694.

90. T. Mioković, V. Schulze, O. Vöhringer, D. Löhe, Influence of cyclic temperature changes on the microstructure of AISI 4140 after laser surface hardening, Acta Mater. 55 (2) (January 2007) 589–599.

91. V. Kostov, J. Gibmeier, A. Wanner, Local residual stress distributions induced by repeated austenite-martensite transformation via laser surface hardening of steel AISI 4140, Mater. Sci. Forum 681 (March 2011) 321–326.

92. I.Yu. Smurov, A.A. Uglov, A.M. Lashyn, P. Matteazzi, L. Covelli, V. Tagliaferri, Modelling of pulse-periodic energy flow action on metallic materials, Int. J. Heat Mass Transf. 34 (4–5) (1991) 961–971.

93. M. Kalyon, B.S. Yilbas, Repetitive laser pulse heating analysis: pulse parameter variation effects on closed form solution, Appl. Surf. Sci. 252 (6) (2006) 2242–2250. 15 January.

94. S.Z. Shuja, B.S. Yilbas, S.M.A. Khan, Laser consecutive pulse heating and phase change: influence of spatial distribution of laser pulse intensity on melting, Int. J. Therm. Sci. 48 (10) (2009) 1960–1966.

95. B. Mahmoudi, M.J. Torkamany, A.R. Sabour Rouh Aghdam, J. Sabbaghzade, Laser surface hardening of AISI 420 stainless steel treated by pulsed Nd:YAG laser, Mater. Des. (1980-2015) 31 (5) (May 2010) 2553–2560.

96. J. Jiang, L. Xue, S. Wang, Discrete laser spot transformation hardening of AISI O1 tool steel using pulsed Nd:YAG laser, Surf. Coat. Technol. 205 (21–22) (2011) 5156–5164.

97. A.K. Nath, A. Gupta, F. Benny, Theoretical and experimental study on laser surface hardening by repetitive laser pulses, Surf. Coat. Technol. 206 (8–9) (2012) 2602–2615.

98. H. Ki, S. So, S. Kim, Laser transformation hardening of carbon steel sheets using a heat sink, J. Mater. Process. Technol. 214 (11) (2014) 2693–2705.

99. S. Kim, S. So, H. Ki, Controlling thermal deformation using a heat sink in laser transformation hardening of steel sheets, J. Mater. Process. Technol. 216 (2015) 455–462.

100. J.R. Bradley, S. Kim, Laser transformation hardening of iron-carbon and iron-carbon chromium steels, Metallurgical transactions A, Phys. Metall. Mater. Sci. 19 A (8) (1988) 2013–2025.

101. Sangwoo So, Hyungson Ki (2013) 'Effect of specimen thickness on heat treatability in laser transformation hardening', in International Journal of Heat and Mass Transfer, vol. 61, p.266–276.

102. B. Jin, M. Li, T. Woo Hwang, Y. Hoon Moon, Feasibility studies on underwater laser surface hardening process. Adv. Mater. Sci. Eng. 2015 (2015) 6, 845273. https://doi.org/10.1155/2015/845273. Hindawi Publishing Corporation.

103. T. Sibalija, V. Majstorovic, Advanced Multi response Process Optimization, Springer International Publishing, 2016.

104. A. Issa, Computational Control of Laser Systems for Micro-Machining, Dublin City University, 2007.

105. P. Dinesh Babu, G. Buvanashekaran, K. R. Balasubramanian, Experimental investigation of laser transformation hardening of low alloy steel using response surface methodology, Int J Adv Manuf Technol (2013) 67:1883–1897.

106. P. Dinesh Babu, G. Buvanashekaran & K. R. Balasubramanian, The Elevated Temperature Wear Analysis of Laser Surface–Hardened EN25 Steel Using Response Surface Methodology, Tribology Transactions (2015), 58: 602–615.

107. S. Guarino, M. Barletta, Abdelkarim Afilal, High power diode laser surface hardening of low carbon steel: Fatigue life improvement analysis, Journal of Manufacturing Processes 28 (2017) 266-271.

108. D. A. Lesyk, S. Martinez, B.N. Mordyuk, V.V. Dzhemelinskyi, A. Lamikiz, G. I. Prokopenko, Effect of laser heat treatment combined with ultrasonic impact treatment on the surface topography and hardness of carbon steel AISI 1045, Optics and Laser technology (2019), 111, 424-438.

109. Mahmoud Moradi, Mojtaba karamiMoghadam, High power diode laser surface hardening of AISI 4130; statistical modelling and optimization, Optics and Laser Technology (2019), 111, 554-570.

110. Changrong Chen, Xianbin Zeng, Qianting Wang, Guofo Lian, Xu huang, Yan Wang, Statistical modeling and optimization of microhardness transition through depth of laser hardened AISI 1045 carbon steel, Optics and Laser Technology (2020), 124, 105976.

111. Mahmoud Moradi, Hossein Arabi, Mahmoud Shamsborhan, "Multi-objective optimization of high power diode laser surface hardening process of AISI 410 by means of RSM and desirability approach", Optik (2020), 163619.

112. D. S. Badkar, K. S. Pandey, G. Buvanashekaran, "Effects of laser phase transformation hardening parameters on heat input and hardened-bead profile quality of unalloyed titanium", Trans. Nonferrous Met. Soc. China 20 (2010) 1078-1091.

113. A.R. Hamad, J.H. Abboud, F.M. Shuaeib, K.Y. Benyounis, "Surface hardening of commercially pure titanium by laser nitriding: Response surface analysis", Advances in Engineering Software 41 (2010) 674–679.

114. Sagar V. Telrandhe, Jayabalan Bhagyaraj, Sushil Mishra, Shyamprasad Karagadde, A new approach to control and optimize the laser surface heat treatment of materials, Journal of Materials Processing Tech. 262 (2018) 493-502.

115. Noureddine Barka, Abderrazak El Ouafi, Effects of Laser Hardening Process Parameters on Case Depth of 4340 Steel Cylindrical Specimen-A Statistical Analysis, Journal of Surface Engineered Materials and Advanced Technology (2015), 5, 124-135.

116. Rachid Fakir, Noureddine Barka, Jean Brousseau, Gabriel Caron-Guillemette, Numerical Investigation by the Finite Difference Method of the Laser Hardening Process Applied to AISI-4340, Journal of Applied Mathematics and Physics (2018), 6, 2087-2106.

117. Leung, M.K., H. Man, and J. Yu, Theoretical and experimental studies on laser transformation hardening of steel by customized beam. International Journal of Heat and Mass Transfer, 2007. 50(23): p. 4600-4606.

118. Shiue, R. and C. Chen, Laser transformation hardening of tempered 4340 steel. Metallurgical Transactions A, 1992. 23(1): p. 163-170.

119. Ashby, M. and K.E. Easterling, The transformation hardening of steel surfaces by laser beams-I. Hypo-eutectoid steels. Acta Metallurgica, 1984. 32(11): p. 19351939-19371948.

120. Ki, H., S. So, and S. Kim, Laser transformation hardening of carbon steel sheets using a heat sink. Journal of Materials Processing Technology, 2014. 214(11): p. 2693-2705.

121. Sun, P., et al., Laser surface hardening of 42CrMo cast steel for obtaining a wide and uniform hardened layer by shaped beams. The International Journal of Advanced Manufacturing Technology, 2014. 70(5-8): p. 787-796.

122. Shuja, S. and B. Yilbas, Laser multi-beam heating of moving steel sheet: Thermal stress analysis. Optics and lasers in Engineering, 2013. 51(4): p. 446-452.

123. Li, R., et al., A Comparative Study of High-Power Diode Laser and CO_2 Laser Surface Hardening of AISI 1045 Steel. Journal of materials engineering and performance, 2014. 23(9): p. 3085-3091.

124. Moncayo, M.A., et al., Laser surface modification of alumina: integrated computational and experimental analysis. Ceramics International, 2013. 39(6): p. 6207-6213.

125. Ahmed, N., K. Voisey, and D. McCartney, Investigation into the effect of beam shape on melt pool characteristics using analytical modelling. Optics and Lasers in Engineering, 2010. 48(5): p. 548-554.

126. Semak, Vladimir V., B. Damkroger, and S. Kempka. "Temporal evolution of the temperature field in the beam interaction zone during laser material processing." Journal of Physics D: Applied Physics 32.15 (1999): 1819.

127. Obergfell, K., V. Schulze, and O. Vöhringer. "Simulation of phase transformations and temperature profiles by temperature controlled Laser hardening: influence of properties of base material." Surface engineering 19.5 (2003): 359-363.

128. Kong, Fanrong, S. Santhanakrishnan, and Radovan Kovacevic. "Numerical modeling and experimental study of thermally induced residual stress in the direct diode Laser heat treatment of dual-phase 980 steel." The International Journal of Advanced Manufacturing Technology 68.9-12 (2013): 2419-2430.

129. Yan, B. G., and J. C. Liu. "Calculation of laser transformation hardening with circular beam." Materials Technology 27.1 (2012): 5-7.

130. Jerniti, Ahmed Ghazi, Abderazzak El Ouafi, and Noureddine Barka. "Single Track Laser Surface Hardening Model for AISI 4340 Steel Using the Finite Element Method." Modeling and Numerical Simulation of Material Science 6.02 (2016): 17.

131. A. Khajeh, S.A.J. Jahromi, The finite element analysis of the surface transformation hardening process using the power control strategy in order to reduce edge effect problems, Comput. Mater. Sci. 88 (1) (June 2014) 151–155.

132. Sehyeok Oh, Hyungson Ki, "Prediction of hardness and deformation using a 3-D thermal analysis in laser hardening of AISI H13 tool steel", Applied Thermal Engineering 121 (2017) 951-962.

133. Stefano Guarino and Gennaro Salvatore Ponticelli, "High Power Diode Laser (HPDL) for Fatigue Life Improvement of Steel: Numerical Modelling", Metals 2017, 7, 447.

134. V. R. Barath, M. Tak, R. Padmanaban, and G. Padmanabham, "Adaptive Process Control for Uniform Laser Hardening of Complex Geometries Using Iterative Numerical Simulation," Materials Performance and Characterization 8, no. 6 (2019): 1178–1191.

135. Saeed Talesh Alikhani, Mohammad Kazemi Zahabi, Mohammad Javad Torkamany, Seyed Hasan Nabavi, "Time-dependent 3D modeling of the thermal analysis of the high-power diode laser hardening process", Optics and Laser Technology 128 (2020) 106216.

136. S. B. Hosseini, K. Ryttberg, J. Kaminski, U. Klement (2012) 'Characterization of the Surface Integrity induced by Hard Turning of Bainitic and Martensitic AISI 52100 Steel', in Procedia CIRP 1, p.494 – 499.

137. Hoon Hwang and Bruno C. De Cooman, Influence of the Initial Microstructure on the Spheroidization of SAE 52100 Bearing Steel, steel research int. 87 (2016) No. 1.

138. J. V. Lyons and M. J. Hudson. Machining properties of high-carbon chromium bearing steels. Technical Report Special Report 94, Iron and Steel Institute, London, U.K., 1967.

139. H. K. D. H. Bhadeshia. Steels for bearings. Progress in Materials Science, 57:268–435, 2012.

140. D. Luo, M.J. Peet, S. W. Ooi, P. Yan, Z. Yin, H.K.D.H. Bhadeshia (2014), 'Materials science and technology', Vol. 30, p.1282-1286.

141. L. Karmazin. Experimental study of the austenitization process of hypereutectoid steel alloyed with small amounts of silicon, manganese and chromium, and with an initial

structure of globular cementite in a ferrite matrix. Materials Science & Engineering A, 142:71–77, 1991.

142. E. V. Zaretsky. Rolling bearing steels – a technical and historical perspective. Materials Science and Technology, 28:58–69, 2011.

143. A. P. Voskamp. Microstructural Changes During Rolling Contact Fatigue. PhD thesis, Technical University of Delft, 1996.

144. A. T. W. Barrow, J. H. Kang, and P. E. J. Rivera-Diaz del Castillo. The $\varepsilon \to \eta \to \theta$ transition in 100Cr6 and its effect on mechanical properties. Acta Materialia, 60(6):2805–2815, 2012.

145. M.J. Balart, A. Bouzina, L. Edwards, M.E. Fitzpatrick (200

146. 'The onset of tensile residual stresses in grinding of hardened steels', Materials Science and Engineering A, vol. 367, p.132–142.

147. J H Kang, P E J Rivera-Diaz-del-Castillo (2013), 'Carbide dissolution in bearing steels', Computational Materials Science, Vol.67, p.364-372.

148. Wenwen Song, Pyuck-pa Choi, Gerhard Inden, Ulrich Prahl, DierkRaabe, and Wolfgang Bleck (2014) 'On the Spheroidized Carbide Dissolution and Elemental Partitioning in High Carbon Bearing Steel 100Cr6', in Metallurgical and Materials Transactions A, vol. 45A, p. 595-606.

149. Leonardo Orazi, Erica Liverani, Alessandro Ascari, Alessandro Fortunato, Luca Tomesani. Laser surface hardening of large cylindrical components utilizing ring spot geometry, CIRP Annals 63 (2014) 233-236.

150. Guy Claus, and M. Seifert, High speed rotation hardening of steel shafts and holes with high power diode lasers, ICALEO (2007) congress proceedings, P543.

151. N. Ahmed, K.T. Voisey, D.G. McCartney, Investigation into the effect of beam shape on melt pool characteristics using analytical modelling, Optics and Lasers in Engineering 48 (2010) 548–554.

152. T. L. Bergman, A. S. Lavine, F. P. Incropera, and D. P. DeWitt, Fundamentals of Heat and Mass Transfer (Hoboken, NJ: Wiley, 2011).

153. Design and Analysis of Experiments, 10th Edition. Douglas C. Montgomery. ISBN: 978-1-119-49244-3 June 2019.

154. D.C. Montgomery, Design and Analysis of Experiments, John Wiley, New York, 2009.

155. A. Khorram, M. Ghoreishi, CO2 laser welding of Ti6Al4V alloy and the effects of laser parameters on the weld geometry, Lasers Eng 21 (2011) 135–148.

156. A. Khorram, M. Ghoreishi, Laser assisted brazing of Inconel 718: the effects of process parameters and subsequent optimization, Lasers Eng 31 (2015) 333–350.

157. ASTM E975-03 (2008) Standard Practice for X-Ray Determination of Retained Austenite in Steel with Near Random Crystallographic Orientation", ASTM International, West Conshohocken, PA, U.S.A.

158. B. Winiarski, M. Benedetti, V. Fontanari, M. Allahkarami, J.C. Hanan, P.J. Withers (2016), 'High Spatial Resolution Evaluation of Residual Stresses in Shot Peened Specimens Containing Sharp and Blunt Notches by Micro-hole Drilling, Micro-slot Cutting and Micro-X-ray Diffraction Methods', Experimental Mechanics, vol.56, p.1449–1463.

159. Seyyed Hesamodin Talebi, Mohammad Jahazi and Haikouhi Melkonyan, "Retained Austenite Decomposition and Carbide Precipitation during Isothermal Tempering of a Medium-Carbon Low-Alloy Bainitic Steel", Materials (Basel). 2018 Aug; 11(8): 1441.

160. B. D. Cuillity: Elements of X-ray Diffraction, Addison-Wesley Publishing Company, USA, (1978).

161. R. K. Khatirkar, P. Yadav and S. G. Sapate: ISIJ Int., 52 (2012), 1370.

162. D. Shtansky, K. Nakai, Y. Ohmori, Acta Mater. 1999, 47, 2619.

163. Y. L. Tian, R. W. Kraft, Metall. Trans. A 1987, 18, 1403.

164. G. H. Zhang, J. Y. Chae, K. H. Kim, D. W. Suh, Mater. Charact. 2013, 81, 56.

165. A. S. Pandit, H. K. D. H. Bhadeshia, P. Roy. Soc. A-Math. Phy. 2012, 468, 2767.

166. Z. X. Li, C. S. Li, J. Zhang, B. Qiao, Z. Z. Li, Metall. Mater. Trans. A 2015, 46, 3220.

167. M. Spezzapria, A. G. Settimi, L. Pezzato, M. F. Novella, M. Forzan, F. Dughiero, S. Bruschi, A. Ghiotti, K. Brunelli, M. Dabal, Steel Res. Int. 2017, 88, 1.

168. Nandita Gupta, S.K. Sen (2006) 'Spheroidization Treatment for Steels', in Defence Science Journal, vol. 56, No. 4, pp. 665-676.

169. E. De Moor, S. Lacroix, A.J. Clarke, J. Penning & J.G. Speer, "Effect of Retained Austenite Stabilized via Quench and Partitioning on the Strain Hardening of Martensitic Steels", Metallurgical and Materials Transactions A volume 39, Article number: 2586 (2008).

170. Private correspondence, Technical Forum 00-1 'Retained Austenite: It's Impact on Bearing Performance', BRENCO Inc. (www.brencoqbs.com).

171. Guanghua Zhou, Song Deng, Wenting Wei and Qinglong Liu, "Effect of multiple deep cryo-treating and tempering on microstructure and property evolution of high carbon bearing steel", Mater. Res. Express 7 (2020) 066529.

172. Y. Totik, R.Sadeler, H.Altun, M.Gavgali, 'The effects of induction hardening on wear properties of AISI 4140 steel in dry sliding conditions', Materials and Design 24(2003) 25-30.

173. Y.J. Cao, J.Q. Sun, F. Ma, Y.Y. Chen, X.Z. Cheng, X. Gao, K. Xie, 'Effect of the microstructure and residual stress on tribological behavior of induction hardened GCr15 steel', Tribology International 115(2017) 108–115.

174. Ji YP, Wu SJ, Xu LJ, Li Y, Wei SZ, ''Effect of carbon contents on dry sliding wear behavior of high vanadium high speed steel', Wear (2012) 294–295:239–45.

175. T Lohner, J Mayer, K Michaelis, B-R Hohn and K Stahl (2015) 'On the running-in behavior of lubricated line contacts', Proc IMechE Part J: Journal of Engineering Tribology 0(0) p.1–13.

176. A.D. Anoop, A.S. Sekhar, M. Kamaraj, K. Gopinath (2015), 'Numerical evaluation of subsurface stress field under elastohydrodynamic line contact for AISI 52100 bearing steel with retained austenite', Vol. 330-331, p.636-642.

177. L. Wang, R.J.K Wood, T.J. Harvey, S. Morris, H.E.G. Powrie, I. Care (2003), 'Wear performance of oil lubricated silicon nitride sliding against various bearing steels', Vol. 255, p. 657-668.

178. Vipin Goyal, Sandan Kumar Sharma, B. Venkata Manoj Kumar (2015), 'Effect of lubrication on tribological behavior of martensitic stainless steel', Materials Today proceedings Vol.2, p. 1082-1091.

179. Ibrahim Gunes, Adem Cicek, Kubilay Aslantas, Fuat Kara, "Effect of Deep Cryogenic Treatment on Wear Resistance of AISI 52100 Bearing Steel", Trans Indian Inst Met (2014) 67(6):909–917.

180. Aydar Akchurin, Rob Bosman, Piet M. Lugt (2017), 'Generation of Wear Particles and Running-In in Mixed Lubricated Sliding Contacts', Tribology International, Vol. 110, p.201-208.

181. Elliot Biro (2013) 'Heat affected zone softening kinetics in Dual Phase and Martensitic steels', PhD thesis.

182. Wen Cui, David San-Martin, Pedro E.J. Rivera-Diaz-del-Castillo, 'Towards efficient microstructural design and hardness prediction of bearing steels - An integrated experimental and numerical study', Materials and Design (2017), 464-475.

183. T. Miokovic, V. Schulze, O. Vohringer, D. Lohe (2007) 'Influence of cyclic temperature changes on the microstructure of AISI 4140 after laser surface hardening', in Acta Materialia vol. 55, p.589–599.

184. Sangwoo So, Hyungson Ki (2013) 'Effect of specimen thickness on heat treatability in laser transformation hardening', in International Journal of Heat and Mass Transfer, vol. 61, p.266–276.

185. R. Akhtar, A. Hussain, W.A Farooq, M. Aslam, '"Laser Surface Hardening of GCr15 Bearing Steel Ring", in: Key Engineering Materials Vol. 442 (2010) p.130-36.

186. Sangwoo So, Hyungson Ki (2013) 'Effect of specimen thickness on heat treatability in laser transformation hardening', in International Journal of Heat and Mass Transfer, vol. 61, p.266–276.

187. R. Akhtar, A. Hussain, W.A Farooq, M. Aslam, '"Laser Surface Hardening of GCr15 Bearing Steel Ring", in: Key Engineering Materials Vol. 442 (2010) p.130-36.

188. Donato Sorgente, Ottavio Corizzo, Antonio Ancona, Leonardo Daniele Scintilla, 'Laser hardening of AISI 52100 bearing steel with a discrete fiber laser spot', Conference paper in: Proceedings of SPIE- The International Society for Optical Engineering (2014).

189. Wenwen Song, Pyuck-pa Choi, Gerhard Inden, Ulrich Prahl, Dierk Raabe, and Wolfgang Bleck (2014) 'On the Spheroidized Carbide Dissolution and Elemental Partitioning in High Carbon Bearing Steel 100Cr6', in Metallurgical and Materials Transactions A, vol. 45A, p. 595-606.

190. K. H. Habig, E. Broszeit, A. W. J. De Gee, 'Friction and Wear Tests on Metallic Bearing Materials for Oil Lubricated Bearings', Wear (1981), Vol. 69, p.43 - 54.

191. Vipin Goyal, Sandan Kumar Sharma, B. Venkata Manoj Kumar (2015), 'Effect of lubrication on tribological behavior of martensitic stainless steel', Materials Today proceedings Vol.2, p. 1082-1091.

192. Y. Totik, R.Sadeler, H.Altun, M.Gavgali, 'The effects of induction hardening on wear properties of AISI 4140 steel in dry sliding conditions', Materials and Design 24(2003) 25-30.

193. Peter J. Blau, 'On the nature of running-in', Tribology International 38(2005) 1007-1012.

194. Y.J. Cao, J.Q. Sun, F. Ma, Y.Y. Chen, X.Z. Cheng, X. Gao, K. Xie, 'Effect of the microstructure and residual stress on tribological behavior of induction hardened GCr15 steel', Tribology International 115(2017) 108–115.

195. Liu, H.T. Lu, Z.S. Sun, Y.Z., 'Status and development of residual stress on the surface in the cutting', Aviation Precision Manufacturing Technology 44(2008), 554-558.

196. Kong, D.J. Hua, T.S. Ding, J.N. Yuan, N.Y. Chen, J.F., 'Effects of laser quenching on residual stresses and wear resistance of grey cast iron', Lubrication Engineering 34(2009), 53-54.

197. Shuwen Wang, Feiyan Yan, Ao Chen (2016), 'Tribological effects of laser surface texturing and residual stress', Industrial Lubrication and Tribology.

198. Ji YP, Wu SJ, Xu LJ, Li Y, Wei SZ, ''Effect of carbon contents on dry sliding wear behavior of high vanadium high speed steel', Wear (2012) 294–295:239–45.

199. L. Wang, R.J.K Wood, T.J. Harvey, S. Morris, H.E.G. Powrie, I. Care (2003), 'Wear performance of oil lubricated silicon nitride sliding against various bearing steels', Vol. 255, p. 657-668.

200. A.D. Anoop, A.S. Sekhar, M. Kamaraj, K. Gopinath (2015), 'Numerical evaluation of subsurface stress field under elastohydrodynamic line contact for AISI 52100 bearing steel with retained austenite', Vol. 330-331, p.636-642.

201. N. Muthu Nilavan, G. Rajaram (2017), 'Effect on lubrication regimes with silicon nitride and bearing steel balls', Tribology International, vol.116, p.403-413.

202. Aniruddha Gupta, Ashish Kumar Nath (2011) 'Temperature Field of Repetitive Laser Pulse Irradiation and Its Effect on Laser Surface Hardening', in Applied Mechanics and Materials vol. 110-116.

203. Ashish Kumar Nath, Aniruddha Gupta, Frederick Benny (2012) 'Theoretical and experimental study on laser surface hardening by repetitive laser pulses', in Surface & Coatings Technology, vol. 206, p.2602–2615.

204. T. Miokovic, V. Schulze, O. Vohringer, D. Lohe (2007) 'Influence of cyclic temperature changes on the microstructure of AISI 4140 after laser surface hardening', in Acta Materialia vol. 55, p.589–599.

205. Y Lakhtin (1975), Engineering Physical Metallurgy Textbook, MIR Publishers.

206. Sangwoo So, Hyungson Ki (2013) 'Effect of specimen thickness on heat treatability in laser transformation hardening', in International Journal of Heat and Mass Transfer, vol. 61, p.266–276.

207. Wenwen Song, Pyuck-pa Choi, Gerhard Inden, Ulrich Prahl, DierkRaabe, and Wolfgang Bleck (2014) 'On the Spheroidized Carbide Dissolution and Elemental Partitioning in High Carbon Bearing Steel 100Cr6', in Metallurgical and Materials Transactions A, vol. 45A, p. 595-606.

208. E C Santos, K Kida, T. Honda, H Koike, J. Rozwadowska (2012), 'Fatigue strength improvement of AISI 52100 bearing steel by induction heating and repeated quenching', Materials Science, Vol.47, p.5.

209. C. Soriano, J. Leunda, J. Lambarri, V. GarcíaNavas, C. Sanz (2011) 'Effect of laser surface hardening on the microstructure, hardness and residual stresses of austempered ductile iron grades', in Applied Surface Science, vol. 257, p.7101–7106.

210. Epp Jeremy, SurmHolger, Kessler Olaf, Hirsch Thomas (2007) 'In situ X-ray phase analysis and computer simulation of carbide dissolution of ball bearing steel at different austenitizing temperatures', in Acta Materialia 55 (17), 5959-5967.

211. Elliot Biro (2013) 'Heat affected zone softening kinetics in Dual Phase and Martensitic steels', PhD thesis.

212. A. Filep , M. Benke M , V. Mertinger , G. Buza (2015) 'Residual stress in plain carbon steel induced by laser hardening', in Materials Science Forum, vol. 812, p.321-326.

213. E. Liverani, A.H.A. Lutey, A. Ascari, A. Fortunato, L. Tomesani (2016) 'A complete residual stress model for laser surface hardening of complex medium carbon steel components', in Surface & Coatings Technology, vol. 302, p.100–106.

214. V. Kostov; J. Gibmeier; A. Wanner (2017) 'Spatially resolved temporal stress evolution during laser surface spot hardening of steel', in Journal of Materials Processing Technology vol. 239 p: 326—335.

215. C. Soriano, J. Leunda, J. Lambarri, V. GarcíaNavas, C. Sanz (2011) 'Effect of laser surface hardening on the microstructure, hardness and residual stresses of austempered ductile iron grades', in Applied Surface Science, vol. 257, p.7101–7106.

216. Neil S Bailey, Wenda Tan, Yung C Shin (2009) 'Predictive modeling and experimental results for residual stresses in laser hardening of AISI 4140 steel by a high power diode laser' in Surface & Coatings Technology vol. 203, p.2003–2012.

217. Kong DJ, Hua TS, Ding JN, Yuan NY, Chen JF (2009) 'Effects of laser quenching on residual stresses and wear resistance of grey cast iron', Lubrication Engineering, 21-54.

218. T Lohner, J Mayer, K Michaelis, B-R Hohn and K Stahl (2015) 'On the running-in behavior of lubricated line contacts', Proc IMechE Part J: Journal of Engineering Tribology 0(0) p.1–13.

219. Y. Totik, R. Sadeler, H. Altun, M. Gavgali (2003) 'The effects of induction hardening on wear properties of AISI 4140 steel in dry sliding conditions', Materials and Design, vol. 24, p. 25-30.

220. L. Wang, R.J.K Wood, T.J. Harvey, S. Morris, H.E.G. Powrie, I. Care (2003), 'Wear performance of oil lubricated silicon nitride sliding against various bearing steels', Vol. 255, p. 657-668.

221. A.D. Anoop, A.S. Sekhar, M. Kamaraj, K. Gopinath (2015), 'Numerical evaluation of subsurface stress field under elastohydrodynamic line contact for AISI 52100 bearing steel with retained austenite', Vol. 330-331, p.636-642.

222. N. Muthu Nilavan, G. Rajaram (2017), 'Effect on lubrication regimes with silicon nitride and bearing steel balls', Tribology International, vol.116, p.403-413.

223. Aydar Akchurin, Rob Bosman, Piet M. Lugt (2017), 'Generation of Wear Particles and Running-In in Mixed Lubricated Sliding Contacts', Tribology International, Vol. 110, p.201-208.

224. Vipin Goyal, Sandan Kumar Sharma, B. Venkata Manoj Kumar (2015), 'Effect of lubrication on tribological behavior of martensitic stainless steel', Materials Today proceedings Vol.2, p. 1082-1091.

225. G. Sutter, N. Ranc (2010), 'Flash temperature measurement during dry friction process at high sliding speed', Vol. 268, p.1237-1242.

226. T. Miokovic, V. Schulze, O. Vohringer, D. Lohe (2007) 'Influence of cyclic temperature changes on the microstructure of AISI 4140 after laser surface hardening', in Acta Materialia vol. 55, p.589–599.

227. Sangwoo So, Hyungson Ki (2013) 'Effect of specimen thickness on heat treatability in laser transformation hardening', in International Journal of Heat and Mass Transfer, vol. 61, p.266–276.

228. Ashish Kumar Nath, Aniruddha Gupta, Frederick Benny (2012) 'Theoretical and experimental study on laser surface hardening by repetitive laser pulses', in Surface & Coatings Technology, vol. 206, p.2602–2615.

229. D. S. Badkar, K. S. Pandey, G. Buvanashekaran, Effects of laser phase transformation hardening parameters on heat input and hardened-bead profile quality of unalloyed titanium, Trans. Nonferrous Met. Soc. China 20 (2010), 1078-1091.

230. Leonardo Orazi, Erica Liverani, Alessandro Ascari, Alessandro Fortunato, Luca Tomesani. Laser surface hardening of large cylindrical components utilizing ring spot geometry, CIRP Annals 63 (2014) 233-236.

231. L. Giorleo, A. Liu, B. Previtali, Apparent Spot in Circular Laser Hardening: Effect of Process Parameters, Int. J Mater Form (2010) Vol. 3 Suppl 1:1119 – 1122.

232. Sehyeok Oh, Hyungson Ki, "Prediction of hardness and deformation using a 3-D thermal analysis in laser hardening of AISI H13 tool steel", Applied Thermal Engineering 121 (2017), 951-962.

233. Saeed Talesh Alikhani, Mohammad Kazemi Zahabi, Mohammad Javad Torkamany, Seyed Hasan Nabavi, "Time-dependent 3D modeling of the thermal analysis of the high-power diode laser hardening process", Optics and Laser Technology 128 (2020) 106216.

234. Francisco Cordovilla, Angel Carcia-Beltran, Paula Sancho, Jesus Dominguez, Leonrado Ruiz-de-Lara, Jose L Ocana, "Numerical/experimental analysis of the laser surface hardening with overlapped tracks to design the configuration of the process for Cr-Mo steels", Materials and Design 102 (2016), 225 -237.

235. Soundarapandian Santhanakrishnan, Rodovan Kovacevic, "Hardness prediction in multi-pass direct diode laser heat treatment by on-line surface temperature monitoring", Journal of Materials Processing Technology 212 (2012), 2261-2271.

236. Hongwei Xu, W. Wayne Chen & Kun Zhou, Yumei Huang , Q. Jane Wang, "Temperature field computation for a rotating cylindrical workpiece under laser quenching", Int J Adv Manuf Technol (2010) 47:679–686.

237. Tsung-Pin Hung, Chao-Ming Hsu, Hsiu-An Tsai, Shuo-Ching Chen, Zong-Rong Liu, "Temperature Field Numerical Analysis Mode and Verification of Quenching Heat Treatment Using Carbon Steel in Rotating Laser Scanning", Materials (2019) 12(3), 534.

238. Tsung-Pin Hung, Hao-En Shi and Jao-Hwa Kuang, "Temperature Modeling of AISI 1045 Steel during Surface Hardening Processes", Materials 2018, 11(10), 1815.

239. Mahmoud Moradi, Mojtaba karami Moghadam, High power diode laser surface hardening of AISI 4130; statistical modelling and optimization, Optics and Laser Technology (2019), 111, 554-570.

240. Rachid Fakir, Noureddine Barka, Jean Brousseau, "Case study of laser hardening process applied to 4340 steel cylindrical specimens using simulation and experimental validation", Case Studies in Thermal Engineering 11 (2018), 15-25.

241. Peipei Sun, Shaoxia Li, Gang Yu, Xiuli He, Caiyun Zheng, Weijian Ning, "Laser surface hardening of 42CrMo cast steel for obtaining a wide and uniform hardened layer by shaped beams", Int J Adv Manuf Technol (2014) 70:787–796.

242. Sagar V. Telrandhe, Jayabalan Bhagyaraj, Sushil Mishra, Shyamprasad Karagadde, A new approach to control and optimize the laser surface heat treatment of materials, Journal of Materials Processing Tech. 262 (2018) 493-502.

243. D.C. Montgomery, Design and Analysis of Experiments, John Wiley, New York, 2009.

244. A. Khorram, M. Ghoreishi, CO_2 laser welding of Ti6Al4V alloy and the effects of laser parameters on the weld geometry, Lasers Eng 21 (2011) 135–148.

245. A. Khorram, M. Ghoreishi, Laser assisted brazing of Inconel 718: the effects of process parameters and subsequent optimization, Lasers Eng 31 (2015) 333–350.

246. H. Sohrabpoor, A. Issa, A. Al Hamaoy, I.U. Ahad, E. Chikarakara, K. Bagga, D. Brabazon, Advances in Laser Materials Processing, Chapter 24; 2018, Development of Laser Processing Technologies via Experimental Design, pp. 707-729.

247. Noureddine Barka, Abderrazak El Ouafi, Effects of Laser Hardening Process Parameters on Case Depth of 4340 Steel Cylindrical Specimen-A Statistical Analysis, Journal of Surface Engineered Materials and Advanced Technology (2015), 5, 124-135.

248. Mahmoud Moradi, Mojtaba karamiMoghadam, High power diode laser surface hardening of AISI 4130; statistical modelling and optimization, Optics and Laser Technology (2019), 111, 554-570.

249. D. S. Badkar, K. S. Pandey, G. Buvanashekaran, Effects of laser phase transformation hardening parameters on heat input and hardened-bead profile quality of unalloyed titanium, Trans. Nonferrous Met. Soc. China 20 (2010), 1078-1091.

250. Mahmoud Moradi, Hossein Arabi, Mahmoud Shamsborhan, Multi-Objective Optimization of High Power Diode Laser Surface Hardening Process of AISI 410 by means of RSM and Desirability Approach, Optik (2020), Vol. 202, 163619.

251. Ali Khorrama, Akbar Davoodi Jamaloei, Moslem Paidar, Xinjin Cao, Laser cladding of Inconel 718 with 75Cr3C2+25(80Ni20Cr) powder: Statistical modeling and optimization, Surface and coatings technology 378 (2019) 124933.

252. Changrong Chen, Xianbin Zeng, Qianting Wang, Guofo Lian, Xu huang, Yan Wang, Statistical modeling and optimization of microhardness transition through depth of laser hardened AISI 1045 carbon steel, Optics and Laser Technology (2020), 124, 105976.

253. Luca Giorleo, Elisabetta Ceretti, Claudio Giardini (2013) Fe modeling of the apparent spot technique in circular laser hardening. Int J Adv Manuf Technol 69:1961–1969.

254. S. Sashank, P. Dinesh Babu, P. Marimuthu, Experimental studies of laser borided low alloy steel and optimization of parameters using response surface methodology, Surface and Coatings Technology 363 (2019), 255-264.

255. Sagar V. Telrandhe, Jayabalan Bhagyaraj, Sushil Mishra, Shyamprasad Karagadde, A new approach to control and optimize the laser surface heat treatment of materials, Journal of Materials Processing Tech. 262 (2018) 493-502.

256. K. Obergfell, V. Schulze and O. Vohringer, "Classification of microstructural changes in laser hardened steel surfaces", Materials Science and Engineering A 355, S. 348-356 (2003).

257. Sangwoo So, Hyungson Ki (2013) 'Effect of specimen thickness on heat treatability in laser transformation hardening', in International Journal of Heat and Mass Transfer, vol. 61, p.266–276.

258. Wen Cui et al., "Towards efficient microstructural design and hardness prediction of bearing steels – An integrated experimental and numerical study", Materials and Design 133, 464-475 (2017).

259. Kong D J, Hua T S, Ding J N, Yuan NY, Chen JF, "Effects of laser quenching on residual stresses and wear resistance of grey cast iron", Lubrication Engineering, 21-54 (2009).

260. Wenwen Song, Pyuck-pa Choi, Gerhard Inden, Ulrich Prahl, Dierk Raabe, and Wolfgang Bleck (2014) 'On the Spheroidized Carbide Dissolution and Elemental Partitioning in High Carbon Bearing Steel 100Cr6', in Metallurgical and Materials Transactions A, vol. 45A, p. 595-606.

LIST OF PUBLICATIONS

International and National Journal Publications

1. **E. Anusha, Adepu Kumar, S M Shariff**, "Numerical and Statistical Modelling of High Speed Rotating Diode Laser Surface Hardening Process on a Steel Rod", Optics and laser Technology (2021), vol.143, 107309.

2. **E. Anusha, Adepu Kumar, S M Shariff**, "Finite Element Analysis and Experimental Validation of High-Speed Laser Surface Hardening Process", International Journal of Advanced Manufacturing Technology (2021), https://doi.org/10.1007/s00170-021-07303-z

3. **E. Anusha, Adepu Kumar, S M Shariff**, "Diode laser surface treatment of bearing steel for improved sliding wear performance", Optik- International Journal for Light and Electron Optics (2020), vol. 206, 163357.

4. **E. Anusha, Adepu Kumar, S M Shariff**, "A novel method of laser surface hardening treatment inducing different thermal processing condition for Thin-sectioned 100Cr6 steel", Optics and Laser Technology (2020), vol. 125, 106061.

5. **E. Anusha, Adepu Kumar, G. Padmanabham, S M Shariff**, "Novel Technique of Controlling Heat Input for Core Retention & Reduction in Distortion in Laser Surface Treatment of Bearing Racer", Article in Bulletin of ILA (2018), Vol.29, No.3, Pg.35-45.

International Conferences

1. **E. Anusha, Adepu Kumar, S M Shariff,** "Diode Laser Surface Treatment of Bearing Steel for Improved Sliding Wear Performance", 22nd International Conference on Wear of Materials (WOM), April 14-18th 2019, Florida, US.

2. **E. Anusha, Adepu Kumar, G. Padmanabham, S M Shariff,** "Novel Technique of Controlling Heat Input for Core Retention & Reduction in Distortion in Laser Surface Treatment of Bearing Racer", 27th DAE-BRNS National Laser Symposium, Dec 2018.

Manuscripts under preparation

1. **E. Anusha, Adepu Kumar, S M Shariff,** "Study on the influence of different prior-treatment conditions on conventional and laser surface hardening processes on improving sliding wear resistance".

2. **E. Anusha, Adepu Kumar, S M Shariff,** "Modelling of heat flow during single-pulse laser hardening process on bearing steel using COMSOL: An approach with experimental validation".

Patent (to be filed based on patentability)

1. **E. Anusha, Adepu Kumar, S M Shariff,** "An improved process and apparatus for high speed laser strengthening of cylindrical metallic components for engineering applications".

CURRICULUM VITAE

1	Name	E. Anusha
2	Date of birth	04th September 1993
3	Educational qualifications	
	B.E (2014)	M.V.S.R Engineering College, Nadergul, R.R.Dist.
	Specialization	Mechanical Engineering
	Pursuing PhD	National Institute of Technology, Warangal
4	Research Interests	Materials Characterizations, Laser Surface Processing, Hardening, Tribology of metals, Numerical Simulations
5	Permanent Address	H.no: 9-5-237, Flat no.202, S V Sama Yadi Reddy Nilayam, Road No.3, Street No.1, East Maruthi Nagar, Champapet, Hyderabad, Telangana -500079
	Email	anusha.epparla@gmail.com
	Contact number	7382413886